Your Brain on Plastic: Measuring the Physiological to Transcriptomic Responses of Human Microglia to Consumer-Grade Micro- and Nanoplastics

by

Seth Alexander Paul Vogt

A thesis submitted to the Graduate Faculty of
Auburn University
in partial fulfillment of the
requirements for the Degree of
Master of Science

Auburn, Alabama
May 2nd, 2026

Keywords: Microplastics, Nanoplastics, Human Health, Human Brain, Secondary Microplastics, Polystyrene

Approved by

Dr. Priscila Falagan Lotsch, Associate Professor of Biological Sciences
Dr. Katharine Horzmann, Associate Professor of Pathobiology
Dr. Aaron Rashotte, Professor of Biological Sciences
Dr. Pengyu Chen, Francis Family Associate Professor of Mechanical Engineering

Abstract

The production of plastics has reached record levels, with nearly half a billion metric tonnes produced annually. As such, there have been staggering increases in the amount of mismanaged- along with landfill-bound plastic waste across the globe. This has lead to increasing contamination of microplastics (MPs), or plastics smaller than 5 mm, caused by degradation of consumer plastics. Further break down of MPs can lead to the formation of nanoplastics (NPs), or plastics smaller than 1 µm. Both MPs and NPs (MNPs) have been detected in nearly every human organ, including the brain, leading to an increased public concern about their impact on the body. However, the vast majority of studies that seek to understand the impacts of MNPs rely on industrially manufactured, "pristine" polystyrene (PS) nanobeads to serve as a proxy for the "real-world" plastics that are found in the human body. While these particles can be beneficial to understand some of the basic perturbations of plastics in the body, they are far too heterogeneous in terms of size, shape, and composition to accurately model the polydisperse MNPs that have been found in human organs. The absence of studies using relevant plastic models has led to concern in the field as the general interpretation of the impacts of these ubiquitous contaminants remains loosely connected to the real-life situation. This work aims to bridge this research grasp by not only understanding the impacts of real-world MNPs derived from common plastic consumer items, cups and forks, but also comparing these impacts against pristine PS-NPs that are commonly used in toxicological studies. The impact that these pristine particles have, with diameters ranging from 50 - 100 nm (PS-50), are directly contrasted against the impacts elicited by cup-derived and fork-derived plastics (Cup- and Fork-MNPs) on the *in vitro* brain target human microglial clone 3 (HMC3) cells. Plastics used for exposure underwent extensive material characterization, including size, morphology, surface charge, trace-metal

contamination, and composition. Microglial cells, which comprise nearly 10% of the brain' cellular composition, are the primary immune cells of the central nervous system (CNS) and are commonly used in neuro-degenerative studies to measure the immune response of the brain. By exposing these cells to physiologically-relevant concentrations of both real-world Cup- and Fork-MNPs and comparing the impacts to exposure of pristine PS-50 NPs, the discrepancies between the two plastic conditions can be identified and used to elucidate potential shortcomings of previous studies in the field.

In the first chapter of this study, a comprehensive review of plastic generation, MNP accumulation, and human exposures are detailed in order to serve as a basis for the study's impact. In the second chapter, HMC3 cells were exposed to 0.1, 1.0, and 10 µg/mL concentrations of real-world and pristine MNPs for 72 hours in order to elucidate the physiological responses of the brain's immune system. By focusing on redox homeostasis, inflammatory signaling, and mitochondrial function, an assessment of the cellular responses to MNPs can be made in order to understand the functional changes that may be seen in the brain. In the third chapter, HMC3 cells were exposed to the same plastics at 0.1 µg/mL, the lowest concentration tested, for 72 hours and had their transcriptome sequenced in order to assess the impacts of MNPs on the brain at the gene-expression level. This allows for a detailed understanding of the cellular response in microglia that may be overshadowed by transcriptional and translational lag time or cellular adaptations. Overall, pristine NPs were seen to elicit a heightened response relative to real-world MNPs through decreased mitochondrial respiration, mitochondrial membrane depolarization, decreases in ATP production, stronger inflammatory signaling, and greater redox perturbation, suggesting distress. Contrarily, real-world MNPs displayed an adaptive cell stress response profile through lessened, often nonsignificant disruptions to many of these same parameters. This was further supported through the pristine NP-exposed cells' enriched endoplasmic reticulum (ER) stress and tRNA aminoacylation pathways relative to real-world MNPs, suggesting significantly different stress profiles even at the lowest concentration of MNPs tested. In both real-world MNP-exposed samples,

collagen formation-dominated expression profiles were observed, with both Cup- and Fork-MNPs sharing similar transcriptomic enrichments.

Overall, this works serves to support the necessity of utilizing representative plastic particles to model the effects of MNPs on the human body, specifically the brain. The variations in biological responses between real-world and pristine plastics at both the physiological level as well as the transcriptomic level underscore this fact, as pristine particles were shown to evoke stronger stress responses relative to real-world MNPs. By better understanding the effects caused by MNPs from consumer products, researchers can more accurately assess the risks posed by plastics and develop more effective mitigation strategies.

Artificial Intelligence Use Disclosure Statement

In preparation of this thesis, the following Artificial Intelligence (AI) tools were used: Perplexity AI, OpenAI's ChatGPT and Prism, and Anthropic's Claude. These tools were used primarily for the purposes of researching, outlining, grammatical and syntactical adjustments, code development in LaTex, R, and bash, and proofreading. The author acknowledges full responsibility for the intellectual content of this work and has ensured that any AI-assisted sections have been thoroughly reviewed and edited for accuracy and appropriate academic style. Any AI-generated content was modified before incorporation into the final document to maintain scholarly integrity of this research. AI did not generate or modify raw data, did not perform unsupervised statistical analyses, and was not used to fabricate, alter, or selectively report results. All code, outputs, figures, and conclusions presented in this thesis were reviewed, validated, and, where necessary, independently reproduced by the author.

Acknowledgments

I would like to recognize Dr. Priscila Falagan Lotsch for her unwavering support during my graduate career and Dr. Ábner Magalhães Nunes for his vital assistance with experimental design and data analysis. I extend my gratitude towards the members of my committee for their guidance in my project and towards the faculty members of the University who have helped further my interest and knowledge in both biological sciences and materials engineering. Additionally, I thank my friends, parents, and fellow laboratory members Bruce and Beverly for their support in these past two years.

Table of Contents

List of Tables

List of Figures

Chapter 1

Plastics as an Emerging Health Concern in Human Livelihood

1.1 Global Plastic Production

Plastics, defined as a substance with a high composition of polymeric material, have become an essential part of the modern day global economy [1]. With nearly every consumer good produced containing a plastic element, it is fair to say that the world would not operate as it does today without this vital discovery. The first synthetic plastic material was synthesized in 1907 by Leo Baekeland in New York, named Bakelite [2]. By combining phenol and formaldehyde under intense pressure and temperature, Baekland was able to formulate a thermoset with high degrees of cross-linkage, providing the structural rigidity needed to use the material to form consumer goods. Despite the known reaction between the two precursors, Baekeland was the first to create a commercially viable product that was brought to market [3].

The desirable properties of this plastic, including heat, electrical, and chemical resistance, led to the molding of the first plastic materials. Even under high temperature conditions, Bakelite was able to maintain structural rigidity, beating out previous industry-dominating materials such as shellac, ebonite, and celluloid [4]. The novelty in this polymeric material was its electrical resistance, which led to its incorporation into a vast majority of the consumer electronic devices that rose to prominence in the turn of the century, most notably radios and telephones [5].

The desire for plastics in products has only grown in the years since, driven by their desirable properties. In order to match demand of industrial use, the production of plastics worldwide has reached year-over-year records. Modern plastic production has reached new highs, with an estimated 460 million metric tonnes (MMT) produced in 2024 alone [6]. This

unprecedented level of production rivals that of even conventional materials, with paper production put at an estimated 420 MMT in the year previous [7]. When including rubber with plastic manufacturing, which itself is almost entirely a synthetic polymer, the estimated worldwide market value exceeds half a trillion in United States (US) dollars [8].

Today, plastics have found their way into an even wider variety of products, including food packaging [9, 10], cosmetics [11], and even medical devices [12]. By far, plastics are most commonly used in packaging, with over 30% of plastics produced (146 MMT) going towards this category (Figure 1.1) [13, 14]. With the market grown to having included many varieties of plastics, the use-cases of polymer class materials have reached new heights. Advancements in polymer science and material engineering have lead to breakthroughs in their uses, including antimicrobial bio-polymers [15] and more adaptable thermosets [16]. Between these innovations, growing global populations, and increased manufacturing capabilities, an estimated 884 MMT of plastic are expected to be produced annually by 2050 [17].

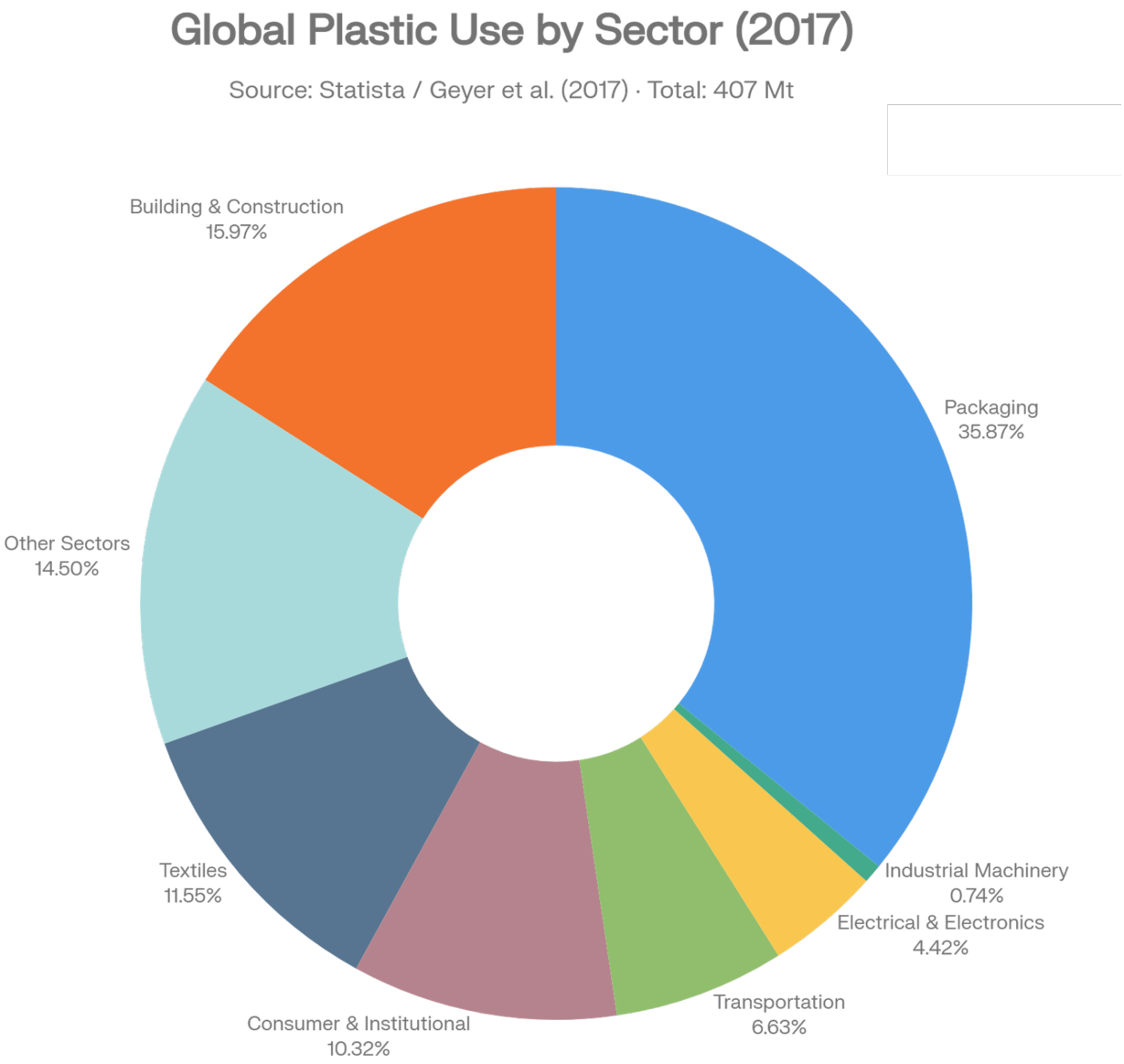

Figure 1.1: The Production of Plastics by Industry. From data reported by Geyer et al in 2017 and published on Statista, total global plastic production ranged to approximately 407 million metric tonnes (MMT) in 2017. Packaging represented the largest share (146 Mt; 35.9%), followed by building and construction (65 MMT; 16.0%), textiles (47 MMT; 11.5%), consumer and institutional products (42 MMT; 10.3%), transportation (27 MMT; 6.6%), electrical/electronics (18 MMT; 4.4%), industrial machinery (3 MMT; 0.7%), and other sectors (59 MMT; 14.5%). Figure created in Python.

1.2 Improper Plastic Disposal and Environmental Contamination

With nearly half a billion metric tonnes of plastics produced annually, it can be easily inferred that some portion is mismanaged. And indeed, emerging studies have shown this to be the case. It is estimated that in the time since 1950, well over 6,300 MMT of plastic have been designated as waste [13]. From this amount, the vast majority (4,900 MMT) have been left to decay in mass landfills, with only 600 MMT having ever been recycled. The "Big Seven" plastics (PE, PP, polyvinyl chloride [PVC], PET, polyurethane [PU], polyester [PES] and PS) account for over 90% of plastics produced, and none show any considerable ability to biodegrade [13].

Extensive quantities of plastic goods are disposed of directly into the environment, with an estimated 20 MMT of plastic waste entering streams, rivers, and oceans globally each year [18]. A vast majority of mismanaged plastic waste is generated in Asia, with China, Indonesia, India, and the Philippines responsible for millions of metric tonnes annually [19]. Outside of Asia, Egypt and Kenya lead the African plastic waste, while Brazil and Argentina lead the Americas. North America, Oceania, and Europe produce a total amount of mismanaged waste less than that of some of the largest cities in Asia.

The majority of plastics do not disappear in human lifespans. The degradation of plastics allows for these particulate pollutants to persist in the environment for timeframes up to hundreds or even thousands of years. To truly dispose of plastics, incineration plants must expend a vast amount of energy in order to combust or pyrolyze the waste, breaking down the chemical structure [13]. However, even this strategy remains flawed, as plastics have been detected to remain in ash as well as release into the atmosphere from flue gas of incineration facilities [20, 21].

While landfills present a major avenue for disposal, they are not the only endpoints for plastics. As previously mentioned, mismanaged plastic waste is a vast contributor to the pollutant's exposure in the environment [19, 22, 23]. Additionally, incineration plants are able to spread these particles far across the globe with plastic contamination in the ashes

and gases produced by combustion and pyrolysis processes [20, 21]. Even mundane human activities such as laundry has been found to release PES fibres, with an estimated average of 200 mg of plastics released per kilogram of washed fabrics [24].

Once in the environment, plastics are able to circulate for hundreds or even thousands of years [25]. In aquatic ecosystems, plastics can be ingested by microorganisms and larger fish, whether inadvertently or by mistaking particles for food [26, 27]. These particles can then traverse the food chain, making their way into consumer-desired fish species and into the the human body (Figure 1.2) [28, 29].

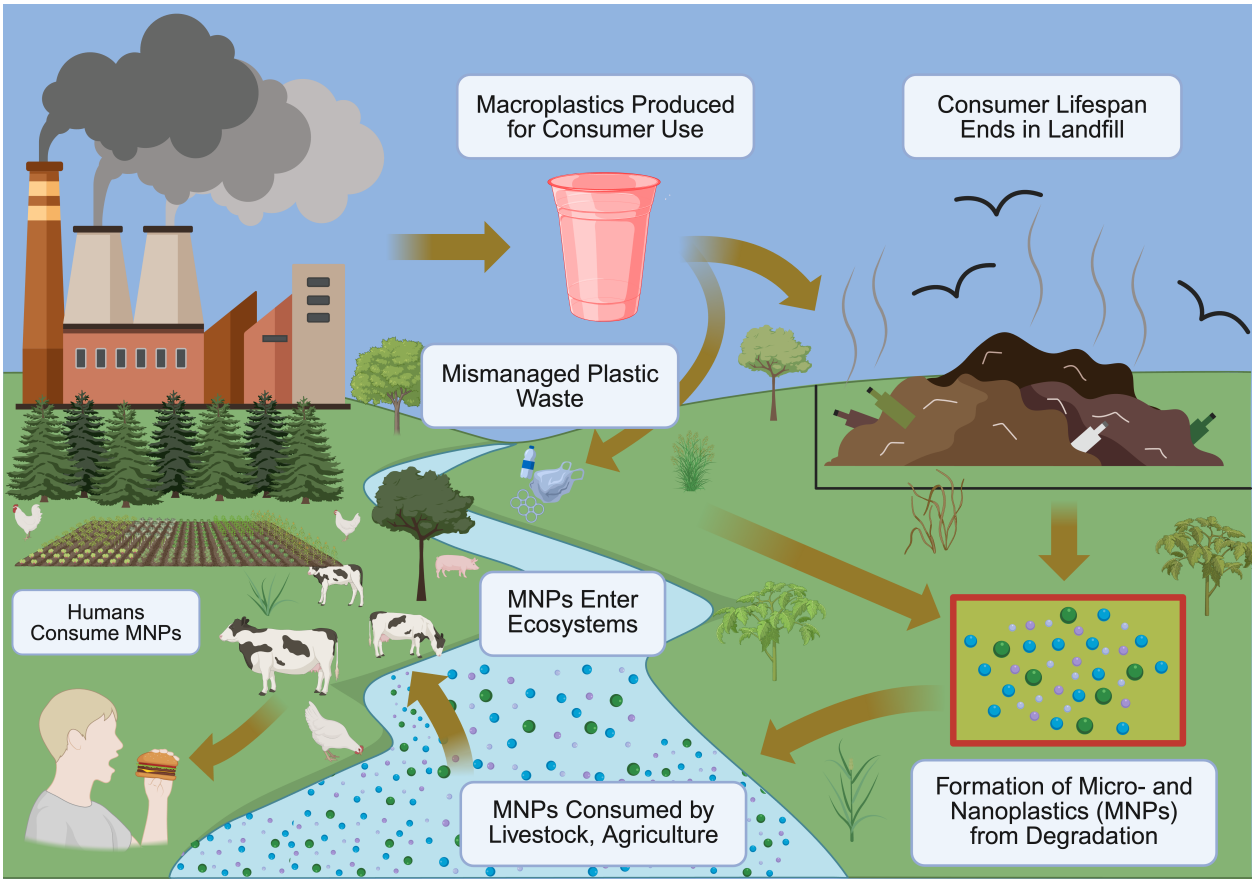

Figure 1.2: The Plastic Cycle. Plastics created for the express purpose of consumer goods often end up in landfills. Plastics are then able to degrade into micro- and nanoplastic (MNP) fragments, where they can serve as a vector for other contaminants in the environment. MNPs are able to escape landfills as leachate, where they can end up in the watershed. This water can then be directly consumed by humans, or used in agricultural or livestock applications, making their way into the food chain where they can be ingested by humans. Figured created in BioRender.

Even the most remote species are not insulated from anthropogenic plastic pollution. A newly described *Eurythenes* amphipod inhabiting the hadal zone of the Mariana Trench was found to contain MPs in its gastrointestinal tract, and thus consequently named *Eurythenes plasticus* to reflect this pervasive contamination [30]. Plastics have also been detected far from direct emission sources in lower and upper layers of the atmosphere, ranging from a few meters to 20 kilometers in elevation, where nanoplastics are often the dominant fraction and have been measured at concentrations up to 2.3 µg/m^3 [31, 32].

With a clear economic incentive behind their production and use, it does not remain a mystery as to why plastic is one of the leading materials on the planet. However, by consequence of the chemical structure of polymers themselves, the degradation rates of plastics are among some of the lowest of any material. Whereas ordinary organic materials are degraded by principles dictated by the Earth's carbon cycle, organic plastics do not share the same fate [33].

1.3 Micro- and Nanoplastics Generation

Plastics with a high degree of cross-linkage exhibit a higher degree of stability relative to linear polymers [34]. Networked polymers display a lessened mobility and increased rigidity. Given the connection between multiple polymeric chains through covalent bonding, the network becomes more energetically stable in its conformation. Thus, a higher energy is necessary in order to break apart the bonds and corresponding structure. Because of this principle, chemical decomposition of these materials requires a much greater energetic input, indirectly increasing their lifespan. Plasticizers and other additives to plastics can also act to extend the lifespan by providing further chemical stability [35].

Plastics are often found to be broken down through processes such as thermal-, ozonic-, mechanical-, catalytic-, biological-, and photo-degradation [36] (Figure 1.3). While typically sufficient to clear organic matter, due to the aforementioned principles, these mechanisms can drag the lifespan of plastics for up to thousands of years [37]. Polymers such as polystyrene

(PS), polyethylene (PE), polypropylene (PP), and polyethylene terephthalate (PET) show a degradation rate of less than 1 µm per year, indicating the persistence of these incredibly common materials in the environment [38]. Land-based degradation experiments typically yield the longest lifespan of plastics, where direct exposure to sunlight and biological systems such as fungi and bacteria often increase the rates at which polymeric units can be broken down [39].

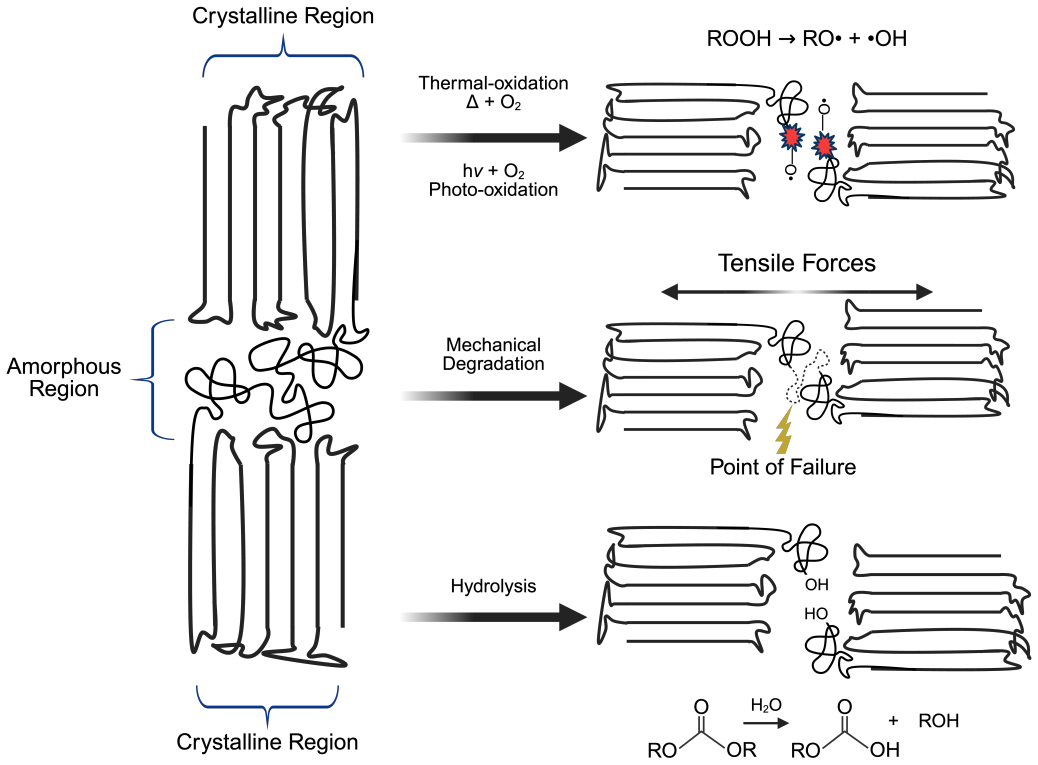

Figure 1.3: Examples of Plastic Degradation Processes. Figured created in BioRender.

Semicrystalline polymers such as plastics contain regions of regular lattices, or crystalline regions, along with segments of randomly arranged chains with lower density and higher mobility, or amorphous regions [40]. As plastics break down, they fragment into smaller pieces along amorphous regions [41, 42, 43]. These lower-energy regions possess higher free volume, allowing for oxidation, hydrolytic, and radiative processes to occur at a higher frequency. Additionally, as stresses accumulate, the forces are disproportionately directed

to these regions so that scissions are able to propagated while preserving the more resilient crystalline regions.

The mechanisms through which plastics degrade include chemical and physical, and their efficacy depend on the polymer chemistry, morphology, and environment. Nearly each pathway involves the fragmentation of polymer backbones or side chains, reducing the covalent bond strength of the structure. As the material transitions from ductile, elastic-dominated to brittle, inelastic behaviour, it becomes much more susceptible to fragmentation into smaller-sized particles [44]. As scissions grow, number-average molecular weight drops and the crystallinity increases. This is able to decrease the glass transition temperature (Tg), which is defined as the temperature where amorphous regions of polymers become more flexible or rubbery [45].

Hydrolytic degradation is one such mechanism consistent with this phenomenon. Seen primarily in polymers hydrolysable backbones such as PES, polyamides (PA), and PU, water acts as a nucleophile across susceptible bonds, cleaving the structure [46]. In the presence of elevated temperatures, thermal degradation becomes a dominant driver of bond scission within the polymer. When oxygen and sunlight are present, this process is further exacerbated through thermo-oxidative and photo-oxidative pathways. Thermal- and photo-generated radicals react with oxygen to form reactive oxygen species (ROS) that propagate chain decomposition [47, 41].

An additional set of processes that contribute to fragmentation include mechanical and stress degradation. Through repeated abrasion, loading, and stress, cracks and scissions are localized in amorphous regions to the point of structural failure. Hydrolysis and oxidation can form initial points of failures, which fail more readily at lower stress energies [48].

While these processes take extended periods to fully remove consumer-sized plastics from landfills, they readily contribute to the formation of small plastic fragments. The degradation of macroplastics, or plastics above 5 mm, can lead to the formation of microplastics (**MPs**) [49]. The conditions for these events are intensified in landfills, where plastic waste

are exposed to extreme thermal and weather cycles, biological agents, and chemical agents [50]. Microplastics are defined by the Environmental Protection Agency (EPA) as plastic fragments with a single size-dimension below 5 mm [49]. They can be further distinguish as primary microplastics, or those manufactured to be in the designated size range, and secondary microplastics, or those formed from the degradation of macroplastics [51]. It is estimated that hundreds of thousands of tonnes of secondary microplastics are emitted annually [52].

From secondary microplastics, further degrading effects can lead to the formation of nanoplastics (**NPs**), or plastics with a single size dimension smaller than 1 µm [53]. These are estimated to be much more abundant, yet harder to detect due to their small size [54]. Together, these micro- and nanoplastics **(MNPs)** can remain unburdened for thousands of years, slowing the decay processes of plastics even further (Figure 1.4) [25].

MNPs that are formed in landfills are able to accumulate toxins, metals, biotics, and even antibiotics that are improperly disposed of in landfills, serving as a vector for other harmful contaminants [55]. However, they are not contained properly within current waste management systems. Studies have found over 25 polymer compositions to be in the runoff, or leachate, from landfills worldwide, with PE, PP, PS, PVC, and PET to be the most abundant [56]. Among these, fragmented plastics in the size range of 1 mm and smaller were found to be the most abundant.

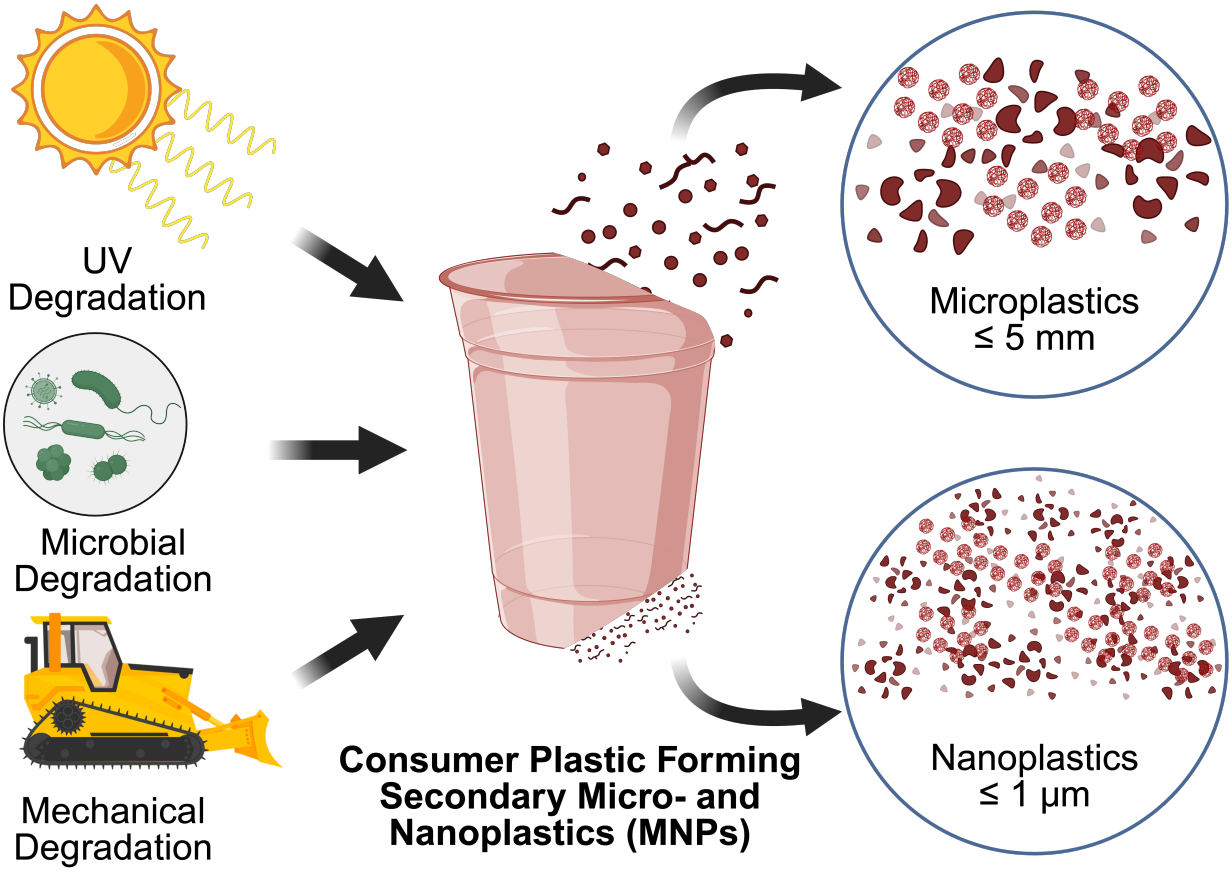

Figure 1.4: The Formation of Micro- and Nanoplastics (MNPs). Microplastics (MPs) are defined by the United States Environmental Protection Agency as plastic particles smaller than 5 mm. Nanoplastics (NPs), while the definition varies amongst the literature, is typically defined as plastic particles smaller than 1 µm. Figured created in BioRender.

1.4 Human Exposure to MNPs

1.4.1 Routes of Exposure

Humans are chronically exposed to MNPs through multiple pathways. As part of the natural environment, plastics contaminate air, water, soils, and indoor dust, creating a persistent exposure background that even newly discovered species cannot escape. Beyond these "external" environmental sources, humans also encounter MNPs through plastics intentionally used in food systems and consumer goods, including packaging, cosmetics, food-grade materials, textiles, and household products, further increasing the total exposure burden.

Together, ingestion, inhalation, and dermal absorption provide the three primary routes in which MNPs are able to enter the human body (Figure 1.5).

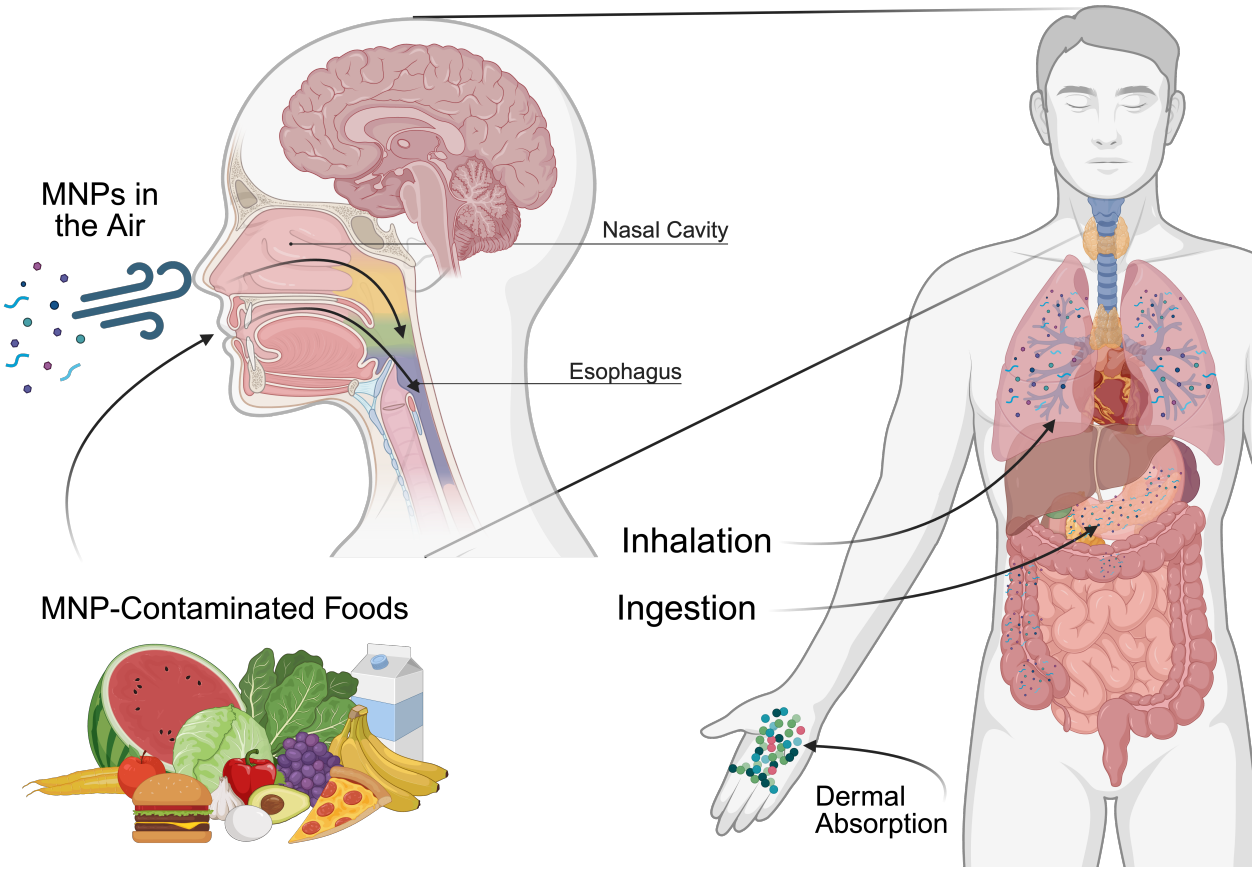

Figure 1.5: Routes Through Which Humans Uptake Micro- and Nanoplastics (MNPs). Primarily, MNPs are inhaled from the atmosphere, where they can be released through processes such as incineration or released from plastic products. Ingestion is a close section, where foods and beverages, along with the equipment used to consume them, contain plastics that can directly enter the body. Dermal absorption remains a third route, where smaller nanoplastics are able to directly pass through the skin and enter soft tissue. Figure created in BioRender.

Ingestion

Among the recognized exposure routes, ingestion is known to be a key factor, with an estimated average human uptake of 52,000 particles per year [23]. MNPs enter diverse ecosystems such as marine, freshwater, and agricultural systems, where they can be taken up by primary producers and bio-magnified through food webs, and ultimately appear in

foods of both plant and animal origin [57]. Consequently, humans can indirectly ingest these particles via contaminated drinking water, seafood, produce, and processed foods derived from contaminated raw materials.

Studies have shown that vast quantities of human-cultivated seafoods contain plastics, with oysters harvested from California show an average of 1.8 particles per oyster, and mesopelagic species from the Northern Pacific show an average of 2.1 particles per fish [26, 27, 28]. In both instances, the methods of detection were from microscopy, indicating that smaller NPs could be present but remain undetectable.

Land-based agricultural products also present a significant source of human exposure. MNPs are detected in agricultural soil across the globe, driven by landfill leachate, compost application, and wastewater irrigation [58]. Once in soil, these particles persist and can accumulate over time, creating a reservoir that is in direct contact with crop root systems throughout the growing season. MNPs are able to be directly uptaken with plants, including through both the roots and leaves [59, 60]. Studies show that larger NPs, specifically those over 100 nms, are preferentially uptaken. Plastics of larger sizes are often unable to be uptaken due to the cell walls preventing entry into the organism. Whether crops are directly consumer by humans or fed to livestock for cultivation, MNPs in edible plants creates another aspect of dietary exposures. Common fruits, vegetables, grains, and livestock such as pigs, cows, and chicken have been shown to present detectable levels of MNPs [61, 62].

It is not just the foods that are eaten that are routes for MNP exposure, but what materials are used to process, store, and transport these products to the consumer. The modern food infrastructure relies heavily on plastics at each stage of the supply chain, with processing equipment, single use packaging, films, bottles, and storage containers all containing high amounts of polymeric materials [10, 63]. Numerous studies have found MNPs in consumer foods, beverages, and even garnishes. Pre-prepared foods and packaged meals are a major source, with the processing required for these quick meals requiring an extensive use of plastic materials [9, 64]. Tap-water was first discovered to contain MNPs

around 2018, where a landmark study found roughly 5.5 particles/L across samples globally, with the morphology found to be primarily fibrous [65]. Bottled beverages such as water, beer, and soft drinks have also been shown to contain high levels of MNPs, whether from a tainted source that contained plastics already or from the release of plastics from their storage vessels [66, 67, 68]. Even simple ingredients such as salt has been shown to contain high levels of plastic contamination, mostly coming from the oceans in which the sea salt was harvested [69, 70].

The preparation of fresh foods at home can present another major source of MNPs that are able to find their way into the human body [71]. PS kitchen- and tableware such as spatulas, cutting boards, serving utensils, forks, and knives have all been shown to release thousands of particles per use in food preparation [72, 73]. Plastic cups alone provide a significant source, with their regular use leading to an estimated 90,000 particles ingested per year [74]. Further studies involving agitation of cups in hot water find billions of particles released per litre, with increased heat and time often correlating to increased MNP release [75].

Plastic containers used to store prepared foods compound additional MNPs on top of those already present in raw ingredients and processed meals. Long-term storage in PP containers leads to the passive release of millions to billions of MNPs under room-temperature and refrigerated conditions [64]. Certain containers designed for infants have been shown to release up to 4 million MPs and 2 billion NPs per square centimeter of container surface area within 3 minutes of microwaving.

Inhalation

The predominant route of human exposure to plastic particles is believed to be inhalation, with United Nations estimates indicating that the average adult inhales approximately 121,000 particles per year [23]. More recent work indicates that this may be a substantial

underestimate, with a 2025 study reported inhalation rates on the order of 70,000 MP particles per person per day, representing an approximate 200-fold increase compared to earlier projections [76]. In that study, more than 95% of the measured MPs were in the 1–10 µm size range, and model-based extrapolations of the particle size distribution suggested that inclusion of nanoplastics could increase total inhaled particle numbers by a further 20- to 400-fold, but requires conformation. Plastics that were identified inside residential environments were concentrated at a median 528 MPs/m^3, while inside vehicles the concentration skyrockets to over 2200 MPs/m^3.

A common narrative originally supported and circulated by the World Wildlife Fund (WWF) and published in top journals stated that humans inhale approximately 5 grams worth of plastics a week, an equivalent mass that goes into the manufacturing of a credit card [77, 78]. While this statistic has been debated in the field, with rebuttals claiming the actual amount is closer to 4 µg/week for the average person based on more rigorous mass calculations, it remains evident that a non-negligible amount of plastics are entering the human airways over the course of their lifespans [79].

Indoor environments display orders of magnitude higher concentrations of MNPs, even in dense urban environments [80]. Studies from Seoul have found an 1.8-fold increased in MPs in indoor spaces compared to those directly outside [81]. The United Nations found an average 40-fold increase across global indoor and outdoor environments, with up to 3,000 plastic particles per 50 cubic meters in indoor environments compared to just 75 outdoors [23].

Dermal Absorption

The uptake of plastics through the dermis remains a plausible but less detailed exposure route. Simple contacts with polymers, such as cosmetics containing polymers, handling consumer goods, and synthetic textile clothing and bedding, provide a vector for which smaller

sized particles are able to penetrate the skin. Studies have shown that while larger particles may struggle to pass the dermal barrier, NPs and small MPs may be able to penetrate through intercellular and follicular pathways [82, 83, 84]. This remains and under-studied mechanism despite its contribution to the impact of plastic accumulation in humans. While generally agreed to be lesser when compared with inhalation and ingestion, the importance of the skin's role in MNP is vital as numerous cosmetic products contain primary MNPs [11, 85]. Everyday consumer goods that nearly every human uses daily, such as toothpaste, shampoos, shower gels, deodorants, hair products, and nail products, contain primary-MNPs specifically manufactured to be in this size range and serve a purpose in the product, functional or otherwise.

Emerging studies show that particles below 1 µm can be internalized into the dermis, and more readily taken up by damaged or bruised skin. Quite ironically, many ointments and remedies for these aliments contain MNPs, not to mention the bandages or coverings used to help heal them [86]. In a similar vain, many cosmetic formulations for health applications, including soaps, cleansing oils, and micellar waters, have been found to contain thousands of plastics per litre of solution [87].

Overall, the evidence suggests that while the dermal absorption of MNPs is a likely contributor of plastic accumulation in humans, it is likely a minor factor in the overall scope of plastics ingested and inhaled. Further studies and investigations into the availability of these particles and the frequency at which the skin is able to uptake plastics. Targeted in vivo and in vitro studies are required to accurately quantify the uptaken in dermal systems, particularly in dermal injury conditions.

1.4.2 MNPs in the Human Body and Potential Impact on Human Health

MNPs enter the body through the main passages of the gut and lung systems, yet display an ability to traverse the body to present themselves in various other internal organ systems. While the excretion of plastics has been shown through stool, urine, and exhalation,

indicating that MNPs are able to be cleared by the body whether by chance or function, significant concentrations of particles have been found throughout the scope of the body [88, 89]. A review from 2024 shows that 8 major organ systems were found to contain significant levels of MPs: the cardiovascular system, lymphatic system, digestive system, endocrine system, integumentary system, respiratory system, reproductive systems of both sexes, and urinary systems were all discovered to contain these particles [90]. There is also validation of excretion of these particles through urine and stool as well as other secretions produced by the body including breastmilk, semen, and meconium. However, many other studies elucidate the presence of MNPs in nearly every other bodily system as well. Plastics isolated from these samples are a mixture of various polymers exhibiting a range of sizes [91].

Plastics are becoming recognized as persistent pollutants in living systems given their tendency to bioaccumulate. Recent studies on cadavers have demonstrated the buildup of MNPs in multiple vital organs, including the liver, kidneys, lungs, heart, and brain [92, 93]. Notably, the study from Nihart has been able to show that organ samples taken from 2024 present significant increases relative to samples from 2016 in the concentrations of MNPs in human brains moreso than the liver. Interestingly, concentrations in kidneys remained consistent in the same time period, suggesting that MNPs accumulate in certain organs preferentially. These are consistent with the theory that MNPs accumulate progressively *in vivo*. Together, these findings indicate that chronic exposure to plastic particulates yields an increasing burden on the body over time, raising concerns that MNPs may reach toxic concentrations in sensitive tissues over the human lifespan. Despite widespread human exposure and the demonstrated accumulation of MNPs in tissues, the understanding of their health effects remains very limited [94, 89]. Importantly, the vast majority of studies in the literature have relied on pristine, commercially available spherical micro-and nanobeads, which fail to capture the heterogeneous sizes, shapes, and compositions of MNPs encountered in real-world exposures [95, 96]. Some also argue that pristine plastic particles may

not accurately represent engineered nanoparticles (ENPs) due to their higher heterogeneity and tendency to fragment, which are not found in ENPs used for drug delivery or other therapeutic systems [97]. Instead, they should be categorized as an entirely separate class of materials as they fall outside of the established definitions of these material classes.

The accumulations, morphologies, and physicochemical properties of MNPs found in the major human systems vary, likely due to their exposure route. Ingestion, inhalation, and dermal absorption each serve to introduce MNPs through distinct pathways, and thus the particles which are able to pass varying physiological barriers differ. Particle size, surface chemistry, and composition may further regulate bioaccumulation and bioavailability. As a result, each organ system presents a unique MNP profile.

The Lungs and Associated Airways

Given the mounting evidence on inhalation of MNPs, the lungs and associated airways are perhaps the most obvious to suspect plastics. Some of the earliest work that found MPs in human airways dates back to 2022, where bronchoalveolar lavage fluid (BALF) was extracted from patients [98]. Researchers found an average of 9.75 particles per 100 mL of BALF, with the vast majority of particles presenting fibrous morphologies and only a small fraction showing a fragmented morphology. Previous studies had found MNPs in the lungs of autopsy patients, where plastic fragments were below 5.5 µm while fibrous polymers presented nearly thrice this size, but where much less numerous [99]. Subsequent BALF studies using Raman identification confirmed these findings, with the majority of samples containing particles smaller than 50 µm [100]. Interestingly, this study showed the most numerous particle type to be fragments rather than fibres, opposing the findings of previous studies [98].

From multiple studies of autopsied individuals, an evidenced association can be made between the number of MNPs in a patient's airways and lung cancer. The greatest particle concentrations were found in patients who had died from malignancies in the lungs,

bronchi, and trachea, and more recent surgical findings have identified higher concentrations of MNPs in cancerous tissues when compared to healthy tissue [101]. This study was also able to correlate a significantly increased level of aluminum and calcium in the particles of lung adenocarcinoma patients compared to those in healthy lungs. This not only supports the understanding that MNPs are able to serve as a vector for heavy metals and other contaminants they may encounter, but also the hypothesis that these particles may induce carcinogenesis or accumulate preferentially in malignant tissues. However, current data remains insufficient to distinguish causation from correlation.

Apart from carcinomas, MNPs have also been associated with a variety of other disorders in the human airways. A recent review concluded that across a wide range of *in vitro* and *in vivo* models, MNP exposure consistently induces excessive reactive oxygen species (ROS) accumulation, trigger of reduction-oxidation (Redox) signaling pathways, and decrease in the antioxidant defense system activation [102]. Pathways including MAPK, NF-$\kappa\beta$, TLR4/NOX2, and cGAS-STING were shown to display significant levels of variation when compared to healthy tissues. *In vitro* studies have shown that PS particles in the lung have been associated with epithelial barrier disruption, chronic obstructive pulmonary disease (COPD), pulmonary fibrosis, and extracellular matrix (ECM) remodeling similar to that seen in asthmas [34, 103, 104].

The Gut and Digestive System

Mirroring the lung and airway's expectation for plastic accumulation due to its role in plastic uptake, the gastrointestinal tract is a primary interface for ingested MNPs. Multiple studies have detected MNPs in human stool, with a recent report showing 3.5 particles per gram of excrement in the range of 50 - 5000 µm [88, 105]. Samples from individuals with inflammatory bowel disease (IBD) were shown to contain significantly higher concentrations of MPs than those from healthy individuals, with PET and PA fragments and fibres being the most numerous [106]. There was an additional validation between MP concentrations and

the severity of IBD, hinting at a potential correlation. Looking further upstream, plastics ranging from 51.5 to 4,789.1 µm were found at an average concentration of 245.5 particles per stomach in cadavers, with the majority of plastic morphologies being fibrous followed by fragmented [107]. The larger concentrations and particles sizes are estimated to come directly from the foods and beverages ingested by the individual. As there is essentially no filtration by the body from what is ingested to what ends up in the digestive system, the stomach and intestinal system presents the best gauge of ingested particles [108].

Beyond their presence, evidence in human and mammalian models indicates that the accumulation of plastics can perturb the gastrointestinal homeostasis [109]. Exposure of PS-MNPs to human colorectal cancer cell lines (Caco-2) have shown disruptions to mitochondrial membrane potential ($\Delta\Psi_m$), membrane transporter activity, and increased susceptibility to arsenic toxicity [110]. In adult mice models, chronic MNP exposure led to intestinal barrier and immune dysfunction, with the composition of the gut microbiota shown to alter in response [111]. Similar impacts have been seen in humans, where MP exposures have been shown to decrease short-chain fatty acid abundance as well as significant changes in volatile organic compound (VOC) release [112, 113].

Renal and Urinary Systems

The kidneys and urinary tract provide another logical site to suspect plastic accumulation given their role in filtering blood and excreting waste. Evidence in human samples has now confirmed this, with MNPs being found in renal tissues as well as urine samples [114]. Raman spectroscopy observations on nephrectomy samples that were paired to urine samples was able to confirm PS particles in the range of 1 -2 9 µm in kidneys, while particles excreted in urine to be smaller with a range of 3 - 13 µm, providing some of the first experimental evidence for plastic accumulation in kidneys [115]. These findings imply that plastics from the bloodstream are able to deposit in nephritic tissues and show excretory behaviour.

In mammalian model organisms, experiments have been conducted to better understand the impact plastics may have on the human body. A recent study found that after 35 days of exposure to PS-NPs, renal tissues displayed a significantly lessened antioxidant defense capability, overall kidney weight, and induce a significant increase in mitophagy, or clearance of dysfunctional mitochondria, when compared to mice which were not exposed to plastics [116]. Complementary studies found PS-MP exposure in rats to corroborate a decrease in organ weight and organ index as well as oxidative stress, inflammation, and even apoptosis of renal cells [117]. While studies are more limited in humans, there are reports indicating that MNPs are able to act as a vector for known toxicants in kidneys, namely metals and organic pollutants [118, 35, 114].

Blood and Circulatory System

The vascular network provides the main method by which MNPs are able to traverse the body and distribute to distal organs. First quantified in 2022, a blend of PET, PE, and PP were determined to circulate at a concentration of **1.6 μg/mL** [119]. While the exact mechanism of how plastics transfer from ingestion and inhalation to the bloodstream are not yet identified, it is speculated that certain sizes and shapes of particles are preferentially selected to cross epithelial barriers in the gut and lungs [120, 91]. Ironically, it has also been shown that intravenous injections and infusion therapies are able to administer plastics directly to the circulatory system, with varying syringes and needles found to contain PE, PA, PS, PC, and PP fragments [121, 122]. Through this method, the estimated MNP release per person per year hovers around 10 particles, indicating an overall negligible route of exposure, yet remains a cause for concern with how medical devices contribute to plastic exposure [12].

There have been direct investigations into the type and concentration of differing particle types that are found to circulate the body. In 2024, another study found the concentrations of plastics to range from 1.84 to 4.65 µg/mL, validating previous works [123]. Twenty-four different polymer types were found across blood samples, with PE, PS, ethylene propylene diene

monomers (EPDM), PA, and ethylene–vinyl acetate/ethylene vinyl alcohol (EVA/EVOH) found to comprise roughly 75% of the particles found. Phthalates were also detected as the most prevalent additive to these particles, with 20% of blood samples containing these particles. Phthalates are common plasticizers, used to amend the flexibility of polymers as well as other aspects, and are well known endocrine disruptors with known toxicity concerns in humans [124].

High concentrations of circulating MPs were positively correlated with alterations in hemostatic and inflammatory markers, including prolonged activated partial thromboplastin time (aPTT) and elevated fibrinogen and C-reactive protein (CRP), indicating activation of coagulation pathways and systemic inflammation [125]. The extended aPTT as well as increased fibrinogen both serve as pro-thrombotic markers, with both being linked to cardiovascular risk [126, 127]. Another study has linked high concentrations of MPs with chronic disease risk, with hypertension, diabetes, and stroke risks all derived from the presence of plastics in the blood [128]. Experimental models validate these observations, where chronic exposure to MNPs accelerated atherosclerosis and plaque formations in mice [129]. Male mice were shown to be much more susceptible, leaving a gap in knowledge of how MNPs elicit such changes.

Circulating MNPs in the bloodstream are able to be distributed to distal organs, although a mechanism for how they are able to exit the bloodstream is still widely theorized. While they have been shown to both damage and cross other epithelial barriers such as those in the gut, there is a gap in the literature for understanding how plastics are able to escape the bloodstream [120, 130, 131]. Despite the uncertainty in the mechanism, the evidence of MNP accumulation in otherwise inaccessible bodily components elucidates the operation of this mechanism. With plastics being quantified in lymphatic, skeletal, and adipose tissues, the bloodstream as a vector for plastics remains the most likely explanation [132, 133, 134, 135, 136].

While circulating, plastics are able to form a bio-corona, or layer of proteins, lipids, antibodies, sugars, and other biomolecules around the surface of the particle [137, 138]. Governed primarily by electrostatic, hydrophobic, and entropic interactions, available biomolecules from the bloodstream can be adhered to the particle. There are often two layers described in the literature: the layer closest to the particle is dictated as the hard corona, while secondary layers are dictated as the soft corona [139]. Biomolecules with higher binding affinities are able to quickly bind to the core of the particle, and do so in a less-reversible mechanism. Components of the soft corona then bind to the hard corona, which display lower binding affinities and are able to reversibly adsorb to the particle. In the context of MNPs, the formation of the bio-corona is able to dictate the toxicological response from the host system [140]. Not only does the corona formation in the biological system itself determine the particle's attributes, but the so called eco-corona, or contaminants that the plastics interact with before being uptaken, have a drastic impact on the fate of the host [141, 142].

The corona formed on MNPs greatly enhances its uptake, bioavailability, and bioaccumulatory effects [143, 138]. The hydrodynamic size is entirely determined by the corona, where a thicker corona can directly increase the functional size of the MNP. The zeta potential, or charge on the surface of the particle, is determined primarily by the corona as well, masking that of the original particle [144]. Coronas can assist originally hydrophobic MNPs into becoming more hydrophilic, improving stability and suspension time [145]. Contrarily, the composition of biocoronas can also elicit how a biological host responds. A study using induced pluripotent stem cells found that pro-inflammatory proteins in MNP biocoronas exhibited a correlation in interleukin (IL) 6 and 8 release, while ROS-related proteins in the corona was correlated with increased ROS [146]. These aspects directly impact not only the bioavailability of particles, but also how a host may respond to internalized particles.

The Brain and Nervous System

Perhaps the most vital organ to the human body, not even the brain shows immunity to the accumulation of plastic particulates. The brain appears to be contain high concentrations of MNPs. A study from 2025 showed that an approximate 11- and 12- fold MNPs increase in the brain when compared with samples from the same patient set's liver and kidney, respectively [92]. The same study also found that the concentrations of plastics in the brain were significantly increased when compared to a selection of samples from just 8 years prior. While this was also observed in the liver samples, the kidney showed no change in concentration, underscoring its role in particle clearance [147]. The particles detected in the brain shared a similar compositional makeup to those in the liver and kidney, with PE accounting for the vast majority trailed closely by PP, and PVC. MNP concentration in brains of individuals diagnosed with dementia prior death was significantly higher (over a 5-fold increase) compared to samples from healthy patients. This is supported by works from earlier in the same year, which found a positive correlation between the concentration of particles administered to mice and neuro-behavioral abnormalities [148].

The blood-brain barrier (BBB) is a specialized, selectively permeable interface between vasculature and the parenchyma, regulating ions, macromolecules, and biotics which seek to enter the brain [149]. Certain metabolites, unfavorable proteins, and neurotoxic materials are excluded from the central nervous system (CNS) through this protective layer, with specific transport proteins and tight-junction molecules serving to ensure the nominal function of neurons, glia, and astrocytes [150]. However, PS-NPs have been found to be able to cross the otherwise impermeable barrier *in vitro* [131]. Emerging evidence has shaped understanding of how MNPs are able to cross the BBB. NPs in the realm of 1 nm can diffuse across endothelial layers, while larger, 200 nm PS-NPs spheres have been found to cross a BBB-on-a-chip model with a much higher efficacy than larger sizes or rod-shaped PS-NPs [151, 152]. This supports that particle size and shape are largely important for determining endothelial transport. Engineered nanoparticles serving as drug carriers with modified sugars

and amino acids have also been shown to hijack endogenous BBB-transports, indicating that the composition of the bio-corona is largely influential to brain contamination [153]. One recent study has related the formation and composition of biocoronas around MNPs to their ability to enter the brain using both computational and experimental validations [154]. NPs were found to enter the brain after just 2 hours of exposure in mice. Through computational modeling, they found PS-NPs with cholesterol coronas presented much lower thermodynamic barriers of entry ($\approx$ -170 kJ/mol) when compared to those with protein coronas (218 kJ/mol), indicating BBB deformation through biocorona composition. Given the correlation between hypercholesterolemia and increased risk for Alzheimer's disease, it is possible that the elevated concentrations of this sterol lead to the observed increases of MNPs in the brain of dementia patients [155, 92].

MNPs have been found accumulate in mice brains after oral ingestion, with the exposure to spherical PS-MPs (2 - 5 µm) associated with altered behavior after exposure to low (2.5 µg/mL) and high (125 µg/mL) doses [156]. Changes in glial fibrillary acidic protein (GFAP) concentrations, found primarily in astrocytes and serves as a neuroinflammatory marker observed for the early stages of Alzheimer's disease, were also seen in mice exposed to varying concentrations of PS-MNPs [157]. These corroborate similar findings of MNPs accumulating in the brain, immune marker modulations, and cognitive dysfunction in mouse models [158]. Mice exposed to pristine PS-MPs have shown an impaired memory and decreased learning capabilities, with mice showing difficulties in hippocampus-dependent assessments such as the Morris water maze [159]. PS-MPs were shown to have accumulated in the hippocampus, leading to increased inflammation and synaptic receptor activity, which disrupt synaptic plasticity. Another study showed that mice exposed to pristine PS-NPs presented NPs accumulated in the brain, leading to increased oxidative stress and inflammatory response, and even necroptosis in human endothelial BBB-model cells [131]. Interestingly, cognitive impairment in mice was correlated with the preferential accumulation of PS-NPs (30- 50 nm) in microglia following oral ingestion (0.5 - 50 mg/kg body weight) [160]. In this study,

even at the lowest tested concentration of 0.5 mg/kg of body weight, a significant amount of NPs could be detected in the brain structure, with apparent dose-dependent accumulation effect. Damage was observed in the neurons, where the highest dose of 50 mg/kg body-weight showed an overall significant decrease in the total number of neurons. In addition, microglia, brain macrophages, were shown to have been activated leading to neuronal damage [160].

Considering in vitro studies with human cell lines, a study using a human neuroblastoma cell-line, SH-SY5Y, found that exposure to pristine PS-NPs induced a dose-dependent drop in cell viability, ATP concentration, and mitochondrial membrane potential ($\Delta\Psi_m$) while showing a dose-dependent increase in ROS concentrations and apoptotic-associated proteins such as Caspase-3,9, and Aparf-1 [161]. Additionally, PS-NPs were shown to trigger autophagy, indicated by increased LC3-II levels and Beclin-1. These findings elucidate a mechanism where mitochondrial dysfunction orchestrates PS-NP-induced neurotoxicity through autophagy activation and apoptosis *in vitro*, underscoring a plausible pathological basis for potential nanoplastics-linked neuro-degeneration. While criticisms may arise due to the cell-line given their neuroblastoma origin and associated alterations when compared to healthy brain tissue, key neuronal phenotypes and signaling pathways remain in-check, and thus provide a legitimate basis for the findings [162, 163]. Another study showed that PS-MNPs were phagocyted by human microglial clone cells (HMC3) following 24 hours of exposure and the presence of these particles led to microglia death by apoptosis [164]. This process was shown to be favorable for NPs and small MPs, with PS particles of 10 µm not being uptaken [164].

1.5 Aims

While the presence of MNPs has been confirmed in the human brain, there remain gaps in the literature on potential adverse effects they may elicit. One of the largest setbacks in the field of is the use of so-called "pristine" MNPs, which are primary plastics produced with

the express purpose of industrial or biological use. They are manufactured to be homogeneous in size and often present a spherical morphology, which do not serve as an accurate representation for what is found in the environment nor isolated from human samples. In both instances, these plastics are characterized by a heterogeneous mixture of polymers with different shapes and wide range of sizes [165, 97].

The vast majority of studies in the field that attempt to gauge the impacts of MNPs on brain health use these pristine MNPs [95, 94]. While they may serve as an appropriate proxy, the results of studies using such systems cannot be accurately extrapolated of the effects of real-world MNPs. Additionally, many studies that seek to understand the impacts of MNPs in the brain often come from animal models, particularly mice, which do not accurately represent what is seen in human brains. Significant differences in transcriptomic profiles along with regional- and age-related discrepancies between the organisms muddle the comparisons that can be drawn by the effects that are observed [166, 167].

Hence, this study aims to fill the gaps in the literature by assessing the impact of MNPs derived from consumer products using a human-based, neural *in vitro* model and relevant human physiological concentrations. To better replicate real-world exposure, MNPs were produced from common plastic consumer products shown to release significant quantities of particles, such as plastic cups and forks. Primary-like human brain macrophages, or microglia, were chosen as the *in vitro* target as they comprise roughly 10% of the brain's cellular composition and have a large population in the hippocampus, where MNPs have been shown to accumulate [168, 159]. In addition to this, microglia have been shown to undergo activation when exposed to plastics, indicating a shift to an increased inflammatory state [131]. Neuroinflammation mirrors what is observed in a wide variety of neurodegenerative disorders, such as Alzheimer's Disease (AD), Parkinson's Disease (PD), amyotrophic lateral sclerosis (ALS), and multiple sclerosis (MS), suggesting the possible link between plastic exposure in the brain and this afflictions [169, 170, 171]. Commercial PS nanobeads (PS-50; Spherotech) were chosen as a reference to compare against the impacts of the so called

"real-world" MNPs (Cup- and Fork-MNPs) as these NPs are by far the most abundantly used in the literature.

The first aim of this study was to assess the effects of well-characterized real-world MNPs in human microglia at physiologically relevant concentrations (0.1, 1, and 10 µg/mL) after 72 hours to elucidate potential neurotoxic outcomes and compare to pristine PS-50-exposed cells. Toxicity outcomes were evaluated based on cell physiology parameters and correlated to physicochemical features of the MNPs. The results of this chapter is being submitted to the ACS Environmental Science & Technology (IF: 10.4).

The second aim of this study was to characterize the transcriptomic profile of microglia cells exposed to a low concentration (0.1 µg/mL) of real-world MNPs and evaluate the biological pathways altered by these MNPs after 72 hours. Next-generation RNA sequencing (RNA-seq) was conducted, and the gene expression profile was compared among Cup- and Fork-Derived MNP samples and pristine PS-50 samples. This approach enables comprehensive profiling of transcriptional alterations, allowing the identification of differentially expressed genes and associated biological pathways.

Chapter 2

Pristine Nanoplastics and Consumer Product-Derived Micro- and Nanoplastics Differentially Modulate Microglial Mitochondrial Function and Inflammatory Responses

2.1 Abstract

Micro- and nanoplastics (MNPs) are global environmental contaminants increasingly detected in human tissues, including the brain, raising concerns about their potential contribution to neuroinflammation and neurodegenerative disorders. However, most toxicological studies rely on pristine, monodisperse polymer nanobeads that fail to accurately represent heterogeneous particles generated through the degradation of consumer plastics. Here, the effects of pristine 50 nm polystyrene nanoplastics (PS-50) are compared with relevant MNPs derived from the mechanical fragmentation of disposable plastic cups and forks on human microglial primary-like cells. Cells were exposed to physiologically relevant low concentrations of MNPs, and endpoints related to neurotoxicity such as oxidative stress, mitochondrial function, mitochondrial turnover, and inflammatory responses, were evaluated. Pristine PS-50 NPs induced pronounced oxidative stress and mitochondrial dysfunction at low doses and impaired cellular bioenergetics. These changes were accompanied by mitochondrial stress responses such as mitophagy and compensatory mitochondrial biogenesis. In contrast, consumer product-derived MNPs elicited moderate oxidative stress and mitochondrial remodeling while largely preserving bioenergetic capacity, suggesting adaptive cellular responses. Notably, Fork-derived MNPs led to a more robust increase in pro-inflammatory cytokine release compared to PS-50. Together, these findings reveal that pristine nanoplastics can substantially overestimate mitochondrial toxicity compared with environmentally derived MNPs and highlight mitochondrial stress responses as central mechanisms governing

microglial interactions with plastic particles. These results emphasize the need to incorporate realistic particle sources and physicochemical complexity into experimental designs to improve the environmental and biomedical relevance of nanoplastic risk assessments. The general approach is shown in Figure 2.1.

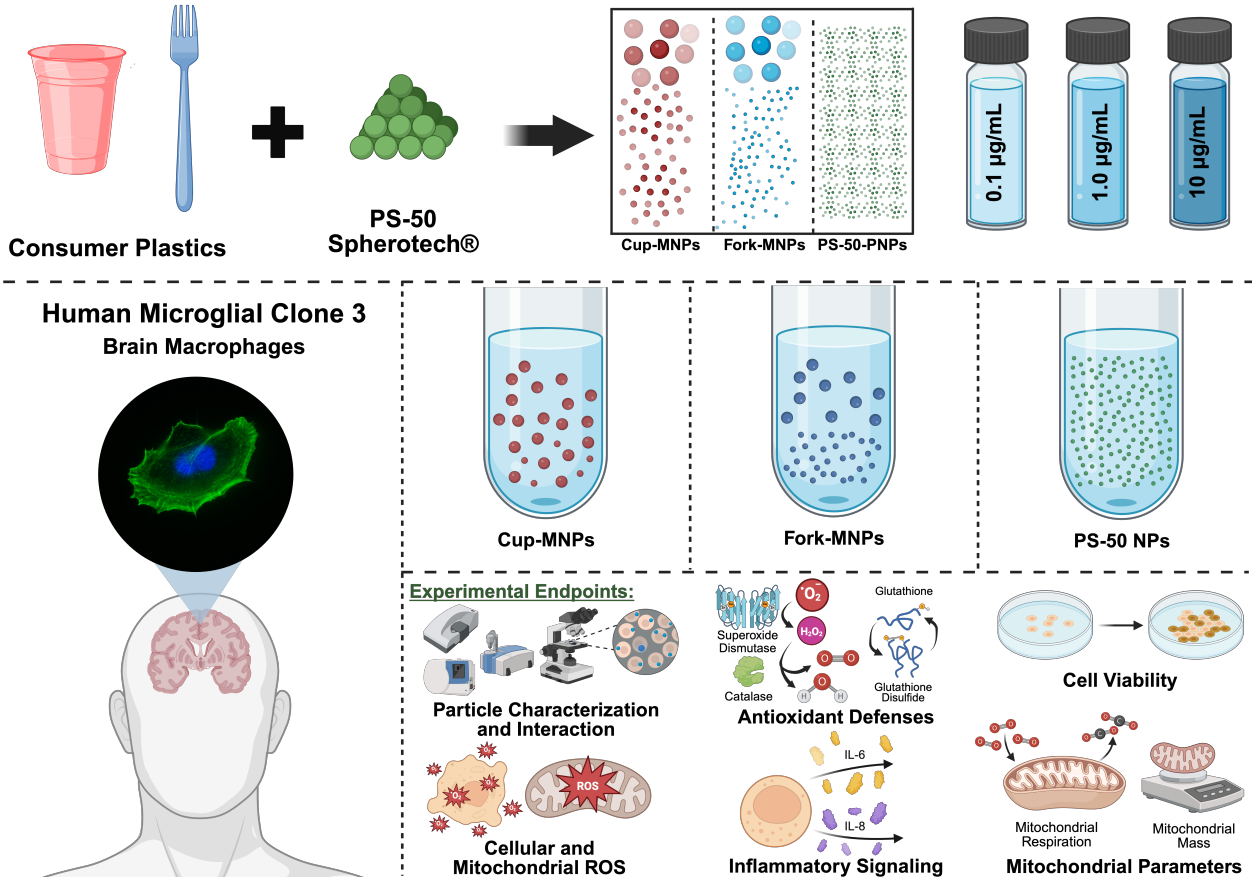

Figure 2.1: Experimental Workflow. Plastic tableware (cups and forks) were formed into micro- and nanoplastic (MNP) samples through cryomilling and administered to human microglial cells (Human Microglial Clone 3; HMC3) with 0.1, 1.0, and 10 µg/mL doses. These were compared against pristine polystyrene nanoplastics (PS-50-PNPs), commonly used in plastic toxicological studies as a stand-in for environmentally relevant plastics, along with unexposed cells. Following rigorous material characterization of each plastic sample, cells were exposed to physiologically relevant doses of MNPs for 72 hours. A variety of cellular endpoints were measured, including viability, MNP-biological interaction, redox status, inflammatory signaling, and mitochondrial statuses. Figure created in BioRender.

2.2 Introduction

Plastics have become a ubiquitous part of everyday lives [6]. With hundreds of millions of metric tonnes (MMT) produced annually, the escalation of the use of the material is predicted to reach nearly a billion metric tonnes by 2050 [17, 13]. Over 75% of plastic waste has been shown to end up in landfills, where they can remain for thousands of years [172, 37]. Plastics can become contaminated with other pollutants from landfills and the environment, such as heavy metals, drugs, toxicants, and microbes [55]. Even in incineration facilities, the plastics are not able to completely break down, as evidence suggests that plastics are left behind in the ashes of the combustion processes as well as released into the atmosphere from the flue gasses [20, 21]. Nearly 200 MMT of plastic are mismanaged globally, with the majority coming from Asia [173]. This mismanaged plastic often finds its ways into local ecosystems, particularly rivers, estuaries, lakes, and oceans [18, 27, 52].

Plastics gradually degrade over tens, hundreds, and even thousands of years [38]. Some polymeric materials such as polystyrene (PS), polyvinyl chloride (PVC), and polyethylene (PE) have been shown to degrade at a rate of less than one micron per year, demonstrating the persistence of these materials on a timescale longer than human lives. Through the various discussed degradation methods, consumer-grade plastics are able to form microplastics (MPs), which are defined by the United States Environmental Protection Agency (EPA) as plastics with a single size dimension below 5 mm [49]. MPs formed from these degradation methods can be further classified as secondary MPs, as opposed to primary MPs which are specifically manufactured to be within the aforementioned size dimensions [51]. Continual breakdown of macro- or microplastics can lead to the formation of nanoplastics (NPs), commonly agreed to be fragments with a single size dimension below 1 nm [53].

Combined, micro- and nanoplastics (MNPs) are able to leach from landfills, mismanaged plastic waste, incineration plants, and even consumer items into the environment and human body [56]. MNPs can be found in agricultural products such as grains, fruits, vegetables, and livestock that are consumed by humans [60, 61, 62, 57, 28]. Additionally, MNPs in the air can

be directly inhaled by humans, providing another major route of exposure [174, 23, 76, 31]. Dermal absorption is a third, but less significant route for plastic exposure where NPs are able to pass through the dermis and enter the body [83, 82, 84]. Together, these routes of plastic exposure have been evidenced to allow MNPs to accumulate in the body, being found in nearly every major organ and organ system [90, 132, 175, 176, 115, 120].

Most concerningly is the accumulation of plastics in the human brain, with the concentrations of particles increasing over time [92]. Evidence also suggests a correlation between neurological conditions such as dementia and MNPs in the brain, with patients that had dementia displaying a near ten-fold increase in the amount of plastics in the brain. When combined with previous studies that link plastic uptake and neuro-inflammation and neuronal death, the threat of plastics in the human brain has garnered a public health crisis [131, 161]. The same studies have also shown that microglia, the primary immune macrophages of the brain, undergo activation into an inflammation-driven state, which can lead to neuronal damage and neurodegeneration over extended periods [177, 178].

In order to better understand the brain's immune response to the plastic exposure humans face daily, this study utilizes primary-like human microglia (Human Microglial Clone Cells, **HMC3**) exposed to physiologically relevant concentrations of MNPs. With the average plastic concentration of the blood found to be 1.6 ± 2.3 µg/mL, corresponding doses of 0.1, 1.0, and 10 µg/mL were chosen to be administered to the cells [119]. To most-accurately model the contamination that is seen in the brain, consumer-grade, single-use plastic cups and forks were used as "real-world" samples Cup-MNPs and Fork-MNPs. Additionally, 50 - 100 nm pristine PS-NPs (PS-50), by far the most common material used in MNP studies, were exposed to cells at identical concentrations in order to understand the accuracy of these particles as a model and the shortcomings they may present [94, 97].

2.3 Materials and Methods

2.3.1 Reagents and Chemicals

Phosphate-Buffer Saline (PBS, 21-040-CV, Corning, Corning, New York, USA), Hanks' Balanced Salt Solution (HBSS, SH30268.01, Cytiva, Marlborough, Massachusetts, USA) Fetal Bovine Serum (FBS, 35-010 CV) Corning, Corning, New York, USA), 0.4 % Trypan Blue solution (K940, VWR-Avantor), Dulbecco's modified eagle medium (10-013-CV, Corning, DMEM/High Glucose), Penicillin: Streptomycin (16777-164, HyClone, Logan, Utah, USA). All necessary solutions were prepared with ultrapure water (Barnstead™MicroPure™Water Purification System, 50132370, Thermo Scientific).

2.3.2 Equipment

Echo Revolution Fluorescent Microscope (Discover Echo, San Diego, California, USA), Varioskan Lux Microplate Reader (ThermoFisher Scientific, Waltham, Massachusetts, USA), MACSQuant Analyzer 10 (Miltenyi Biotec, Bergisch Gladbach, Germany), Countess 3 Automated Cell Counter (ThermoFisher Scientific), CytoFLEX LX (Beckman Coulter, Brea, California, USA), Seahorse XFe96 Analyzer (Agilent, USA), Avio 220 Max (Perkin Elmer, Waltham, MA, USA), Olympus BX51 Microscope (Olympus, Tokyo, Japan) fitted with Enhanced Darkfield Illuminator (Cytoviva, Auburn, AL, USA), Pulverisette 14™ miller (FRITSCH, Idar-Oberstein, Germany), Nicolet iS50 FTIR (ThermoFisher Scientific), Zeiss EVO 50 SEM (Zeiss AG, Oberkochen, Germany), Litesizer™500 (Anton Paar, Graz, Austria).

2.3.3 Real-World MNP Synthesis from Cups and Forks

Real-world MNPs were generated from consumer grade plastic kitchenware. Very common red disposable drinking cups and plastic forks were purchased from a local grocery store and prepared in a previously described methodology [179]. Briefly, plastic cups and forks

were cut into sub-20 mm fragments inside of a sterilized laminar flow cabinet to minimize contamination. These fragments were then chilled in liquid nitrogen (LN_2) and cryomilled in a Pulverisette 14™miller (Fritsch). After milling, particles above 120 µm were removed through sieving, with the remaining fraction stored in sterile glass vials. Stock solutions of 1 mg/mL in sterile ultrapure water were prepared in sterile glass bottles and stored in room temperature conditions and away from natural and artificial light to minimize degradation.

SPHERO™polystyrene nanoparticles (PS-50) ranging from 50 to 100 nm diameter (Average: 75 nm) were purchased from an online vendor and stored in ultrapure water following the removal of sodium azide.

2.3.4 MNP Characterization

Extensive characterization of physicochemical properties amongst all MNP samples were conducted. To analyze the material composition of the real-world MNPs, attenuated total reflectance Fourier-transform infrared spectroscopy (ATR-FTIR) was conducted using the Nicolet iS50 FTIR with a Diamond ATR crystal (ThermoFisher Scientific). Analyses of chemical structure and composition were performed using Omnic32 Software (ThermoFisher Scientific) and corresponding library.

Real-world MNP size and morphology were assessed with the Zeiss EVO 50 Scanning Electron Microscope (SEM; Zeiss AG) at 20 kV acceleration voltage. Images were captured at a range of 500X to 1600X. Particle size analyses were performed in ImageJ (National Institutes of Health, Bethesda, MD, USA) with an average of 181 particles measured per real-world MNP sample. For visual representation, measurements were binned into 10 µm groups.

For further size analyses, dynamic light scattering (DLS) measurements were recorded for filtered particle fragments. After being subjected to a 0.45 µm filter (Fisher Scientific), particles in ultrapure water were analyzed using the Litesizer™500 (Anton Paar). The zeta potential of both real-world MNPs and pristine PS-50 NPs were also measured using the

Litesizer™500, allowing for the analysis of surface charge after the particles were allowed to form a biocorona and resuspended in complete cell media.

In order to determine the concentrations of trace metals in the MNP samples, inductively coupled plasma optical emission spectroscopy (ICP-OES) was performed using an Avio 220 Max (PerkinElmer). Briefly, MNPs were digested in 20% aqua-regia in new scintillation vials and left to dissolve overnight while shaking at 600 rpm. The next day, samples were diluted in sterile ultrapure water before analysis. Multielement Standard Solution 1 for ICP (TraceCERT®, Buchs, Switzerland) was used as the calibrant before each run, allowing for the detection of lead, zinc, cadmium, copper, chromium, nickel, barium, and silver at concentrations of 5 ppb and above.

2.3.5 Cell Culture and MNP Exposure to HMC3

Human microglial clone 3 (HMC3; ATCC CRL-3304) cells were purchased online and cultured according to the supplier's recommendations. Briefly, cells were cultured in DMEM high-glucose media (Cytiva) at 37°C and a 5% CO_2 atmosphere in T-75 flasks (VWR-Avantor). Complete cell media consisted of the DMEM high-glucose, 5% FBS (Corning), and a 1% penicillin:streptomycin mix (Meditech). Cells used in experiments were from passage three (P3) up to passage eighteen (P18).

Prior to exposure to cells, MNP solutions were sonicated at 40 kHz for 30 minutes. Immediately following this, the particles were allowed to incubate in FBS for approximately 24 hours at 600 rpm in an orbital shaker to allow for biocorona formation and prevent aggregation and agglomeration. After this period, complete cell culture media was used to perform serial dilutions to the appropriate exposure concentrations.

2.3.6 Cell Viability

To assess the potential cytotoxicity of MNPs, cell viability was performed after 24-, 48-, and 72-hour exposure windows to plastics of 0.1, 1.0, and 10 µg/mL concentrations.

Five thousand cells were plated in 48-well plates (VWR-Avantor) and allowed to attach for 24 hours. Following duplicate washes in HBSS, cells were exposed to the appropriate dose and sample. At each endpoint, viability was assessed using trypan blue exclusion assay (VWR-Avantor) with a Countess 3 Automated Cell Counter (ThermoFisher Scientific). The percentage of live cells was reported as a fold change (FC) relative to the viability of unexposed cells at each timepoint (n=4).

2.3.7 MNP Uptake using Flow Cytometry

To establish the percentage of HMC3 that had uptaken MNP samples, Nile Red fluorescent dye (Biotium, Fremont, CA, USA) was used to stain the particles. Stock MNP solutions (1 mg/mL) were mixed with an equal volume of 10 µg/mL Nile Red dye in ultrapure water and allowed to incubate for 2 hours at 70°C in a laboratory oven (Thelco Precision Scientific Model 16). Excess dye was removed through 7 centrifugations at 3250 g for 10 minutes in Amicon® Ultra-2 centrifugal filter tubes (Sigma-Aldrich, St. Louis, MO, USA), each time adding ultrapure water to drive off dye agglomerations. The stained particles were recovered through resuspension in sterile ultrapure water at an equivalent volume of stock MNP solution added in order to preserve the original concentration. These suspensions then underwent identical preparation as unstained particles for exposure to HMC3.

For quantifying the uptake of these particles, 50,000 cells were plated in 1.5 mL in six-well plates for 24 hours and then exposed to the stained MNP solutions for 72 hours. Following this exposure, MNP-media was aspirated and the wells were washed twice in HBSS. Cells were trypsinized and pelleted through centrifugation, and washed twice more in HBSS through centrifugation at 400 g for four minutes. Cells were resuspended in 250 µL HBSS and placed into the wells of 96-well plates before reading. The MACSQuant® Analyzer 10 (Miltenyi Biotec) was used on channel B3 (800V; 488 nm excitation, 655-730 nm emission) in order to detect cells with sufficient fluoresencent signatures. 10,000 cells were uptaken for each replicate (n=3). Viable, single cells were selected from forward scatter (FSC) and side

scatter (SSC) gating parameters in FlowJo V11 (BD Biosciences, Franklin Lakes, NJ, USA), and HMC3 that had particles uptaken were defined as events where the fluorescent intensity was above the 99th percentile of control cell populations in the same fluorescent readings.

2.3.8 MNP-HMC3 Interactions by CytoViva

Enhanced darkfield hyperspectral microscopy (CytoViva) was used in order to visualize the interactions between HMC3 cells and MNPs. Using an Olympus BX51 fitted with the CytoViva enhanced darkfield condenser, Olympus UPLFN100X OI2 objective, and Specim ImSpector V10E spectrograph (Specim, Oulu, Finland) coupled to a pco.pixelfly 1.4 CCD camera (Excelitas, Pittsburgh, PA, USA), scattered light from 400 - 1000 nm was captured with a spectral resolution of approximately 2 nm. Briefly, 5,000 cells were plated on microscope slides (VWR-Avantor) and allowed to attach for 24 hours. Following HBSS washes, cells were exposed to MNP samples at 1.0 µg/mL for 72 hours. MNP media was aspirated and the cells washed twice with HBSS before imaging in 20 µL HBSS. MNP solutions without cells were also imaged in HBSS in order to construct spectral libraries of each MNP sample, which would be used to validate the plastic's interactions with HMC3. Images were taken at 100% illumination from a 150 W halogen lamp (Fibre-Lite DC-950, Dolan-Jenner Industries, Boxborough, MA, USA) and 0.25 second exposure. Image processing was performed in ENVI 4.8 (L3Harris Geospatial, Stamford, CT, USA), where halogen light corrections and spectral angle mapping (SAM) were performed for each image. Using a 0.075 radian matching angle, spectral angle libraries from the MNP solutions were applied and filtered in their corresponding cell-exposure images, allowing for the detection of plastic fragments in cells. Spectral matches were colored and overlaid atop the original images to visualize the interaction.

2.3.9 Cytosolic ROS Quantification

The concentrations of cytosolic reactive oxygen species (ROS) were assessed through cytometric fluorescence. Using 2',7'-dichlorodihydro-fluorescein diacetate (H_2DCFDA) (Biotium, Cat. No. 10058), the concentration of ROS correlated to the fluorescence per cell. HMC3 cells were plated in six-well plates at a density of 50,000 cells per 1.5 mL and allowed to attach for 24 hours. After washing in HBSS, appropriate MNP solutions were applied for 72 hours. Before reading, cells were incubated in 10 µM DCFDA for 30 minutes, while the positive control group received an additional 200 µM tert-butanol (TBOH) incubation preceding DCFDA. Cells were washed twice with PBS, trypsinized, and washed twice more in HBSS through centrifugation at 400 g for 4 minutes. Cells were resuspended in 250 µL HBSS and analyzed with the MACSQuant® Analyzer 10. The B2 channel (475 V; 488 nm excitation, 565-605 nm emission) was used to quantify fluorescent intensity per cell. In FlowJo, FSC and SSC gating were performed to determine single, viable cells, and the average fluorescence per replicate (n=3) were compared against unexposed cell means.

2.3.10 Mitochondrial ROS and Membrane Potential

To complement cytosolic ROS concentrations, the levels of mitochondrial ROS (mtROS) were similarly assessed using MitoROS™ 580 (AAT Bioquest, Pleasanton, California, USA). HMC3 cells were plated in six-well plates at a density of 50,000 cells per 1.5 mL and allowed to attach for 24 hours. After washing in HBSS, appropriate MNP solutions were applied for 72 hours. Before reading, cells were incubated in 1X MitoROS™ for 30 minutes, while the positive control group received an additional 10 µM antimycin A (J63522.MA, Thermo Fisher Scientific) and rotenone (R8875, Sigma-Aldrich) incubation for 30 min prior to MitoROS™ to induce mitochondrial ROS production. Cells were washed twice with PBS, trypsinized, and washed twice more in HBSS through centrifugation at 400 g for 4 minutes. Cells were resuspended in 250 µL HBSS and analyzed with the MACSQuant® Analyzer 10.

In order to assess mitochondrial membrane potential ($\Delta\Psi_m$), an identical protocol was followed, substituting MitoROS™ for Tetramethylrhodamine ethyl ester (TMRE) at a concentration of 100 nM. For the positive control, 10 µM carbonyl cyanide m-chlorophenyl hydrazone (CCCP) was incubated concurrently with the TMRE. Analyses of both mtROS and $\Delta\Psi_m$ MACSQuant® Analyzer 10's B2 channel (575V; 488 nm excitation, 565-605 nm emission). Single, viable cells were selected in FlowJo through FSC and SSC gating, and average fluorescence per replicate (n=3) were compared against unexposed cell means.

2.3.11 Antioxidant Enzyme and Biomolecule Concentration

The concentrations of superoxide dismutase (SOD), catalase (CAT), reduced glutathione (GSH), and oxidized glutathione (GSSG) were assessed using the VarioSkan Lux Plate Reader (ThermoFisher Scientific). HMC3 cells were plated in six-well plates at a density of 50,000 cells per 1.5 mL and allowed to attach for 24 hours. After washing in HBSS, appropriate MNP solutions were applied for 72 hours. Cell lysates were captured after exposure using SDS-free Halt Protease Inhibitor (Thermo Scientific). The Catalase Activity Assay Kit (Abcam, ab83464, Cambridge, UK), Superoxide Dismutase Activity Assay Kit (Abcam, ab65354), Amplite™ Glutathione Peroxidase Assay Kit (AAT Bioquest, 11560), and Amplite™ Rapid Fluorimetric Glutathione GSH/GSSG Ratio Assay Kit (AAT Bioquest, 10060) were each used to quantify their associated molecule's concentration. Lysates were additionally quantified by Pierce BCA Protein Assay Kit (ThermoFisher Scientific) to ensure normalized reporting. Results were reported as fold-changes relative to unexposed cell's concentrations of these biomolecules.

2.3.12 ATP Production

To assess ATP in HMC3 exposed to MNPs, the ReadiUse™Rapid Luminometric ATP (AAT Bioquest 21601) was performed. HMC3 cells were plated in 96-well plates at a density of 10,000 cells per 100 µL and allowed to attach for 24 hours. After washing in HBSS,

appropriate MNP solutions were applied for 72 hours. Before reading, 100 µL of the assay reagent was added to each well and incubated at room temperature in dark conditions for 15 minutes. Luminescent intensity was recording with the VarioSkan Lux, and results were reported as fold-changes relative to unexposed cells.

2.3.13 Mitochondrial Oxygen Consumption and Cellular Metabolism

The Seahorse XFe96 Analyzer (Agilent, Santa Clara, California, USA) was used to measure the oxygen consumption rates (OCR) and extracellular acidification rates (ECAR) in accordance with the Cell Mito Stress Test Kit (103015-100, Agilent). Using the specialized Seahorse XF 96-well plates required by the machine, 10,000 cells in 100 µL were plated and allowed to attach for 72 hours. After washing in HBSS, appropriate MNP solutions were applied for 72 hours. The assay was performed in accordance to the manufacturers protocol [180]. Briefly, real-time OCRs and ECARs were collected following the injections of specific mitochondrial electron transport chain complex inhibitors in the following order, each approximately 20 minutes apart: Oligomycin (1.5 μM, 99 %, Sigma-Aldrich), FCCP (0.25 μM, 98%, Sigma-Aldrich), and Antimycin A & Rotenone (0.5 μM, Thermo Fisher Scientific and Sigma-Aldrich; respectively). Data was normalized by Pierce BCA protein assay kit (ThermoFisher Scientific).

2.3.14 Supernatant Cytokine Release

Concentrations of interleukin-6 (IL-6) and interleukin-8 (IL-8) were assessed through colorimetric ELISA sandwich kits (Invitrogen 88-7066 and 88-7346, respectively). HMC3 cells were plated in six-well plates at a density of 50,000 cells per 1.5 mL and allowed to attach for 24 hours. After washing in HBSS, appropriate MNP solutions were applied for 72 hours. After this time point, culture medium was collected from each replicated and centrifuged at 400 g for 4 minutes to remove debris. The remaining supernatant was stored at -80°C until read.

The ELISA kits were followed in accordance with the associated protocol. Briefly, capture antibodies were adhered to 96-well plates overnight, followed by the addition of thawed supernatant and overnight incubation. Appropriate detection antibodies were added thereafter, followed by horseradish peroxidase and chromogenic substrate 3,3',5,5'-tetramethylbenzidine. After a 15-20 minute incubation, sulfuric acid was added to halt the reaction, and measurements were taken using the VarioSkan Lux at both 450 nm and 570 nm, with the latter being subtracted from the former for background correction. For each incubation step, the well plates were shaken at 600 rpm for 10 minutes before and after the addition of any subsequent reagents. Assay performance was validated through calibrant curves along with a bacterial lipopolysaccharide (LPS; Invitrogen 00-4976-93) exposure to HMC3 at 50, 100, and 200 nM as a positive control for cytokine induction. Data was reported as fold-changes of MNP sample cytokine concentrations relative to those of unexposed cells.

2.3.15 Mitochondrial Mass and Mitophagy

To quantify the relative mitochondrial mass in HMC3 exposed to MNPs, MitoTracker™ Green FM (M46750, Thermo Fisher Scientific) was assessed through flow cytometry. HMC3 cells were plated in six-well plates at a density of 50,000 cells per 1.5 mL and allowed to attach for 24 hours. After washing in HBSS, appropriate MNP solutions were applied for 72 hours. Before reading, cells were incubated in 100 nM MitoTracker™ for 30 minutes. Cells were washed twice with PBS, trypsinized, and washed twice more in HBSS through centrifugation at 400 g for 4 minutes. Cells were resuspended in 250 µL HBSS and analyzed with the MACSQuant® Analyzer 10. The B1 channel (350V; 488 nm excitation, 500-550 nm emission) was used to assess the fluorescence per cell, with 10,000 cells quantified per replicated (n=3). Single, viable cells were selected in FlowJo by FSC and SSC gating, and the average fluorescence per replicate was compared against non-MNP exposed cell means.

To verify mitophagy, two methodologies were employed. First, the colocalization of mitochondria and lysosomes were assessed using MitoTracker™ Green FM and LysoBrite™

Red(22645, AAT Bioquest), respectively. Ten thousand HMC3 cells were seeded in confocal dishes (75856-742, VWR Avantor) and allowed to attach for 24 hours. Following a wash in HBSS, cells were exposed to appropriate MNP solutions for 72 hours. Cells were washed twice more in HBSS and incubated in 100 nM MitoTracker™ for 20 minutes followed by 1X™ for 15 minutes. Samples were washed thrice and imaged with the Echo Revolution fluorescent microscope with FITC (25 % LED power, 200 ms exposure) and TxRED (5% LED power, 100 ms exposure) channels. To assess the colocalization, ImageJ was used to separate image color channels, where ROIs were overlaid and the pixel mean gray intensity per channel was graphed. Data were plotted in OriginPro 2025b (OriginLab Corporation, Northampton, MA, USA) to show the fluorescent intensity overlap along the length of the ROI.

Mitophagy was confirmed further through the use of MtPhagy Dye (MT02, Dojindo, Kumamoto, Japan). HMC3 cells were plated in six-well plates at a density of 50,000 cells per 1.5 mL and allowed to attach for 24 hours. After washing in HBSS, appropriate MNP solutions were applied for 72 hours. A day prior to reading, cells were incubated in 100 nM MtPhagy dye for 30 minutes and returned to MNP media for the remaining 24 hours. Cells were washed twice with PBS, trypsinized, and washed twice more in HBSS through centrifugation at 400 g for 4 minutes. Cells were resuspended in 250 µL HBSS and analyzed with the CytoFLEX LX cytometer (Beckman Coulter) on the FL3-H channel (488 nm excitation, 690 ± 25 nm emission). Single, viable cells were selected in FlowJo by FSC and SSC gating, and the average fluorescence per replicate was compared against control cell means.

2.3.16 MNP Autofluorescent Validation

In order to insure plastics would not interfere with fluorimetric analyses, excitation and emission spectra of MNPs were caputred in the VarioSkan Lux Microplate Reader. Aqueous stocks at 1 mg/mL for real-world MNPs and 100 µg/mL for PS-50 NPs were read in 96-well plates to discover excitation spectra through absorbance readings. From the recorded

peak absorbance wavelength, the emission spectra fluorescence were observed. Both Cup-MNPs and PS-50 NPs were not observed to contain significant excitation or emission spectra. Fork-MNPs showed an excitation peak around 300 nm and a corresponding emission spectra from this peak around 410-450 nm, far outside the range that each experimental assay was performed (Figure A.2).

2.3.17 Statistical Analysis

Statistical variations between HMC3 exposed to MNPs and HMC3 not exposed to plastics were performed using one-way analysis of variance (ANOVA) with by Dunnett's post hoc test. All statistical models were performed in GraphPad Prism V10.5 (GraphPad Software, San Diego, CA, USA). Quantified data are represented as the mean ± standard deviation (SD) as calculated from independent replicates. P-values ≤ 0.05 were considered to be statistically significant.

2.4 Results and Discussion

2.4.1 Physicochemical Characterization of MNPs

In order to accurately understand the impacts the MNPs have on HMC3, a complete understanding of the physical and chemical properties is required. Attenuated total reflectance Fourier-transform infrared spectroscopy (ATR-FTIR) was performed on the real-world MNP samples. The results showed the plastics most closely resemble PS, with characteristic transmission bands at at 3031 cm^{-1} and 2919 cm^{-1} correlating to aromatic C-H and CH_2 vibrations, respectively. Distinct absorption features at 1600, 1488, and 1453 cm^{-1} were attributed to the C=C bonds found along aromatic benzene rings. Additionally, bands located at 754 and 706 cm^{-1} were correlated to those of C-H bending vibrations, confirming the presence of PS. These spectral characteristics validate that both Cup-MNPs and Fork-MNPs predominantly consist of PS, allowing for direct comparative analyses between the two samples without concern for material composition differences. Given that the pristine plastic group

is also comprised of PS, comparisons between treatments can be assessed with respect to morphology and size rather than composition.

Previous nano-toxicological studies indicate that particle size and morphology dictate their interactions and impact on biological systems, indicating a crucial step in understanding the impacts of MNPs on HMC3 cells [181, 182]. Scanning electron microscopy (SEM, Zeiss EVO 50) was performed on the real-world MNP samples in order to calculate bulk particle size and understand the morphology (Figure 2.2b and c). Both real-world samples consisted of a heterogeneous mixture of irregular, spherical-shaped particles that most resemble those of fragments, mirroring those abundantly found in the human body [92, 99, 100, 106]. Cup-MNPs presented an average size of 41.3 ± 27.4 µm, and Fork-MNPs were similarly sized at 40.5 ± 25.2 µm. Cup-MNPs displayed a size distribution ranging from 10 to 50 µm for 85% of particles, with 98% measuring below 90 µm (Figure 2.2c). Fork-MNPs exhibited a similar distribution, with 73% of particles between 10 and 50 µm, and 90% below 90 µm (Figure 2.2c). Both groups display sizes synonymous with those found in the human body, particularly the brain [92]. These size ranges also match the profiles of plastics found to naturally release from consumer plastics, allowing for more accurate analyses of the impacts on the human brain [183, 74].

The zeta potential was assessed for real-world MNPs along with PS-50 to understand the surface charge that these particles exert. Measurements of the particles in complete cell media showed each sample to exert a negative, yet near-neutral charge, indicative of biocorona formation from the serum present in the media (Figure 2.2d).

Given the limitations in SEM for viewing both micro- and nano- size fragments, DLS was performed on the particles following subjugation to a 0.45 µm filter. Hydrodynamic size analyses were then conducted by dynamic light scattering (DLS) measurements. Cup-MNPs displayed bimodal peaks at 20.05 nm ± 11.66 nm and 117.03 nm ± 40.59 nm, and Fork-MNPs showed similar bimodalism at 8.86 nm ± 2.57 nm and 56.03 nm ± 27.85 nm.

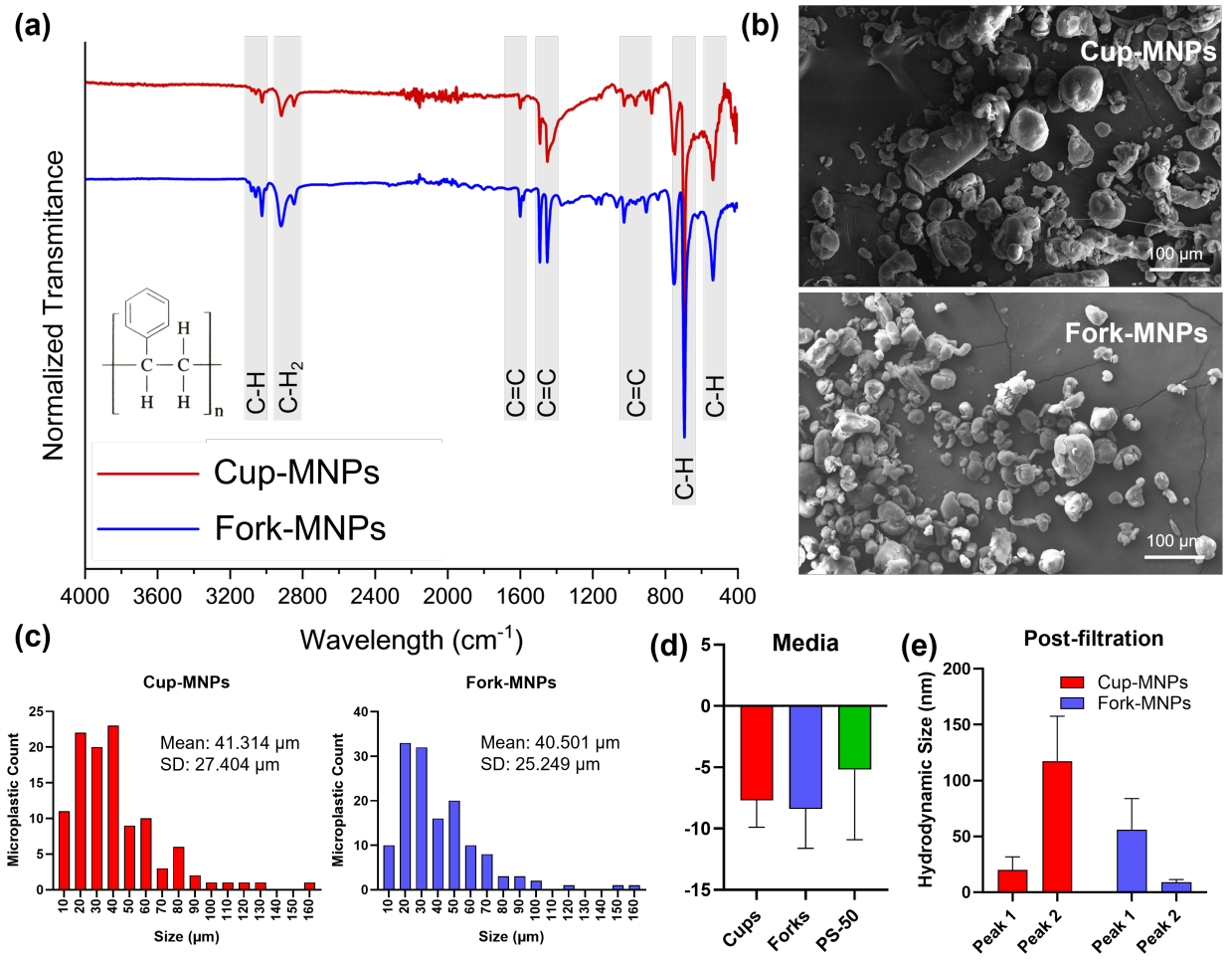

Figure 2.2: Characterization of Micro- and Nanoplastics (MNPs). (a) Attenuated total reflectance Fourier-transform infrared spectroscopy (ATR-FTIR) spectra of Cup- and Fork-MNPs. (b) Scanning electron microscopy (SEM) images displaying representative morphologies of the real-world MNP samples (c) Size distribution of MNPs determined from SEM images (n = 111 for Cup-MNPs; n = 140 for Fork-MNPs). (d) Zeta potential of MNPs in cell culture medium. (e) Hydrodynamic diameter of MNPs in media measured by DLS, showing a bimodal distribution after filtration through a 0.45 µm filter.

Forks were found to display significantly smaller particles when compared to those of Cup-MNPs, and even smaller than those of PS-50, which range from 50 - 100 nm per the manufacturer's specifications. Nano-sized fractions in both the real-world and pristine samples allows for comparable assessments between the morphological and structural differences between the two, with PS-50 lacking many of the microstructures that are seen in real-world nanoplastics [97, 54]. The inclusion of both sample types allows for a systematic analysis for

how the human brain interacts with these polymeric materials, better informing their use in further studies on how plastics impact the body.

The synthesis of polymers can involve heavy metals for pigmentation, additives, plasticizers, and metallocatalysts for elongation [40]. Metals frequently seen in synthetic plastics include lead (Pb), cadmium (Cd), chromium (Cr), mercury (Hg), nickel (Ni), and zinc (Zn) [35]. Additionally, these elements can be absorbed by plastics in the environment, namely landfills, before they find their way into the human body [55]. While often considered to homogeneously plastic, MNPs' interactions with known toxicants can drastically alter their toxicological profile [184, 185, 186]. Trace metal concentrations of the MNP samples were analyzed by Inductively Coupled Plasma Optical Emission Spectroscopy (ICP-OES). The concentrations of each of these elements was below the limit of detection, indicating the MNPs to be free of metal contamination (Figure A.1).

2.4.2 Interactions between HMC3 and MNPs

In order to gauge cytotoxicity, HMC3 cells were exposed to Cup-MNPs, Fork-MNPs, and PS-50 NPs at doses of 0.1, 1.0, and 10 µg/mL and analyzed at 24, 48, and 72 hour endpoints by trypan blue. No significant losses in cell viability were observed for any condition, but instead a slight increase was observed after 72 hours in Cup- and Fork-MNP samples (Figure 2.3a). Microglia have been shown to increase proliferative pathways under acute stresses, namely increases in reactive oxygen species (ROS) [171, 169, 187]. Thus, the 72 hour time point was chosen for further analyses.

Microglia possess the ability to phagocytose, with dying cells, pathogens, and cellular debris being a primary target [188]. HMC3 have been shown to uptake smaller, pristine PS particles in previous studies[164]. Because of this, it was predicted that the real-world MNPs would be detectable interacting and internalized with the cells. Both flow cytometry and enhanced darkfield hyperspectral imaging (CytoViva, Inc) were used in order to quantify and visualize these events, respectively. MNP samples were stained with Nile Red and exposed

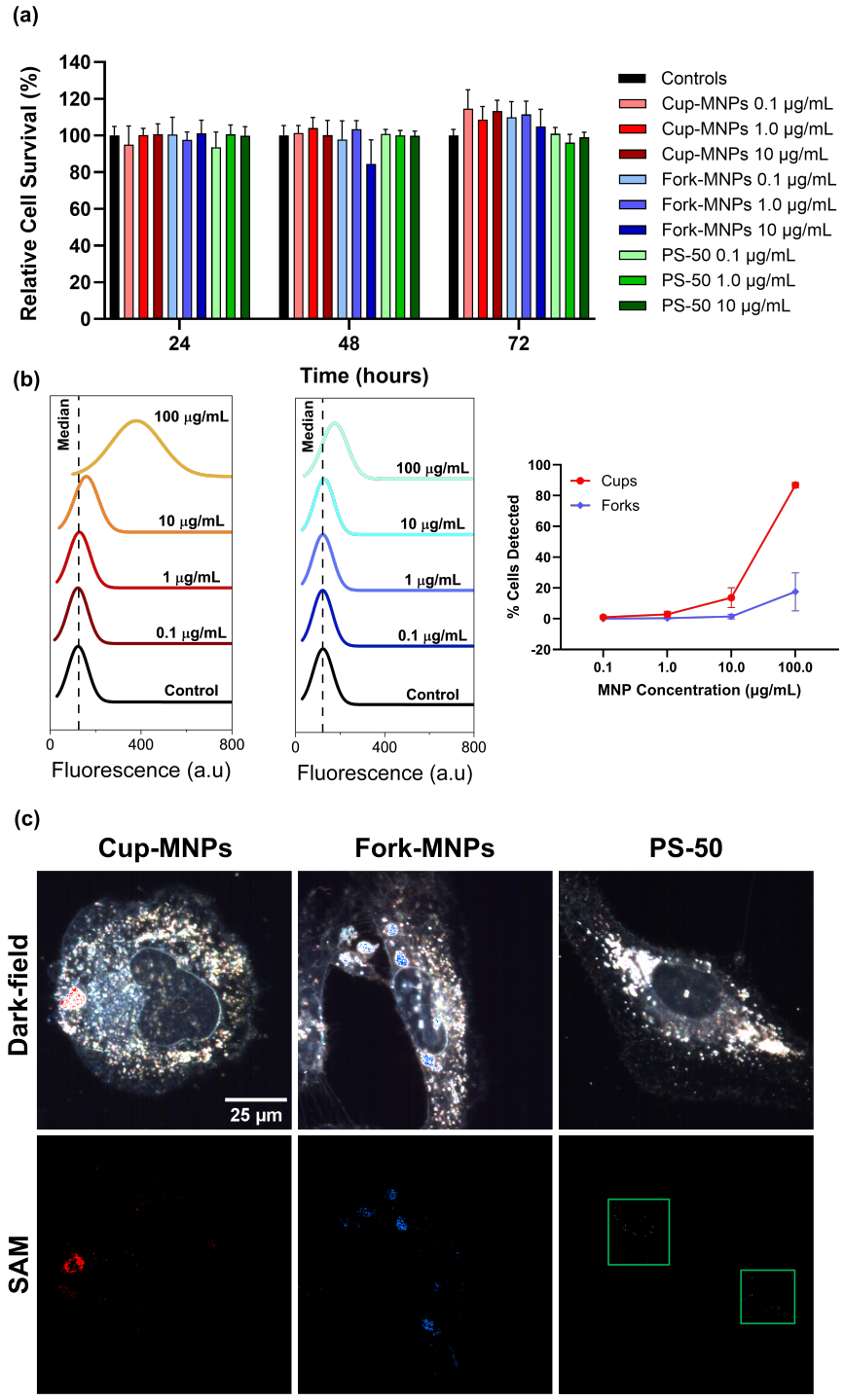

Figure 2.3: Interactions of MNPs with HMC3 Cells. (a) Viability of HMC3 exposed to 0.1, 1.0, and 10 µg/mL MNPs for 24, 48, and 72 hours (n=4). (b) Quantification of Cup- and Fork-MNP uptake, respectively, after 72 hours using Nile Red and flow cytometry (n=3; mean of 10,000 cells uptaken per experiment) (c) Hyperspectral enhanced darkfield microscopy analyses of HMC3 exposed to 1 µg/mL MNPs for 72 hours; SAM, Spectral Angle Mapper. Data are shown as mean ± SD; one-way ANOVA followed by Dunnett's post hoc test was used to compare each treatment group with the control.

to cells at a range of 0.1, 1.0, 10, and 100 µg/mL for 72 hours. The higher concentration of 100 µg/mL was selected in order to validate what has been seen in previous studies with higher concentrations.

Cells exposed to Cup-MNPs were found to significantly fluoresce at and above 1.0 µg/mL, where Fork-MNPs were significantly detectable at and above 10 µg/mL (Figure 2.3b). Prior studies using similar methodologies for environmentally-relevant MNPs have detected significant fluorescence only above much higher concentrations, with detection typically only seen above 50 µg/mL [189]. At 100 µg/mL, 86% of cells exposed to Cup-MNPs were shown to uptake the particles compared to only 17% of cells exposed to the same concentration of Fork-MNPs (Figure 2.3b).

PS-50 particles were not able to be detected at any concentration using this methodology, which is believed to be a result of their size. Previous studies have reported detection limitations with this method for particles smaller than approximately 100 nm, meaning the PS-50 samples along with nano-fraction real-world MNPs would remain undetectable [190, 191]. Smaller particles lack sufficient area to retain enough dye signal and display faster dye desorption rates for analysis with flow cytometry. Given the higher proportion of NPs in Fork-MNPs, this principle could explain the lower detectable uptake of the particles compared to Cup-MNPs.

These results imply that MNP uptake detection is dependent on size. The Cup-MNPs showed much higher uptake when compared to Fork-MNPs at each concentration along with larger size fragments in both bulk and nano-fractions. Macrophages have been previously shown to preferentially phagocytose pristine PS spheres in the 2-3 µm range, as particles in this range are able to fit in between the membrane ruffles present in these cells [192]. These correspond to the sizes of many naturally phagocytosed debris, such as apoptotic bodies and beta-amyloid plaques (Aβ-plaques) [193, 194]. Additionally characteristics such as surface

roughness and rigidity are able to influence particle uptake, with increased roughness increasing surface area for initial attachment and stiffer particles deforming less and providing an easier target to uptake [195].

The interactions between MNPs and HMC3 were additionally observed using CytoViva hyperspectral darkfield microscopy. Label-free MNPs were able to be visualized in direct contact with cells at concentrations of 1.0 µg/mL, providing confirmation that MNPs are present in cellular microenvironments (Figure 2.3c). Each MNP sample was visible at this concentration, which is one of the lowest concentrations at which label-free plastics have been able to be shown to interact with cells [94]. By directly confirming the presence of label-free particles, a more accurate representation of particle-cell interactions can be assessed. The labeling process itself impacts the behavior of the particle, including corona formation and free-dye kinetics [196, 197].

2.4.3 Pristine PS-NPs Elicit Greater Redox Imbalances Compared to Real-World MNPs

To determine whether ROS contributed to the increased cell viability observed after exposure to Cup- and Fork-MNPs, intracellular ROS concentrations were quantified by flow cytometery after 72 hours of exposure. Both real-world MNP samples elicited a statistically significant, yet moderate increase in ROS production above 1.0 µg/mL, while Fork-MNPs increased ROS as low as 0.1 µg/mL (Figure 2.4a). PS-50 exposure produced a much stronger, nearly two-fold increase of ROS above 1.0 µg/mL relative to untreated controls. Moderate ROS increases are known to coincide with various cellular processes, including proliferative signaling and antioxidant defense increases, while excessive ROS accumulation drives oxidative stress and cellular distress [187, 198, 199]. Given that mitochondria represent a major source of intracellular ROS, mitochondrial ROS (mtROS) levels were also assessed (Figure 2.4b). Although there were no statistically significant changes, Cup- and Fork-MNPs were shown to decrease mtROS while PS-50 elicited a slight increase at 1.0 and 10 µg/mL.

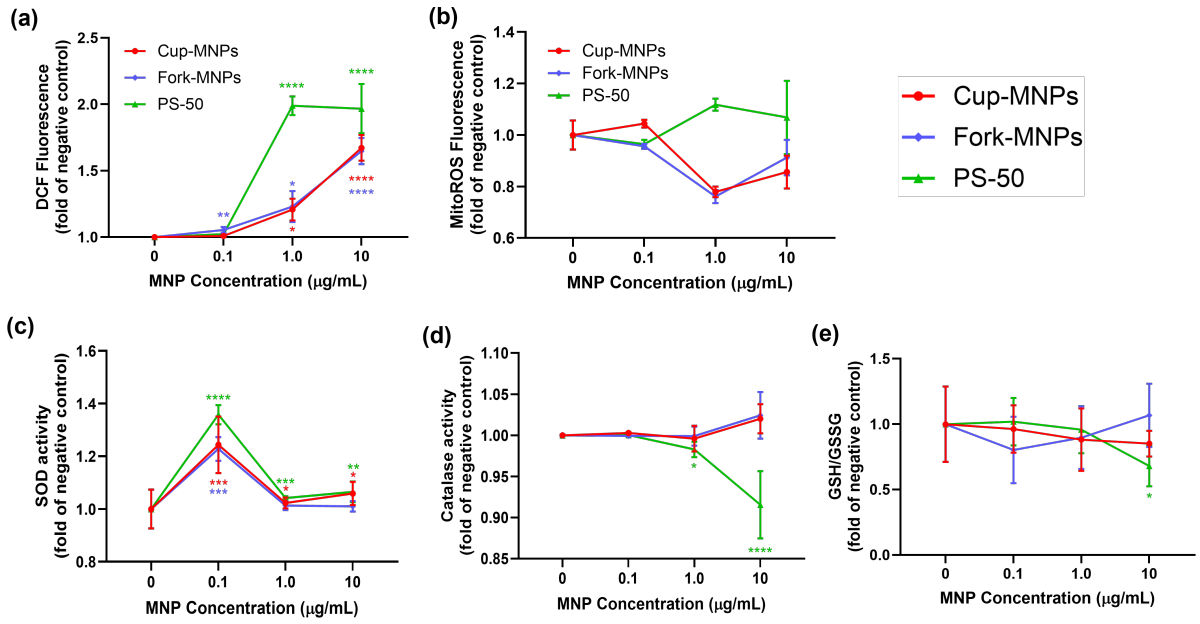

Figure 2.4: Effects of MNPs on Microglial Redox Balance Following 72 Hour Exposure. (a) Quantification of general ROS levels using the 2',7'-DCFDA assay measured by flow cytometry (n=3; mean of 10,000 cells uptaken per replicate); 200 μM tBuOOH was used as a positive control. (b) Quantification of mitochondrial ROS by flow cytometry using MitoROS fluorescent dye, with fluorescence normalized to controls (n=3; average of 10,000 cells per experiment); antimycin A and rotenone (10 μM each) were concurrently used as a positive control. (c) Superoxide dismutase (SOD) activity. (d) Catalase activity. (e) GSH/GSSG ratio. Data are presented as mean $\pm$ SD; one-way ANOVA followed by Dunnett's test was used to compare multiple treatment group means against the control group mean; $* \ p < 0.05$, $** \ p < 0.01$, $*** \ p < 0.001$, $**** \ p < 0.0001$.

To evaluate whether MNP exposure disrupted redox homeostasis, key antioxidant defenses were quantified in HMC3 cells. Total superoxide dismutase (SOD) activity, responsible for the catalyzation of superoxide radicals to hydrogen peroxide, was found to be significantly upregulated in cells exposed to both real-world MNPs and PS-50 (Figure 2.4c). For each sample, the lowest concentration of 0.1 µg/mL exhibited the highest concentrations of SOD, consistent with an early adaptive response to increased ROS. In contrast, catalase activity, responsible for the decomposition of hydrogen peroxide, did not exhibit a corresponding increase (Figure 2.4d). Catalase activity remained largely consistent across samples at lower concentrations, but higher doses of PS-50 were shown to elicit significant decreases in the

enzymatic function, suggesting compromised redox capacity as supported by the heightened ROS accumulation seen in PS-50 1.0 and 10 µg/mL concentrations.

The ratio of reduced to oxidized glutathione (GSH/GSSG) was assessed to understand the overall redox state of HMC3 cells exposed to MNPs (Figure 2.4e). A modest increase in the GSH/GSSG ratio was observed in Fork-MNPs at 10 µg/mL, while Cup-MNP and PS-50 samples caused a dose-dependent decrease in the ratio, with PS-50 at 10 µg/mL showing a significant decrease compared to unexposed cells. Given the glutathione system represents the major mitochondrial antioxidant buffer, a reduced GSH/GSSG ratio indicates perturbed mitochondrial redox balance and heightened susceptibility to oxidative injury [200, 201]. Decreases in GSH/GSSG ratio are closely associated with mitochondrial dysfunction and are frequently reported in mitochondrial-related pathologies, including neurodegenerative disorders such as Parkinson's Disease and Alzheimer's Disease [202, 203, 204].

Combined, these findings indicate Cup- and Fork-MNPs elicit a low-to-moderate increase in ROS levels, with HMC3 cells attempting to counterbalance through adaptive antioxidant responses. In contrast, the pristine PS-50 NPs overwhelm cellular redox mechanisms, leading to reduced antioxidant capacity and persistent oxidative stress. Pristine NPs are characteristic inducers of oxidative stress, with similar doses of PS-NPs shown to elicit heightened ROS amongst *in vitro* and *in vivo* targets [205, 206, 207, 95]. Consumer product-derived MNPs such as those used in this experiment do not appear to provoke oxidative stress to the same extent as PS-50, potentially as a result of the lesser fraction of highly-reactive nanoscale particles [208]. This lack of a pronounced oxidative stress-response was similarly reported in zebrafish brains following long-term exposure to real-world plastics that where fabricated from similar consumer items (plastic bags, straws, bottles) and psudeo-weathered through UV exposure [209].

2.4.4 Pristine PS-NPs Induce Mitochondrial Dysfunction, Real-World MNPs Trigger Mitochondrial Adaptive Response

The cellular redox state is tightly interconnected with mitochondrial dysfunction. Oxidative phosphorylation (OXPHOS) within mitochondria generates ATP to meet cellular energy demands, which depends on the mitochondrial membrane potential ($\Delta\Psi_m$) to drive electron transport across the inner mitochondrial membrane. During this process, ROS are produced as byproducts of electron transport chain (ETC) function [210, 211]. Thus, mitochondrial dysfunction constituently results in elevated RIS generation and oxidative stress. To assess the impact of MNP exposure on OXPHOS function, mitochondrial respiration and oxygen consumption rates (OCR) were quantified using the Seahorse XF Mito Stress Test on HMC3 cells after 72-hour exposure to plastics (Figure 2.5).

Mitochondrial stress responses differed in accordance with particle dose, size, and physicochemical characteristics. Exposure to the pristine PS-50 sample elicited a general decrease, significant or otherwise, across each respiratory parameter at all concentrations. This correlates appropriately to the observed elevation in total and mitochondrial ROS in PS-50 samples (Figure 2.4a & b). Perturbed mitochondrial respiration has been reported across various *in vitro* models exposed to doses over 5 µg/mL PS-NPs, including liver, lung, and brain cells [212, 213]. A common brain cell model, SH-SY5Y, has shown dysregulation of mitochondrial Complex I as a primary driver in PS-NP induced respiratory deficits [161, 212]. The 5 µg/mL dose at which these conditions were observed in prior studies is five-fold higher than the minimal dose at which mitochondrial respiratory defects were observed here (1 µg/mL), which may be a result of more efficient PS-NP internalization by microglial phagocytosis when compared to neuronal models [169].

Basal respiration, ATP-linked respiration, and proton leak were modestly reduced in cells exposed to 1 µg/mL of Cup-MNPs (Figure 2.5d, e, & f). At the increased dose of 10 µg/mL, both basal and ATP-linked respiration returned to control values, while maximal and spare respiratory capacity were shown to be elevated, and proton leak was significantly

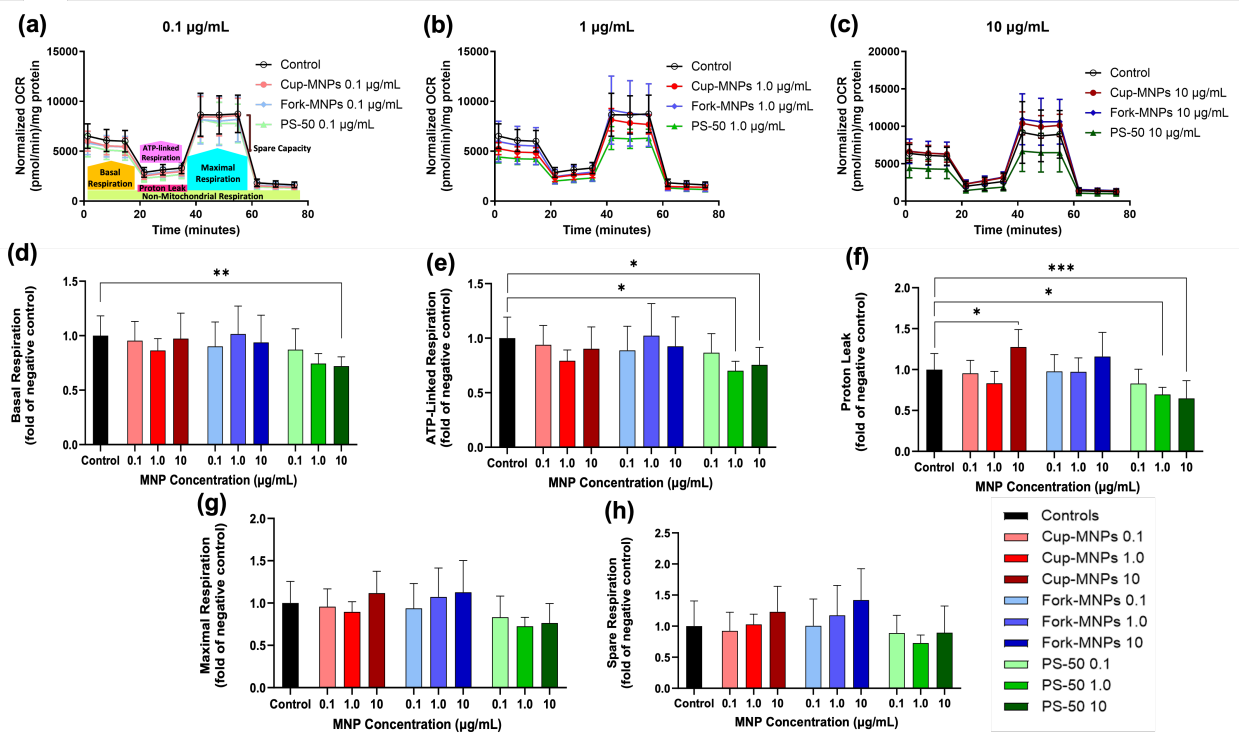

Figure 2.5: Mitochondrial respiration parameters in HMC3 after 72-hour exposure to MNPs. The Seahorse XFe96 Analyzer was used to quantify oxygen consumption rates (OCR) in control and MNP-exposed cells at (a) 0.1 µg/mL, (b) 1.0 µg/mL, and (c) 10 µg/mL. Key parameters of mitochondrial respiration were then derived, with (d) basal respiration (oxygen consumption used to meet cellular ATP demand), (e) ATP-linked respiration (fraction of basal respiration coupled to ATP production), (f) proton leak (fraction of basal respiration not coupled to ATP synthesis), (g) maximal respiration (maximum OCR achieved under conditions of uncoupled respiration), and (h) spare respiratory capacity (the difference between maximal and basal respiration, reflecting the cell's ability to meet increased energetic demand or respond to stress) plotted separately amongst each concentration. Data are presented as mean ± SD (n= 8 for 0.1 and 1 μg/mL; n=11 for 10 μg/mL); One-way ANOVA followed by Dunnett's test was used to compare multiple treatment group means against the control group mean; $* \ p < 0.05$, $**$ $p < 0.01$, $***$ $p < 0.001$, $****$ $p < 0.0001$.

upregulated (Figure 2.5f, g, & h). This trend is indicative of adaptive mitochondrial response to Cup-MNP-induced stress. While increased proton leak lowers coupling efficacy, it may concurrently stimulate excessive ROS formation by modulating $\Delta\Psi_m$, conferring protection against oxidative injury [214, 215]. This aligns with the observed low to moderate ROS concentrations observed in Cup-MNP-exposed HMC3. In cells exposed to Fork-MNPs, a trend toward mitochondrial compensation was observed, as evidenced through elevated respiratory parameters, although no concentration of Fork-MNP exposure elicited statistically significant changes. However, the elevated proton leak, maximal respiration, and spare capacity observed at 10 µg/mL matches those seen in Cup-MNPs, supporting the adaptive mitochondrial response characterized by restorative upregulation of OXPHOS under intermediate stress conditions [216, 217].

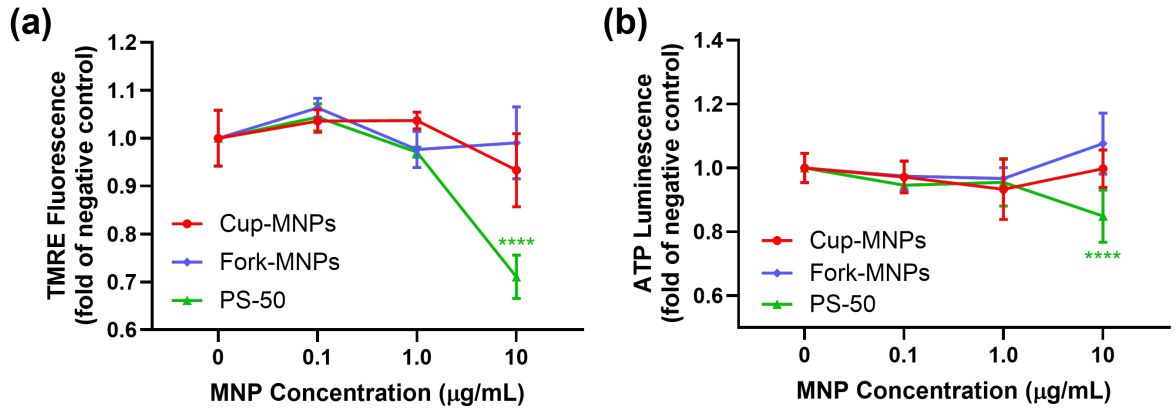

Figure 2.6: Effects of MNPs at varying concentrations on mitochondrial membrane potential ($\Delta\Psi_m$) and ATP concentrations in HMC3 cells. (a) Quantification of $\Delta\Psi_m$ in HMC3 exposed to MNPs for 72 hours and in untreated controls, assessed through flow cytometry using TMRE fluorescent dye. Cells exposed to 10 µM CCCP were included as a positive control (fluorescence values normalized to control; n=3; mean of 10,000 uptaken per replicate). (b) Intracellular ATP levels assessed by ReadiUse™ Rapid Luminometric ATP Assay Kit compared to unexposed cells (n=4). Data are presented as mean ± SD (n= 8 for 0.1 and 1 μg/mL; n=11 for 10 μg/mL); One-way ANOVA followed by Dunnett's test was used to compare multiple treatment group means against the control group mean; $* \ p < 0.05$, $** \ p < 0.01$, $*** \ p < 0.001$, $**** \ p < 0.0001$.

The $\Delta\Psi_m$ and intracellular ATP content were assessed in HMC3 following MNP exposure (Figure 2.6a & b). Only slight deviations in $\Delta\Psi_m$ were detected for all concentrations

for the real-world Cup- and Fork-MNPs, with the highest dose of 10 µg/mL showing moderate decreases in Cup-MNPs. However, PS-50 treatments in HMC3 cells at 10 µg/mL showed statistically significant decreases in $\Delta\Psi_m$ with a parallel decrease in ATP levels, consistent with overt mitochondrial dysfunction. Similar mitochondrial defects have been described in neurons from mice exposed to pristine PS-NPs of similar sizes for four weeks [218]. This has been further corroborated in SH-SY5Y cells, where reductions in $\Delta\Psi_m$ and ATP were reported in PS-NP doses from 5 - 500 µg/mL [212]. By comparison, the moderate decline in $\Delta\Psi_m$ observed in HMC3 exposed to 10 µg/mL of Cup-MNPs was not accompanied by ATP declines. Both real-world MNP samples did not result in a decrease of ATP, consistent with the observed enhancement of OXPHOS activity, indicating the preservation of mitochondrial compensatory capacity in response to MNP-induced stress.

HMC3 are dependent on OXPHOS pathways for sufficient energy to maintain homeostasis and cellular function, including immune defense mechanisms [219]. Impairment of mitochondrial respiration can promote a metabolic shift toward glycolytic pathways, and thus the extracellular acidification rate (ECAR), a proxy for glycolytic and related acidifying metabolism, was measure in PS-50 treated HMC3 cells to assess changes in metabolism (Figure 2.7). Exposure to PS-50 at 1 and 10 µg/mL led to the reduction of ECAR relative to unexposed cells. The concomitant decrease in OXPHOS and ECAR indicates general metabolic suppression rather than compensatory redistribution of ATP production at these doses.

The combined data indicate that exposure to pristine PS-50 NPs is able to induce a suppression of metabolic activity through a reduction in respiration markers, diminished ATP without a compensatory mechanism, lowered $\Delta\Psi_m$, and increased ROS generation, all of which are indicative of mitochondrial dysfunction. The early stages of these phenomena can be seen at doses as low as 1.0 µg/mL, with 10 µg/mL showing much stronger evidence for impairment. These perturbations align with cellular phenotypes typically associated with

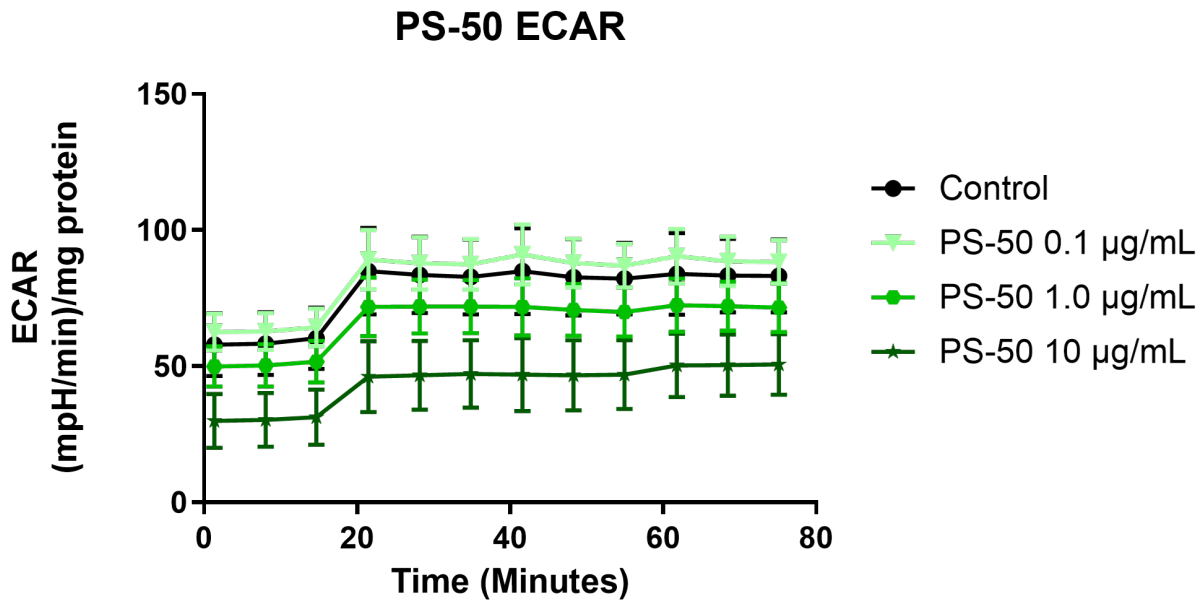

Figure 2.7: Extracellular acidification rate (ECAR) of HMC3 cells exposed to varying concentrations of pristine PS-50 (n=6). Data are presented as mean ± SD (n= 8 for 0.1 and 1 μg/mL; n=11 for 10 μg/mL); One-way ANOVA followed by Dunnett's test was used to compare multiple treatment group means against the control group mean; $* \ p < 0.05$, $** \ p < 0.01$, $*** \ p < 0.001$, $**** \ p < 0.0001$.

neurodegenerative disorders [170, 171]. These impacts are noticeably absent in the real-world Cup- and Fork-MNP samples, with only moderate ROS increases and cellular activity associated with adaptive mitochondrial responses at equivalent doses.

2.4.5 Mitochondrial Remodeling Following Exposure to MNPs

The condition at which mitochondria function is essential to sustain bioenergetic demands and prevent irregular organelle accumulation. Elevated concentrations of ROS that are sustained over time are able to promote mitophagy, an autophagic pathway responsible for the clearance of dysfunctional mitochondria by lysosomes [220, 221]. In conditions of elevated mitochondrial dysfunction, such as Parkinson's Disease, mitophagic clearance has been seen to be elevated, with defective mitochondria preferentially targeted [222]. To assess

whether MNP exposure alters mitochondrial mass and turnover, MitoTracker Green FM fluorescence was quantified in HMC3 cells by flow cytometry (Figure 2.8a). This dye presents the advantage of $\Delta\Psi_m$-free fluorescence, targeting mitochondrial membrane proteins.

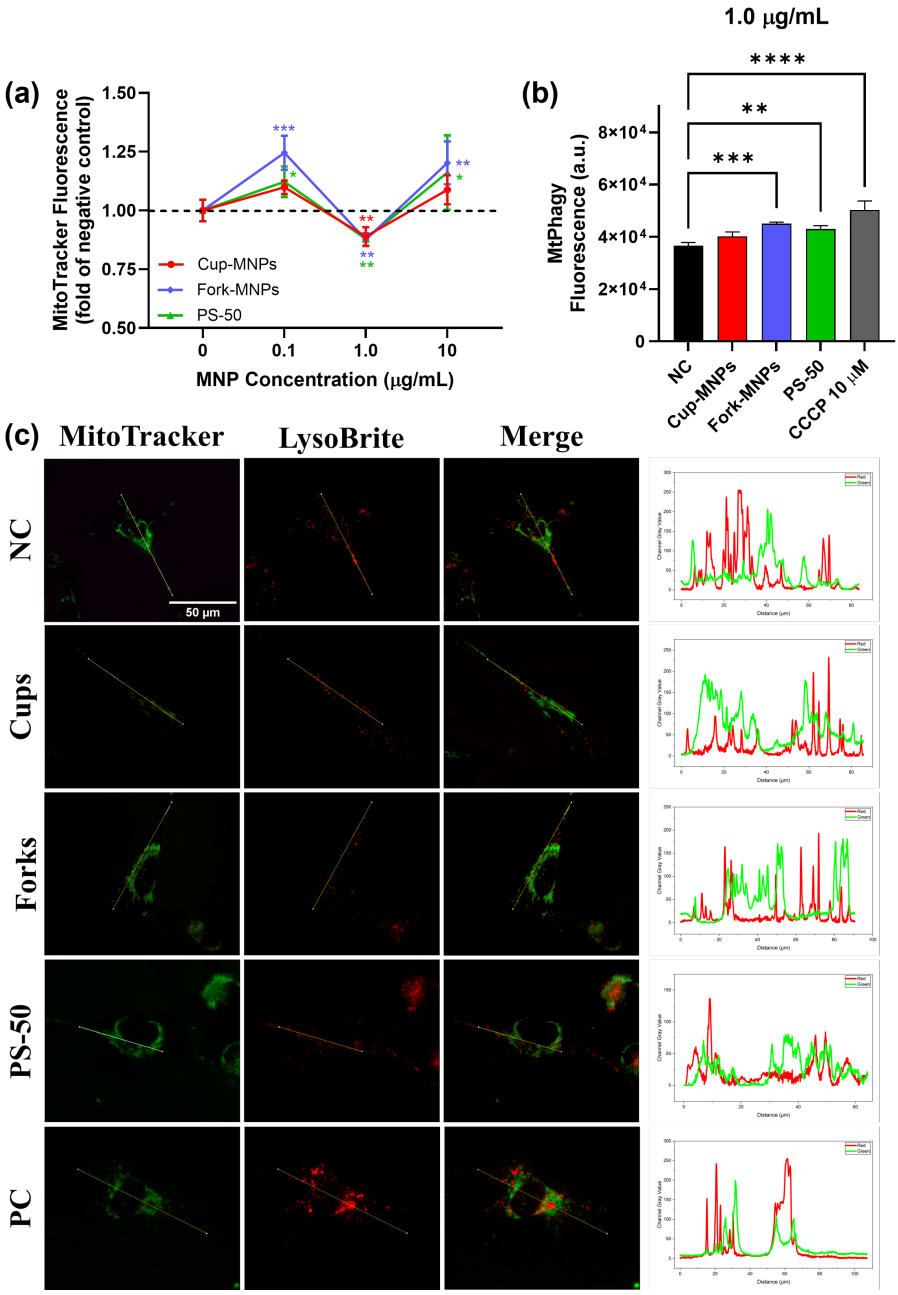

Figure 2.8: Mitochondrial remodeling in HMC3 cells exposed to varying MNP concentrations. (a) Mitochondrial mass quantified by flow cytometry using MitoTracker Green FM (n=3, mean 10,000 cells uptaken per replicate). (b) Mitophagic activity validated using MtPhagy dye in HMC3 cells exposed to 1.0 µg/mL of each MNP sample (n=4; mean 10,000 cells uptaken per replicate). (c) Representative fluorescent microscopy confirming the co-localization of dysfunctional mitochondria with lysosomes, stained using MitoTracker Green FM and LysoBrite Red, respectively. Cells exposed to 10 µM CCCP were used as a positive control (PC) for mitophagic experiments, while cells not exposed to MNPs were used as the negative control (NC). Data are presented as mean ± SD. One-way ANOVA followed by Dunnett's test was used to compare multiple treatment group means against the control group mean; $* \ p < 0.05$, $** \ p < 0.01$, $*** \ p < 0.001$, $**** \ p < 0.0001$.

Mitochondrial mass exhibited dose-dependent variations across all MNP sample types. At 0.1 µg/mL, Fork-MNPs and PS-50 NPs exhibited a statistically significant increase in mass, while Cup-MNPs were increased yet not significant. Fork-MNPs displayed the greatest increase in fluorescence, correlated to the adaptive response in early stress conditions. This increase is correlated with activation of mitochondrial biogenesis, a process involved in expanding mitochondrial networks to compensate for oxidative damage in irregular organelles and sustain metabolic function [223, 224]. Complementary to this, Fork-MNPs at 0.1 µg/mL were shown to significantly increase ROS at a modest concentration, as well as a reduction in the GSH/GSSG ratio (Figure 2.4), indicating the early-onset disruption to cellular homeostasis.

Interestingly, exposure to each MNP sample at 1.0 µg/mL resulted in a significant decrease in mitochondrial mass, likely indicative of cellular protection through dysfunctional mitochondrial clearance by the means of mitophagic pathways. Two separate methodologies were employed in order to investigate this phenomenon, with col-localization of mitochondria and lysosomes assessed by fluorescent microscopy and the mitophagy indicator aptly named MtPhagy quantified through flow cytometry, both at the 1.0 µg/mL dose (Figure 2.8b & c). Mitochondria were visually seen to be localized with lysosomes in higher proportions in MNP samples when compared to unexposed HMC3 cells, aligning closely with cells exposed the known mitophagy inducer CCCP. Additionally, Fork-MNPs and PS-50 samples showed significantly increased MtPhagy fluorescence, indicating substantial evidence for autophagic clearance of the dysfunctional mitochondria. While not significant, Cup-MNPs also displayed a moderate increase in fluorescence in comparison to the control, aligning with the lesser extent of mitochondrial mass lost seen by MitoTracker Green FM.

At 10 µg/mL, mitochondrial mass reverted to increased levels compared to the control for all treatment groups, suggestive of a compensatory biogenic response with the goal of normalizing homeostasis following stress-induced mitophagy. In the PS-50-exposed HMC3, this

increase was found to occur concurrently with a more pronounced mitochondrial dysfunction, implying biogenesis was insufficient to restore mitochondrial integrity to pre-exposure levels. Similar PS-NP samples have been shown to trigger excessive mitophagy in previous *in vitro* models, with the effects reported at concentrations above 5 µg/mL [212].

2.4.6 MNPs Induce Pro-Inflammatory Cytokine Release From HMC3

Microglia display a functional phenotype which is distinctly correlated to metabolic activity, and disruptions in the mitochondrial OXPHOS pathways are key regulators of stress adaptations, inflammatory signaling, and stress adaptation [168, 168, 225, 226]. In order to measure the potential immune-associated impact seen with mitochondrial perturbations, the concentrations of pro-inflammatory cytokines interleukin-6 (IL-6) and interleukin-8 (IL-8) were quantified in HMC3 culture supernatants following 72 hours of MNP exposure (Figure 2.9a & b). These inflammatory markers serve as a widely-used indicator of microglial activation, and display heightened concentrations during inflammatory and immune responses in the central nervous system (CNS) [227, 228].

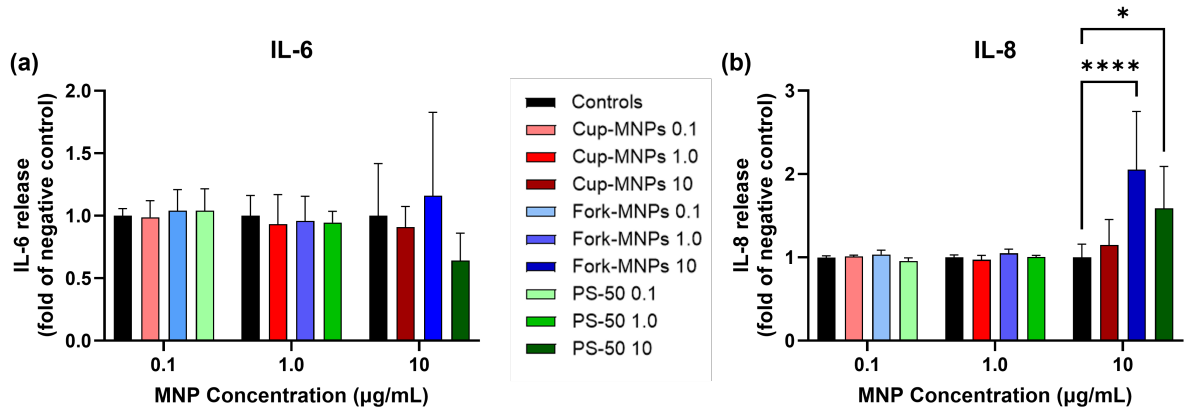

Figure 2.9: MNP-induced cytokine secretion in HMC3. ELISA-quantified concentrations of (a) IL-6 and (b) IL-8 were quantified from the media supernatant following exposure to MNPs for 72 hours. Data are presented as mean ± SD ($n = 4$). One-way ANOVA followed by Dunnett's test was used to compare multiple treatment group means against the control group mean; $* \; p < 0.05$, $* * \;\; p < 0.01$, $* * * \; p < 0.001$, $* * * * \;\; p < 0.0001$

At the lower concentrations of 0.1 and 1.0 µg/mL, no significant variations in cytokine release were detected in relation to unexposed cells. However at 10 µg/mL, Fork-MNPs showed an elevated released profile for both IL-6 and IL-8, with the latter showing drastically significantly increased levels. HMC3 exposed to PS-50 NPs mirrored this significant increase in IL-8, but a nonsignificant decrease in IL-6 production. The increased IL-8 release from PS-NPs is consistent with previous *in vitro* studies where human lung and neural stem cells along with monocytes display a similarly-activated profile [229, 230, 231]. These findings corroborate studies where PS-NPs elicit pronounced *in vivo* neuroinflammation after crossing the blood-brain barrier (BBB), where microglia have shown to enter an activated state and upregulated pro-inflammatory cytokines through NF-κB and TLR9/MyD88 signaling cascades, contributing to neurodegenerative pathology [131, 160, 232, 233]. ROS are recognized modulators of these inflammatory pathways, and thus expatiate neuroinflammatory responses [234].

Following this trend, both PS-50 and Fork-MNPs increased ROS production in HMC3 at 10 µg/mL, suggesting oxidative stress participates in the inflammatory release profile observed. Cytokine responses driven by NPs have been documented in non-neuronal systems, as real-world polyamide (PA) NPs enhanced IL-8 expression in BEAS-2B, a human lung cell model, through NF-κB signaling [235]. This NP-induced inflammation occurred independently of ROS production, providing evidence that this mechanism may have duplicate pathways that lead to similar results.

Brain immune system modulation of plastics is supported by findings in mice exposed to PS-MNPs, where microglia are shown to preferentially accumulate the plastics [164]. Multiple studies validate that PS-NPs, particularly those below 100 nm, evoke more pronounced neuroinflammatory response both *in vitro* and *in vivo* when compared to larger MNPs [205, 236]. Given Fork-MNPs contain both a larger nanofraction and smaller nanofragments compared to Cup-MNPs and PS-50, respectively, their increased capacity to release pro-inflammatory cytokines aligns with these previous studies. Even when compared to

PS-50, Fork-MNPs elicited an elevated inflammatory response, highlighting the potential shortcomings of using pristine PS-NPs to understand the impacts of plastics in humans. The additional surface roughness and rigidity deviations compared to pristine NPs are likely to further stimulate immune effects of real-world MNPs, and further investigations are warranted to understand the mechanistic effects that these particles have on the human brain.

2.5 Conclusions

This study investigated the impacts and deviations of biological effects between "real-world" MNPs and pristine PS-NPs in human microglial cells, HMC3. The results demonstrate pristine PS-50 NP samples elicit a strong response in the disruption of mitochondrial homeostasis, ROS production, and immune response. Mitochondrial dysfunction, characterized by the loss of $\Delta\Psi_m$, lessened ATP production, and reduction of respiratory parameters, was accompanied by the clearance of damaged mitochondria, evidenced through mitophagic and biogenic pathways. In contrast, MNPs derived from common consumer goods, plastic cups and forks, demonstrated a distinct physiological response at the same concentrations. Despite similar oxidative stress and mitochondrial remodeling profiles, HMC3 cells presented more robust metabolic profiles and the heightened adaptability in bioenergetics, consistent with cellular stress compensation. Fork-MNP exposure was still found to present an elevated pro-inflammatory cytokine release profile when compared to PS-50, demonstrating the importance of the physicochemical properties of plastics found in the body and those used to study such effects.

Pristine NPs demonstrating a heightened biological response compared to real-world MNPs is most likely a result of a combination of factors. These include deviations in the specific surface area (SSA), number of particles, and physicochemical properties. Given the real-world samples contain particles 1000-fold larger than PS-50 NPs, far fewer particles are physically present to constitute the equivalent mass concentration. Assuming comparable densities, PS-50 samples could contain more than 10^8-times as many particles than both Cup-

and Fork-MNP samples, yielding an increase in specific surface area on the order of 10^3. This heightened reactive surface available for interaction with biological systems could present an explanation for the variations in bioenergetic pathways, as studies have shown higher SSAs can lead to stronger decrease in metabolic activities and increased ROS production [237, 238]. Pristine NPs also display an extraordinary degree of homogeneity when compared to real-world MNPs, with fragmented particles displaying large deviations in eccentricity, roughness, rigidity, surface defects, and microstructure. These features exhibit drastic variations in the biocorona formation process, from kinetics to biomolecule absorption profiles, which can dictate a particle's behavior in biological systems [137, 97, 239].

Together, these findings present evidence that pristine PS-NPs may exaggerate mitochondrial toxicity when compared to consumer-derived, "real-world" MNPs, underscoring the importance in selecting appropriate samples for the studies of plastics in the human body *in vitro*. Additionally, mitochondrial reprogramming and associated mechanisms are highlighted as key mechanisms of microglia's response to plastic accumulation. This work serves to further validate the role of plastics in neuroinflammation and potential contributions to neurodegenerative behaviors. Most importantly, the results indicate that pristine PS-NPs, which are widely used as a model for more realistic plastics that accumulate in the human body, do not accurately reflect the biological impacts that more relevant MNPs display in the human brain. The incorporation of physiologically relevant particles, including physicochemical properties as well as the dose at which they are administered, must be considered in experimental design strategy to best understand the threat that is faced by individuals across the globe. These factors, along with representative chronic-exposure studies, will provide the most accurate assessments to the effects of future real-world MNP accumulations with *in vitro* targets.

Chapter 3

Transcriptomic Analyses of Microglial Cells Exposed to a Low-Dose of Real-World Micro- and Nanoplastics

3.1 Abstract

The increasing prevalence of micro- and nanoplastics (MNPs) detected in the environment and the human brain has led to growing concerns over their possible neurotoxic effects. While studies aim to understand the mechanistic impacts of these particles, they often utilize non-representative, so-called "pristine" polystyrene (PS) nanoplastics (NPs). While these can be relevant for understanding the broader impact driven by plastics in the human brain, the previous study has shown how distinct biologically impacts can be driven by the physicochemical properties of MNPs. As such, pristine PS-NPs present a homogeneous, monodisperse profile that does not accurately reflect the particles that have been observed in the human brain. These differences observed on a physiologically level would be compounded on a molecular and gene expression level, ruling out their use for representative studies. In this study, the effects of pristine PS-NPs with diameters ranging from 50 - 100 nm (PS-50) are compared against MNPs generated from the degradation of common plastic consumer tableware, cups and forks, which have shown to readily degrade, on the gene-expression level. Human brain microglia (Human Microglial Clone 3; HMC3) were exposed to 0.1 µg/mL of either PS-50 NPs, cup-derived MNPs (Cup-MNPs), or fork-derived MNPs (Fork-MNPs) for 72 hours, with their transcriptomes analyzed using next generation RNA sequencing (RNA-seq). Differential gene expression analyses along with gene set enrichment analyses (GSEA) were conducted to understand the variations amongst transcriptional profiles presented in microglia exposed to pristine and real-world plastics. Pristine PS-50 NPs were found to strongly enrich endoplasmic reticulum (ER)-stress and unfolded protein response

(UPR) pathways relative to the real-world MNPs, suggesting heightened stress sensitivity in microglia exposed to pristine particles. Contrarily, both real-world MNP samples were found to upregulate ECM remodeling and collagen production pathways relative to PS-50, which has been previously shown to modulate immune response. While real-world MNPs induced many complementary pathways, Fork-MNPs were found to enrich interleukin 10 (IL-10) signaling pathways relative to both pristine PS-NPs and Cup-MNPs, emphasizing the role of particle size in the cellular response. Collectively, these results accentuate how the physicochemical properties of plastic particles drive their biological response in microglia, which affirms the importance of utilizing physiologically-relevant MNPs in studies gauging their biological impacts, particularly at the gene-expression level. The general approach of this study is shown in Figure 3.1.

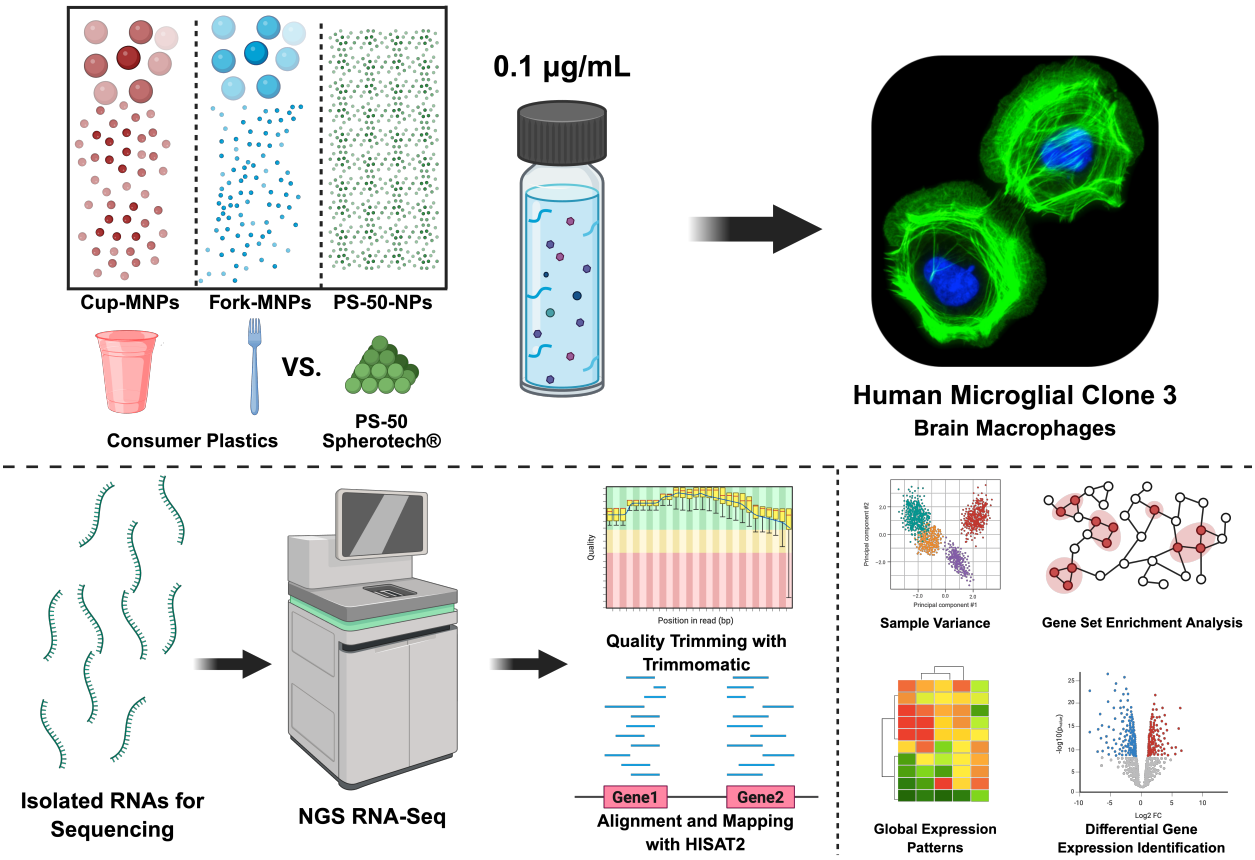

Figure 3.1: Experimental Design. Plastic tableware (cups and forks) were cryomilled to form micro- and nanoplastic (MNP) samples. These real-world particles were exposed to human microglial cells (Human Microglial Clone 3; HMC3) at 0.1 µg/mL for 72 hours. Alternatively, pristine polystyrene nanoplastics (PS-50 NPs) were exposed to HMC3 at an identical concentration to study the variations between pristine and real-world MNPs. Following material characterization, next generation RNA sequencing (NGS RNA-Seq) was performed to determine the transcriptome profiles of cells exposed to each plastic condition, n=3. Sample variations, gene set enrichment analyses, differential gene identifications, and global expression trends were analyzed to determine the gene-expression responses to real-world and pristine MNPs

3.2 Introduction

Plastic contamination of the environment has been evidenced to lead to bioaccumulation of the material in humans. From consumer plastic goods, fragmentation into microplastics (MPs), or plastics below 5 mm, as well as nanoplastics (NPs), or plastics below 1 µm, have been shown to enter the human body through inhalation, ingestion, and even dermal absorption [49, 53, 23]. Previous studies have shown that micro- and nanoplastics (MNPs)

preferentially accumulate in the brain, leading to concerns about their impacts on human health and relation to neurodegenerative diseases [92, 131].

Studies that focus on understanding the toxicological effects of plastics on the brain often utilize pristine nanoplastics, which are unable to accurately model "real-world" MNPs due to their homogeneous size and shape profile. Previous studies in understanding biomaterial interactions have demonstrated the physicochemical properties of particles have a significant impact on the fate of the biological system [181, 182]. Very few studies have adopted the use of "real-world" MNPs, created from consumer products that are commonly used and shown to readily release plastics into the environment or even human bodies directly. Plastic cups, for instance, are estimated to leach 90,000 particles per year following the use of such products 4-5 times a week [74]. Additional plastics in food-facing processes have been shown to release up to billions of plastics, with everything ranging from preparation to packaging to storage contributing to plastics in comestibles [72, 63, 10, 64, 73, 75].

Previous studies have highlighted the importance of plastic origin in toxicological studies [165, 97], with previous findings suggesting pristine polystyrene (PS) NPs may exaggerate biological effects when compared to more environmentally relevant MNPs. Previously, cell physiology parameters have shown to differ across pristine PS-50 and real-world samples in human brain microglia (Human Microglial Clone 3, HMC3) at identical concentrations. Among the differences observed, distinct variations in oxidative stress and mitochondrial responses were shown, with the pristine particles eliciting a much stronger stress response along with pronounced mitochondrial respiratory dysregulation. Even at 0.1 µg/mL, the lowest concentration tested, significant changes were observed in cells exposed to real-world MNPs for reactive oxygen species (ROS) concentrations, antioxidant activity, and mitochondrial mass after 72 hours. In order to gauge the magnitude of these impacts and understand molecular-level changes, in-depth investigations of gene-expression were warranted.

Previous analyses that have sought to explore the transcriptomic profiles of cells exposed to MNPs have relied on pristine PS-NPs, missing what effects might be seen by more representative MNPs. A transcriptomic analysis of PS nanoplastics in BV-2 microglial cells used doses of 25 – 75 µg/mL to identify NF-κB-mediated neuroinflammation, including TNF-α upregulation [240]. Similarly, a characterization of PS-MNPs in pulmonary fibroblasts employed concentrations ranging from 1 – 50 µg/mL for RNA-seq profiling, which found differential gene expression profiles across particles both 0.1 and 1 µm, including variations in mitochondrial function and oxidative phosphorylation (OXPHOS) pathways [241]. Both studies utilized commercially-available PS-MNPs, which lack the heterogeneity of physicochemical properties that are seen in the body. This underscores the need for an investigation into the gene-expression of human brain-model system exposed to relevant plastics.

In this study, transcriptomic profiling of microglial cells was conducted to identify the molecular pathways and mechanisms responsible for biological responses to real-world MNPs exposures. MNPs derived from two commercially available plastic products shown to leach plastics, polystyrene cups and forks, were exposed to HMC3 at 0.1 µg/mL in order to more accurately represent real-world human exposure scenarios. These results were compared against HMC3 exposed to pristine PS-NPs ranging from 50 – 100 nm in diameter (PS-50) at an equivalent dose. Additionally, Cup- and Fork-MNP-exposed cells were briefly contrasted to better understand how the physicochemical properties of the real-world MNPs influence biological response. Differentially expressed genes (DEGs) were identified and subsequently analyzed to determine statistically significant transcriptional changes across treatments. From these DEGs, co-expression networks were constructed to elucidate gene expression patterns, revealing functionally related gene clusters and providing insight into the biological pathways altered by real-world MNPs. Transcriptomic analyses revealed changes in cell homeostasis, with real-world MNP samples eliciting higher responses in ECM-remodeling-associated pathways, while pristine PS-50 NPs were shown to upregulate tRNA aminoacylation and endoplasmic reticulum (ER) stress pathways.

3.3 Materials and Methods

3.3.1 Reagents and Chemicals

Phosphate-Buffer Saline (PBS, 21-040-CV, Corning, Corning, New York, USA), Hanks' Balanced Salt Solution (HBSS, SH30268.01, Cytiva, Marlborough, Massachusetts, USA) Fetal Bovine Serum (FBS, 35-010 CV) Corning, Corning, New York, USA), Dulbecco's modified eagle medium (10-013-CV, Corning, DMEM/High Glucose), Penicillin:Streptomycin (16777-164, HyClone, Logan, Utah, USA), DNAse and RNAse Free Water (821932, MP Biomedicals), RNAzol RT (RN 190, Molecular Research Center, Cincinnati, Ohio, USA), Pure Ethyl Alcohol: Molecular Biology Grade (E7023, Sigma-Aldrich, St. Louis, MO, USA). All necessary solutions were prepared with ultrapure water (Barnstead™MicroPure™Water Purification System, 50132370, Thermo Scientific).

3.3.2 Preparation of Real-World Micro- and Nanoplastics and Physicochemical Characterization

Cup- and Fork-MNPs were prepared according to a previously described protocol [179]. Consumer grade plastic cups and forks were purchased from a local grocery chain and subsequently cut into fragments inside a sterile laminar flow hood to prevent contamination. These fragments were allowed to cool in liquid nitrogen (LN_2) before they were cryomilled into MNP fragments (Pulversiette 14™, Fristch, Idar-Oberstein, Germany) over repeated cycles. Larger sized particles were removed through sieving (120 µm; Fristch, Idar-Oberstein, Germany), leaving environmentally relevant sized-MNPs for exposure. Stock solutions were stored in ultrapure water at 1 mg/mL away from light and heat sources.

Commercially available pristine PS-NP (PS-50) samples were purchased from Spherotech (Cat. No: PP-008-10, Lake Forest, Illinois, USA) with a diameter ranging from 50 nm to 100 nm, with an average diameter of 75 nm. These pristine particles were used as a reference to compare against the effects of real-world MNPs.

The MNPs were characterized in depth in previous works to better understand their physicochemical properties. Briefly, bulk- and nanofragment-sized particles were measured through scanning electron microscopy (SEM; Zeiss EVO 50) and dynamic light scattering (DLS; Anton Paar Litesizer 500), respectively. The zeta potential of the MNPs with biocoronas were measured through electrophoretic light scattering (ELS; Litesizer 500). To quantify trace metal concentrations of some of the most frequently found contaminants and metallocatalysts, inductively coupled optical emission spectroscopy (ICP-OES) was performed using Multielement Standard Solution 1 for ICP (TraceCERT®; lead, zinc, cadmium, copper, chromium, nickel, barium, and silver) Particle composition of real-world MNPs was assessed through attenuated total reflectance Fourier-transform infrared spectroscopy (ATR-FTIR; iS50 FTIR, ThermoFisher).

3.3.3 HMC3 Cell Culture, Exposure to MNPs and RNA Extraction

Human microglial clone 3 (HMC3) cells were obtained from the American Type Culture Collection (ATCC CRL-3304, Manassas, Virginia, USA) and cultured in T-75 flasks (VWR-Avantor, 10062-860) prior to RNA extraction. DMEM media (Cytiva) was completed with a 10% FBS (Corning) and 1% antibiotic mixture consisting of penicillin and streptomycin (Mediatech), and allowed to grow in a humidified incubator at 37°C and 5% carbon dioxide.

Before MNP exposure to the cells, fresh MNP media was prepared as specified in a previous methodology. Briefly, MNPs were ultrasonicated at the 35 kHz range (97043-992, VWR, Radnor, Pennsylvania, USA) for 30 minutes before incubation in FBS overnight, allowing for biocorona formation to avoid aggregation. The PS-50 NPs were not ultrasonicated and were directly mixed with FBS for biocorona formation. Following overnight incubation in FBS in orbital shaking, all particles were resuspended in cell media and serial dilutions of the MNP solutions were achieved in complete media to result in 0.1 µg/mL solutions of each sample.

Fifty thousand HMC3 cells were plated in six-well plates with 1.5 mL of complete media and allowed to attach overnight. Following a wash in HBSS, cells were subjected to 1.5 mL of 0.1 µg/mL MNP-medias in triplicate (Cup-MNPs, Fork-MNPs, or PS-50 NPs). After 72 hours of exposure, RNAs were isolated from the HMC3 using RNAzol RT (Molecular Research Center) in accordance with the manufacturer's protocol. Briefly, cells were lysed using RNAzol, with DNA, proteins, and polysaccharides separated with the addition of water and centrifugation. The remaining RNAs were isolated and cleansed by quadruplicate washes in 75% molecular grade ethanol (E7023, Sigma-Aldrich) and resuspended in RNAse free water.

3.3.4 RNA quality control

The RNeasy Plus Kit (Qiagen, Venlo, Netherlands) was used in order to ensure the complete removal of gDNA. RNA concentration was quantified using a Qubit™4 Fluorometer (Q33226, Invitrogen) in combination with StrandBrite Green (17658, AAT Bioquest), following the manufacturers' protocols. RNA purity was ensured using NanoDrop One (ThermoFisher Scientific) and RNA integrity was evaluated in 1% agarose gel electrophoresis. RNAs with 260/280 and 260/230 absorbance ratios above 1.8 and good integrity were selected for further analysis. Samples were stored at -80°C until needed.

3.3.5 Next-Generation RNA Sequencing

RNA samples were sent to the High-Throughput Sequencing and Genotyping Unit of the Roy J Carver Biotechnology Center at the University of Illinois Urbana-Champaign for sequencing. RNA libraries were prepared and quality-checked prior to sequencing on the Illumina NovaSeq X Plus platform using a 10B flow cell (150-nucleotide paired-end reads). A total of 233,708,802 paired-end reads were generated with an average of 25,967,644.67 reads per sample. The sequencing data were stored as FASTQ files, and a quality report of 0.5% of the samples was generated using MultiQC [242].

3.3.6 RNA-seq data analysis

FASTQ files were transferred to the Alabama Supercomputer for preliminary processing. The raw paired-end reads were quality filtered with Trimmomatic v0.39 using a standardized trimming pipeline [243]. Any residual adapter sequences were first removed, followed by the removal of the first 10 bases from each read to eliminate positional biases. Subsequent trimming based on base-calling quality scores were applied to both 5' and 3' ends, truncating reads at the first based with a Phred quality score below 30 ($Q < 30$). Then, a sliding window of 6 bases was employed to remove any read in which the mean quality score within the window fell below Q30. Any remaining reads shorter than 36 nucleotides were removed, removing approximately 13% of the raw paired-end reads. A resulting 202,378,748 paired-end reads were analyzed with FastQC in order to ensure only the highest quality samples would be considered for downstream alignment and expression quantification (Figure B.2).

Reads were aligned using HISAT2 v2.2.0 to the latest version of the GENCODE human genome (v49) with an average of 98.92% overall alignment per sample [244, 245]. Aligned reads were counted using StringTie v2.2.1 and stored as CSV files [246]. All processed read data files will be submitted to Gene Ontology Omnibus (GEO) repository.

Differential Gene Expressions

For differential expression (DE) analyses, raw gene counts were imported into R (RStudio v2025.09.1+401; R v4.5.2) and processed using DESeq2 (v1.48.2). Genes with less than 50 cumulative counts across all samples were excluded prior to analysis. Pairwise comparisons between each group (Cup-MNPs vs. PS-50, Fork-MNPs vs. PS-50, and Fork-MNPs vs. Cup-MNPs) were assessed with a negative binomial linear model with Wald testing. Adjusted p-values (p-adj) were calculated using the Benjamini-Hochberg (BH) method to correct for multiple comparisons, and genes with a p-adj < 0.05 were considered differentially expressed. Variance-stabilizing transformations (VST) were applied for the visualization of

dispersion estimates, principal component analyses, sample-to-sample distance matrices, and further downstream analyses.

To identify genes with significant expression differences across treatments, a one-way ANOVA was applied across each gene across all samples using VST-normalized counts. Resulting p-values were adjusted for multiple comparisons using the BH false discovery rate correction method. The top 500 genes ranked by p-adj were selected for visualization in both clustered and hierarchical structures. Expression values for these genes were converted to row-wise Z-scores, mean-centered and scaled by standard deviation per gene.

These genes were additionally viewed through their protein product's interaction using STRING Database (String DB; v12.0). Briefly, the top 500 genes ranked by p-adj from the one-way ANOVA were entered into String DB, and visualized based on evidenced interactions. Each protein pairing was assigned a confidence score (0 - 1.0) based on their known, predicted, and related interactions. K-clustering was selected, identifying the smallest number of possible clusters between the protein groups using the highest confidence interaction metric (0.9) provided through the program. Genes that were found to not interact with any other gene, or that were not found in the String DB, were hidden from the visualization.

Gene Set Enrichment Analysis

Gene set enrichment analysis (GSEA v4.4.0) was performed on VST-normalized RNA-seq counts using the Reactome v2026.1 gene set collection [247, 248, 249]. Expression data were exported in GCT format and Ensembl gene IDs were collapsed to HGNC gene symbols using the Human Ensembl Gene ID MSigDB chip annotation file (v2026.1), yielding 17,997 genes for analysis. GSEA (Desktop, v4.4.0) was run using the Reactome canonical pathway gene set collection (C2.cp.reactome.v2026.1.Hs.symbols.gmt), with gene set size filters of 15 – 500 members and 1,000 gene set permutations. Four pairwise comparisons were performed through a set-seed (149) t-test ranking: Cup-MNPs vs. PS-50, Fork-MNPs vs. PS-50, Cup-MNPs vs. Fork-MNPs, and PS-50 vs. the combined real-world sample group (Cup-

and Fork-MNPs). Gene sets with FDR q-value < 0.05 and $|\text{NES}| \geq 1.5$ were considered significantly enriched.

The resulting Reactome pathways were plotted in Cytoscape (v3.10.3) using EnrichmentMap (v3.5) to visualize related pathways [250]. For each comparison, gene sets with FDR q-value < 0.05 were imported and represented as nodes, with node size proportional to gene set size and node color reflecting the normalized enrichment score (NES; red color indicating enrichment in the first-named group, blue color indicating enrichment in the second-named group). Edges were drawn between gene sets sharing significant gene overlap, using a Jaccard similarity coefficient cutoff of 0.375 for visualization.

3.4 Results and Discussion

3.4.1 Physicochemical Properties of MNPs

The material characteristics of the MNPs exposed to human microglial cells (HMC3) are discussed in detail in the preceding chapter. Briefly, the real-world samples Cup-MNPs and Fork-MNPs are composed mostly of polystyrene (PS) as indicated by Fourier-transform infrared (FTIR) spectrographs, suggesting that the differences observed between samples can be attributed to various other physicochemical properties. The bulk sizes of Cup- and Fork-MNPs were identified by SEM to be 41.3 ± 27.4 µm and 40.5 ± 25.2 µm, respectively. Particle size analysis by this methodology revealed that 85% of measured Cup-MNPs and 73% of measured Fork-MNPs fell within the 10–50 µm size range, matching the sizes of fragments found to form from cups and tableware [74, 73]. Apart from the size, the morphology was also assessed through SEM and found both samples to be comprised of fragment morphologies, which align with those found in the brain [92]. Additionally, Inductively Coupled Plasma Optical Emission Spectroscopy (ICP-OES) revealed that samples were free of contamination of lead, zinc, cadmium, copper, chromium, nickel, barium, or silver in any plastic sample, common metals found in plastic samples.

Nano-sized fragments of the real-world plastic solutions were detected through Dynamic Light Scattering (DLS) after filtration through 0.45 µm syringe filters. Fork-derived samples presented far smaller fragments relative to Cup-derived particles, with bimodal peaks at both 8.86 ± 2.57 nm and 56.03 ± 27.85 nm, while Cup-derived samples displayed peaks at 20.05 ± 11.66 nm and 117.03 ± 40.59 nm. Thus, both real-world samples contain particles smaller than those in the PS-50 sample, which reportedly range from 50 - 100 nm. The zeta potential of all MNPs in complete cell media was found to be slightly negative for each MNP sample, indicating the successful formation of biocoronas around each sample [137]. Biocoronas, or "crowns" of biomolecules surrounding the MNPs, allow for more representative modeling of the plastics found in the bloodstream, which adsorb proteins, lipids, and other molecules from circulation. Moreover, the formation of the biocorona disrupts the aggregation of MNPs in the cellular environment and directly influences their cell uptake and cell fate. Studies have been shown that NPs presenting a biocorona rich in cholesterol are more prone to cross the blood-brain barrier (BBB) by lowering the thermodynamic barriers necessary to reach the brain [123, 154].

3.4.2 Variance of Transcriptomic Data Reveals Distinct Biological Responses to Pristine PS-50 and Real-World MNPs

The transcriptomic profiles of HMC3 cells exposed to 0.1 µg/mL Cup-MNPs, Fork-MNPs, and PS-50 NPs (n=3) generated 233,708,802 paired-end reads (Figure B.2a) with an average Phred-33 quality score (Q) of 39.7 across all samples (Figure B.1). Poor quality-scored and short reads were trimmed, leaving 202,378,748 paired-end reads to be mapped to the reference genome. Of the 62,700 analyzed genes, 38,405 (61.3%) had at least one read mapped across all samples, while the remaining 24,295 (38.7%) genes showed no detectable expression.

For additional noise reduction in downstream processing, genes with a combined count of less than 50 reads across all samples were discarded from consideration. After variance-stabilizing transformations were applied for normalization before initial data visualization was performed. Dispersion estimations displayed an expected inverse relationship between gene dispersion and mean, normalized counts, with final shrunken estimates primarily localized along the fitted trend (Figure 3.2a). Principal component analysis (PCA) revealed that PC1 and PC2 accounted for 22% and 16% of total variance, respectively, however there was a distinct lack of intra-sample clustering amongst the axes (Figure 3.2b). While PS-50 samples demonstrated relatively tight clustering, Cup- and Fork-MNPs exhibited greater extents of dispersion, suggesting biological heterogeneity in gene-expression response to real-world MNP exposures.

This may be partially attributable to the vast heterogeneity exhibited by the real-world MNP samples. Unlike the pristine PS-50 NPs, manufactured under tolerances and rigorously quality controlled to produce a monodisperse and homogeneous population of particles, MNPs derived from consumer goods display highly polydisperse physicochemical characteristics, particularly size and surface area [165, 251]. Polydispersity can provide challenges across MNP studies for exposure and treatment reproducibility as the physicochemical characteristics of one exposure may not precisely match that of another group [146, 252]. Dosimetry by mass-concentration alone is a recognized limitation in MNP toxicology, as particle number and specific surface area (SSA) are understood to greatly impact biological response [95, 181, 238, 253]. The tighter clustering of PS-50 replicates is consistent with this interpretation, as the monodispersity of pristine PS-NPs would be expected to exhibit higher reproducibility in biological responses.

Despite the observed heterogeneity between samples, the analysis was determined to be a viable understanding of the impacts of MNPs on the human brain as HMC3 remain one of the most widely used microglial models in neuro-toxicological research [254]. Additionally, DESeq2's empirical Bayes dispersion modeling is robust to moderate biological variability

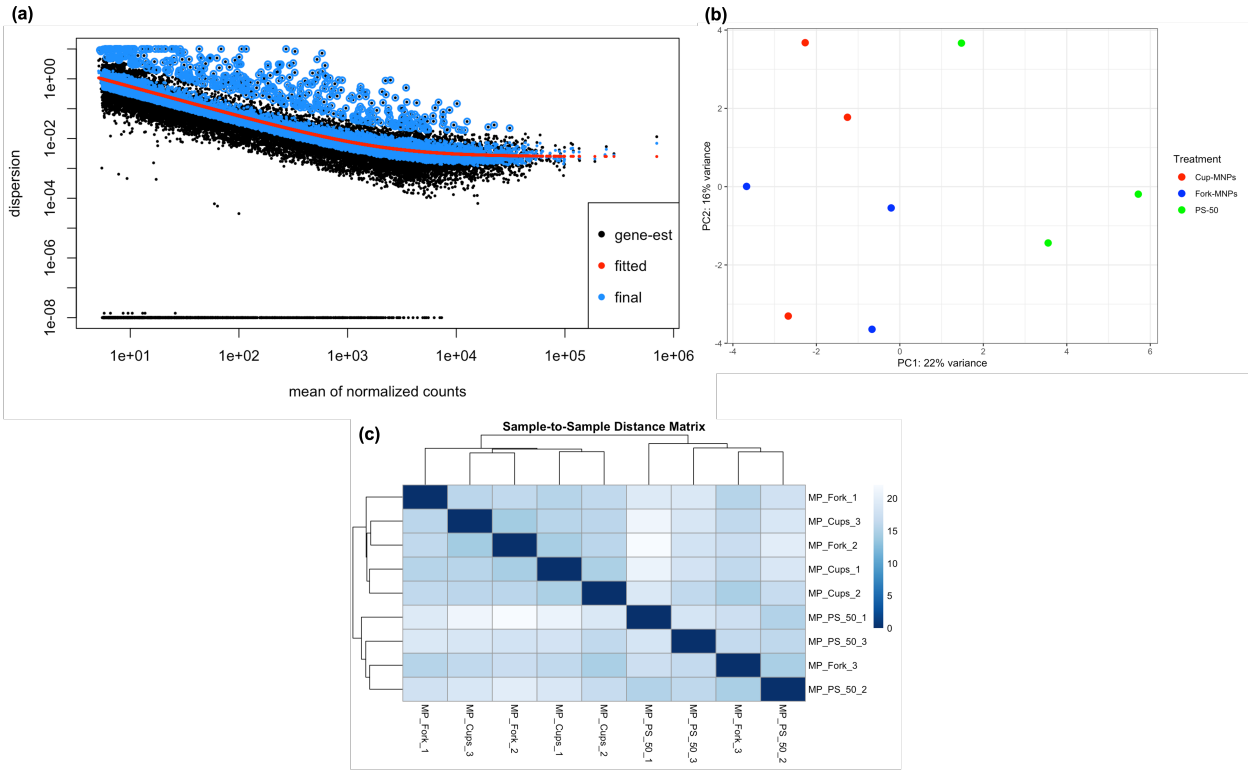

Figure 3.2: Transcriptional Trends Amongst Human Microglia Exposed to Pristine and Real-World MNPs. (a) Per-gene dispersion estimates (black) were plotted against mean normalized counts and fit to a parametric trend (red) using DESeq2's empirical Bayes shrinkage procedure. Final shrunken dispersion estimates (blue) reflect values pulled toward the fitted trend, reducing the influence of sampling noise on genes with low counts. (b) Principal component analyses (PCA) between variance stabilized transformation (VST) counts plotted in two dimensions. Each point represents one biological replicate (n = 3) across Cup-MNPs, Fork-MNPs, and PS-50 NPs. (c) Sample-to-sample distance matrix between each sample combination (n=3) from VST counts.

as evidenced by the well-fitted dispersion estimates observed across all treatment groups [255, 256].

To further analyze the variation amongst replicates, a sample-to-sample distance matrix was analyzed, revealing that the samples did not segregate cleanly by treatment group (Figure 3.2c). The third Fork-MNP sample (MP_Fork_3) was found to cluster more similarly to the PS-50 replicates than to the other Fork-MNP replicates, indicating a closer transcriptional profile to HMC3 exposed to PS-50 than to either real-world MNP sample. This sample was retained in the analysis, but cautiously analyzed downstream for potential

deviations. For the remained of the real-world samples, there were slight variations in the clustering, with Cup- and Fork-MNP samples being shown to cluster together, yet this could be expected given the similar molecular responses shown in HMC3 exposed to 0.1 µg/mL.

3.4.3 Global Gene Expression Changes in Microglia Following Exposure to Pristine NPs and Real-World MNPs

To further identify genes exhibiting significant expression variation across treatments, a one-way analysis of variance (ANOVA) was applied to variance stabilized transformation (VST)-normalized expression values, and corrected by the BH procedure. The top 500 most significant DEGs were selected and visualized through Z-score heatmap. Hierarchical clustering revealed consistent responses among samples, with two dominant gene clusters observed: a larger cluster characterized by strong upregulation in PS-50 samples with moderate downregulation in both real-world MNP samples, and a smaller cluster presenting genes strongly downregulated in PS-50 samples while moderately upregulated across real-world MNP samples (Figure 3.3a). Notably, pristine PS-50 NPs were shown to elicit vastly different responses compared to real-world Cup- and Fork-MNP samples, suggesting that physicochemical differences between samples, such as size, morphology, surface area, which are correlated to cell uptake and intracellular fate, activates fundamentally distinct transcriptional responses.

The divergent transcriptional profiles between PS-50 NPs and real-world MNPs may be attributed to the size-dependent differences in cellular uptake. The PS-50 NPs, with an average diameter of 75 nm, are at a sizes associated with preferentially clathrin-mediated endocytosis, where 80 nm fragments are found to be optimally internalized [257]. In contrast, while the heterogeneous Cup- and Fork-MNPs contain fragments around this size (Cup-MNPS: 20.05 nm ± 11.66 nm and 117.03 nm ± 40.59 nm; Fork-MNPs: 8.86 nm ± 2.57 nm and 56.03 nm ± 27.85 nm), there is likely a substantial fraction in the optimal phagocytic range of 500 nm to 3 µm [258]. This process involves cytoskeletal-driven uptake of particles rather than protein (clathrin or caveolin)-driven uptaken, which can extent to particles

sized around 10 - 15 µm, though to a lesser extent. Critically, for a mass-concentration dosage, smaller nanoscale particles present an exponentially great number of particles with an equivocally higher SSA, increasing the frequency of membrane engagement and uptake events per cell. In HMC3, this allows for a greater magnitude of ROS production and downstream transcriptional activation for nanoplastic-exposed cells, consistent with the distinct gene cluster observed exclusively in PS-50-treated samples.

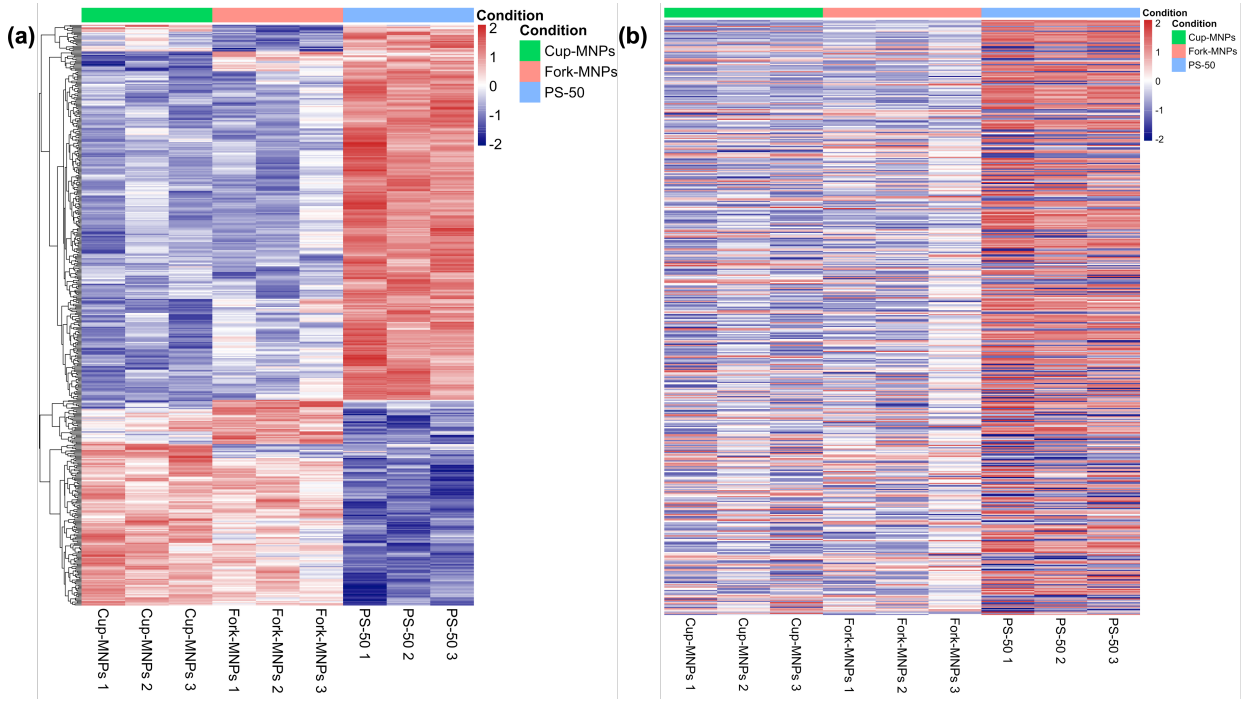

Figure 3.3: Heatmap Presenting Global Transcriptomics Changes in HMC3 Cells Following Exposure to Different MNPs after 72 Hours. Each row represents one gene and Each column corresponds to one sample. (a) Hierarchical complete linkage clustering of the top 500 ANOVA significant genes across all samples. (b) The same 500 significant genes without clustering, presented in order of significance from top to bottom. One-way ANOVAs were applied to VST-normalized expression values, adjusted using the Benjamini-Hochberg method. Row-wise Z-score scaling was applied to each gene independently, normalizing expression relative to that gene's mean and standard deviation across all samples to enable direct visual comparison of relative expression patterns between treatment groups. Color scale represents Z-score magnitude, with red indicating relative upregulation and blue indicating relative downregulation. n = 3 replicates per treatment condition.

To assess whether statistical strength was implicated with a particular treatment, the same top 500 ANOVA-significant genes were plotted without hierarchical clustering. Instead,

genes are ranked from most to least significant by BH-adjusted p-value (false discovery rate; FDR) (Figure 3.3b). No clear directional gradient was observed, implying ANOVA significance was driven by magnitude of variance over uniform directional effects.

In both clustered and significance-ordered heatmaps, it is observed that the third Fork-MNP replicate (Fork-MNPs 3) displayed low Z-score magnitudes relative to its replicates, as well as each sample group. Fork-MNPs 3 appears as a near-white column in Figure 3.3, whereas the other replicates show higher-magnitude changes. This suggests the sample may represent a transcriptionally muted profile, aligning with what was seen in the sample-distance matrix and PCA.

The protein products of these genes were assessed through a STRING Database (StringDB) network to investigate functional relationships (Figure 3.4). Network construction was performed on the highest interaction score (0.9) to validate the close interactions, finding 27 clusters of proteins through evidenced connections. The largest network by far related to tRNA aminoacylation and aminoacyl-tRNA biosynthesis (Red), which contains 11 aminoacyl-tRNA synthetase (ARS) genes (*AARS1, EPRS1, GARS1, IARS1, LARS1, MARS1, NARS1, NARS2, SARS1, TARS1, WARS1*) and 7 endoplasmic reticulum (ER)-stress/unfolded protein response (UPR) genes (*DDIT3, XBP1, ATF2, BCL2, APAF1, PMAIP1, ITPR1*). Of these 40 genes, 36 were found to be associated with upregulation in PS-50 NP-exposed cells, with every ARS and ER-stress/UPR gene belonging to this category. This cluster's unilateral PS-50 enrichment suggests these plastics activate integrated stress response (ISR) pathways [259]. Interestingly, increased expression of ARS's has been found to reduce peripheral neuropathy and protein synthesis defects in mouse models, suggesting a possible therapuetic signaling pathway that is otherwise absent in real-world MNPs [260].

One of the second largest groups, consisting of 7 proteins (*PAPOLG, FIP1L1, CDC5L, PLRG1, CRNKL1, CWC25, U2AF2*), was found to be associated with the U2-type spliceosomal complex. Similarly, 5 of these genes were found to be upregulated in PS-50 NP-exposed HMC3. These spliceosomal stress-related genes are a likely artifact of downstream

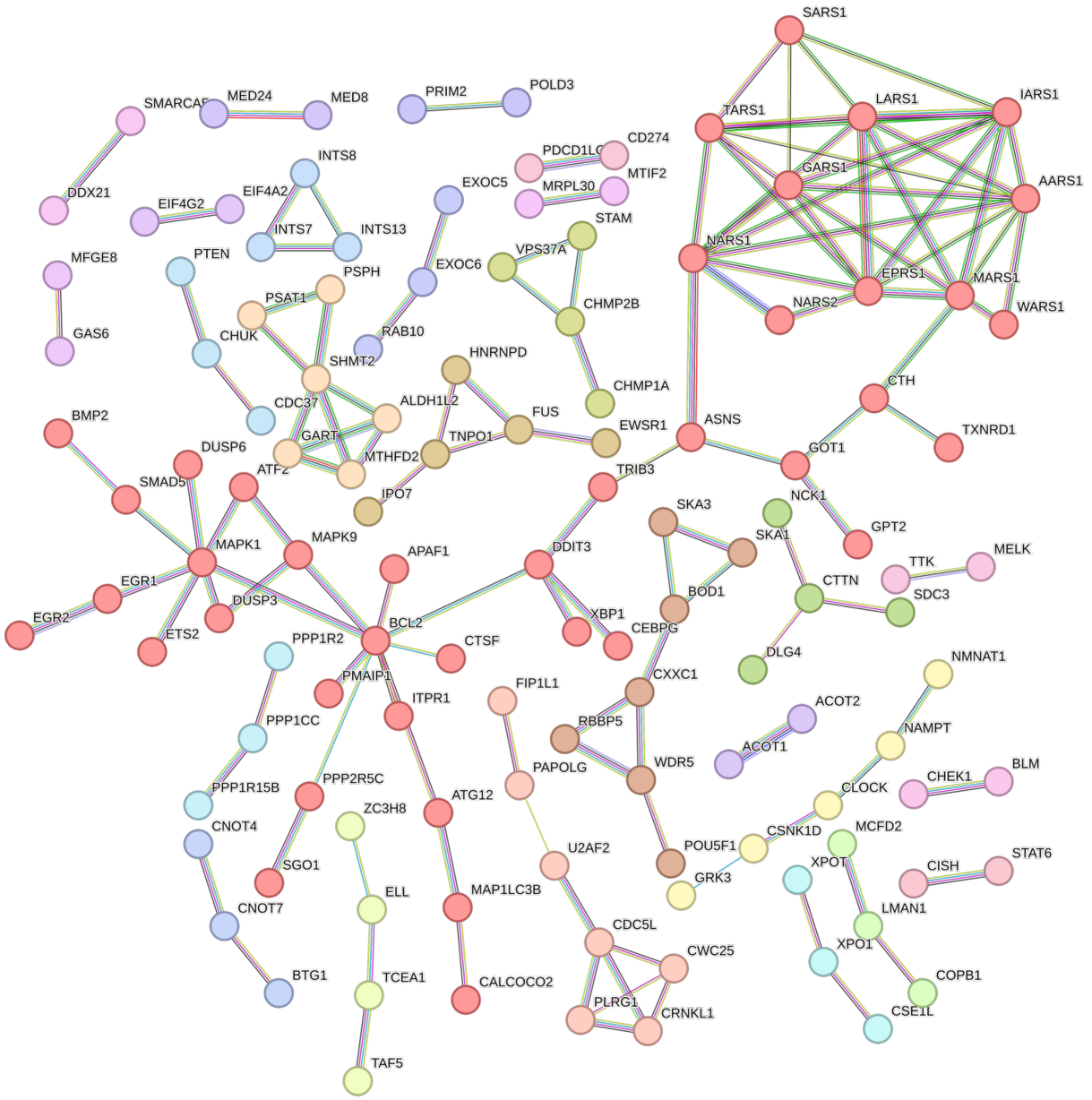

Figure 3.4: STRING Protein-Protein Interaction Network of The Top 500 DEG (One-way ANOVA). The protein products of the DEGs genes were visualized by evidenced interactions using STRING Database with the highest-confidence threshold (≥ 0.9). Network nodes are colored by cluster membership as determined by k-clustering (k = 27). Network edges are colored by evidence supporting these interactions - green: neighborhood evidence; red: gene fusion; blue: co-occurrence; black: co-expression; yellow: text mining; light blue: database-curated; pink: experimentally determined. Disconnected nodes were removed for visualization.

ISR impacts, with the pathway being shown to disrupt spliceosomal function through eIF2α phosphorylation-dependent mechanisms [261]. Two of these largest networks observed are shown to be PS-50 driven, mirroring the larger proportion of the ANOVA-significant genes shown to be upregulated in PS-50 NP-exposed cells. The higher degree of networking among these genes additionally implies a unified, reproducible stress response in PS-50-exposed HMC3 cells, which may reflect the homogeneity of monodisperse PS-50 particles driving consistent, reproducible effects across replicates.

3.4.4 DEG Analyses Suggest That Particle Physicochemical Features Dictate Transcriptomic Changes in Microglia

In order to observe changes in gene expression between HMC3 exposed to 0.1 µg/mL of different MNPs, pairwise comparisons across samples were performed using DESeq2 to identify differentially expressed genes (DEGs)(Figure 3.5).

In Cup-MNPs and PS-50 NPs, 1,288 DEGs were identified with 804 upregulated in PS-50-treated cells against 484 upregulated in Cup-MNP-treated cells (Figure 3.5a). When comparing cells treated with Fork-MNPs against PS-50 NPs, 694 DEGs were identified with 458 upregulated in Fork-MNP samples and 236 upregulated in PS-50 samples. When both real-world MNP sample exposures were compared against each other, only 9 DEGs were found, with 7 upregulated in Fork-MNP samples and 2 upregulated in Cup-MNP samples (Figure 3.5b & c). These changes closely reflect what was observed in the cellular responses of HMC3 exposed to these same MNP samples at identical concentrations, where both real-world samples displayed similar biological responses and contrasted the elevated responses of PS-50 NP exposure compared to unexposed cells.

Overlapping DEGs across samples were identified to assess treatment similarities (Figure 3.5b & c). To determine the extent of transcriptional overlap, DEGs shared between each pairwise treatment comparison were cataloged, revealing convergent and divergent gene expression patterns. Both Cup- and Fork-MNPs upregulated 181 shared genes relative to

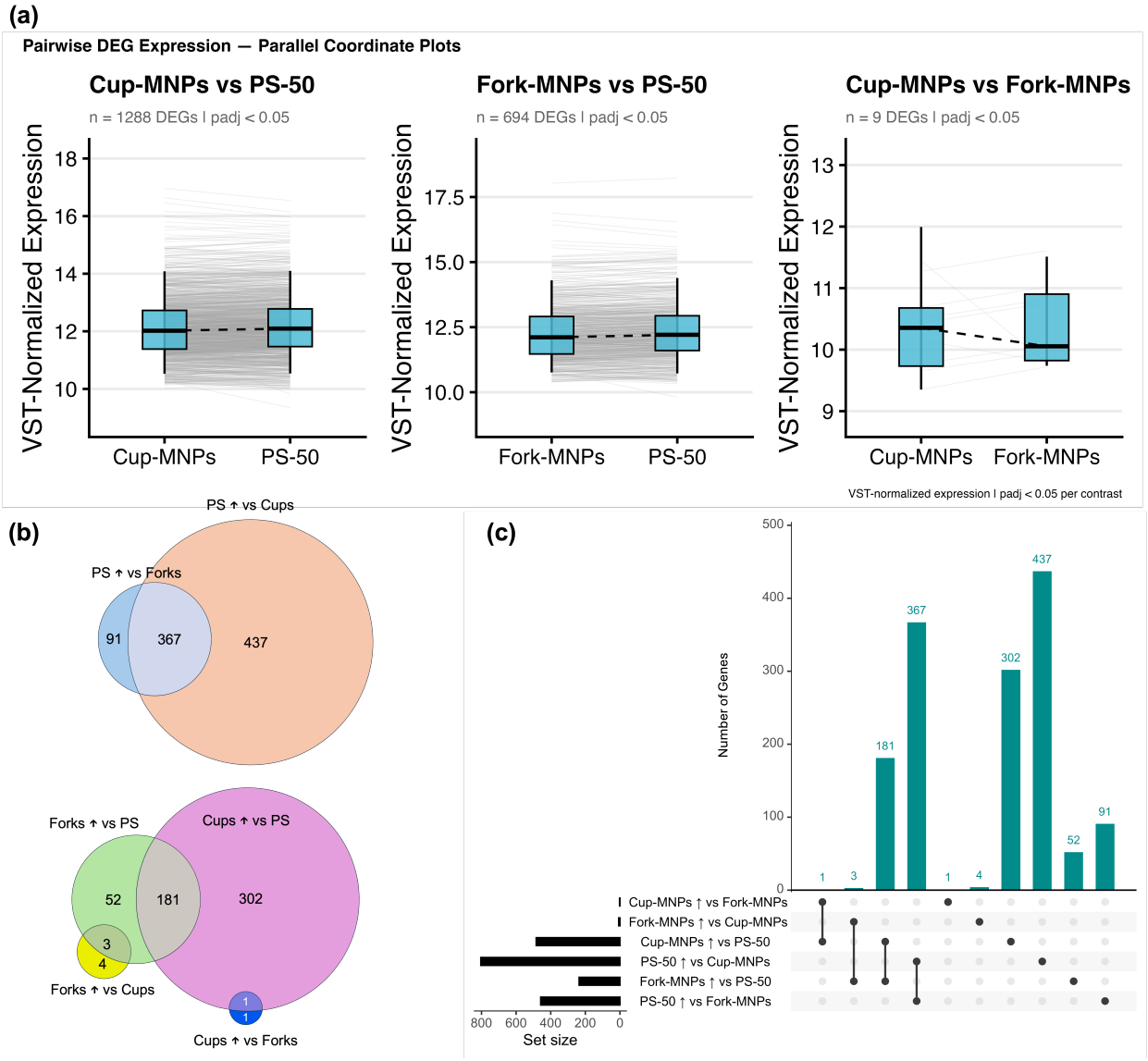

Figure 3.5: Differentially Expressed Genes in HMC3 Cells Exposed to Different MNPs for 72 hours. (a) The number of significant differentially expressed genes (DEGs) along with their normalized expressions were plotted across each sample (Cup-MNPs vs PS-50; Fork-MNPs vs PS-50; Cup-MNPs vs Fork-MNPs), identifying differential gene-expression changes between real-world and pristine samples. Significant DEGs that overlap between treatments are visualized in (b) Venn diagrams and (c) an UpSet plot, showing high degrees of overlapping between genes that were upregulated in both real-world MNP samples as well as genes that were upregulated in PS-50-exposed cells against real-world samples.

HMC3 cells exposed to PS-50 NPs, suggesting that heterogeneous real-world MNPs activate overlapping biological responses distinct from those induced in pristine models. Interestingly, PS-50 treatments shared a greater number of DEGs against both real-world samples combined, totaling 367. This could indicate that while PS-50 drives a larger transcriptional response, a substantial portion of that response is absent in environmentally relevant particles. These overlapping gene sets likely reflect conserved cellular mechanisms that are triggered regardless of particle morphology, while the divergent DEGs may relate to morphology-dependent uptake and downstream recovery.

3.4.5 Gene Set Enrichment Analysis Identifies Shared Responses in Microglia Exposed to Real-World MNPs

To identify biological pathways correlated with the DEGs found in the pairwise comparisons, Gene Set Enrichment Analysis (GSEA) was performed on VST-normalized data from DESeq2. From GSEA, 17,997 genes were analyzed, with 1065 gene sets remaining after gene set filtration. Four comparisons were performed: Cup-MNPs vs. PS-50, Fork-MNPs vs. PS-50, Cup-MNPs vs. Fork-MNPs, and PS-50 vs. both Cup- and Fork-MNPs. Gene sets with FDR q-value < 0.05 and absolute normalized enrichment scores (NES) ≥ 1.5 were considered significantly enriched.

Cup-MNPs vs. PS-50

Considering HMC3 treated with Cup-MNPs against PS-50 NPs, 26 Reactome pathways were found to be enriched, with 19 enriched in Cup-MNP samples while 7 were enriched in PS-50 samples (Figure 3.6a). Cup-MNP samples showed much greater networking among the enriched pathways, specifically in pathways related to extracellular matrix (ECM) structure. Namely, the collagen chain trimerization pathway (NES 2.56; FDR $q < 0.001$), assembly of collagen fibril pathway (NES 2.50; FDR $q < 0.001$), and the collagen biosynthesis and modifying enzyme pathway (NES 2.44; FDR $q < 0.001$) exhibited some of the strongest

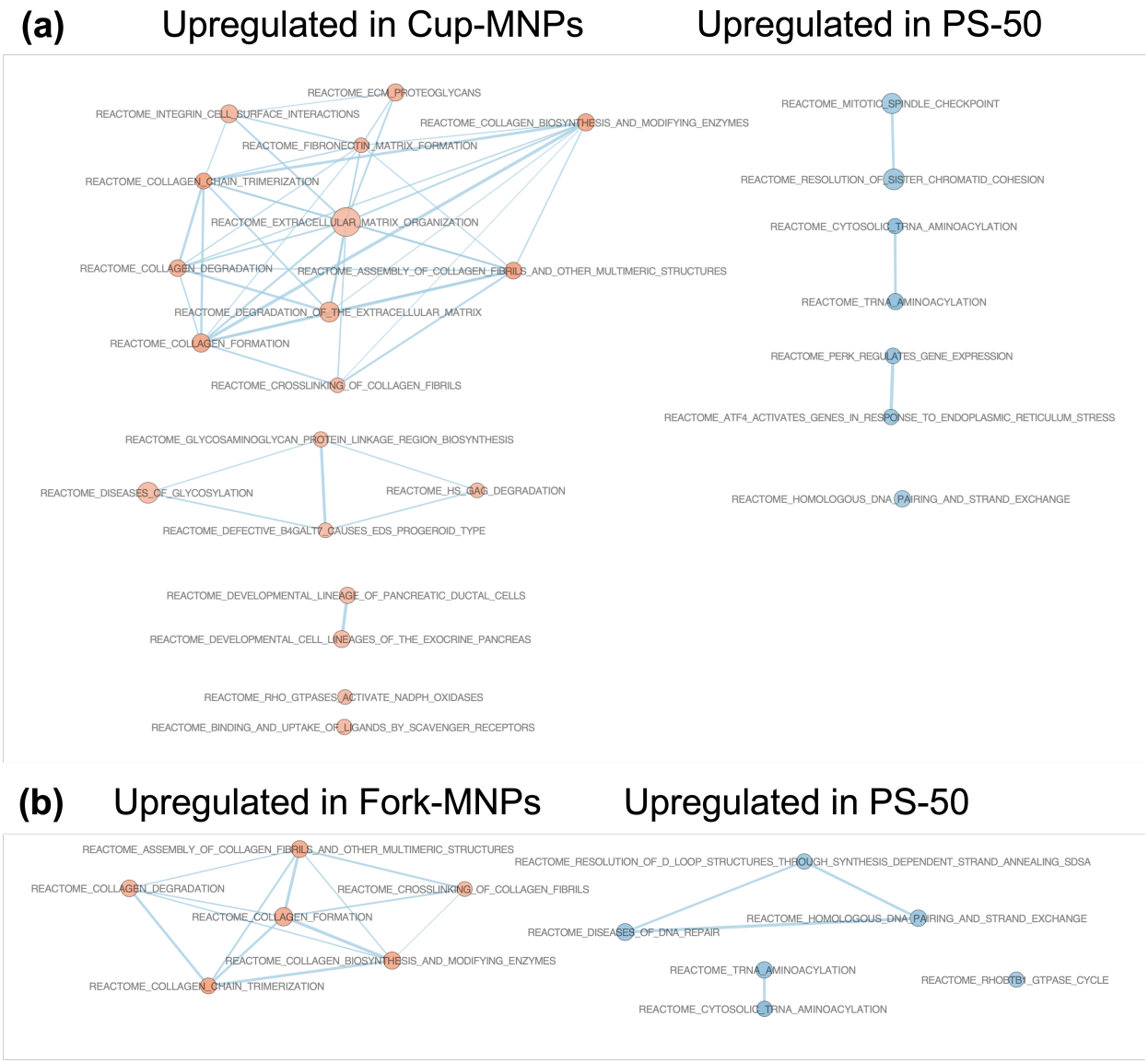

Figure 3.6: Gene Set Enrichment Analysis Pathway Networks Between Each Real-World and Pristine MNP Sample. Enrichment maps depicting significantly enriched Reactome pathways in (a) Cup-MNPs vs. PS-50 and (b) Fork-MNPs vs. PS-50. Each node represents a Reactome gene set, with node size proportional to gene set size. Edges connect gene sets with a gene overlap similarity coefficient ≤ 0.375 (Jaccard). Node color reflects the normalized enrichment score (NES): red indicates enrichment in the first-named group, blue indicates enrichment in the second-named group, and color intensity scales with NES magnitude. Only gene sets with FDR q-value < 0.05 and absolute NES above 1.5 are displayed. GSEA was performed using GSEA v4.4.0 with gene set permutation (n = 1,000), Reactome gene sets (MSigDB C2 v2026.1), and gene set size filters of 15–500 genes. Networks were constructed and visualized in Cytoscape v3.10.3 using the EnrichmentMap app.

enrichment, suggesting microglia exposed to Cup-MNPs may show dysregulated extracellular matrices relative to cells exposed to pristine PS-NPs (Figure 3.7). These impacts were driven largely by leading-edge genes responsible for the construction of collagen molecules - *COL7A1*, *COL1A1*, *COL1A2*, *COL18A1*, and *COL9A3* -comprise the first five leading-edge genes of the named enriched pathways.

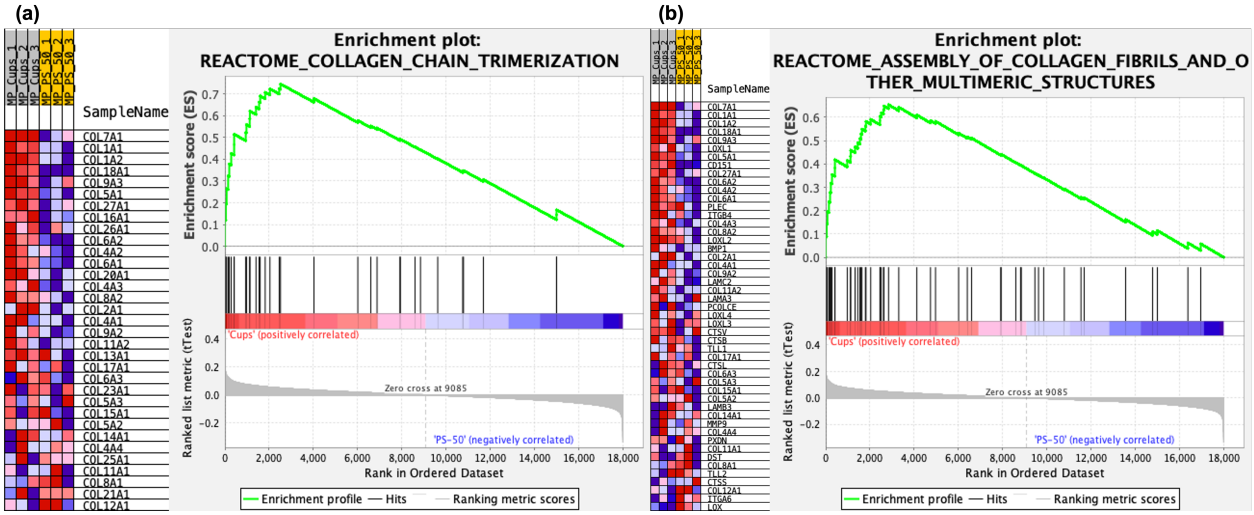

Figure 3.7: Gene Set Enrichment Analysis of the Top Two Enriched Reactome Pathways in Cup-MNP-Treated HMC3 Relative to PS-50. Enrichment plots for (a) Collagen Chain Trimerization and (b) Assembly of Collagen Fibrils and Other Multimeric Structures are shown along with specific gene enrichment heatmaps. Running enrichment score is shown as the green trend line across the ranked gene list by the t-test ranking metric. Genes associated with Cup-MNP treatment are shown on the left in red while genes associated with PS-50 are shown in the right as blue. Vertical tick marks indicate the position of the genes in the set in the ranked list. Heatmaps display relative expression levels of each gene in the set, following the same color scheme as the enrichment plots.

The collagen trimerization pathway is a conserved, intracellular process with specific regulatory control. Within the ER and Golgi, procollagen α-chains assemble into a triple helix before translocation into the ECM, where they are able to assemble larger fibrils [262, 263]. While this pathway may be typically associated with fibroblasts, macrophages are capable of directly synthesizing and depositing collagen in their microenvironment, primarily during the M2-polarization (alternatively activated macrophages) during repairs or immunosuppression[264]. This ECM component can help regulate and influence activation

of neighboring cells, where increased collagen density has been shown to elicit immunosuppressive phenotypes in RAW 264.7 macrophages [265]. This increased collagen density is consistent with ECM compositions often observed in tumor microenvironment, where cancer-associated fibroblasts and other tumor-associated cells promote tumor growth through high-collagen ECMs [266, 267]. Upregulation of this pathway in macrophages can be often signaled through TGF-β1 secretion by activated microglia [268]. In vivo, activated microglia secrete TGF-β1, which promotes collagen deposition along with fibroblasts and further amplifies local ECM accumulation. In pathological contexts, SPP1+ macrophages co-operate with resident fibroblasts to drive a collagen-dense, immunosuppressive microenvironment that actively favors tumor progression [269].

Each "*COL*" gene encodes for a pro-α collagen chain, the primary building block of the overall collagen structure. Three pro-α chains form a right-handed coil as a triple helix to form procollagen, which is further processed into mature tropocollagen and self-assembles into cross-linked fibrils via lysyl oxidase-mediated covalent bonding [262, 270]. Macrophages cultured *in vitro* attach through fibronectin matrices, forming the base layer of what will become the ECM [271, 272]. Layers of collagen then form atop this fibronectin scaffold, with the fibronectin matrix providing structural support for collagen I fibril structures [273]. This hierarchical assembly is not merely structural but is tightly regulated by cell–matrix signaling pathways. In particular, integrin-mediated interactions with the ECM activate mechanotransduction cascades that influence matrix remodeling.

Integrin mechanotransduction is mediated through the yes-associated protein (*YAP*) pathway, which regulates collagen gene expression along with various inflammatory responses [274, 275]. On stiff substrates, reduced Hippo pathway activity allows for the accumulation of YAP in the nucleus, which drives expression of TEAD target genes (*CTGF*, *TGF-β1*) that indirectly promote "*COL*" gene upregulation [275, 276].

The introduction of larger MPs in cell culture, such as the 40 µm particles observed in Cup-MNP samples, may mechanically disrupt substrate rigidity [277]. Bulk PS presents

a stiffness of approximately 3 GPa, while brain ECM, one of the softest tissues in the human body, presents a stiffness of about 1 kPa [278, 279]. The addition of these plastics in culture substrates may effectively stiffen the local microenvironment, leading to the aforementioned collagen cascade. Increased ECM stiffness is often observed in cancers, with studies suggesting that the stiffening of the ECM can actually directly promote a favorable tumor microenvironment [266]. In the tumor microenvironment, it increased ECM stiffness is often reported to be approximately 45 kPa, which can induce a feedback loop. Notably, this pathological stiffening is driven primarily by hyaluronic acid and proteoglycan accumulation in brain tissue rather than Collagen I, which serves as the dominant stiffening agent in peripheral tissues where macrophage-driven fibrosis predominates [266]. However, these findings still suggest that MNP-induced disruptions of the microenvironment of HMC3 may engage pro-tumorigeneic behaviors through increased fibrotic activity.

Many studies have shown that substrate stiffness can greatly alter particle uptake, with some even showing size-dependent kinetics [280, 281]. On softer substrates, particle uptake has been shown to increase by six-fold, with macrophages displaying a two-fold increase relative to stiffer substrates [281]. This regulation of endocytosis is mediated through YAP signaling, where increased substrate stiffness reduces focal adhesion and suppresses endocytic capacity. Consequently, if MNP presence in cell's microenvironment is able to stiffen the substrate, a suppression of further MNP uptake may emerge as a feedback mechanism. This suppression disproportionately affects larger particles, with substrate stiffness-dependent uptake shown to decrease with increasing particle size. This aligns with the reduced cellular homeostatic disruptions observed with real-world MNPs compared to pristine nanoplastics as well as the hypothesized increase in internalization of PS-50 NPs through endocytosis.

In HMC3 cells exposed to PS-50 NPs, fewer pathways were shown to be enriched compared to Cup-derived MNPs treatment, with a lesser extent of connectivity between the pathways (Figure 3.6a). The Reactome pathways involving tRNA aminoacylation, ER

stress, mitotic spindle checkpoints, and sister chromatid cohesion were all shown to be up-regulated by PS-50 NPs, suggesting proteomic stress, genomic instability, and translational dysregulation. The top two enriched pathways, cytosolic tRNA aminoacylation (NES 2.49; FDR q < 0.001) and tRNA aminoacylation (NES 2.41; FDR q < 0.001), identified leading edge genes associated with aminoacyl-tRNA synthetases (ARSs) (Figure 3.8). The ARSs *MARS1, SARS1, FARSB, CARS1, LARS1, EPRS1, YARS1, AARS1, WARS1, TARS1, IARS1, NARS1,* and *GARS1* were all shown as leading edge genes, which encode for the majority of enzymes responsible for charging tRNA molecules with their associated amino acids during translation [282].

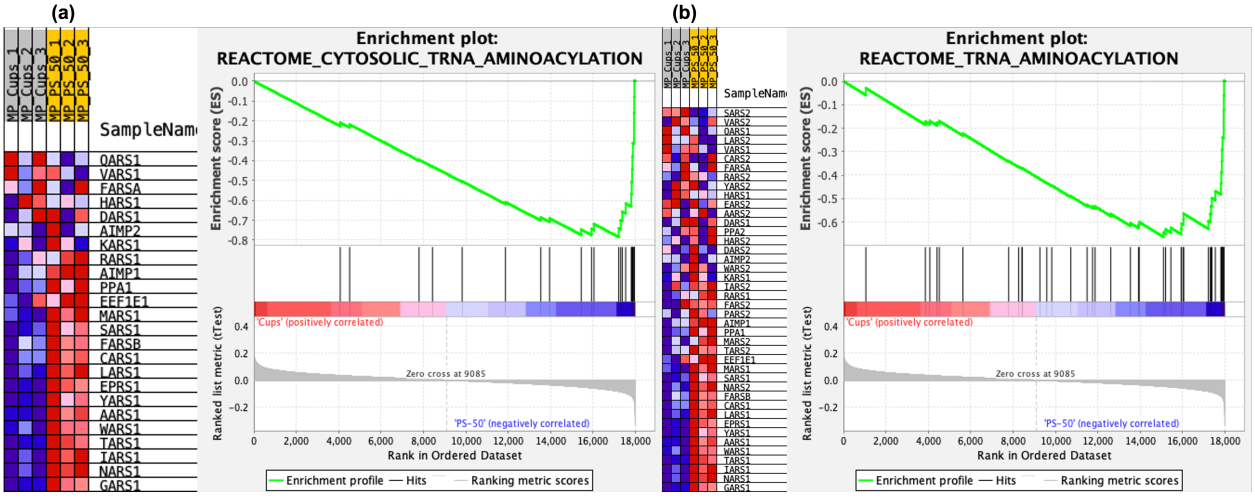

Figure 3.8: Gene Set Enrichment Analysis of the Top Two Enriched Reactome Pathways in PS-50-Treated HMC3 Relative to Cup-MNPs. Enrichment plots for (a) Cytosolic tRNA Aminoacylation and (b) tRNA Aminoacylation are shown along with specific gene enrichment heatmaps. Running enrichment score is shown as the green trend line across the ranked gene list by the t-test ranking metric. Genes associated with Cup-MNP treatment are shown on the left in red while genes associated with PS-50 are shown in the right as blue. Vertical tick marks indicate the position of the genes in the set in the ranked list. Heatmaps display relative expression levels of each gene in the set, following the same color scheme as the enrichment plots.

Previous studies have shown that organisms (mice, zebrafish, and swordtail fish) exposed to pristine PS-MNPs presented increased aminoacyl-tRNA biosynthesis and amino acid production [283, 284, 285]. These mechanisms are often interpreted as a compensation to proteostatic stress, consistent with the enrichment of ER stress pathways [286]. Under

ER stress conditions, activation of the PERK-eIF2α-ATF4 axis pathway boosts ARS and amino acid transporters for anabolic recovery [287]. This is further supported by the enriched ATF4-mediated ER stress response and PERk regulation pathways in microglial cells exposed to pristine PS-NPs. Pristine MNP-induced ER stress is commonly reported in both *in vivo* and *in vitro* contexts, with mice lungs and primary epithelial goat cells showing the activation of the same pathways in response to ER stress [288, 289]. Interestingly, these previous findings have all been conducted with both MPs and NPs, suggesting that ER stress and the resulting PERK-eIF2α-ATF4 axis pathway activation independent of size.

A benchmark study investigating the relation between ARS upregulation and tumorigenesis found similar enrichment of ARS mRNA expression in 8 out of 10 cancers examined [290]. Specifically, *MARS*, encoding for methionyl-tRNA synthetase, was found to be overexpressed in various gliomas and glioblastomas. This gene was identified as a leading edge gene in macrophages exposed to PS-50. Further studies have identified *AIMP1*, *WARS*, and other ARSs to be associated with glioblastomas, further suggesting the exposure of HMC3 to pristine PS-NPs may lead to tumorigenesis [291]. These claims can be further supported through the observed enrichment of Mitotic Spindle Pathway and Resolution of Sister Chromatid Cohesion pathways. Leading edge genes from these pathways, including *CDK1*, *SKA1/2*, and *CLASP2*, are responsible for proliferative regulation and often observed upregulated in cancers, suggesting their overexpression may contribute to dysregulated mitotic progression and increased proliferative capacity [292, 293, 294]. Specifically, the overexpression of *CDK1*, a master regulator of the G_2/M transition, has been broadly documented across multiple cancer types including glioma, where its upregulation is associated with premature mitotic entry, suppression of apoptotic signaling, and even mitochondrial fission[292, 295]. Mitochondrial fission producing smaller mitochondria fragments often results in reduced mitochondrial respiration, decreased mitochondria membrane potential, and impaired oxidative phosphorylation. These mitochondrial changes were observed previously when HMC3 cells were treated with low doses of PS-NPs.

Similarly, increased *SKA1/2* expression has been reported in various cancers, promoting cell cycle progression and suppressing apoptosis [293, 296]. These studies have also found that *SKA1* worsens glioblastoma prognosis and can promote malignancy, further supporting the claims. Many of these pathways are found upregulated in cells presenting nanoparticle-induced stress,and were seen to be elevated significantly in cells exposed to higher dose of PS-50 (Figure 2.4a) [297, 298, 299]. However, the viability of HMC3 exposed to 0.1 µg/mL PS-50 after 24, 48, and 72 hours did not show a significant increase relative to unexposed cells, nor was the viability higher than any real-world MNP sample (Figure 2.3a). This may be due to consistent viability despite increased proliferation, which was not evaluated in the present work.

Fork-MNPs vs. PS-50

When considering HMC3 treated with Fork-MNPs against the cells treated with PS-50 NPs, 12 Reactome pathways were found to be enriched, with an even split between pathways enriched in each sample (Figure 3.6b). Similar to the previous analysis, the Fork-MNP pathways showed a higher degree of connection between the enriched pathways, with all 6 pathways showing at least 3 connections between them. Each of these pathways directly tied to the Collagen Formation pathway (NES 2.25; FDR $q < 0.001$), which was also seen enriched in Cup-MNP samples compared to PS-50 (NES 2.41; FDR $q < 0.001$). For both of real-world sample's comparison against PS-50, the top five enriched pathways remained the same: Collagen Chain Trimerization, Assembly of Collagen Fibrils and Multimeric Structures, Collagen Biosynthesis and Modifying Enzymes, Collagen Formation, and Collagen Degradation were all seen significantly enriched in order of lowest to highest FDR q-value.

Although not significant by this study's criteria, one notable enriched pathway induced by Fork-MNPs exposure compared to PS-50 exposure was the Interleukin 10 (IL-10) Signaling (NES 1.72, FDR $q = 0.142$) (Figure 3.9a). This pathway, which was noticeably not enriched in Cup-MNPs compared against PS-50, serves as an anti-inflammatory signal with particular

mechanotransduction relevance in microglia. The YAP and associated Hippo pathway has been shown to regulate IL-10 secretion in HMC3 through the nuclear translocation of the protein [276, 300]. A recent study has shown that in HMC3, the growth substrate has direct impacts on the secretion of IL-10, with stiffer substrates eliciting significantly greater IL-10 release from YAP nuclear localization when compared to the same cells grown on softer substrates [301]. This regulation was found to be dependent on actin polymerization, with inhibited F-actin assembly showing significantly reduced YAP nuclear localization and IL-10 secretion. This study also elucidates how stiffer matrices may increase microglial proliferation, as decreased LATS1/2 kinase activity limits YAP phosphorylation, providing higher nuclear translocation and increased IL-10 secretion while decreasing IL-6 [302]. Despite this, Fork-MNPs were shown to elicit elevated IL-6 concentrations at 10 µg/mL, suggesting an alternative pathway of activation for the cytokine. This upregulation likely reflects a parallel, dose-dependent NF-κB-mediated innate immune response to the Fork-MNPs operating independently of YAP.

Fork-MNPs vs. Cup-MNPs

When comparing Fork-MNP against Cup-MNP samples, the only significantly enriched pathway among either group was the same IL-10 Secretion pathway (Figure 3.10a). With strong enrichment in Fork-MNPs (NES 2.20; FDR q = 0.008), these results suggest that the physicochemical properties of Fork-MNPs directly influence the anti-inflammatory cytokine's release. The IL-10 Secretion pathway contain shows *IL10RA* to be a leading edge gene in Fork-MNPs against Cup-MNPs, suggesting an increased capacity to respond to IL-10 (Figure 3.9b). Additionally, *JAK1* and *STAT3* are shown to be moderately enriched in the same comparison, suggesting that relative to Cup-MNPs, Fork-MNPs are consistent with the active IL-10 signaling axis. Both of these genes are direct downstream transducers of IL-10 signaling, with JAK1 associating constitutively with IL10RA and undergoing phosphorylation upon IL-10 binding. Subsequently, this protein phosphorylates STAT3, which dimerizes

and translocates to the nucleus to drive anti-inflammatory transcriptional programs including SOCS3-mediated suppression of pro-inflammatory cytokine production [303, 304].

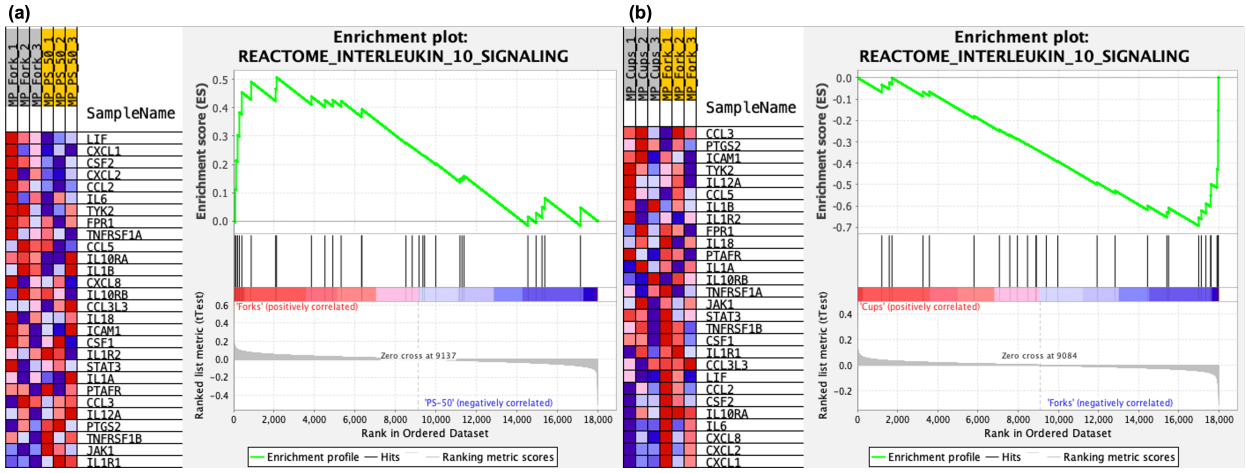

Figure 3.9: Gene Set Enrichment Analysis of the Reactome IL-10 Signaling Pathway in Fork-MNP-Treated HMC3. Enrichment plots for (a) Fork-MNPs versus PS-50 and (b) Cup-MNPs versus Fork-MNPs are shown alongside gene-level enrichment heatmaps for the Reactome Interleukin 10 Signaling pathway. The running enrichment score is shown as the green trend line across the ranked gene list, ordered by t-test ranking metric. In (a), genes positively correlated with Fork-MNP treatment are shown on the left in red, while genes positively correlated with PS-50 are shown on the right in blue. In (b), genes positively correlated with Cup-MNP treatment are shown on the left in red, while genes positively correlated with Fork-MNPs are shown on the right in blue. Vertical tick marks indicate the position of each gene set member within the ranked list. Heatmaps display relative expression levels of each gene in the pathway gene set across all samples, following the same directional color scheme as the enrichment plots, with red indicating higher relative expression and blue indicating lower relative expression.

Perhaps paradoxically, interleukin 6 (*IL-6*) was shown to be a leading edge gene in both conditions, suggesting that the anti-inflammatory IL-10 pathway seeks to dampen the inflammation being produced by the MNPs (Figure 3.9). However, IL-6 is an established upstream inducer of IL-10 transcription through STAT3 activation and subsequent binding to the IL-10 promoter, forming a negative feedback loop wherein inflammatory stimulus drives its own counter-regulation [305, 306]. This pattern is consistent with an acute inflammatory resolution phenotype, where pro-inflammatory signaling (IL-6, CXCL1, CXCL2, CCL2) and its IL-10-mediated counter-regulatory response are concurrent rather than exclusive [307].

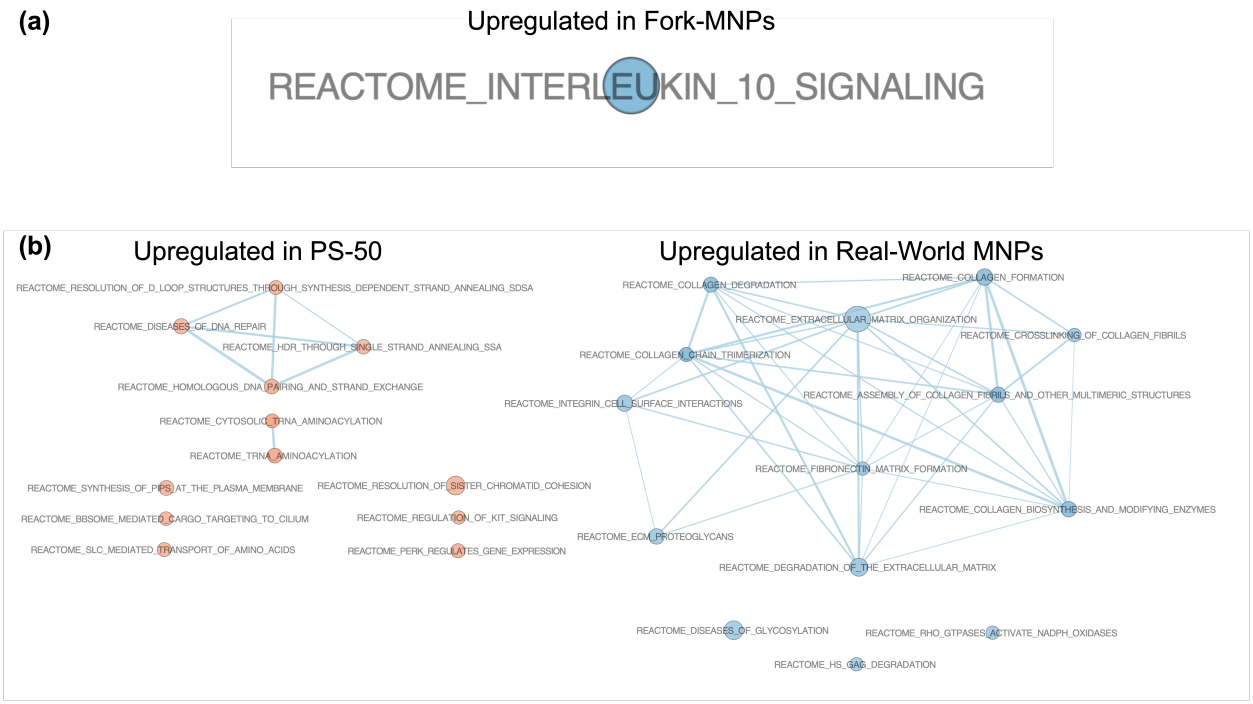

Figure 3.10: Gene Set Enrichment Analysis Pathway Networks in Intra-Real-World MNPs and Inter-Plastic Conditions. Enrichment maps showing (a) Cup-MNPs vs. Fork-MNPs and (b) PS-50 vs. combined real-world samples (Cup-MNPs and Fork-MNPs). Edges connect gene sets with a gene overlap similarity coefficient ≤ 0.375 (Jaccard). Node color reflects the normalized enrichment score (NES): red indicates enrichment in the first-named group, blue indicates enrichment in the second-named group, and color intensity scales with NES magnitude. Only gene sets with FDR q-value < 0.05 and absolute NES above 1.5 are displayed. GSEA was performed using GSEA v4.4.0 with gene set permutation (n = 1,000), Reactome gene sets (MSigDB C2 v2026.1), and gene set size filters of 15–500 genes. Networks were constructed and visualized in Cytoscape v3.10.3 using the EnrichmentMap app.

Taken together, these findings suggest that Fork-MNPs elicit a more pronounced inflammatory response relative to Cup-MNPs, which in turn activates a stronger compensatory IL-10 at 0.1 µg/mL signaling response, potentially reflecting differences in physicochemical properties. This is further supported by the increased inflammation caused by Fork-MNP samples at higher concentrations (10 µg/mL), where IL-6 and IL-8 presented increased quantification relative to unexposed and PS-50-exposed HMC3 (Figure 2.9a).

Fork-derived MNPs presented nanoscale particles smaller than PS-50 or Cup-derived ones (8.86 ± 2.57 nm) as well as larger MPs (100 to 160 µm) compared to Cup-MNPs (Figure 2.2c). One study showed elevated IL-10 secretion in mice exposed to real-world MPs

derived from PP and PE cutting boards (10.4 µm and 27.4 µm, respectively), furthering the hypothesis that these larger, representative MPs may induce anti-inflammatory signaling [308]. Another study utilizing PS MPs (3.0 ± 0.5 µm) and NPs (74.28 ± 0.26 nm) exposed to mice macrophages found IL-10 to be heightened in the MP samples relative to NP samples across a range of concentrations while simultaneously displaying significantly lowered IL-6 [309]. Validated through these studies, the impact of larger plastics seems to invoke an anti-inflammatory effect at lower concentrations despite an increase of IL-6 and IL-8 at higher concentrations (Figure 2.9). One possible explanation for this phenomenon could relate to the heterogeneity of the particles, where real-world MNP samples contain both micro- and nano-sized fragments.

In the brain, microglia are the primary players in IL-10 production and signaling, with anti-inflammatory "M2" microglia secreting the cytokine to reduce inflammation [310, 311, 312]. This observed increase could support the adaptive immune response observed in cells exposed to Fork-MNPs at a low dose. Given the nonsignificant elevation in ROS and IL-6 secretion in HMC3 at 0.1 µg/mL in Fork-MNPs, a compensatory elevated IL-10 secretion could support the cell's ability to adapt.

PS-50 vs. Fork- and Cup-Derived MNPs

Upon the analysis of PS-50 against both real-world samples combined, many of the same pathways were shown to be strongly enriched (Figure 3.10b). In real-world samples, Collagen Chain Trimerization (NES 2.59; FDR $q < 0.001$) and associated pathways remained significantly enriched, while PS-50 maintained Cytosolic tRNA Aminoacylation (NES 2.46; FDR $q < 0.001$) as its strongest enriched pathway. Pristine PS-NPs such as these have been shown to directly disrupt aminoacyl-tRNA and amino acid biosynthesis in mice, most likely due to their enhanced ability for internalization (nanosize) [313]. Enhanced internalization and the much higher SSA of these nanoparticles would also directly bring more proteins into the cells, as the biocorona formed through FBS incubation is believed to be comprised

primarily of albumin protein. This internalization is further amplified by the biocorona itself, as albumin and other adsorbed serum proteins may present receptor-binding domains [314, 315]. Once internalized, these proteins in the biocorona are degraded in lysosomes through ATP-mediated proteolysis pathways, where the elevated amino acid concentrations could represent the need for increased ARS activity [316]. This process has been directly demonstrated in cancer cells, where the nanoparticle-associated protein corona is degraded within lysosomes, and the resulting amino acid byproducts are actively recycled into macromolecule biosynthesis [317]. The aminoacylation charging, an energy-driven reaction requiring ATP, could explain the loss of ATP in HMC3 exposed to PS-50 if this trend holds true at higher concentrations (Figure 2.6b).

The results seen in PS-50 NP-exposed HMC3 cells have been found in other models exposed to non-plastic nanoparticles as well. Silver (AgNPs), gold (AuNPs), and zinc-oxide (ZnONPs) nanoparticles have been repeatedly reproted to induce ER-stress and activate UPR pathways across both *in vitro* and *in vivo* models. AgNPs (0.2 - 5 µm; 5 µg/mL) exposed to human retinal cells for 18 hours were shown to activate hallmark genes in the PERK-eIF2α-ATF4 pathway, including the direct phosphorylation of PERK [318]. This same phosphorylation of PERK was observed with ZnONPs (150 nm) exposed to human umbilical vein endothelial cells (HUVECs) at noncytoxic concentrations (240 µM) after just 4 hours, with Chinese hamster ovary (CHO) cells showing similar results after 8 hours [319]. HUVECs exposed to the same ZnONP dose also showed upregulated *DDIT3* expression after 8 hours. AuNPs presenting both sphere- and rod-morphologies exposed to isolated human polymorphonuclear leukocytes (PMNs) were another group showed to induce UPR pathway activation [320]. After just 5 minutes of exposure to rods (24 x 6 nm) at a concentration of 5,000 AuNPs/PMN ($\approx$15.7 nM), XBP1s were already spliced and translocated to the nucleus, with subsequent upregulation of the oxidative protein folding mediators Ero1L and PDI by 30 min, and full BiP induction confirmed at 60 min. This indicates the ER-stress as an early response to the particles, suggesting that nanoparticle-induced ER-stress and

UPR pathway regulation may represent a conserved, material-agnostic cellular response to particle internalization.

3.4.6 Biologically Relevant DEGs Reinforce Enriched ECM and ER-Stress Pathways

While gene-expression pathways and heatmap visualization of genes can display global, it can lack the statistical power and interpretation of differential expression on a per-gene basis. To address this, volcano plots were constructed for each pairwise comparison. Although DEGs were initially identified with DESeq2 and a BH-adjusted p-value, genes with a meaningful change in expression level are much more prevalent to be considered. Thus, genes were considered "biologically relevant DEGs" if the absolute fold change (FC) exceeded 1.5 ($|\log_2 \mathrm{FC}| \geq 0.585$) with a BH-adjusted p-value < 0.05, a commonly used threshold to enrich for genes with statistical and impactful biological expression. Stricter cutoff values provided insufficient genes for analysis.

Distinct differences in the number and directionality of DEGs were observed across pairwise comparisons (Figure 3.11). When compared against HMC3 exposed to PS-50 NPs, Cup-MNPs showed the greatest number of biologically relevant DEGs, with 18 upregulated and 12 downregulated in the Cup-MNP samples (Figure 3.11a). The Fork-MNP against PS-50 comparison produced 9 upregulated and 4 downregulated DEGs in Fork-MNPs relative to PS-50 (Figure 3.11b). In both real-world MNP samples versus pristine PS-50 exposure comparisons, the majority of DEGs were upregulated in the MNP treatment groups, suggesting that real-world MNPs elicit a stronger activation transcriptional response relative to PS-50 in HMC3 cells. The Cup-MNPs against Fork-MNPs comparison yielded the fewest DEGs with only 8 total — 2 upregulated and 6 downregulated in Cup-MNPs relative to Fork-MNPs (Figure 3.11c). This data indicates that, despite originating from distinct source materials, the two real-world MNP preparations drive broadly similar transcriptional responses, with

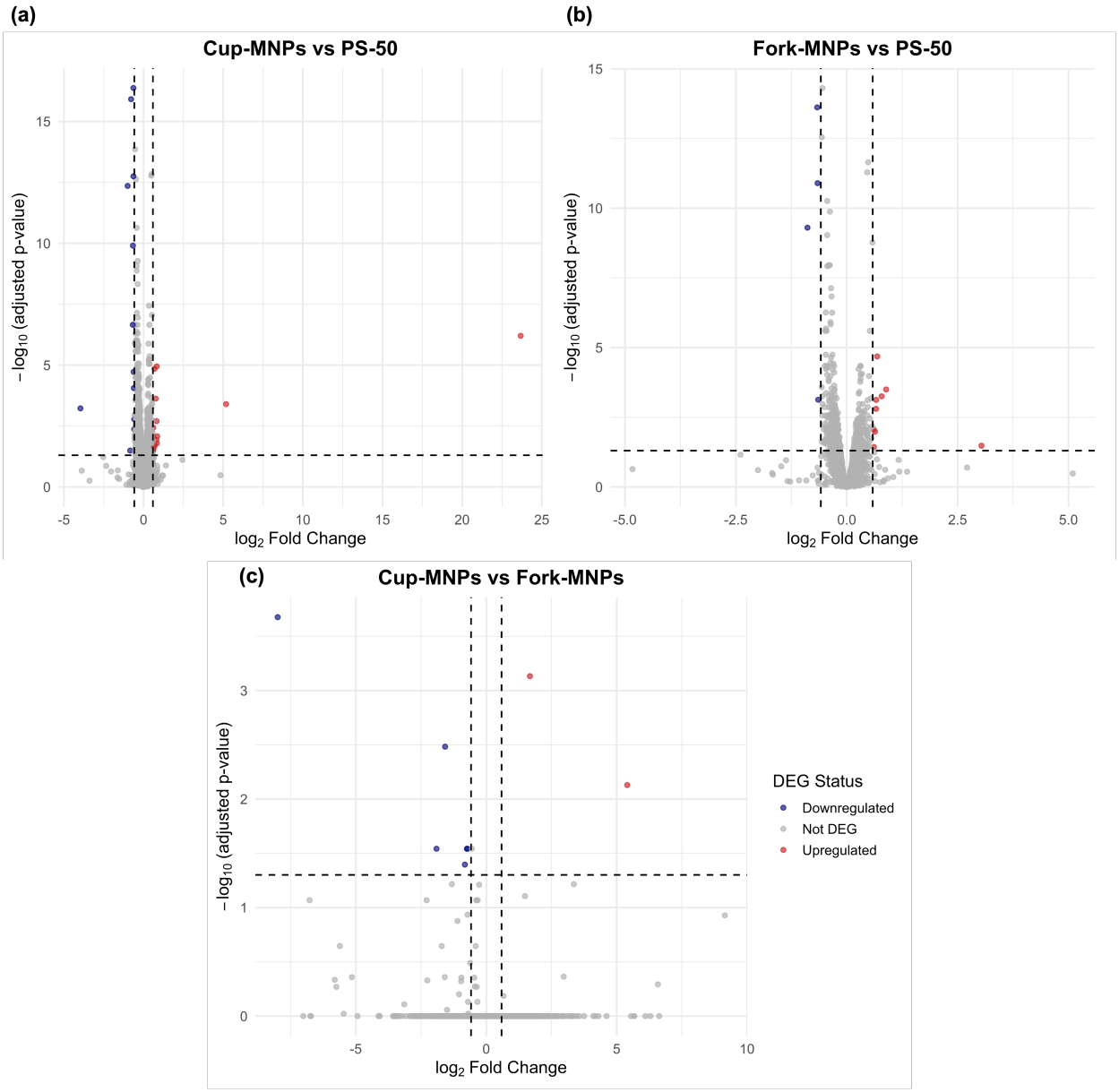

Figure 3.11: Volcano Plots of Pairwise Differential Gene Expression. Differentially expressed genes (DEGs) with substantial impact in HMC3 cells were determined for each comparison group, (a) Cup-MNPs vs. PS-50, (b) Fork-MNPs vs. PS-50, and (c) Cup-MNPs vs. Fork-MNPs. Each point represents a single gene, plotted by $\log_2$fold-change against negative $\log_{10}$ BH-adjusted p-value. Genes in red are shown to be upregulated to the first-named treatment group, with a linear fold change above or below 1.5, while genes in blue are downregulated. Dashed lines represent the threshold values. n=3 replicates per treatment condition.

only modest differences in gene expression between them. With both of these samples comprised of PS with similar size and morphology profiles, this highly similar cellular responses

further highlights the role of the physicochemical properties in plastics exposed to biological systems.

The pristine PS-50 NP exposure produced a significant number of DEGs with identifiable biological relevance in HMC3 cells compared to Cup-MNP exposure. The pro-inflammatory cytokine gene *CXCL8*, encoding for interleukin-8 (IL-8), was shown to be significantly up-regulated in PS-50 NP-exposed HMC3 (FC 1.79; p-adj = 0.03). The IL-8 secretion was significant in HMC3 exposed to PS-50 NPs at 10 µg/mL, suggesting that the impact is observed primarily at the transcript level compared protein level (Figure 2.9b). Additional neuroinflammation-associated genes found upregulated by PS-50 exposure include *EGR1* (FC 1.72; p-adj = 2.05E-20) and *PTX3* (FC 1.58, p-adj = 1.05E-13), which are shown to play roles in Parkinson's and other neurodegenerative diseases [321, 322]. Moreover, several DEGs were shown to be directly relate to ER stress and ATF4-driven pathways, such as *DDIT3* (FC 1.60; p-adj = 2.21E-07) and *TRIB3* (FC 1.56; p-adj 4.22E-17). Upregulation of *DDIT3* and related genes have been shown to be upregulated in rainbow trout exposed to PS-NPs *in vivo* [323]. The observed ER-stress signatures in PS-MNP studies suggest the pathway to be particularly susceptible to plastic-induced biological responses, similar to what it is observed to other types on nanoparticles (ref)[181, 324, 325]. Notably, these effects are typically reported at concentrations orders-of-magnitude larger than the 0.1 µg/mL tested in this study [326, 327].

Similarly, *ASNS* was shown to be significantly upregulated in PS-50-exposed HMC3 cells when compared to cells exposed to Cup-MNPs (FC 1.56; p-adj = 1.77E-13), consistent with GSEA enrichment of aminoacylation pathways in this sample. As a canonical ATF4 transcription target induced by ER stress and unfolded protein response (UPR), *ASNS* up-regulation further supports the hypothesis that the greater SSA of pristine PS-NPs allows greater biocorona protein adsorption with greater interaction, driving a stronger response [317, 328]. This interpretation is further supported by upregulation of the ER-stress response gene *INHBE*, which presented an even stronger transcriptional response (FC 2.00; p-adj

4.41E-13). Together, *ASNS*, *INHBE*, *DDIT3*, and *TRIB3* are transcriptionally activated downstream of ATF4, which is selectively translated through PERK-mediated phosphorylation of eIF2α at Ser51, collectively constituting a coherent PERK–eIF2α–ATF4 integrated stress response in PS-50 NP-exposed HMC3 (Figure 3.12).

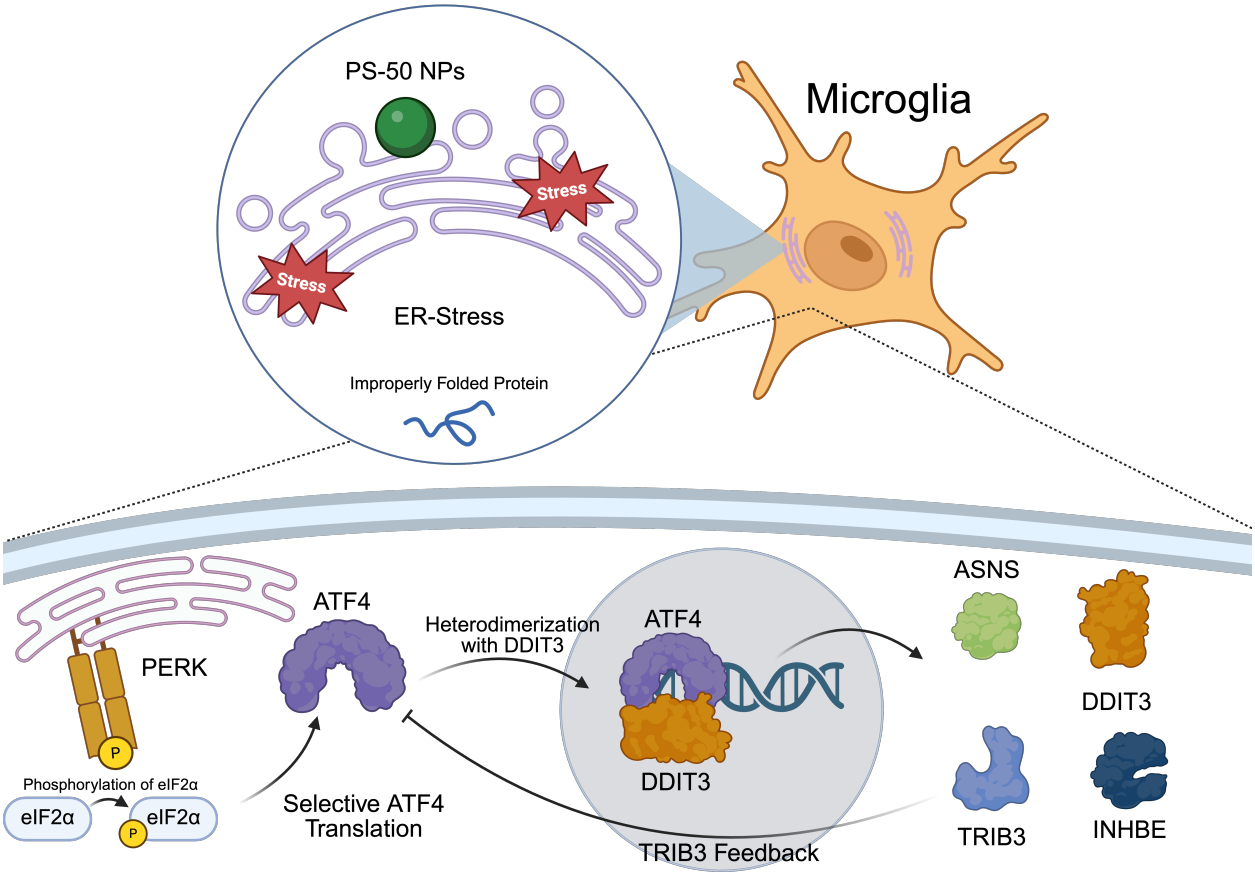

Figure 3.12: ER Stress-Mediated PERK–eIF2α–ATF4 Integrated Stress Response Pathway in Microglia. Polystyrene 50 nm nanoparticles (PS-50 NPs) have been suggested to induce endoplasmic reticulum (ER) stress in microglia, characterized by transcriptional upregulation of PERK–eIF2α–ATF4 pathway target genes. The ER-transmembrane kinase PERK is activated and phosphorylates the translation initiation factor eIF2α at Ser51. The phosphorylated eIF2α results in translational derepression of ATF4 mRNA. The resulting ATF4 protein translocates to the nucleus where it can heterodimerize with DDIT3, itself an ATF4 transcriptional target, to form a bZIP heterodimer transcription factor capable of driving transcription of downstream stress-response genes including ASNS (asparagine synthetase; amino acid homeostasis), DDIT3 (pro-apoptotic effector), TRIB3 (tribbles pseudokinase 3), and INHBE (inhibin subunit beta E; activin E/TGF-β axis). TRIB3 then exerts a negative feedback inhibition on ATF4 transcriptional activity, halting pathway output under transient stress conditions. Collectively, this pathway regulates the adaptive recovery in PS-50 NP-exposed human microglia (HMC3).

Several biologically significant genes were found to be upregulated in Cup-MNPs relative to PS-50 relating to collagen expression. *CARMN* displayed strong upregulation (FC 1.70; p-adj = 0.000238094), which has been found to increase collagen deposition, ECM accumulation, and cell migration in CRISPR-activated human hepatic cells [329]. Additionally, *UBXN11*, which regulates actin cytoskeleton organization and stress fibres through its interaction with Rnd-subfamily GTPases (RND1/2/3), was additionally seen with higher expression (FC 1.61; p-adj = 1.42E-05) [330]. Upstream of cytoskeletal impacts, *PLEKHG4* (FC [1.74]; p-adj = 0.011774451), a guanine nucleotide exchange factor (GEF) that activates Rac1, Cdc42, and RhoA, provides additional evidence for cytoskeletal and ECM-regulatory pathway activation [331]. RhoA presents as a major upstream regulator of the YAP pathway, promoting YAP translocation by inhibiting LATS1/2 activity [332]. Together, the upregulation of *CARMN*, *UBXN11*, and *PLEKHG4* in Cup-MNP-exposed HMC3 cells supports a transcriptional state regulating cytoskeletal tension and ECM deposition, consistent with the observed GSEA pathway enrichments.

The genes *EGR1*, *ASNS*, and *INHBE* were significantly upregulated in HMC3 exposed to PS-50 NPs when compared to Fork-MNPs (Figure 3.11 b). In this comparison, *INHBE* was shown to change its expression relative to real-world MNPs to a similar extent (FC 1.85; p-adj = 5.00E-10), strengthening the hypothesis that pristine NPs activate the PERK–eIF2α–ATF4 pathway to a greater extent. The fourth biologically-relevant DEG in this set, *LURAP1L*, enhances NFκB activation, which is seen in many neuroinflammatory conditions such as Alzheimer's disease and Parkinson's disease [333, 334, 335].

In both real-world MNP samples, *KIF12* and the largely uncharacterized *ENSG00000258728* were significantly upregulated relative to PS-50. The former, a brain-specific kinesin tryptic peptide, is one of the strongest upregulated proteins in Alzheimer's disease, where it plays role in microtubule transport [336, 337]. The latter is a protein coding gene whose annotations relate to interleukin-6 (IL-6) receptor activity as an *GALT-IL11RA* read-through [338].

In HMC3 cells exposed to Fork-MNPs relative to PS-50 NPs (Figure 3.11b), a partially overlapping but distinct set of ECM-associated genes was upregulated. *TNFAIP3* (FC 1.52; p-adj = 0.008619373), encoding the ubiquitin-editing enzyme A20, is a suppressor of both NF-κB and TGF-β/SMAD-dependent fibrogenic processes [339]. Most importantly to the context of ECM regulation, *TNFAIP3* has been shown as an activator of the Hippo-YAP signaling pathway [340]. This gene was also seen to be significantly upregulated in Fork-MNPs compared to Cup-MNPs (FC 1.65; p-adj = 0.028688122) (Figure 3.11c), reinforcing the importance of particle morphology in the YAP pathway. *NDRG1* (FC 1.61; p-adj = 2.09E-05), a stress-response protein, has recently been established as a transcriptional target of the Hippo pathway effector YAP [341]. Upon activation and nuclear translocation, YAP directly binds to the *NDRG1* promoter to drive its expression. YAP knockdown correspondingly decreases *NDRG1* levels, providing substantial evidence to Hippo/YAP pathway's prevalence in Fork-MNP-exposed cells [342].

3.5 Conclusion

In this study, it is demonstrated that human microglial responses to plastic particles are strongly governed by particle physicochemical properties, particularly size and morphology. Using a transcriptomic approach, marked differences between pristine polystyrene nanoplastics (PS-50) and heterogeneous, real-world MNPs derived from consumer plastics are revealed at 0.1 µg/mL. Pairwise comparisons showed the greatest divergence in gene expression between PS-50 and cup-derived MNPs, followed by PS-50 and fork-derived MNPs, highlighting the dominant role of nanoscale particle fractions in driving cellular responses. The enhanced uptake and intracellular accumulation of PS-50 NPs, due to their small size and high surface area, likely underlie their pronounced induction of cellular stress.

Transcriptomic analyses revealed that PS-50 exposure triggers a stress-dominated response characterized by activation of the PERK–eIF2α–ATF4 integrated stress response (ISR), consistent with endoplasmic reticulum perturbation and unfolded protein response

(UPR)-like signaling. Concomitant enrichment of pathways associated with tRNA aminoacylation, linked to various pathological conditions, including cancer, autoimmune disorders, and metabolic conditions; mitotic spindle checkpoint regulation; and sister chromatid cohesion suggests broader impacts on translational control and cell cycle regulation, raising concerns regarding long-term cellular homeostasis. These findings are consistent with the high surface reactivity and bioavailability of nanoscale particles, which amplify their biological impact relative to larger plastic fragments.

In contrast, real-world MNPs induced transcriptional programs primarily associated with extracellular matrix (ECM) organization, cytoskeletal remodeling, and mechanotransduction. Gene set enrichment analyses implicate activation of the Hippo/YAP signaling axis as a central regulator of these responses, likely reflecting the mechanical perturbations imposed by irregularly shaped, heterogeneous particles. Notably, these effects were observed at low concentrations (0.1 µg/mL), underscoring the sensitivity of mechanotransductive pathways to particle morphology and suggesting that physical interactions with the cellular microenvironment represent a key mechanism of MNP action.

Although both Cup- and Fork-MNP samples elicited broadly similar transcriptional responses, Fork-MNPs exhibited a distinct transcriptional signature relative to Cup-MNPs. This was primarily characterized by significant enrichment of the IL-10 signaling pathway, including upregulation of *IL10RA, JAK1, and STAT3*. This profile indicates activation of the JAK/STAT3 anti-inflammatory axis in microglia treated with Fork-MNPs, which can induce a neuroprotective phenotype. These findings are consistent with previous reports showing that YAP nuclear localization, promoted by increased matrix stiffness, can drive IL-10 secretion in microglia in an actin-dependent manner. Collectively, these observations suggest that while both real-world MNP samples induce extracellular matrix remodeling and mechanotransductive signaling, Fork-MNP samples may engage this pathway more strongly, potentially due to their higher content of smaller nanoscale particles. Despite these differences, the remarkably low number of differentially expressed genes between real-world MNP

samples indicate that both preparations converge on a broadly shared transcriptional response program. These shared responses are further supported by the cellular responses in the previous study.

Together, these transcriptomic findings reinforce and mechanistically extend cellular and molecular observations, demonstrating that the physicochemical properties of plastic particles, particularly size and morphology, play a decisive role in shaping biological responses *in vitro*. The widespread reliance on pristine, monodisperse nanoplastic standards may therefore misrepresent the biological impact of environmentally relevant MNPs. Collectively, the data provides a transcriptome-wide perspective on the interactions between real-world MNPs and human microglia, underscoring the importance of incorporating physicochemically representative particles into MNP toxicology studies to improve their environmental and biomedical relevance.

Chapter 4

Conclusions and Future Directions

The work presented provides a multi-level investigation into the biological impacts of environmentally relevant micro- and nanoplastics on human microglial cells, contrasting real-world consumer-derived MNPs against pristine polystyrene nanoplastics commonly employed as experimental placeholders in the field. Across both cellular and molecular endpoints as well as transcriptome-wide analyses, a consistent, reproducible narrative was discovered: the physicochemical properties of MNP samples used in plastic studies, particularly morphologies, is a relevant variable that shapes the biological response of microglia. Particle size and shape play pivotal roles in these responses, supporting not only previously observed findings in MNP studies, but in the wider field of mechanistic nanotoxicology.

At the cellular level, pristine PS-50 NPs elicited pronounced mitochondrial dysfunction in HMC3, characterized by significant reduction in mitochondrial membrane potential, ATP-linked respiration, and maximal respiratory capacity. This was accompanied by elevated cytosolic and mitochondrial ROS productions, with a strong inflammatory response. These findings are consistent with phenotypes observed in neurodegenerative conditions, such as Alzheimer's and Parkinson's disease, and their occurrence at mass-equivalent concentrations to real-world MNPs highlights a critical area of concern in existing literature. In contrast, real-world Cup- and Fork-MNPs, formed from the degradation of consumer-grade goods, elicited adaptive responses at identical mass concentrations. HMC3 displayed compensatory redox activity, preserved respiratory profiles, and overall greater bioenergetic resilience. However, Fork-MNPs evoked elevated IL-6 and IL-8 release at the highest tested concentration, exceeding even the PS-50 response, underscoring that real-world particles are

not uniformly less bioactive than pristine plastics. These divergent outcomes are most readily explained by the orders-of-magnitude difference in particle number, specific surface area, and morphology between pristine and real-world samples at equivalent mass dosimetry.

At the molecular level, differences in transcriptomics profiles among pristine and real-world MNPs were further observed and supported through differential gene expression and pathways enrichment. Pairwise differential expression analyses identified over one thousand DEGs between real-world and pristine NP-exposed cells. Real-world MNPs upregulated gene conditions centered on extracellular matrix remodeling, collagen fibril assembly, actin cytoskeletal organization, and mechanotransduction, while PS-50 NPs drove a transcriptional response dominated by PERK/eIF2α/ATF4 stress response with mitotic dysregulation presentations. The similarities between Cup- and Fork-MNP transcriptional responses, with only 9 significant DEGs, further highlights the shared physicochemical properties as the key driver in microglial response to plastic. The IL-10 secretion pathway enriched in Fork-MNPs further demonstrates the differences the nanofraction-particles contributed to meaningful transcription regulation, mirroring the heightened inflammatory phenotype observed at the cellular level at higher concentrations.

Together, the data presented relay several key conclusions. Perhaps most importantly, pristine polystyrene nanoparticles cannot be used to accurately model the biological impacts of MNPs that are seen in nature and the human body, and their continued use as model particles risks the nuanced understanding of plastics as a risk to human health. Particle morphology, namely size and shape, play unequivocal roles in determining the outcome of biological-material interactions, and as such should be taken into consideration in experimental design to accurately mirror what is most likely to be uptaken by humans. Several important limitations amongst these findings are noted. The use of HMC3 as an *in vitro* target cannot fully encapsulate the diverse response by the complex immune system of the brain, nor present an understanding of how neurons may be impaired. The polydispersity of real-world MNP preparations, while precisely controlled and performed repeatedly

to highly similar results, inevitably contributes to inter-replicate variability. This can be most clearly evidenced in the transcriptional response of the third Fork-MNP sample as well as the measures of sample clustering and principal component analysis. While physiologically relevant, where the differing lifestyle choices of individual persons can directly influence plastic accumulation over time and particle intake itself is stochastic, the experimental mass-concentration dosimetry remains an imperfect attribute.

Future directions of this work should prioritize the adjustment of these potential shortcomings. The effect of real-world MNPs at longer, more representative exposure times greater than 72-hours would allow for the resolution of many pathways to be observed. A more representative model for plastic dynamics would also serve to better simulate how a cell would come into contact with a plastic particle: microfluidics or organ-on-a-chip systems can provide physiologically relevant kinetics to how microglia interact with MNPs *in vivo*. For the validations of the presented findings, functional validation of the Hippo/YAP pathway in real-world samples would provide conformation of the transcriptional model proposed. Elastic moduli measurements of ECM stiffness can further support these claims and advance the understanding of how cell microenvironments influence their responses *in vitro*. Additionally, the validation of the PERK/eIF2α/ATF4 stress response pathway in PS-50-exposed HMC3 would validate the proposed mechanisms with pristine particles, allowing for a detailed understanding of how pristine and real-world particle types differ

The accumulation of plastics in the human brain represents one of the most consequential, yet least understood environmental health challenges of the twenty-first century. Plastics have been detected in nearly every fraction of the human body, even in the most vital of organs. The particles found in the body are not pristine, but rather derived from consumer-grade products and mismanaged industrial waste. As this work has demonstrated, the physical form of plastics is inseparable from its biological impact. The hopes of better understanding the "plastic-pandemic" being faced by every individual lies in the use of representative experimental models, which accurately reflect the physicochemical properties of

the particles which are already inside of the body. This fact remains fundamental for producing science capable for informing the clinical, regulatory, and public health responses. Real-world plastics are already inside of us - the obligation is to now understand the impacts they present.

Bibliography

[1] International Organization for Standardization. ISO 472:2023 – Plastics — Vocabulary. https://www.iso.org/obp/ui/en/#iso:std:iso:472:ed-4:v1:en, 2023.

[2] Leo H Baekeland. The synthesis, constitution, and uses of bakelite. *Industrial & Engineering Chemistry*, 1(3):149–161, 1909.

[3] Adolf Baeyer. Ueber die verbindungen der aldehyde mit den phenolen. *Berichte der Deutschen Chemischen Gesellschaft*, 5:280–282, 1872.

[4] WA Zinzow and Thomas Hazen. Electrical properties of certain bakelite materials. *Industrial & Engineering Chemistry*, 27(8):899–902, 1935.

[5] American Chemical Society. *The Bakelizer*: Commemorative Booklet to Designate the Original Bakelizer as a National Historic Chemical Landmark, November 1993. National Historic Chemical Landmark, National Museum of American History, Smithsonian Institution.

[6] International Union for Conservation of Nature. Plastic pollution: Issues brief, May 2024. Accessed: 2025-08-28.

[7] Food and Agriculture Organization of the United Nations. Production volume of paper and paperboard worldwide from 1961 to 2024 (in million metric tons). https://www.statista.com/statistics/270314/global-paper-and-cardboard-production/, January 2026.

[8] Statista. Value added from the manufacture of the plastics and rubber market worldwide in 2025, with a forecast for 2029 (in billion U.S. dollars). https://www.statista.com/statistics/1060583/global-market-value-of-plastic/, September 2025. Graph.

[9] Cui-Lan Bai, Liang-Ying Liu, Jia-Liang Guo, Li-Xi Zeng, and Ying Guo. Microplastics in take-out food: are we over taking it? *Environmental Research*, 215:114390, 2022.

[10] Qing-Fang Guan, Huai-Bin Yang, Yu-Xiang Zhao, Zi-Meng Han, Zhang-Chi Ling, Kun-Peng Yang, Chong-Han Yin, and Shu-Hong Yu. Microplastics release from victuals packaging materials during daily usage. *EcoMat*, 3(3):e12107, 2021.

[11] Ana L. V. Cubas, Raquel T. Bianchet, Ingrid M. A. S. de Reis, and Isabel C. Gouveia. Plastics and microplastic in the cosmetic industry: Aggregating sustainable actions aimed at alignment and interaction with un sustainable development goals. *Polymers*, 14(21):4576, 2022.

[12] Len Czuba. 2 - application of plastics in medical devices and equipment. In Kayvon Modjarrad and Sina Ebnesajjad, editors, *Handbook of Polymer Applications in Medicine and Medical Devices*, Plastics Design Library, pages 9–19. William Andrew Publishing, Oxford, 2014.

[13] Roland Geyer, Jenna R. Jambeck, and Kara Lavender Law. Production, use, and fate of all plastics ever made. *Science Advances*, 3(7):e1700782, 2017.

[14] Statista. Distribution of global plastic production by industrial sector worldwide, 2025. Statista.

[15] Shubhajit Sarkhel, Samandeep Kaur, Rahul Das, Aditi Sharma, Ankan Kheto, Debapam Saha, and Yogesh Kumar. Antimicrobial active packaging with biopolymers and natural extracts: sustainable solutions and technological challenges. *Sustainable Food Technology*, 2025.

[16] Guofeng Ye, Cheng Wang, Yong Guo, Qingshan Yang, and Siqi Huo. Vitrimer as a sustainable alternative to traditional thermoset: recent progress and future prospective. *ACS Polymers Au*, 5(5):445–457, 2025.

[17] Monika Dokl, Anja Copot, Damjan Krajnc, Yee Van Fan, Annamaria Vujanović, Kathleen B Aviso, Raymond R Tan, Zdravko Kravanja, and Lidija Čuček. Global projections of plastic use, end-of-life fate and potential changes in consumption, reduction, recycling and replacement with bioplastics to 2050. *Sustainable Production and Consumption*, 51:498–518, 2024.

[18] Stephanie B. Borrelle, Jeremy Ringma, Kara Lavender Law, Cole C. Monnahan, Laurent Lebreton, Alexis McGivern, Erin Murphy, Jenna Jambeck, George H. Leonard, Michelle A. Hilleary, Marcus Eriksen, Hugh P. Possingham, Hannah De Frond, Leah R. Gerber, Beth Polidoro, Akbar Tahir, Miranda Bernard, Nicholas Mallos, Megan Barnes, and Chelsea M. Rochman. Predicted growth in plastic waste exceeds efforts to mitigate plastic pollution. *Science*, 369(6510):1515–1518, 2020.

[19] Laurent Lebreton and Anthony Andrady. Future scenarios of global plastic waste generation and disposal. *Palgrave Communications*, 5(1):6, 2019.

[20] Zhan Yang, Fan Lü, Hua Zhang, Wei Wang, Liming Shao, Jianfeng Ye, and Pinjing He. Is incineration the terminator of plastics and microplastics? *Journal of Hazardous Materials*, 401:123429, 2021.

[21] Ting Su, Huasheng Wang, Xiangyu Gu, Shuo Liu, Yusu Xiong, Shuang Deng, and Songgeng Li. Atmospheric microplastics emission from municipal solid waste incineration power plant: Field evidence and characterizations. *Journal of Hazardous Materials Letters*, 6:100149, 2025.

[22] Roman Lehner, Christoph Weder, Alke Petri-Fink, and Barbara Rothen-Rutishauser. Emergence of nanoplastic in the environment and possible impact on human health. *Environmental Science & Technology*, 53(4):1748–1765, 2019. PMID: 30629421.

[23] UN Environment Programme. From pollution to solution: A global assessment of marine litter and plastic pollution, 2021.

[24] Michela Volgare, Francesca De Falco, Roberto Avolio, Rachele Castaldo, Maria Emanuela Errico, Gennaro Gentile, Veronica Ambrogi, and Mariacristina Cocca. Washing load influences the microplastic release from polyester fabrics by affecting wettability and mechanical stress. *Scientific Reports*, 11(1):19479, 2021.

[25] Saba Yousafzai, Mujahid Farid, Muhammad Zubair, Nafeesa Naeem, Wardha Zafar, Sheharyaar Farid, Shafaqat Ali, et al. Detection and degradation of microplastics in the environment: a review. *Environmental Science: Advances*, 4(8):1142–1165, 2025.

[26] Agata Witczak, Laura Przedpełska, Kamila Pokorska-Niewiada, and Jacek Cybulski. Microplastics as a threat to aquatic ecosystems and human health. *Toxics*, 12(8):571, 2024.

[27] Leonardo Alberghini, Alessandro Truant, Serena Santonicola, Giampaolo Colavita, and Valerio Giaccone. Microplastics in fish and fishery products and risks for human health: A review. *International journal of environmental research and public health*, 20(1):789, 2022.

[28] Luca Alberghini, Alessia Truant, Simona Santonicola, Giampaolo Colavita, and Vincenzo Giaccone. Microplastics in fish and fishery products and risks for human health: A review. *International Journal of Environmental Research and Public Health*, 20(1):789, 2022.

[29] Seth Vogt. Created with biorender.com, 2026. Figure created using BioRender.

[30] Johanna N. J. Weston, Priscilla Carrillo-Barragan, Thomas D. Linley, William D. K. Reid, and Alan J. Jamieson. New species of eurythenes from hadal depths of the mariana trench, pacific ocean (crustacea: Amphipoda). *Zootaxa*, 4748(1):zootaxa.4748.1.9, 2020.

[31] Shanye Yang, Guy Brasseur, Stacy Walters, Pablo Lichtig, and Cathy WY Li. Global atmospheric distribution of microplastics with evidence of low oceanic emissions. *npj Climate and Atmospheric Science*, 8(1):81, 2025.

[32] Daria Tatsii, Silvia Bucci, Taraprasad Bhowmick, Johannes Guettler, Lucie Bakels, Gholamhossein Bagheri, and Andreas Stohl. Shape matters: long-range transport of microplastic fibers in the atmosphere. *Environmental Science & Technology*, 58(1):671–682, 2023.

[33] Bernard P. Boudreau and Barry R. Ruddick. On a reactive continuum representation of organic matter diagenesis. *American Journal of Science*, 291(5):507–538, 1991.

[34] Galina F Levchik, Kun Si, Sergei V Levchik, G Camino, and Charles A Wilkie. The correlation between cross-linking and thermal stability: Cross-linked polystyrenes and polymethacrylates. *Polymer degradation and stability*, 65(3):395–403, 1999.

[35] Andrew Turner and Montserrat Filella. Hazardous metal additives in plastics and their environmental impacts. *Environment International*, 156:106622, 2021.

[36] Baljit Singh and Nisha Sharma. Mechanistic implications of plastic degradation. *Polymer degradation and stability*, 93(3):561–584, 2008.

[37] Christopher P. Ward and Christopher M. Reddy. Opinion: We need better data about the environmental persistence of plastic goods. *Proceedings of the National Academy of Sciences of the United States of America*, 117(26):14618–14621, 2020.

[38] Ali Chamas, Hyunjin Moon, Jiajia Zheng, Yang Qiu, Tarnuma Tabassum, Jun Hee Jang, Mahdi Abu-Omar, Susannah L. Scott, and Sangwon Suh. Degradation rates of plastics in the environment. *ACS Sustainable Chemistry & Engineering*, 8(9):3494–3511, 2020.

[39] Aamer Ali Shah, Fariha Hasan, Abdul Hameed, and Safia Ahmed. Biological degradation of plastics: a comprehensive review. *Biotechnology advances*, 26(3):246–265, 2008.

[40] P.C. Painter and M.M. Coleman. *Essentials of Polymer Science and Engineering*. Raymond F. Boyer Library Collection. DEStech Publications, Incorporated, 2009.

[41] KN Cundiff, Thilo F Morgeneyer, and AA Benzerga. Photo-oxidation of semicrystalline polymers: Effect of stress triaxiality on ductility. *Tomography of Materials and Structures*, 7:100048, 2025.

[42] Trinh Nguyen, Jan Merna, Everett Kysor, Olaf Kohlmann, and David Bernard Levin. Bacterial degradation of low-density polyethylene preferentially targets the amorphous regions of the polymer. *Polymers*, 16(20):2865, 2024.

[43] Nicholas F. Mendez, Vivek Sharma, Michele Valsecchi, Vighnesh Pai, Johnny K. Lee, Linda S. Schadler, Alejandro J. Müller, Shelby Watson-Sanders, Mark Dadmun, Guruswamy Kumaraswamy, and Sanat K. Kumar. Mechanism of quiescent nanoplastic formation from semicrystalline polymers. *Nature Communications*, 16(1):3051, 2025.

[44] B. Fayolle, X. Colin, L. Audouin, and J. Verdu. Mechanism of degradation induced embrittlement in polyethylene. *Polymer Degradation and Stability*, 92(2):231–238, 2007.

[45] Renxuan Xie, Albree R. Weisen, Youngmin Lee, Melissa A. Aplan, Abigail M. Fenton, Ashley E. Masucci, Fabian Kempe, Michael Sommer, Christian W. Pester, Ralph H. Colby, and Enrique D. Gomez. Glass transition temperature from the chemical structure of conjugated polymers. *Nature Communications*, 11(1):893, 2020.

[46] Lindsay N. Woodard and Melissa A. Grunlan. Hydrolytic degradation and erosion of polyester biomaterials. *ACS Macro Letters*, 7(8):976–982, 2018.

[47] Mathew C Celina. Review of polymer oxidation and its relationship with materials performance and lifetime prediction. *Polymer degradation and stability*, 98(12):2419–2429, 2013.

[48] Mehrdad Seifali Abbas-Abadi. The effect of process and structural parameters on the stability, thermo-mechanical and thermal degradation of polymers with hydrocarbon skeleton containing pe, pp, ps, pvc, nr, pbr and sbr. *Journal of Thermal Analysis and Calorimetry*, 143(4):2867–2882, 2021.

[49] U.S. Environmental Protection Agency. Microplastics research, 2025. Accessed: September 2, 2025.

[50] Kshitij Upadhyay and Samir Bajpai. Microplastics in landfills: A comprehensive review on occurrence, characteristics and pathways to the aquatic environment. *Nature Environment & Pollution Technology*, 20, 2021.

[51] Jing Song, Chunhui Wang, and Gang Li. Defining primary and secondary microplastics: a connotation analysis. *Acs Es&T Water*, 4(6):2330–2332, 2024.

[52] EFSA Panel on Contaminants in the Food Chain (CONTAM). Presence of microplastics and nanoplastics in food, with particular focus on seafood. *EFSA Journal*, 14(6):e04501, 2016.

[53] Julien Gigault, Alexandra ter Halle, Magalie Baudrimont, Pierre-Yves Pascal, Fabienne Gauffre, Thuy-Linh Phi, Hind El Hadri, Bruno Grassl, and Stéphanie Reynaud. Current opinion: What is a nanoplastic? *Environmental Pollution*, 235:1030–1034, 2018.

[54] Mikael T Ekvall, Martin Lundqvist, Egle Kelpsiene, Eimantas Šileikis, Stefán B Gunnarsson, and Tommy Cedervall. Nanoplastics formed during the mechanical breakdown of daily-use polystyrene products. *Nanoscale advances*, 1(3):1055–1061, 2019.

[55] Pinjing He, Liyao Chen, Liming Shao, Hua Zhang, and Fan Lü. Municipal solid waste (msw) landfill: A source of microplastics? -evidence of microplastics in landfill leachate. *Water Research*, 159:38–45, 2019.

[56] Mosarrat Samiha Kabir, Hong Wang, Stephanie Luster-Teasley, Lifeng Zhang, and Renzun Zhao. Microplastics in landfill leachate: Sources, detection, occurrence, and removal. *Environmental science and ecotechnology*, 16:100256, 2023.

[57] Klára Cverenkárová, Martina Valachovičová, Tomáš Mackul'ak, Lukáš Žemlička, and Lucia Bírošová. Microplastics in the food chain. *Life*, 11(12):1349, 2021.

[58] Lili Tian, Cheng Jinjin, Rong Ji, Yini Ma, and Xiangyang Yu. Microplastics in agricultural soils: sources, effects, and their fate. *Current Opinion in Environmental Science & Health*, 25:100311, 2022.

[59] Bhakti Jadhav and Agnieszka Medyńska-Juraszek. Microplastic and nanoplastic in crops: possible adverse effects to crop production and contaminant transfer in the food chain. *Plants*, 13(17):2526, 2024.

[60] Shuai Guo, Jing Wang, Haifeng Sun, Juan Wu, Jianhong Xu, and Jianqiang Sun. Foliar uptake and in-leaf translocation of micro (nano) plastics and their interaction with epicuticular wax. *Environmental Science: Nano*, 10(4):1126–1137, 2023.

[61] Gea Oliveri Conti, Margherita Ferrante, Mohamed Banni, Claudia Favara, Ilenia Nicolosi, Antonio Cristaldi, Maria Fiore, and Pietro Zuccarello. Micro- and nano-plastics in edible fruit and vegetables. the first diet risks assessment for the general population. *Environmental Research*, 187:109677, 2020.

[62] Angela Patricia Abad-López, Omar Solano-Trillos, and Carlos David Grande-Tovar. Micro-nanoplastics in livestock and poultry: Emerging components of food matrices. *Journal of Food Composition and Analysis*, page 108956, 2026.

[63] Saúl Vallejos, Miriam Trigo-López, Ana Arnaiz, Álvaro Miguel, Asunción Muñoz, Aránzazu Mendía, and José Miguel García. From classical to advanced use of polymers in food and beverage applications. *Polymers*, 14(22):4954, 2022.

[64] Kazi Albab Hussain, Svetlana Romanova, Ilhami Okur, Dong Zhang, Jesse Kuebler, Xi Huang, Bing Wang, Lucia Fernandez-Ballester, Yongfeng Lu, Mathias Schubert, and Yusong Li. Assessing the release of microplastics and nanoplastics from plastic containers and reusable food pouches: Implications for human health. *Environmental Science & Technology*, 57(26):9782–9792, 2023. PMID: 37343248.

[65] Mary Kosuth, Sherri A. Mason, and Elizabeth V. Wattenberg. Anthropogenic contamination of tap water, beer, and sea salt. *PLOS ONE*, 13(4):1–18, 04 2018.

[66] Abdullah Altunışık. Prevalence of microplastics in commercially sold soft drinks and human risk assessment. *Journal of Environmental Management*, 336:117720, 2023.

[67] Albert A. Koelmans, Nur Hazimah Mohamed Nor, Enya Hermsen, Merel Kooi, Svenja M. Mintenig, and Jennifer De France. Microplastics in freshwaters and drinking water: Critical review and assessment of data quality. *Water Research*, 155:410–422, 2019.

[68] Gerd Liebezeit and Elisabeth Liebezeit. Synthetic particles as contaminants in german beers. *Food Additives & Contaminants: Part A*, 31(9):1574–1578, 2014.

[69] Hyemi Lee, Alexander Kunz, Won Joon Shim, and Bruno A. Walther. Microplastic contamination of table salts from taiwan, including a global review. *Scientific Reports*, 9(1):10145, 2019.

[70] Fahmida Parvin, Jayasree Nath, Tamanna Hannan, and Shafi M. Tareq. Proliferation of microplastics in commercial sea salts from the world longest sea beach of bangladesh. *Environmental Advances*, 7:100173, 2022.

[71] Vilde K Snekkevik, Matthew Cole, Alessio Gomiero, Marte Haave, Farhan R Khan, and Amy L Lusher. Beyond the food on your plate: Investigating sources of microplastic contamination in home kitchens. *Heliyon*, 10(15), 2024.

[72] Matthew Cole, Alessio Gomiero, Adrián Jaén-Gil, Marte Haave, and Amy Lusher. Microplastic and ptfe contamination of food from cookware. *Science of The Total Environment*, 929:172577, 2024.

[73] Yinai Liu, Yu Cao, Huiqi Li, Huanpeng Liu, Liuliu Bi, Qianqian Chen, and Renyi Peng. A systematic review of microplastics emissions in kitchens: Understanding the links with diseases in daily life. *Environment international*, 188:108740, 2024.

[74] Guanyu Zhou, Qidong Wu, Peng Tang, Chen Chen, Xin Cheng, Xin-Feng Wei, Jun Ma, and Baicang Liu. How many microplastics do we ingest when using disposable drink cups? *Journal of Hazardous Materials*, 441:129982, 2023.

[75] Guoqiang Liu, Jian Wang, Mengjie Wang, Rongrong Ying, Xuwei Li, Zhewei Hu, and Ya Zhang. Disposable plastic materials release microplastics and harmful substances in hot water. *Science of the total environment*, 818:151685, 2022.

[76] N. Yakovenko, L. Pérez-Serrano, T. Segur, O. Hagelskjaer, H. Margenat, G. Le Roux, et al. Human exposure to pm10 microplastics in indoor air. *PLOS ONE*, 20(7):e0328011, 2025.

[77] Mohammad S. Islam, Md. Mizanur Rahman, Puchanee Larpruenrudee, Akbar Arsalanloo, Hamidreza Mortazavy Beni, Md. Ariful Islam, YuanTong Gu, and Emilie Sauret. How microplastics are transported and deposited in realistic upper airways? *Physics of Fluids*, 35(6):063319, 06 2023.

[78] World Wide Fund for Nature. Revealed: Plastic ingestion by people could be equating to a credit card a week. `https://wwf.org.au/news/2019/revealed-plastic-ingestion-by-people-could-be-equating-to-a-credit-card-a-week/`, 2019. Accessed: 2026-03-04.

[79] Martin Pletz. Ingested microplastics: do humans eat one credit card per week? *Journal of hazardous materials letters*, 3:100071, 2022.

[80] K. S. Din, M. F. Khokhar, S. I. Butt, A. Qadir, and F. Younas. Exploration of microplastic concentration in indoor and outdoor air samples: Morphological, polymeric, and elemental analysis. *Science of the Total Environment*, 908:168398, 2024.

[81] Muhammad Jahanzaib, Shambhavi Sharma, and Duckshin Park. Microplastics comparison of indoor and outdoor air and ventilation rate effect in outskirts of the seoul metropolitan city. *Emerging Contaminants*, 11(1):100408, 2025.

[82] A. Menichetti, D. Mordini, and M. Montalti. Penetration of microplastics and nanoparticles through skin: Effects of size, shape, and surface chemistry. *Journal of Xenobiotics*, 15(1):6, 2024.

[83] Ovokeroye Akpojevwe Abafe, Stuart Harrad, and Mohamed Abou-Elwafa Abdallah. Assessment of human dermal absorption of flame retardant additives in polyethylene and polypropylene microplastics using 3d human skin equivalent models. *Environment International*, 186:108635, 2024.

[84] M Pileta-Labañino, P Crespo-Barrera, and A Navarro-Frómeta. Human skin and micro-and nanoplastics: a mini-review. *MOJ Ecol. Environ. Sci*, 9:122–125, 2024.

[85] Yuwen Zhou, Veeramuthu Ashokkumar, Ayodeji Amobonye, Gargi Bhattacharjee, Ranjna Sirohi, Vijai Singh, G Flora, Vinay Kumar, Santhosh Pillai, Zengqiang Zhang, et al. Current research trends on cosmetic microplastic pollution and its impacts on the ecosystem: A review. *Environmental Pollution*, 320:121106, 2023.

[86] Anna Kukkola, Andrew J Chetwynd, Stefan Krause, and Iseult Lynch. Beyond microbeads: Examining the role of cosmetics in microplastic pollution and spotlighting unanswered questions. *Journal of Hazardous Materials*, 476:135053, 2024.

[87] R. M. B. Popa, C. Radulescu, I. D. Dulama, R. M. Stirbescu, I. A. Bucurica, A. L. Banica, and S. G. Stanescu. Potential health risk of microplastic exposures from skin-cleansing products. *Toxics*, 13(5):354, 2025.

[88] Christina Hartmann, Ievgeniia Lomako, Carla Schachner, Evelin El Said, Julia Abert, Vito Satrapa, Andreas-Marius Kaiser, Helene Walch, and Sebastian Köppel. Assessment of microplastics in human stool: A pilot study investigating the potential impact of diet-associated scenarios on oral microplastics exposure. *Science of The Total Environment*, 951:175825, 2024.

[89] Richard C. Thompson, Winnie Courtene-Jones, Julien Boucher, Sabine Pahl, Karen Raubenheimer, and Albert A. Koelmans. Twenty years of microplastic pollution research—what have we learned? *Science*, 386(6720):eadl2746, 2024.

[90] Nur Sakinah Roslan, Y. Y. Lee, Y. S. Ibrahim, S. T. Anuar, K. M. K. K. Yusof, L. A. Lai, and T. Brentnall. Detection of microplastics in human tissues and organs: A scoping review. *Journal of Global Health*, 14:04179, 2024.

[91] Anqi Sun and Wen-Xiong Wang. Human exposure to microplastics and its associated health risks. *Environment & Health*, 1(3):139–149, 2023.

[92] Alexander J Nihart, Marcus A Garcia, Eliane El Hayek, Rui Liu, Marian Olewine, Josiah D Kingston, Eliseo F Castillo, Rama R Gullapalli, Tamara Howard, Barry Bleske, et al. Bioaccumulation of microplastics in decedent human brains. *Nature medicine*, 31(4):1114–1119, 2025.

[93] E. Dzierżyński, E. Blicharz-Grabias, I. Komaniecka, R. Panek, A. Forma, P. J. Gawlik, others, and J. Flieger. Post-mortem evidence of microplastic bioaccumulation in human organs: insights from advanced imaging and spectroscopic analysis. *Archives of Toxicology*, 99(10):4051–4066, 2025.

[94] Kinga Vojnits, Andrés de León, Julien Gibon, Philip Barker, Morteza Mahmoudi, and Sepideh Pakpour. A systematic review of the potential neurotoxicity of micro- and nanoplastics: The known and unknown. *Particle and Fibre Toxicology*, 22(1):29, 2025.

[95] Mengzhen Li, Wenhao Ma, James Kar Hei Fang, Jiezhang Mo, Lei Li, Min Pan, Rong Li, Xiaoyun Zeng, and Keng Po Lai. A review on the combined toxicological effects of microplastics and their attached pollutants. *Emerging Contaminants*, page 100486, 2025.

[96] Valentina Tolardo, Davide Magrì, Francesco Fumagalli, Domenico Cassano, Athanassia Athanassiou, Despina Fragouli, and Sabrina Gioria. In vitro high-throughput toxicological assessment of nanoplastics. *Nanomaterials*, 12(12):1947, 2022.

[97] Julien Gigault, Hassan El Hadri, Bao Nguyen, and et al. Nanoplastics are neither microplastics nor engineered nanoparticles. *Nature Nanotechnology*, 16:501–507, 2021.

[98] Carlos Baeza-Martínez, Sonia Olmos, Miguel González-Pleiter, Joaquín López-Castellanos, Eduardo García-Pachón, Mar Masiá-Canuto, Luis Hernández-Blasco, and Javier Bayo. First evidence of microplastics isolated in european citizens' lower airway. *Journal of Hazardous Materials*, 438:129439, 2022.

[99] Luís Fernando Amato-Lourenço, Regiani Carvalho-Oliveira, Gabriel Ribeiro Júnior, Luciana dos Santos Galvão, Rômulo Augusto Ando, and Thais Mauad. Presence of airborne microplastics in human lung tissue. *Journal of Hazardous Materials*, 416:126124, 2021.

[100] G. E. Zakynthinos, I. E. Dimeas, C. Salmas, A. D. Pagonis, I. D. Papanikolaou, E. Oikonomou, K. N. Tourlakopoulos, E. Karetsi, and Z. Daniil. Detection of microplastics in human bronchoalveolar lavage fluid: Preliminary evidence of respiratory exposure to environmental contaminants. *Cureus*, 17(11):e97632, 2025.

[101] Runze Liu, Xiaokang Guo, et al. Formation of metal-microplastic complexes in lung adenocarcinoma is associated with increased risk of cancer progression. *Journal of Hazardous Materials*, 494:138517, 2025.

[102] Seung Eun Lee, Do Yun Kim, Taek Seung Jeong, and Yong Seek Park. Micro- and nano-plastic-induced adverse health effects on lungs and kidneys linked to oxidative stress and inflammation. *Life*, 15(3):392, 2025.

[103] Kuo Lu, Danting Zhan, Yingying Fang, Lei Li, Guobing Chen, Shanze Chen, and Lingwei Wang. Microplastics, potential threat to patients with lung diseases. *Frontiers in Toxicology*, 4:958414, 2022.

[104] Weimeng Shi, Yan Cao, Xiaolong Chai, Qun Zhao, Yingxue Geng, Dan Liu, and Senlin Tian. Potential health risks of the interaction of microplastics and lung surfactant. *Journal of Hazardous Materials*, 429:128109, 2022.

[105] Philipp Schwabl, Sebastian Köppel, Philipp Königshofer, Theresa Bucsics, Michael Trauner, Thomas Reiberger, and Bettina Liebmann. Detection of various microplastics in human stool. *Annals of Internal Medicine*, 171(7):453–457, 2019. PMID: 31476765.

[106] Zehua Yan, Yafei Liu, Ting Zhang, Faming Zhang, Hongqiang Ren, and Yan Zhang. Analysis of microplastics in human feces reveals a correlation between fecal microplastics and inflammatory bowel disease status. *Environmental Science & Technology*, 56(1):414–421, 2022.

[107] Sait Özsoy, Sedat Gündogdu, Sermet Sezigen, Esra Tasalp, Durmuş Arinc Ikiz, and Ahmet Erkan Kideys. Presence of microplastics in human stomachs. *Forensic Science International*, 364:112246, 2024.

[108] E.C. Lavelle, S. Sharif, N.W. Thomas, J. Holland, and S.S. Davis. The importance of gastrointestinal uptake of particles in the design of oral delivery systems. *Advanced Drug Delivery Reviews*, 18(1):5–22, 1995. Non-parenteral Vaccines.

[109] Manasi Agrawal, Alvise Vianello, Mellissa Picker, Laura Simon-Sánchez, Rosemary Chen, Maria Manuela Estevinho, Kaitlyn Weinstein, Jeanette Lykkemark, Tine Jess, Inga Peter, et al. Micro-and nano-plastics, intestinal inflammation, and inflammatory bowel disease: A review of the literature. *Science of the total environment*, 953:176228, 2024.

[110] Bing Wu, Xiaomei Wu, Su Liu, Zhizhi Wang, and Ling Chen. Size-dependent effects of polystyrene microplastics on cytotoxicity and efflux pump inhibition in human caco-2 cells. *Chemosphere*, 221:333–341, 2019.

[111] Zhichun Zhang, Mingkai Xu, Lei Wang, Wu Gu, Xiang Li, Zhiyang Han, Xuanhe Fu, Xiujuan Wang, Xu Li, and Zhencheng Su. Continuous oral exposure to micro-and nanoplastics induced gut microbiota dysbiosis, intestinal barrier and immune dysfunction in adult mice. *Environment international*, 182:108353, 2023.

[112] Xin-Yue Yang, Zhong-Wei Zhang, Guang-Deng Chen, and Shu Yuan. Gut microbiome remodeling induced by microplastic exposure in humans. *Gut Microbes*, 18(1):2617696, 2026.

[113] Elora Fournier, Jeremy Ratel, Sylvain Denis, Mathilde Leveque, Philippe Ruiz, Carine Mazal, Frederic Amiard, Mathieu Edely, Valerie Bezirard, Eric Gaultier, Bruno Lamas, Eric Houdeau, Erwan Engel, Fabienne Lagarde, Lucie Etienne-Mesmin, Muriel Mercier-Bonin, and Stéphanie Blanquet-Diot. Exposure to polyethylene microplastics alters immature gut microbiome in an infant in vitro gut model. *Journal of Hazardous Materials*, 443:130383, 2023.

[114] Muhammad Reva Aditya, Athaya Rahmanardi Muhammad, Vito Adriansyah, Nur Samsu, and Hikmawan Wahyu Sulistomo. Microplastic exposure and its consequences for renal and urinary health: systematic review of in vivo studies. *All Life*, 18(1):2457760, 2025.

[115] Sara Massardo, Daniela Verzola, Stefano Alberti, Claudia Caboni, Matteo Santostefano, Enrico Eugenio Verrina, Andrea Angeletti, Francesca Lugani, Gian Marco Ghiggeri, Maurizio Bruschi, et al. Microraman spectroscopy detects the presence of microplastics in human urine and kidney tissue. *Environment International*, 184:108444, 2024.

[116] Wenyue Qiu, Jiali Ye, Yiman Su, Xinting Zhang, Xiaoyue Pang, Jianzhao Liao, Rongmei Wang, Cuiyan Zhao, Hui Zhang, Lianmei Hu, et al. Co-exposure to environmentally relevant concentrations of cadmium and polystyrene nanoplastics induced oxidative stress, ferroptosis and excessive mitophagy in mice kidney. *Environmental pollution*, 333:121947, 2023.

[117] Wanzhen Wang, Jiafu Guan, Yueying Feng, Liju Nie, Yuanyuan Xu, Hengyi Xu, and Fen Fu. Polystyrene microplastics induced nephrotoxicity associated with oxidative stress, inflammation, and endoplasmic reticulum stress in juvenile rats. *Frontiers in nutrition*, 9:1059660, 2023.

[118] Edoardo La Porta, Ottavia Exacoustos, Francesca Lugani, Andrea Angeletti, Decimo Silvio Chiarenza, Carolina Bigatti, Sonia Spinelli, Xhuliana Kajana, Andrea Garbarino, Maurizio Bruschi, Giovanni Candiano, Gianluca Caridi, Nicoletta Mancianti, Marta Calatroni, Daniela Verzola, Pasquale Esposito, Francesca Viazzi, Enrico Verrina, and Gian Marco Ghiggeri. Microplastics and kidneys: An update on the evidence for deposition of plastic microparticles in human organs, tissues and fluids and renal toxicity concern. *International Journal of Molecular Sciences*, 24(18):14391, 2023.

[119] Heather A. Leslie, Martin J.M. van Velzen, Sicco H. Brandsma, A. Dick Vethaak, Juan J. Garcia-Vallejo, and Marja H. Lamoree. Discovery and quantification of plastic particle pollution in human blood. *Environment International*, 163:107199, 2022.

[120] Suvash C Saha and Goutam Saha. Effect of microplastics deposition on human lung airways: A review with computational benefits and challenges. *Heliyon*, 10(2), 2024.

[121] Bowen Li, Min Li, Dongwei Du, Bin Tang, Wenwen Yi, Miaoni He, Ruijuan Liu, Hairui Yu, Yunjiang Yu, and Jing Zheng. Characteristics and influencing factors of microplastics entering human blood through intravenous injection. *Environment International*, 198:109377, 2025.

[122] Long Zhu, Mindong Ma, Xizhuang Sun, Zhixin Wu, Yanyan Yu, Yulin Kang, Zheng Liu, Qiujin Xu, and Lihui An. Microplastics entry into the blood by infusion therapy: few but a direct pathway. *Environmental Science & Technology Letters*, 11(2):67–72, 2023.

[123] Sophie V. L. Leonard, Catriona R. Liddle, Charlotte A. Atherall, Emma Chapman, Matthew Watkins, Simon D. J. Calaminus, and Jeanette M. Rotchell. Microplastics in human blood: Polymer types, concentrations and characterisation using ftir. *Environment International*, 188:108751, 2024.

[124] Yufei Wang and Haifeng Qian. Phthalates and their impacts on human health. In *Healthcare*, volume 9, page 603. Multidisciplinary Digital Publishing Institute, 2021.

[125] Dong-Wook Lee, Jaehak Jung, Seul-ah Park, Yunjeong Lee, Juyang Kim, Changwoo Han, Hwan-Cheol Kim, Joon Hee Lee, and Yun-Chul Hong. Microplastic particles in human blood and their association with coagulation markers. *Scientific Reports*, 14(1):30419, 2024.

[126] M Woodward, GDO Lowe, A Rumley, and H Tunstall-Pedoe. Fibrinogen as a risk factor for coronary heart disease and mortality in middle-aged men and women: the scottish heart health study. *European heart journal*, 19(1):55–62, 1998.

[127] Rita Carlotta Santoro, Angelo Claudio Molinari, Marzia Leotta, and Tiziano Martini. Isolated prolongation of activated partial thromboplastin time: not just bleeding risk! *Medicina*, 59(6):1169, 2023.

[128] Sai Rahul Ponnana, Tejas Rajagopalan, Tong Zhang, Zhuo Chen, Santosh Kumar Sirasapalli, and Salil Deo. Microplastic concentration, social, and environmental features and their association with chronic disease prevalence: an analysis across us census tracts. *Journal of the American College of Cardiology*, 85(12_Supplement):374–374, 2025.

[129] Changcheng Zhou, X. Li, Y. Wang, et al. Microplastic exposure elicits sex-specific atherosclerosis development in lean low-density lipoprotein receptor-deficient mice. *Environment International*, 206:109938, 2025.

[130] Charlotte E Sofield, Ryan S Anderton, and Anastazja M Gorecki. Mind over microplastics: exploring microplastic-induced gut disruption and gut-brain-axis consequences. *Current issues in molecular biology*, 46(5):4186–4202, 2024.

[131] Shan Shan, Yifan Zhang, Huiwen Zhao, Tao Zeng, and Xiulan Zhao. Polystyrene nanoplastics penetrate across the blood-brain barrier and induce activation of microglia in the brain of mice. *Chemosphere*, 298:134261, 2022.

[132] Lauter E. Pelepenko, Mariana Cassani de Oliveira, Daniela A. Masaro, Glauco M. M. M. Lustosa, Talita Mazon, Roger F. Castilho, Luciene M. dos Reis, Fabrice MacWay, Lucie Hénaut, Saïd Kamel, Loïc Louvet, and Rodrigo B. Oliveira. Effects of microplastics on the bones: a comprehensive review. *Osteoporosis International*, 36(8):1327–1345, 2025.

[133] Xiaoli Guo, Lin Wang, Xiaoyang Wang, Dongbei Li, Hong Wang, Huifang Xu, Yin Liu, Ruihua Kang, Qiong Chen, Liyang Zheng, et al. Discovery and analysis of microplastics in human bone marrow. *Journal of Hazardous Materials*, 477:135266, 2024.

[134] Benedict R. H. Turner, Matti Jubouri, Alun H. Davies, and Mark A. Sephton. Microplastics and nanoplastics: Emerging roles in atheromas, venous, and lymphatic disorders. *Phlebology*, 0(0):02683555251409989, 0. PMID: 41432031.

[135] Guangning Kou, Shuai Yao, Amin Ullah, Shuhao Fang, Erni Guo, and Yacong Bo. Polystyrene microplastics impair brown and beige adipocyte function via the gut microbiota-adipose tissue crosstalk in high-fat diet mice. *Journal of Hazardous Materials*, 492:138225, 2025.

[136] Zuo Sen Yang, Ying Long Bai, Cui Hong Jin, Jun Na, Rui Zhang, Yuan Gao, Guo Wei Pan, Ling Jun Yan, and Wei Sun. Evidence on invasion of blood, adipose tissues, nervous system and reproductive system of mice after a single oral exposure: nanoplastics versus microplastics. *Biomedical and Environmental Sciences*, 35(11):1025–1037, 2022.

[137] T. Lima, K. Bernfur, M. Vilanova, and T. Cedervall. Understanding the lipid and protein corona formation on different sized polymeric nanoparticles. *Scientific Reports*, 10:1129, 2020.

[138] Jonathan Shannahan. The biocorona: a challenge for the biomedical application of nanoparticles. *Nanotechnology reviews*, 6(4):345–353, 2017.

[139] Jacek Sikorski, Magdalena Matczuk, Marta Stepień, Karolina Ogórek, Lena Ruzik, and Maciej Jarosz. Fe3o4 spions in cancer theranostics—structure versus interactions with proteins and methods of their investigation. *Nanotechnology*, 35(21):212001, 2024.

[140] Jiayu Cao, Qing Yang, Jie Jiang, Tatenda Dalu, Aliaksei Kadushkin, Joginder Singh, Rawil Fakhrullin, Fangjun Wang, Xiaoming Cai, and Ruibin Li. Coronas of micro/nano plastics: a key determinant in their risk assessments. *Particle and Fibre Toxicology*, 19(1):55, 2022.

[141] Muhammad Junaid and Jun Wang. Interaction of micro(nano)plastics with extracellular and intracellular biomolecules in the freshwater environment. *Critical Reviews in Environmental Science and Technology*, 52(23):4241–4265, 2022.

[142] Fatima Nasser and Iseult Lynch. Secreted protein eco-corona mediates uptake and impacts of polystyrene nanoparticles on daphnia magna. *Journal of proteomics*, 137:45–51, 2016.

[143] A. F. R. M. Ramsperger, V. K. B. Narayana, W. Gross, J. Mohanraj, M. Thelakkat, A. Greiner, H. Schmalz, H. Kress, and C. Laforsch. Environmental exposure enhances the internalization of microplastic particles into cells. *Science Advances*, 6(50):eabd1211, 2020.

[144] Marianna Barbalinardo, Francesca Chiarini, Gabriella Teti, Francesca Paganelli, Elisa Mercadelli, Andrea Bartoletti, Andrea Migliori, Manuela Piazzi, Jessika Bertacchini, Paola Sena, et al. Surface charge overrides protein corona formation in determining the cytotoxicity, cellular uptake, and biodistribution of silver nanoparticles. *ACS Applied Bio Materials*, 8(6):5032–5043, 2025.

[145] Marion Schvartz, Florent Saudrais, Stephanie Devineau, Stephane Chedin, Frederic Jamme, Jocelyne Leroy, Karol Rakotozandriny, Olivier Tache, Guillaume Brotons, Serge Pin, et al. Role of the protein corona in the colloidal behavior of microplastics. *Langmuir*, 39(12):4291–4303, 2023.

[146] Hugo Brouwer, Mathias Busch, Shuo Yang, Tom Venus, Germaine Aalderink, Juan Francisco Ferrer Crespo, Aliro Villacorta, Alba Hernández, Irina Estrela-Lopis, Sjef Boeren, et al. Toxicity of true-to-life microplastics to human ipsc-derived intestinal epithelia correlates to their protein corona composition. *Journal of hazardous materials*, 495:138908, 2025.

[147] Victor Naumenko, Aleksey Nikitin, Ksenia Kapitanova, Pavel Melnikov, Stepan Vodopyanov, Anastasiia Garanina, Marat Valikhov, Artem Ilyasov, Daniil Vishnevskiy,

Aleksey Markov, et al. Intravital microscopy reveals a novel mechanism of nanoparticles excretion in kidney. *Journal of Controlled Release*, 307:368–378, 2019.

[148] Haipeng Huang, Jiaqi Hou, Mingxiao Li, Fangchao Wei, Yilie Liao, and Beidou Xi. Microplastics in the bloodstream can induce cerebral thrombosis by causing cell obstruction and lead to neurobehavioral abnormalities. *Science advances*, 11(4):eadr8243, 2025.

[149] N Joan Abbott, Adjanie AK Patabendige, Diana EM Dolman, Siti R Yusof, and David J Begley. Structure and function of the blood–brain barrier. *Neurobiology of disease*, 37(1):13–25, 2010.

[150] N Joan Abbott, Lars Rönnbäck, and Elisabeth Hansson. Astrocyte–endothelial interactions at the blood–brain barrier. *Nature reviews neuroscience*, 7(1):41–53, 2006.

[151] Hagit Sela, Hagit Cohen, Paz Elia, Raya Zach, Zeev Karpas, and Yehuda Zeiri. Spontaneous penetration of gold nanoparticles through the blood brain barrier (bbb). *Journal of nanobiotechnology*, 13(1):71, 2015.

[152] Maksymilian Nowak, Tyler D. Brown, Adam Graham, Matthew E. Helgeson, and Samir Mitragotri. Size, shape, and flexibility influence nanoparticle transport across brain endothelium under flow. *Bioengineering & Translational Medicine*, 5(2):e10153, 2020.

[153] Shuai Zha, Haitao Liu, Hengde Li, Haolan Li, Ka-Leung Wong, and Angelo Homayoun All. Functionalized nanomaterials capable of crossing the blood–brain barrier. *ACS nano*, 18(3):1820–1845, 2024.

[154] Verena Kopatz, Kevin Wen, Tibor Kovács, Alison S Keimowitz, Verena Pichler, Joachim Widder, A Dick Vethaak, Oldamur Hollóczki, and Lukas Kenner. Micro- and nanoplastics breach the blood–brain barrier (bbb): Biomolecular corona's role revealed. *Nanomaterials*, 13(8):1404, 2023.

[155] Jason Wee, Sara Sukudom, Saiuj Bhat, Matti Marklund, Niridu Jude Peiris, Camilla M Hoyos, Sanjay Patel, Sharon L Naismith, Girish Dwivedi, and Ashish Misra. The relationship between midlife dyslipidemia and lifetime incidence of dementia: A systematic review and meta-analysis of cohort studies. *Alzheimer's & Dementia: Diagnosis, Assessment & Disease Monitoring*, 15(1):e12395, 2023.

[156] Hangjia Bai, Yanliang Wu, Haini Li, Yining Zhu, Ruijie Che, Fenghe Wang, and Chaofeng Zhang. Cerebral neurotoxicity of amino-modified polystyrene nanoplastics in mice and the protective effects of functional food camellia pollen. *Science of The Total Environment*, 912:169511, 2024.

[157] Lauren Gaspar, Sydney Bartman, Giuseppe Coppotelli, and Jaime M Ross. Acute exposure to microplastics induced changes in behavior and inflammation in young and old mice. *International Journal of Molecular Sciences*, 24(15):12308, 2023.

[158] Julie C. Savage, Micaël Carrier, and Marie-Ève Tremblay. *Morphology of Microglia Across Contexts of Health and Disease*, pages 13–26. Springer New York, New York, NY, 2019.

[159] Chiang-Wen Lee, Lee-Fen Hsu, I-Lin Wu, Yung-Li Wang, Wei-Chen Chen, Yan-Jun Liu, Lu-Tang Yang, Chong-Lun Tan, Yueh-Hsia Luo, Chia-Ching Wang, et al. Exposure to polystyrene microplastics impairs hippocampus-dependent learning and memory in mice. *Journal of Hazardous Materials*, 430:128431, 2022.

[160] Yunn Me Me Paing, Yunkyung Eom, Gyeong Bae Song, Bokyung Kim, Myung Gil Choi, Sungguan Hong, and Sung Hoon Lee. Neurotoxic effects of polystyrene nanoplastics on memory and microglial activation: Insights from in vivo and in vitro studies. *Science of the Total Environment*, 924:171681, 2024.

[161] Qisheng Tang, Tianwen Li, Kezhu Chen, Xiangyang Deng, Quan Zhang, Hailiang Tang, Zhifeng Shi, Tongming Zhu, and Jianhong Zhu. Ps-nps induced neurotoxic effects in shsy-5y cells via autophagy activation and mitochondrial dysfunction. *Brain Sciences*, 12(7):952, 2022.

[162] Lorena Lopez-Suarez, Sana Al Awabdh, Xavier Coumoul, and Caroline Chauvet. The sh-sy5y human neuroblastoma cell line, a relevant in vitro cell model for investigating neurotoxicology in human: Focus on organic pollutants. *Neurotoxicology*, 92:131–155, 2022.

[163] Mackenzie M Shipley, Colleen A Mangold, and Moriah L Szpara. Differentiation of the sh-sy5y human neuroblastoma cell line. *Journal of visualized experiments: JoVE*, (108):53193, 2016.

[164] Wookbong Kwon, Daehwan Kim, Hee-Yeon Kim, Sang Won Jeong, Se-Guen Lee, Hyun-Chul Kim, Young-Jae Lee, Mi Kyung Kwon, Jun-Seong Hwang, Jee Eun Han, Jin-Kyu Park, Sung-Jun Lee, and Seong-Kyoon Choi. Microglial phagocytosis of polystyrene microplastics results in immune alteration and apoptosis in vitro and in vivo. *Science of The Total Environment*, 807:150817, 2022.

[165] Mohamed Zakaria Gouda, Elvis Genbo Xu, and Mohamed Ateia. Why pristine, aged, and real-world microplastics are all essential for environmental research. *Environmental Science & Technology*, 60(1):7–10, 2026. PMID: 41474936.

[166] Shin Lin, Yiing Lin, Joseph R. Nery, Mark A. Urich, Alessandra Breschi, Carrie A. Davis, Alexander Dobin, Christopher Zaleski, Michael A. Beer, William C. Chapman, Thomas R. Gingeras, Joseph R. Ecker, and Michael P. Snyder. Comparison of the transcriptional landscapes between human and mouse tissues. *Proceedings of the National Academy of Sciences*, 111(48):17224–17229, 2014.

[167] Hovy Ho-Wai Wong, Christina You Chien Chou, Alanna Jean Watt, and Per Jesper Sjöström. Neural circuits: Comparing mouse and human brains. *eLife*, 12:e90017, jul 2023.

[168] Diego Gomez-Nicola and V Hugh Perry. Microglial dynamics and role in the healthy and diseased brain: a paradigm of functional plasticity. *The Neuroscientist*, 21(2):169–184, 2015.

[169] Qingyun Li and Ben A Barres. Microglia and macrophages in brain homeostasis and disease. *Nature Reviews Immunology*, 18(4):225–242, 2018.

[170] Chao Gao, Jingwen Jiang, Yuyan Tan, and Shengdi Chen. Microglia in neurodegenerative diseases: Mechanism and potential therapeutic targets. *Signal Transduction and Targeted Therapy*, 8(1):359, 2023.

[171] Luca Muzio, Alice Viotti, and Gianvito Martino. Microglia in neuroinflammation and neurodegeneration: From understanding to therapy. *Frontiers in Neuroscience*, Volume 15 - 2021, 2021.

[172] Jenna R. Jambeck and Imari Walker-Franklin. The impacts of plastics' life cycle. *One Earth*, 6(6):600–606, 2023.

[173] Lourens J. J. Meijer, Tim van Emmerik, Ruud van der Ent, Christian Schmidt, and Laurent Lebreton. More than 1000 rivers account for 80% of global riverine plastic emissions into the ocean. *Science Advances*, 7(18):eaaz5803, 2021.

[174] Mohammad S Islam, Md Mizanur Rahman, Puchanee Larpruenrudee, Akbar Arsalanloo, Hamidreza Mortazavy Beni, Md Ariful Islam, YuanTong Gu, and Emilie Sauret. How microplastics are transported and deposited in realistic upper airways? *Physics of Fluids*, 35(6), 2023.

[175] Sajjad Abbasi and Andrew Turner. Human exposure to microplastics: A study in iran. *Journal of Hazardous Materials*, 403:123799, 2021.

[176] Thomas Horvatits, Matthias Tamminga, Beibei Liu, Marcial Sebode, Antonella Carambia, Lutz Fischer, Klaus Püschel, Samuel Huber, and Elke Kerstin Fischer. Microplastics detected in cirrhotic liver tissue. *eBioMedicine*, 82:104147, 2022.

[177] Guy C. Brown and Anna Vilalta. How microglia kill neurons. *Brain Research*, 1628:288–297, 2015.

[178] Geoffrey T Norris and Jonathan Kipnis. Immune cells and cns physiology: Microglia and beyond. *Journal of experimental medicine*, 216(1):60–70, 2019.

[179] Andrew Barrick, Alison J Boardwine, and Tham C Hoang. Accumulation, depuration, and potential effects of environmentally representative microplastics towards daphnia magna. *Science of The Total Environment*, 950:175384, 2024.

[180] Agilent Technologies. *Agilent Seahorse XFp Cell Mito Stress Test Kit User Guide*. Agilent Technologies, December 2024.

[181] Priscila Falagan-Lotsch, Elissa M Grzincic, and Catherine J Murphy. One low-dose exposure of gold nanoparticles induces long-term changes in human cells. *Proceedings of the National Academy of Sciences*, 113(47):13318–13323, 2016.

[182] Priscila Falagan-Lotsch and Catherine J Murphy. Network-based analysis implies critical roles of micrornas in the long-term cellular responses to gold nanoparticles. *Nanoscale*, 12(41):21172–21187, 2020.

[183] Ariyah Thomas, Joseph Marchand, Guenter D. Schwoerer, Elizabeth C. Minor, and Melissa A. Maurer-Jones. Size distributions of microplastics in the st louis estuary and western lake superior. *Environmental Science & Technology*, 58(19):8480–8489, 2024.

[184] Luís Gabriel Antão Barboza, Luís Russo Vieira, and Lúcia Guilhermino. Single and combined effects of microplastics and mercury on juveniles of the european seabass (dicentrarchus labrax): changes in behavioural responses and reduction of swimming velocity and resistance time. *Environmental pollution*, 236:1014–1019, 2018.

[185] David Boyle, Ana I Catarino, Nathaniel J Clark, and Theodore B Henry. Polyvinyl chloride (pvc) plastic fragments release pb additives that are bioavailable in zebrafish. *Environmental Pollution*, 263:114422, 2020.

[186] Leslie L Morales-Espinoza, Marina Tauche Ferreira, Cleoni Dos Santos Carvalho, Paulo Donato Frighetto, Heidi S Moraes Utsunomiya, Lino F Morales-Paredes, and Renata Fracácio. Biochemical impacts of polyethylene terephthalate microplastics and cadmium on danio rerio under environmental conditions. *Ecotoxicology*, 35(2):24, 2026.

[187] Dominic S. A. Simpson and Peter L. Oliver. Ros generation in microglia: Understanding oxidative stress and inflammation in neurodegenerative disease. *Antioxidants*, 9(8):743, 2020.

[188] Anna Podleśny-Drabiniok, Edoardo Marcora, and Alison M Goate. Microglial phagocytosis: a disease-associated process emerging from alzheimer's disease genetics. *Trends in Neurosciences*, 43(12):965–979, 2020.

[189] Javier Gutiérrez-García, Raquel Egea, Irene Barguilla, Penny Nymark, Alba García-Rodríguez, Boris Guyot, Veronique Maguer-Satta, Ricard Marcos, Laura Rubio, and Alba Hernández. Long-term exposure to real-life polyethylene terephthalate nanoplastics induces carcinogenesis in vitro. *Environmental science & technology*, 2025.

[190] J. Li, F. Huang, G. Zhang, Z. Zhang, and X. Zhang. Separation and flow cytometry analysis of microplastics and nanoplastics. *Frontiers in Chemistry*, 11:1201734, 2023.

[191] Lucas Ainé, Justine Jacquin, Colette Breysse, Catherine Colin, Jean-Michel Andanson, and Florence Delor-Jestin. Microplastics and nanoplastics detection using flow cytometry: Challenges and methodological advances with fluorescent dye application. *MethodsX*, 14:103200, 2025.

[192] Julie A. Champion, Amanda Walker, and Samir Mitragotri. Role of particle size in phagocytosis of polymeric microspheres. *Pharmaceutical Research*, 25(8):1815–1821, 2008.

[193] Christopher D Gregory and Michael P Rimmer. Extracellular vesicles arising from apoptosis: forms, functions, and applications. *The Journal of Pathology*, 260(5):592–608, 2023.

[194] Alberto Serrano-Pozo, Matthew L Mielke, Alona Muzitansky, Teresa Gómez-Isla, John H Growdon, Brian J Bacskai, Rebecca A Betensky, Matthew P Frosch, and Bradley T Hyman. Stable size distribution of amyloid plaques over the course of alzheimer disease. *Journal of Neuropathology & Experimental Neurology*, 71(8):694–701, 2012.

[195] Maksim V Baranov, Manoj Kumar, Stefano Sacanna, Shashi Thutupalli, and Geert Van den Bogaart. Modulation of immune responses by particle size and shape. *Frontiers in immunology*, 11:607945, 2021.

[196] Richard A Murray, Ane Escobar, Neus G Bastús, Patrizia Andreozzi, Victor Puntes, and Sergio E Moya. Fluorescently labelled nanomaterials in nanosafety research: Practical advice to avoid artefacts and trace unbound dye. *NanoImpact*, 9:102–113, 2018.

[197] Tiziana Tenuta, Marco P. Monopoli, JongAh Kim, Anna Salvati, Kenneth A. Dawson, Peter Sandin, and Iseult Lynch. Elution of labile fluorescent dye from nanoparticles during biological use. *PLOS ONE*, 6(10):1–6, 10 2011.

[198] Yuan-Shen Chen, Hui-Xiang Tian, Ding-Chao Rong, Luozixian Wang, Shan Chen, Jun Zeng, Heng Xu, Jie Mei, Lei-Yun Wang, Yu-Ligh Liou, et al. Ros homeostasis in cell fate, pathophysiology, and therapeutic interventions. *Molecular Biomedicine*, 6(1):1–41, 2025.

[199] Dan Li, Zongxian Ding, Kaili Du, Xiangshi Ye, and Shixue Cheng. Reactive oxygen species as a link between antioxidant pathways and autophagy. *Oxidative medicine and cellular longevity*, 2021(1):5583215, 2021.

[200] Jun Pei, Xingyu Pan, Guanghui Wei, and Yi Hua. Research progress of glutathione peroxidase family (gpx) in redoxidation. *Frontiers in pharmacology*, 14:1147414, 2023.

[201] Tsung-Hsien Chen, Hsiang-Chen Wang, Chia-Jung Chang, and Shih-Yu Lee. Mitochondrial glutathione in cellular redox homeostasis and disease manifestation. *International journal of molecular sciences*, 25(2):1314, 2024.

[202] Ondrej Zitka, Sylvie Skalickova, Jaromir Gumulec, Michal Masarik, Vojtech Adam, Jaromir Hubalek, Libuse Trnkova, Jarmila Kruseova, Tomas Eckschlager, and Rene Kizek. Redox status expressed as gsh: Gssg ratio as a marker for oxidative stress in paediatric tumour patients. *Oncology letters*, 4(6):1247–1253, 2012.

[203] Dalal Alkazemi, Abdur Rahman, and Banan Habra. Alterations in glutathione redox homeostasis among adolescents with obesity and anemia. *Scientific reports*, 11(1):3034, 2021.

[204] Ethan Knudsen, Jaxson Tadje, Carter Coggins, and Vishwanath Venketaraman. Glutathione and neurodegenerative diseases: immunopharmacological implications. *Frontiers in Pharmacology*, Volume 16 - 2025, 2026.

[205] Nurshad Ali, Jenny Katsouli, Emma L Marczylo, Timothy W Gant, Stephanie Wright, and Jorge Bernardino De La Serna. The potential impacts of micro-and-nano plastics on various organ systems in humans. *EBioMedicine*, 99, 2024.

[206] Kornelia Kadac-Czapska, Justyna Ośko, Eliza Knez, and Małgorzata Grembecka. Microplastics and oxidative stress—current problems and prospects. *Antioxidants*, 13(5):579, 2024.

[207] Bitian Zhao, Rui Liu, Shuhao Guo, Shiyu Li, Zekai Huang, Yihan Wang, Cuiping Yu, Zhijun Hou, Yuanyuan Zhang, Yanlong Zhang, et al. Large-sized polystyrene microplastics induce oxidative stress in aml12 cells. *Scientific Reports*, 15(1):26616, 2025.

[208] Anja FRM Ramsperger, Enrico Bergamaschi, Marco Panizzolo, Ivana Fenoglio, Francesco Barbero, Ruud Peters, Anna Undas, Sebastian Purker, Bernd Giese, Carina R Lalyer, et al. Nano-and microplastics: a comprehensive review on their exposure routes, translocation, and fate in humans. *NanoImpact*, 29:100441, 2023.

[209] Luís Félix, Paulo Carreira, and Francisco Peixoto. Effects of chronic exposure of naturally weathered microplastics on oxidative stress level, behaviour, and mitochondrial function of adult zebrafish (danio rerio). *Chemosphere*, 310:136895, 2023.

[210] Anatoly A Starkov. The role of mitochondria in reactive oxygen species metabolism and signaling. *Annals of the New York Academy of Sciences*, 1147(1):37–52, 2008.

[211] Nada Ahmed Selim and Andrew P Wojtovich. Mitochondrial membrane potential and compartmentalized signaling: Calcium, ros, and beyond. *Redox Biology*, page 103859, 2025.

[212] Yuji Huang, Boxuan Liang, Zhiming Li, Yizhou Zhong, Bo Wang, Bingli Zhang, Jiaxin Du, Rongyi Ye, Hongyi Xian, Weicui Min, et al. Polystyrene nanoplastic exposure induces excessive mitophagy by activating ampk/ulk1 pathway in differentiated sh-sy5y cells and dopaminergic neurons in vivo. *Particle and fibre toxicology*, 20(1):44, 2023.

[213] Siyi Lin, Hongna Zhang, Chen Wang, Xiu-Li Su, Yuanyuan Song, Pengfei Wu, Zhu Yang, Ming-Hung Wong, Zongwei Cai, and Chunmiao Zheng. Metabolomics reveal nanoplastic-induced mitochondrial damage in human liver and lung cells. *Environmental science & technology*, 56(17):12483–12493, 2022.

[214] Jiali Cheng, Gayani Nanayakkara, Ying Shao, Ramon Cueto, Luqiao Wang, William Y Yang, Ye Tian, Hong Wang, and Xiaofeng Yang. Mitochondrial proton leak plays a critical role in pathogenesis of cardiovascular diseases. *Mitochondrial dynamics in cardiovascular medicine*, pages 359–370, 2017.

[215] Huiliang Zhang, Nathan N Alder, Wang Wang, Hazel Szeto, David J Marcinek, and Peter S Rabinovitch. Reduction of elevated proton leak rejuvenates mitochondria in the aged cardiomyocyte. *Elife*, 9:e60827, 2020.

[216] Christopher F Bennett, Pedro Latorre-Muro, and Pere Puigserver. Mechanisms of mitochondrial respiratory adaptation. *Nature Reviews Molecular Cell Biology*, 23(12):817–835, 2022.

[217] Verónica Eisner, Martin Picard, and György Hajnóczky. Mitochondrial dynamics in adaptive and maladaptive cellular stress responses. *Nature cell biology*, 20(7):755–765, 2018.

[218] Boxuan Liang, Yuji Huang, Yizhou Zhong, Zhiming Li, Rongyi Ye, Bo Wang, Bingli Zhang, Hao Meng, Xi Lin, Jiaxin Du, et al. Brain single-nucleus transcriptomics highlights that polystyrene nanoplastics potentially induce parkinson's disease-like neurodegeneration by causing energy metabolism disorders in mice. *Journal of hazardous materials*, 430:128459, 2022.

[219] S. Ghosh, E. Castillo, E. S. Frias, and R. A. Swanson. Bioenergetic regulation of microglia. *Glia*, 66(6):1200–1212, 2018.

[220] Joel N Meyer, Jessica H Hartman, and Danielle F Mello. Mitochondrial toxicity. *Toxicological Sciences*, 162(1):15–23, 2018.

[221] Qi-Qiang Guo, Shan-Shan Wang, Xiao-You Jiang, Xiao-Chen Xie, Yu Zou, Jing-Wei Liu, Yang Guo, Yu-Han Li, Xi-Yan Liu, Shuang Hao, et al. Mitochondrial ros triggers mitophagy through activating the dna damage response signaling pathway. *Proceedings of the National Academy of Sciences*, 122(40):e2502841122, 2025.

[222] Ana Belen Malpartida, Matthew Williamson, Derek P. Narendra, Richard Wade-Martins, and Brent J. Ryan. Mitochondrial dysfunction and mitophagy in parkinson's disease: From mechanism to therapy. *Trends in Biochemical Sciences*, 46(4):329–343, 2021.

[223] K Palikaras, E Lionaki, and NJCD Tavernarakis. Balancing mitochondrial biogenesis and mitophagy to maintain energy metabolism homeostasis. *Cell Death & Differentiation*, 22(9):1399–1401, 2015.

[224] Igor A. Gak, Sava M. Radovic, Aleksandra R. Dukic, Marija M. Janjic, Natasa J. Stojkov-Mimic, Tatjana S. Kostic, and Silvana A. Andric. Stress triggers mitochondrial biogenesis to preserve steroidogenesis in leydig cells. *Biochimica et Biophysica Acta (BBA) - Molecular Cell Research*, 1853(10, Part A):2217–2227, 2015.

[225] Ruben Orihuela, Christopher A McPherson, and Gaylia Jean Harry. Microglial m1/m2 polarization and metabolic states. *British journal of pharmacology*, 173(4):649–665, 2016.

[226] Peng Zhang, Kosuke Watari, and Michael Karin. Innate immune cells link dietary cues to normal and abnormal metabolic regulation. *Nature immunology*, 26(1):29–41, 2025.

[227] E. D. Pozzo, C. Tremolanti, B. Costa, C. Giacomelli, V. M. Milenkovic, S. Bader, C. H. Wetzel, R. Rupprecht, S. Taliani, F. D. Settimo, and C. Martini. Microglial pro-inflammatory and anti-inflammatory phenotypes are modulated by translocator protein activation. *International Journal of Molecular Sciences*, 20(18):4467, 2019.

[228] Richard M Ransohoff. A polarizing question: do m1 and m2 microglia exist? *Nature neuroscience*, 19(8):987–991, 2016.

[229] Mathias Busch, Gerrit Bredeck, Friedrich Waag, Khosrow Rahimi, Haribaskar Ramachandran, Tobias Bessel, Stephan Barcikowski, Andreas Herrmann, Andrea Rossi, and Roel PF Schins. Assessing the nlrp3 inflammasome activating potential of a large panel of micro-and nanoplastics in thp-1 cells. *Biomolecules*, 12(8):1095, 2022.

[230] Raquel Martin-Folgar, M$^{\underline{a}}$ Carmen González-Caballero, Mónica Torres-Ruiz, Ana I Cañas-Portilla, Mercedes de Alba González, Isabel Liste, and Mónica Morales. Molecular effects of polystyrene nanoplastics on human neural stem cells. *Plos one*, 19(1):e0295816, 2024.

[231] Cristina Milillo, Eleonora Aruffo, Piero Di Carlo, Antonia Patruno, Marco Gatta, Annalisa Bruno, Melania Dovizio, Lisa Marinelli, Marilisa Pia Dimmito, Viviana Di Giacomo, et al. Polystyrene nanoplastics mediate oxidative stress, senescence, and apoptosis in a human alveolar epithelial cell line. *Frontiers in Public Health*, 12:1385387, 2024.

[232] Xiaomei Lu, Qinghua Luo, Jiahao Zhao, Ming Li, and Dandan Liu. Revealing the underlying mechanisms of nanoplastics induces neuroinflammation: From transcriptomic analysis to in vivo and in vitro validation. *Ecotoxicology and Environmental Safety*, 298:118311, 2025.

[233] Yizhe Wei, Gaofang Cao, Jianping Ma, Yanan Mi, Yiming Zhao, Leili Zhang, Bingyan Wang, Huanliang Liu, Kang Li, Yue Shi, et al. Polystyrene nanoplastics induce dna damage and excitotoxicity in whole-brain organoids: The role of the tlr9/myd88 pathway. *Toxics*, 14(1):5, 2025.

[234] Daniel Mihai Teleanu, Adelina-Gabriela Niculescu, Iulia Ioana Lungu, Crina Ioana Radu, Oana Vladâcenco, Eugenia Roza, Bogdan Costăchescu, Alexandru Mihai Grumezescu, and Raluca Ioana Teleanu. An overview of oxidative stress, neuroinflammation, and neurodegenerative diseases. *International journal of molecular sciences*, 23(11):5938, 2022.

[235] IF Gosselink, P Leonhardt, EM Höppener, R Smelt, MJ Drittij, M Davigo, GGH van den Akker, IM Kooter, TJM Welting, FJ van Schooten, et al. Size-and polymer-dependent toxicity of amorphous environmentally relevant micro-and nanoplastics in human bronchial epithelial cells. *Microplastics and Nanoplastics*, 5(1):19, 2025.

[236] Qianwen Ma, Jialin Lei, Yanting Pang, Yu Shen, and Ting Zhang. Neurotoxicity of micro-and nanoplastics: A comprehensive review of central nervous system impacts. *Environment & Health*, 2025.

[237] Mohammad Awashra and Piotr Młynarz. The toxicity of nanoparticles and their interaction with cells: an in vitro metabolomic perspective. *Nanoscale Advances*, 5(10):2674–2723, 2023.

[238] Jingkun Jiang, Günter Oberdörster, Alison Elder, Robert Gelein, Pamela Mercer, and Pratim Biswas. Does nanoparticle activity depend upon size and crystal phase? *Nanotoxicology*, 2(1):33–42, 2008.

[239] L. M. A. Martin, N. Gan, E. Wang, M. Merrill, and W. Xu. Materials, surfaces, and interfacial phenomena in nanoplastics toxicology research. *Environmental Pollution*, 292(Pt B):118442, 2022.

[240] Xiaomei Lu, Qinghua Luo, Jiahao Zhao, Ming Li, and Dandan Liu. Revealing the underlying mechanisms of nanoplastics induces neuroinflammation: From transcriptomic analysis to in vivo and in vitro validation. *Ecotoxicology and Environmental Safety*, 298:118311, 2025.

[241] Joanna Chwiej, Mateusz Wytrwal, Katarzyna Papacz, et al. Tracing micro and nanoplastics toxicity in human pulmonary fibroblasts through integrated raman and transcriptomic analyses. *Scientific Reports*, 15:39459, 2025.

[242] Philip Ewels, Måns Magnusson, Sverker Lundin, and Max Käller. Multiqc: summarize analysis results for multiple tools and samples in a single report. *Bioinformatics*, 32(19):3047–3048, 06 2016.

[243] Anthony M. Bolger, Marc Lohse, and Bjoern Usadel. Trimmomatic: a flexible trimmer for illumina sequence data. *Bioinformatics*, 30(15):2114–2120, 04 2014.

[244] Daehwan Kim, Joseph M. Paggi, Chanhee Park, Christopher Bennett, and Steven L. Salzberg. Graph-based genome alignment and genotyping with hisat2 and hisat-genotype. *Nature Biotechnology*, 37(8):907–915, 2019.

[245] Adam Frankish, Sílvia Carbonell-Sala, Mark Diekhans, Irwin Jungreis, Jane E Loveland, Jonathan M Mudge, Cristina Sisu, James C Wright, Carme Arnan, If Barnes, Abhimanyu Banerjee, Ruth Bennett, Andrew Berry, Alexandra Bignell, Carles Boix, Ferriol Calvet, Daniel Cerdán-Vélez, Fiona Cunningham, Claire Davidson, Sarah Donaldson, Cagatay Dursun, Reham Fatima, Stefano Giorgetti, Carlos Garcıa Giron, Jose Manuel Gonzalez, Matthew Hardy, Peter W Harrison, Thibaut Hourlier, Zoe Hollis, Toby Hunt, Benjamin James, Yunzhe Jiang, Rory Johnson, Mike Kay, Julien Lagarde, Fergal J Martin, Laura Martínez Gómez, Surag Nair, Pengyu Ni, Fernando Pozo, Vivek Ramalingam, Magali Ruffier, Bianca M Schmitt, Jacob M Schreiber, Emily Steed, Marie-Marthe Suner, Dulika Sumathipala, Irina Sycheva, Barbara Uszczynska-Ratajczak, Elizabeth Wass, Yucheng T Yang, Andrew Yates, Zahoor Zafrulla, Jyoti S Choudhary, Mark Gerstein, Roderic Guigo, Tim J P Hubbard, Manolis Kellis, Anshul Kundaje, Benedict Paten, Michael L Tress, and Paul Flicek. Gencode: reference annotation for the human and mouse genomes in 2023. *Nucleic Acids Research*, 51(D1):D942–D949, 11 2022.

[246] Mihaela Pertea, Geo M. Pertea, Corina M. Antonescu, Tsung-Cheng Chang, Joshua T. Mendell, and Steven L. Salzberg. Stringtie enables improved reconstruction of a transcriptome from rna-seq reads. *Nature Biotechnology*, 33(3):290–295, 2015.

[247] Aravind Subramanian, Pablo Tamayo, Vamsi K. Mootha, Sayan Mukherjee, Benjamin L. Ebert, Michael A. Gillette, Amanda Paulovich, Scott L. Pomeroy, Todd R. Golub, Eric S. Lander, and Jill P. Mesirov. Gene set enrichment analysis: A knowledge-based approach for interpreting genome-wide expression profiles. *Proceedings of the National Academy of Sciences*, 102(43):15545–15550, 2005.

[248] V. K. Mootha, C. M. Lindgren, K. F. Eriksson, and et al. Pgc-1α-responsive genes involved in oxidative phosphorylation are coordinately downregulated in human diabetes. *Nature Genetics*, 34:267–273, 2003.

[249] M. Milacic, D. Beavers, P. Conley, C. Gong, M. Gillespie, J. Griss, R. Haw, B. Jassal, L. Matthews, B. May, R. Petryszak, E. Ragueneau, K. Rothfels, C. Sevilla, V. Shamovsky, R. Stephan, K. Tiwari, T. Varusai, J. Weiser, A. Wright, G. Wu, L. Stein, H. Hermjakob, and P. D'Eustachio. The reactome pathway knowledgebase 2024. *Nucleic Acids Research*, 2024.

[250] Ruth Isserlin, Daniele Merico, Veronique Voisin, and Gary D Bader. Enrichment map–a cytoscape app to visualize and explore omics pathway enrichment results. *F1000Research*, 3:141, 2014.

[251] Vera N De Ruijter, Paula E Redondo-Hasselerharm, Todd Gouin, and Albert A Koelmans. Quality criteria for microplastic effect studies in the context of risk assessment: a critical review. *Environmental Science & Technology*, 54(19):11692–11705, 2020.

[252] Natalia P Ivleva. Chemical analysis of microplastics and nanoplastics: challenges, advanced methods, and perspectives. *Chemical reviews*, 121(19):11886–11936, 2021.

[253] Otmar Schmid and Tobias Stoeger. Surface area is the biologically most effective dose metric for acute nanoparticle toxicity in the lung. *Journal of Aerosol Science*, 99:133–143, 2016.

[254] Z. Woolf, T. J. Stevenson, K. Lee, and et al. In vitro models of microglia: a comparative study. *Scientific Reports*, 15:15621, 2025.

[255] Michael I. Love, Wolfgang Huber, and Simon Anders. Moderated estimation of fold change and dispersion for rna-seq data with deseq2. *Genome Biology*, 15(12):550, 2014.

[256] Adam J Freitag, Amanda J Rogers, Jose E Tabora, and Daniel S Treitler. Use of bayesian modeling for risk assessment and robustness evaluation. *Organic Process Research & Development*, 28(2):511–523, 2024.

[257] Maksim V Baranov, Manoj Kumar, Stefano Sacanna, Shashi Thutupalli, and Geert Van den Bogaart. Modulation of immune responses by particle size and shape. *Frontiers in immunology*, 11:607945, 2021.

[258] Preeti Sharma, Anjali Vijaykumar, Jayashree Vijaya Raghavan, Supriya Rajendra Rananaware, Alakesh Alakesh, Janhavi Bodele, Junaid Ur Rehman, Shivani Shukla, Virta Wagde, Savitha Nadig, et al. Particle uptake driven phagocytosis in macrophages and neutrophils enhances bacterial clearance. *Journal of Controlled Release*, 343:131–141, 2022.

[259] Vibhu Prasad. Transmission of unfolded protein response—a regulator of disease progression, severity, and spread in virus infections. *MBio*, 16(2):e03522–24, 2025.

[260] E. L. Spaulding, T. J. Hines, P. Bais, A. L. D. Tadenev, R. Schneider, D. Jewett, B. Pattavina, S. L. Pratt, K. H. Morelli, M. G. Stum, D. P. Hill, C. Gobet, M. Pipis, M. M. Reilly, M. J. Jennings, R. Horvath, Y. Bai, M. E. Shy, B. Alvarez-Castelao, E. M. Schuman, L. P. Bogdanik, E. Storkebaum, and R. W. Burgess. The integrated stress response contributes to trna synthetase–associated peripheral neuropathy. *Science*, 373(6559):1156–1161, 2021.

[261] Lena Ilan, Farhat Osman, Lise Sarah Namer, Einav Eliahu, Smadar Cohen-Chalamish, Yitzhak Ben-Asouli, Yona Banai, and Raymond Kaempfer. Pkr activation and eif2α phosphorylation mediate human globin mrna splicing at spliceosome assembly. *Cell Research*, 27(5):688–704, 2017.

[262] Christopher K Revell, Oliver E Jensen, Tom Shearer, Yinhui Lu, David F Holmes, and Karl E Kadler. Collagen fibril assembly: New approaches to unanswered questions. *Matrix biology plus*, 12:100079, 2021.

[263] Elizabeth G. Canty and Karl E. Kadler. Procollagen trafficking, processing and fibrillogenesis. *Journal of Cell Science*, 118(7):1341–1353, 04 2005.

[264] Filipa C Simões, Thomas J Cahill, Amy Kenyon, Daria Gavriouchkina, Joaquim M Vieira, Xin Sun, Daniela Pezzolla, Christophe Ravaud, Eva Masmanian, Michael Weinberger, et al. Macrophages directly contribute collagen to scar formation during zebrafish heart regeneration and mouse heart repair. *Nature communications*, 11(1):600, 2020.

[265] Anne Mette H Larsen, Dorota E Kuczek, Adrija Kalvisa, Majken S Siersbæk, Marie-Louise Thorseth, Astrid Z Johansen, Marco Carretta, Lars Grøntved, Ole Vang, and Daniel H Madsen. Collagen density modulates the immunosuppressive functions of macrophages. *The Journal of Immunology*, 205(5):1461–1472, 09 2020.

[266] Anna Yui and Madeleine J Oudin. The rigidity connection: matrix stiffness and its impact on cancer progression. *Cancer research*, 84(7):958–960, 2024.

[267] Daniela De Martino and Jose Javier Bravo-Cordero. Collagens in cancer: structural regulators and guardians of cancer progression. *Cancer research*, 83(9):1386–1392, 2023.

[268] Eisuke Ueshima, Masashi Fujimori, Hiroshi Kodama, Diane Felsen, Jie Chen, Jeremy C. Durack, Stephen B. Solomon, Jonathan A. Coleman, and Govindarajan

Srimathveeravalli. Macrophage-secreted tgf-1 contributes to fibroblast activation and ureteral stricture after ablation injury. *American Journal of Physiology-Renal Physiology*, 317(1):F52–F64, 2019. PMID: 31017012.

[269] Juanjuan Wang, Ya Wang, Yuqing Liu, and Rongcun Yang. Spp1+ macrophages in tumor immunosuppression: mechanisms and therapeutic implications. *Frontiers in Immunology*, 16:1711015, 2025.

[270] Jerome Rossert and Benoit de Crombrugghe. Chapter 12 - type i collagen: Structure, synthesis, and regulation. In John P. Bilezikian, Lawrence G. Raisz, and Gideon A. Rodan, editors, *Principles of Bone Biology (Second Edition)*, pages 189–XVIII. Academic Press, San Diego, second edition edition, 2002.

[271] Daniel C Roy and Denise C Hocking. Recombinant fibronectin matrix mimetics specify integrin adhesion and extracellular matrix assembly. *Tissue Engineering Part A*, 19(3-4):558–570, 2013.

[272] Maria Benito-Jardón, Sarah Klapproth, Irene Gimeno-LLuch, Tobias Petzold, Mitasha Bharadwaj, Daniel J Müller, Gabriele Zuchtriegel, Christoph A Reichel, and Mercedes Costell. The fibronectin synergy site re-enforces cell adhesion and mediates a crosstalk between integrin classes. *Elife*, 6:e22264, 2017.

[273] Jane Sottile, Feng Shi, Inna Rublyevska, Hou-Yu Chiang, Joseph Lust, and Jennifer Chandler. Fibronectin-dependent collagen i deposition modulates the cell response to fibronectin. *American Journal of Physiology-Cell Physiology*, 293(6):C1934–C1946, 2007. PMID: 17928541.

[274] Vijaykumar S Meli, Hamza Atcha, Praveen Krishna Veerasubramanian, Raji R Nagalla, Thuy U Luu, Esther Y Chen, Christian F Guerrero-Juarez, Kosuke Yamaga, William Pandori, Jessica Y Hsieh, et al. Yap-mediated mechanotransduction tunes the macrophage inflammatory response. *Science advances*, 6(49):eabb8471, 2020.

[275] Vijaykumar S Meli, Andrew T Rowley, Praveen K Veerasubramanian, Sara E Heedy, Wendy F Liu, and Szu-Wen Wang. Modulation of stiffness-dependent macrophage inflammatory responses by collagen deposition. *ACS Biomaterials Science & Engineering*, 10(4):2212–2223, 2024.

[276] Benjamin Kroeger, Samuel A. Manning, Varshini Mohan, Jieqiong Lou, Guizhi Sun, Sara Lamont, Alex J. McCann, Mathias Francois, Jose M. Polo, Elizabeth Hinde, and Kieran F. Harvey. Hippo signaling regulates the nuclear behavior and dna binding times of yap and tead to control transcription. *Science Advances*, 11(30):eadw4974, 2025.

[277] Anna L. Kersey, Daniel Y. Cheng, Kaivalya A. Deo, Christina R. Dubell, Ting-Ching Wang, Manish K. Jaiswal, Min Hee Kim, Aparna Murali, Sarah E. Hargett, Sumana Mallick, Tanmay P. Lele, Irtisha Singh, and Akhilesh K. Gaharwar. Stiffness assisted cell-matrix remodeling trigger 3d mechanotransduction regulatory programs. *Biomaterials*, 306:122473, 2024.

[278] MatWeb. Polystyrene (general purpose) material properties datasheet, n.d.

[279] Mohammad Khoonkari, Dong Liang, Marleen Kamperman, Frank AE Kruyt, and Patrick van Rijn. Physics of brain cancer: Multiscale alterations of glioblastoma cells under extracellular matrix stiffening. *Pharmaceutics*, 14(5):1031, 2022.

[280] Anna L. Kersey, Daniel Y. Cheng, Kaivalya A. Deo, Christina R. Dubell, Ting-Ching Wang, Manish K. Jaiswal, Min Hee Kim, Aparna Murali, Sarah E. Hargett, Sumana Mallick, Tanmay P. Lele, Irtisha Singh, and Akhilesh K. Gaharwar. Stiffness assisted cell-matrix remodeling trigger 3d mechanotransduction regulatory programs. *Biomaterials*, 306:122473, 2024.

[281] Aaron Lee, Mauro Sousa de Almeida, Daela Milinkovic, Dedy Septiadi, Patricia Taladriz-Blanco, Céline Loussert-Fonta, Sandor Balog, Amelie Bazzoni, Barbara Rothen-Rutishauser, and Alke Petri-Fink. Substrate stiffness reduces particle uptake by epithelial cells and macrophages in a size-dependent manner through mechanoregulation. *Nanoscale*, 14:15141–15155, 2022.

[282] Miguel Angel Rubio Gomez and Michael Ibba. Aminoacyl-trna synthetases. *Rna*, 26(8):910–936, 2020.

[283] Xuebing Chen, Luyao Xu, Qianling Chen, Shuying Su, Jingshen Zhuang, and Dongfang Qiao. Polystyrene micro-and nanoparticles exposure induced anxiety-like behaviors, gut microbiota dysbiosis and metabolism disorder in adult mice. *Ecotoxicology and Environmental Safety*, 259:115000, 2023.

[284] Yuxuan Luo, Zheng Zhang, Xuewei Li, Zile Zhuang, Yihan Li, Xinya Wang, Changqing Liao, Lujia Chen, Qizhi Luo, and Xuncai Chen. Reproductive toxicity and transgenerational effects of co-exposure to polystyrene microplastics and arsenic in zebrafish. *Comparative Biochemistry and Physiology Part C: Toxicology & Pharmacology*, 290:110134, 2025.

[285] Yan-Kun Zhang, Bing-Kun Yang, Chun-Nuan Zhang, Shi-Xiao Xu, and Ping Sun. Effects of polystyrene microplastics acute exposure in the liver of swordtail fish (xiphophorus helleri) revealed by lc-ms metabolomics. *Science of the Total Environment*, 850:157772, 2022.

[286] Nir Gonen, Anatoly Meller, Niv Sabath, and Reut Shalgi. Amino acid biosynthesis regulation during endoplasmic reticulum stress is coupled to protein expression demands. *IScience*, 19:204–213, 2019.

[287] Bo-Jhih Guan, Dawid Krokowski, Mithu Majumder, Christine L Schmotzer, Scot R Kimball, William C Merrick, Antonis E Koromilas, and Maria Hatzoglou. Translational control during endoplasmic reticulum stress beyond phosphorylation of the translation initiation factor eif2α. *Journal of Biological Chemistry*, 289(18):12593–12611, 2014.

[288] Yanhong Chen, Yingqi Liu, Yanli Li, Chenjuan Yao, Jianhua Qu, Juan Tang, Gang Chen, and Yu Han. Acute exposure to polystyrene nanoplastics induces unfolded

protein response and global protein ubiquitination in lungs of mice. *Ecotoxicology and Environmental Safety*, 280:116580, 2024.

[289] Zhanhang Wang, Shujuan Liu, Zefang Cheng, Ganggang Xu, Fu Li, Qiqi Bu, Lei Zhang, Yuxuan Song, and Xiaopeng An. Endoplasmic reticulum stress exacerbates microplastics-induced toxicity in animal cells. *Food Research International*, 175:113818, 2024.

[290] Sunghoon Kim, Sungyong You, and Daehee Hwang. Aminoacyl-trna synthetases and tumorigenesis: More than housekeeping. *Nature Reviews Cancer*, 11(10):708–718, 2011.

[291] Yong-Wan Kim, ChangHyuk Kwon, Juinn-Lin Liu, Se Hoon Kim, and Sunghoon Kim. Cancer association study of aminoacyl-trna synthetase signaling network in glioblastoma. 2012.

[292] Q. Wang, A. M. Bode, and T. Zhang. Targeting cdk1 in cancer: mechanisms and implications. *npj Precision Oncology*, 7:58, 2023.

[293] Shoukai Yu. Overexpression of ska complex is associated with poor prognosis in gliomas. *Frontiers in Neurology*, 12:755681, 2022.

[294] Bisong Zhu, Lin Qi, Sulai Liu, Wentao Liu, Zhenyu Ou, Minfeng Chen, Longfei Liu, Xiongbing Zu, Jun Wang, and Yuan Li. Clasp2 is involved in the emt and early progression after transurethral resection of the bladder tumor. *BMC cancer*, 17(1):105, 2017.

[295] Bowen Xie, Shuangyan Wang, Nian Jiang, and Jian Jian Li. Cyclin b1/cdk1-regulated mitochondrial bioenergetics in cell cycle progression and tumor resistance. *Cancer letters*, 443:56–66, 2019.

[296] Xizhao Wang, Yu Zeng, Mingfeng Zhou, Xian Zhang, Anqi Xu, Jie Lin, Zhiyong Wu, Cheng Xie, Jie Luo, Shengfeng Ding, et al. Ska1 promotes malignant phenotype and progression of glioma via multiple signaling pathways. *Cancer cell international*, 19(1):324, 2019.

[297] Su Jin Kang, Young Joon Lee, Eun-Kyung Lee, and Mi-Kyoung Kwak. Silver nanoparticles-mediated g2/m cycle arrest of renal epithelial cells is associated with nrf2-gsh signaling. *Toxicology letters*, 211(3):334–341, 2012.

[298] Maqsood A Siddiqui, Quaiser Saquib, Maqusood Ahamed, Nida N Farshori, Javed Ahmad, Rizwan Wahab, Shams T Khan, Hisham A Alhadlaq, Javed Musarrat, Abdulaziz A Al-Khedhairy, et al. Molybdenum nanoparticles-induced cytotoxicity, oxidative stress, g2/m arrest, and dna damage in mouse skin fibroblast cells (l929). *Colloids and Surfaces B: Biointerfaces*, 125:73–81, 2015.

[299] Hongmei Chang, Qianqian Wang, Xiaojia Meng, Xinyu Chen, Yaxin Deng, Li Li, Yaqian Yang, Guanling Song, and Huaimiao Jia. Effect of titanium dioxide nanoparticles on mammalian cell cycle in vitro: A systematic review and meta-analysis. *Chemical Research in Toxicology*, 35(9):1435–1456, 2022. PMID: 35998370.

[300] Vijaykumar S Meli, Hamza Atcha, Praveen Krishna Veerasubramanian, Raji R Nagalla, Thuy U Luu, Esther Y Chen, Christian F Guerrero-Juarez, Kosuke Yamaga, William Pandori, Jessica Y Hsieh, et al. Yap-mediated mechanotransduction tunes the macrophage inflammatory response. *Science advances*, 6(49):eabb8471, 2020.

[301] Xue Fang, Haiying Jia, Shaoshan Pan, Qian Liu, Qian Wang, Ye Feng, Weiping Ding, and Tianzhi Luo. Matrix stiffness regulates interleukin-10 secretion in human microglia (hmc3) via yap-mediated mechanotransduction. *Cell Biochemistry and Function*, 43(3):e70061, 2025.

[302] Libin Chen, Xintong Jin, Jian Ma, Bo Xiang, and Xiayu Li. Yap at the progression of inflammation. *Frontiers in cell and developmental biology*, 11:1204033, 2023.

[303] Joan K Riley, Kiyoshi Takeda, Shizuo Akira, and Robert D Schreiber. Interleukin-10 receptor signaling through the jak-stat pathway: requirement for two distinct receptor-derived signals for anti-inflammatory action. *Journal of Biological Chemistry*, 274(23):16513–16521, 1999.

[304] D S Finbloom and K D Winestock. Il-10 induces the tyrosine phosphorylation of tyk2 and jak1 and the differential assembly of stat1 and stat3 complexes in human t cells and monocytes. *The Journal of Immunology*, 155(3):1079–1090, 08 1995.

[305] Lara Campana, Philip J Starkey Lewis, Antonella Pellicoro, Rebecca L Aucott, Janet Man, Eoghan O'Duibhir, Sarah E Mok, Sofia Ferreira-Gonzalez, Eilidh Livingstone, Stephen N Greenhalgh, et al. The stat3–il-10–il-6 pathway is a novel regulator of macrophage efferocytosis and phenotypic conversion in sterile liver injury. *The Journal of Immunology*, 200(3):1169–1187, 2018.

[306] Claudia Niemand, Ariane Nimmesgern, Serge Haan, Patrick Fischer, Fred Schaper, Rolf Rossaint, Peter C Heinrich, and Gerhard Muller-Newen. Activation of stat3 by il-6 and il-10 in primary human macrophages is differentially modulated by suppressor of cytokine signaling 31. *The Journal of Immunology*, 170(6):3263–3272, 03 2003.

[307] Shankar Subramanian Iyer and Gehong Cheng. Role of interleukin 10 transcriptional regulation in inflammation and autoimmune disease. *Critical Reviews™ in Immunology*, 32(1), 2012.

[308] Hai-Jun Gan, Shan Chen, Ke Yao, Xin-Ying Lin, Albert L Juhasz, Dongmei Zhou, and Hong-Bo Li. Simulated microplastic release from cutting boards and evaluation of intestinal inflammation and gut microbiota in mice. *Environmental Health Perspectives*, 133(3-4):047004, 2025.

[309] Xiaoxia Wang, Xiao-Min Ren, Huan He, Fan Li, Kunqian Liu, Fenqing Zhao, Huixiang Hu, Pingping Zhang, Bin Huang, and Xuejun Pan. Cytotoxicity and pro-inflammatory effect of polystyrene nano-plastic and micro-plastic on raw264. 7 cells. *Toxicology*, 484:153391, 2023.

[310] Chiara Porro, Antonia Cianciulli, and Maria Antonietta Panaro. The regulatory role of il-10 in neurodegenerative diseases. *Biomolecules*, 10(7):1017, 2020.

[311] Chao Gao, Jingwen Jiang, Yuyan Tan, and Shengdi Chen. Microglia in neurodegenerative diseases: mechanism and potential therapeutic targets. *Signal Transduction and Targeted Therapy*, 8(1):359, 2023.

[312] Simone Bido, Melania Nannoni, Sharon Muggeo, Diana Gambarè, Giorgia Ruffini, Edoardo Bellini, Laura Passeri, Silvia Iaia, Mirko Luoni, Martino Provinciali, Serena Gea Giannelli, Francesca Giannese, Dejan Lazarevic, Silvia Gregori, and Vania Broccoli. Microglia-specific ¡i¿il-10¡/i¿ gene delivery inhibits neuroinflammation and neurodegeneration in a mouse model of parkinson’s disease. *Science Translational Medicine*, 16(761):eadm8563, 2024.

[313] Junhyuk Lee, Hyeonji Jang, Boyun Kim, and Jewon Jung. Comparative metabolomic approaches to nanoplastic toxicity in mammalian and aquatic systems. *International Journal of Molecular Sciences*, 27(1):50, 2025.

[314] C. C. Fleischer and C. K. Payne. Nanoparticle-cell interactions: molecular structure of the protein corona and cellular outcomes. *Accounts of Chemical Research*, 47(8):2651–2659, 2014.

[315] Parwathy Chandran, Jim E. Riviere, and Nancy A. Monteiro-Riviere. Surface chemistry of gold nanoparticles determines the biocorona composition impacting cellular uptake, toxicity and gene expression profiles in human endothelial cells. *Nanotoxicology*, 11(4):507–519, 2017. PMID: 28420299.

[316] Filippo Bertoli, David Garry, Marco P. Monopoli, Anna Salvati, and Kenneth A. Dawson. The intracellular destiny of the protein corona: A study on its cellular internalization and evolution. *ACS Nano*, 10(11):10471–10479, 2016. PMID: 27797479.

[317] Qin Ji, Colin Blackadar, Atta C. Y. Chang, Jamie L. Y. Wu, Shrey Sindhwani, and Warren C. W. Chan. Cancer cells degrade the nanoparticle protein corona for biosynthesis. *Journal of the American Chemical Society*, 148(9):9478–9493, 2026. PMID: 41739600.

[318] Juan-Hua Quan, Fei Fei Gao, Mina Lee, Jae-Min Yuk, Guang-Ho Cha, Jia-Qi Chu, Hao Wang, and Young-Ha Lee. Involvement of endoplasmic reticulum stress response and ire1-mediated ask1/jnk/mcl-1 pathways in silver nanoparticle-induced apoptosis of human retinal pigment epithelial cells. *Toxicology*, 442:152540, 2020.

[319] Rui Chen, Lingling Huo, Xiaofei Shi, Ru Bai, Zhenjiang Zhang, Yuliang Zhao, Yanzhong Chang, and Chunying Chen. Endoplasmic reticulum stress induced by zinc

oxide nanoparticles is an earlier biomarker for nanotoxicological evaluation. *ACS Nano*, 8(3):2562–2574, 2014. PMID: 24490819.

[320] Ronja Schirrmann, Michael Erkelenz, Kim Lamers, Oliver Sritharan, Milen Nachev, Bernd Sures, Sebastian Schlücker, and Sven Brandau. Gold nanorods induce endoplasmic reticulum stress and autocrine inflammatory activation in human neutrophils. *ACS Nano*, 16(7):11011–11026, 2022. PMID: 35737452.

[321] Caitlin W Lehman, Amy Smith, Jamie Kelly, Jonathan L Jacobs, Jonathan D Dinman, and Kylene Kehn-Hall. Egr1 upregulation during encephalitic viral infections contributes to inflammation and cell death. *Viruses*, 14(6):1210, 2022.

[322] Hong Peng, Lu Zhang, Yufen Tang, Peng Huang, Senlin Luo, Zhou She, Yuqiong Chen, Jinwen Luo, Wangxin Duan, Lingjuan Liu, et al. Exploring ptx3: a promising diagnostic marker and therapeutic target in neurology. *Gene*, page 149724, 2025.

[323] Paolo R Saraceni, Andrea Miccoli, Adeola Bada, Anna Rita Taddei, Marco Mazzonna, Anna Maria Fausto, Giuseppe Scapigliati, and Simona Picchietti. Polystyrene nanoplastics as an ecotoxicological hazard: cellular and transcriptomic evidences on marine and freshwater in vitro teleost models. *Science of the Total Environment*, 934:173159, 2024.

[324] Priscila Falagan-Lotsch and Catherine J Murphy. Network-based analysis implies critical roles of micrornas in the long-term cellular responses to gold nanoparticles. *Nanoscale*, 12(41):21172–21187, 2020.

[325] Amjad Ali Khan, Khaled S Allemailem, Ahmad Almatroudi, Saleh A Almatroodi, Ali Mahzari, Mohammed A Alsahli, and Arshad Husain Rahmani. Endoplasmic reticulum stress provocation by different nanoparticles: an innovative approach to manage the cancer and other common diseases. *Molecules*, 25(22):5336, 2020.

[326] Luna Bridgeman, Alessandra Cimbalo, David López-Rodríguez, David Pamies, and Massimo Frangiamone. Exploring toxicological pathways of microplastics and nanoplastics: Insights from animal and cellular models. *Journal of hazardous materials*, 490:137795, 2025.

[327] Qiumei Wu, Chao Liu, Dan Liu, Yougang Wang, Haomin Qi, Xudong Liu, Yuchao Zhang, Haiyu Chen, Yan Zeng, and Jinquan Li. Polystyrene nanoplastics-induced lung apoptosis and ferroptosis via ros-dependent endoplasmic reticulum stress. *Science of the Total Environment*, 912:169260, 2024.

[328] Mukundh N. Balasubramanian, Elizabeth A. Butterworth, and Michael S. Kilberg. Asparagine synthetase: regulation by cell stress and involvement in tumor biology. *American Journal of Physiology-Endocrinology and Metabolism*, 304(8):E789–E799, 2013. PMID: 23403946.

[329] Yonghe Ma, Jamie Harris, Ping Li, Chengfei Jiang, Hang Sun, and Haiming Cao. An integrative transcriptome subtraction strategy to identify human lncrnas that specifically

play a role in activation of human hepatic stellate cells. *Non-coding RNA*, 10(3):34, 2024.

[330] Hironori Katoh, Amane Harada, Kazutoshi Mori, and Manabu Negishi. Socius is a novel rnd gtpase-interacting protein involved in disassembly of actin stress fibers. *Molecular and cellular biology*, 22(9):2952–2964, 2002.

[331] Meghana Gupta, Elena Kamynina, Samantha Morley, Stacey Chung, Nora Muakkassa, Hong Wang, Shayna Brathwaite, Gaurav Sharma, and Danny Manor. Plekhg4 is a novel dbl family guanine nucleotide exchange factor protein for rho family gtpases. *Journal of Biological Chemistry*, 288(20):14522–14530, 2013.

[332] Steven W Plouffe. Characterization of hippo pathway regulation and the physiological implications of itsdownstream effectors yap and taz.

[333] Xiaobin Ren, Lei Li, Jianhua Wu, Ken Lin, Yongwen He, and Li Bian. Pdgf-bb regulates the transformation of fibroblasts into cancer-associated fibroblasts via the lncrna lurap1l-as1/lurap1l/ikk/iκb/nf-κb signaling pathway. *Oncology Letters*, 22(1):537, 2021.

[334] Adam Cunningham, Emma Barrett, Sebastian Risch, Peter HU Lee, Chan Lee, Abhay Moghekar, Prabir Patra, and Joon W Shim. Nfκb1: a common biomarker linking alzheimer's and parkinson's disease pathology. *Frontiers in Neuroscience*, 19:1589857, 2025.

[335] Barbara Kaltschmidt, Laureen P Helweg, Johannes FW Greiner, and Christian Kaltschmidt. Nf-κb in neurodegenerative diseases: Recent evidence from human genetics. *Frontiers in molecular neuroscience*, 15:954541, 2022.

[336] Aleksandar Florentinus-Mefailoski, Peter Bowden, Philip Scheltens, et al. The plasma peptides of alzheimer's disease. *Clinical Proteomics*, 18:17, 2021.

[337] Masaru Katoh. Characterization of kif12 gene in silico. *Oncology Reports*, 13(2):367–370, 2005. PMID: 15643526.

[338] GeneCards. Ensg00000258728 gene - novel protein (galt-il11ra readthrough), 2026. Database entry.

[339] Lars Vereecke, Rudi Beyaert, and Geert van Loo. The ubiquitin-editing enzyme a20 (tnfaip3) is a central regulator of immunopathology. *Trends in Immunology*, 30(8):383–391, 2009.

[340] Junjie Zhou, Manli Hu, Meiling He, Xiaoming Wang, Dating Sun, Yongping Huang, Xu Cheng, Jiajun Fu, Jie Cai, Tengfei Ma, Song Tian, Yufeng Hu, Fengjiao Hu, Dan Liu, Yanqi He, Lanlan Yan, Zhi-Gang She, Xiao-Jing Zhang, Yan-Xiao Ji, Hui Liu, Hongliang Li, Hailong Yang, and Peng Zhang. Tnfaip3 interacting protein 3 is an activator of hippo-yap signaling protecting against hepatic ischemia/reperfusion injury. *Hepatology*, 74(4):2133–2153, 2021.

[341] Soudeh Ghafouri-Fard, Sara Ahmadi Teshnizi, Bashdar Mahmud Hussen, Mohammad Taheri, and Guive Sharifi. A review on the role of ndrg1 in different cancers. *Molecular Biology Reports*, 50(7):6251–6264, 2023.

[342] Concetta Saponaro, Nicola Gammaldi, Viviana Cavallo, Maria Antonieta Ramírez-Morales, Francesco Alfredo Zito, Margherita Sonnessa, Francesco Vari, Ilaria Serra, Simona De Summa, Anna Maria Giudetti, et al. Insight into the regulation of ndrg1 expression. *International Journal of Molecular Sciences*, 26(8):3582, 2025.

Appendices

Appendix A

Supplemental Figures for Chapter 2

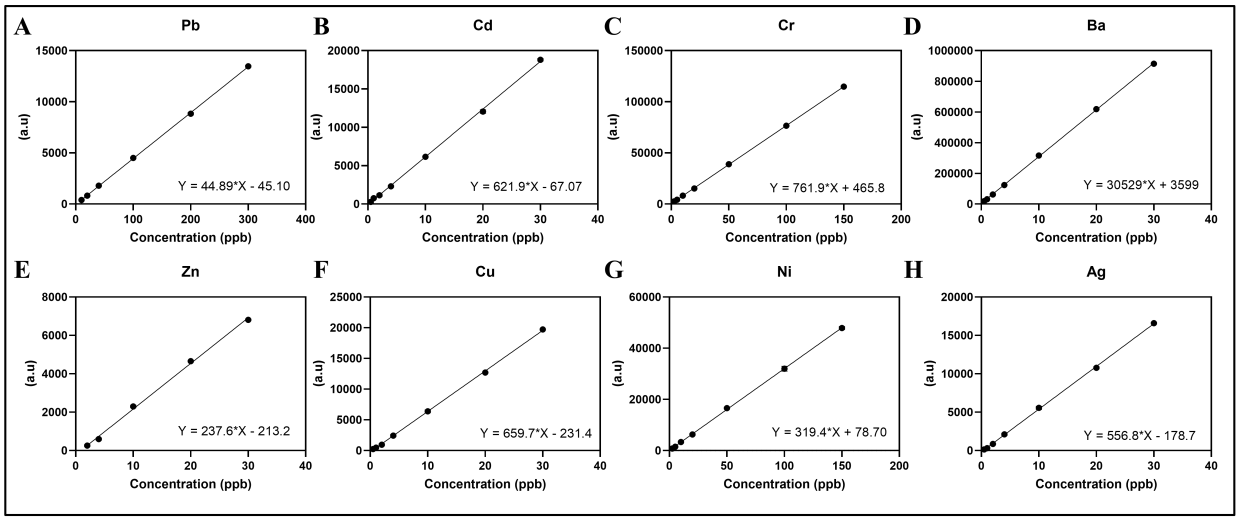

Element	Cup-MNPs (n = 3)	Fork-MNPs (n = 3)	PS-50-PNPs (n = 3)
Pb	< LOD	< LOD	< LOD
Zn	< LOD	< LOD	< LOD
Cd	< LOD	< LOD	< LOD
Cu	< LOD	< LOD	< LOD
Cr	< LOD	< LOD	< LOD
Ni	< LOD	< LOD	< LOD
Ba	< LOD	< LOD	< LOD
Ag	< LOD	< LOD	< LOD

LOD - Limit of Detection

Figure A.1: Inductively Coupled Plasma Optical Emission Spectroscopy (ICP-OES) performed for the detection of commonly used metal contaminants in plastics. For all plastic samples, the contents of lead, zinc, cadmium, copper, chromium, nickel, barium, and silver were below the limit of detection. Accompanying standard curves for the elements (a-h) are presented.

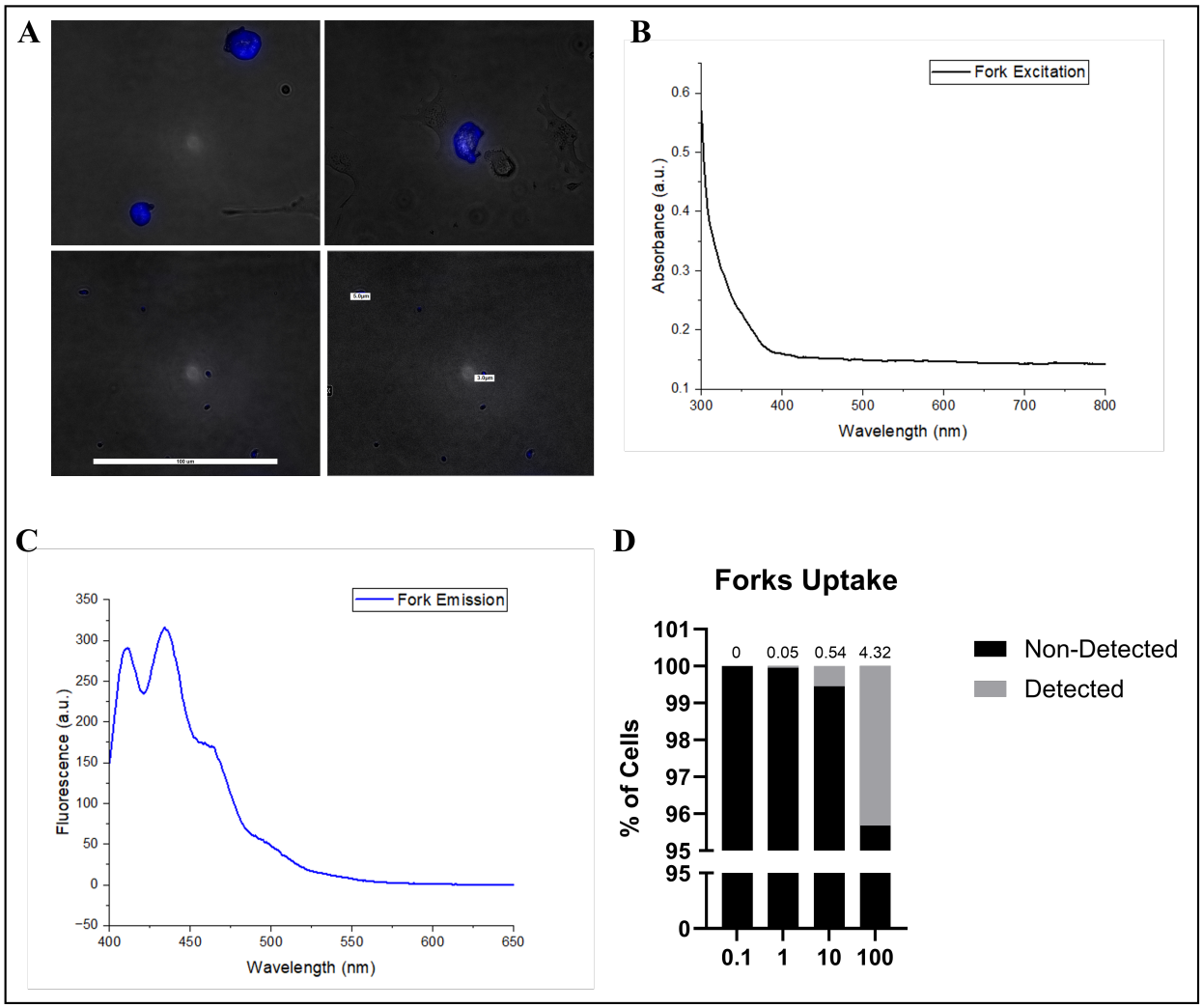

Figure A.2: Autofluorescence of Fork-MNPs. (a) Fork-MNPs visualized through fluorescent microscopy under the DAPI filter on the ECHO Revolution (Excitation 380/30, Emission 450/50). (b) Absorbance of Fork-MNPs plotted, with the corresponding peak excitation band used to capture fluorescent emission spectra (c). (d) Quantification of cells that had uptaken Fork-MNPs based on the autofluorescent principles of the plastic particle, as measured through flow cytometry.

Appendix B

Supplemental Figures for Chapter 3

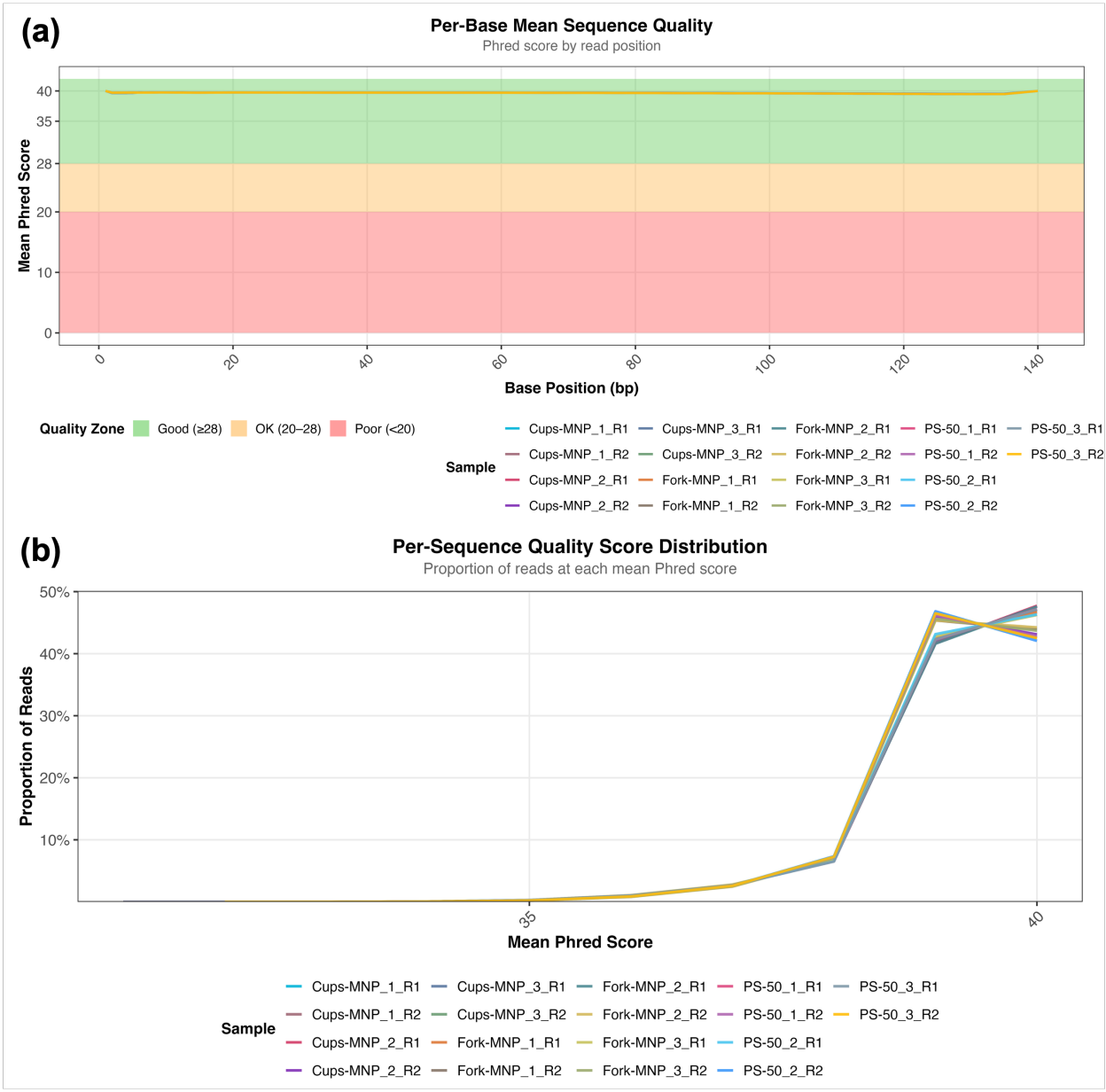

Figure B.1: FastQC Sequence Quality Across Samples. (a) Per-base mean Phred-33 scores plotted across read bases (bp) for each paired-end sample (R1 and R2). All samples maintained mean Phred scores above 35, indicating exceptional read quality after trimming. (b) Per-sequence Phred-33 scores, showing the proportion of reads at each mean quality score. The vast majority of reads were found to be above 38, further validating read quality using the Illumina Novaseq X Plus.

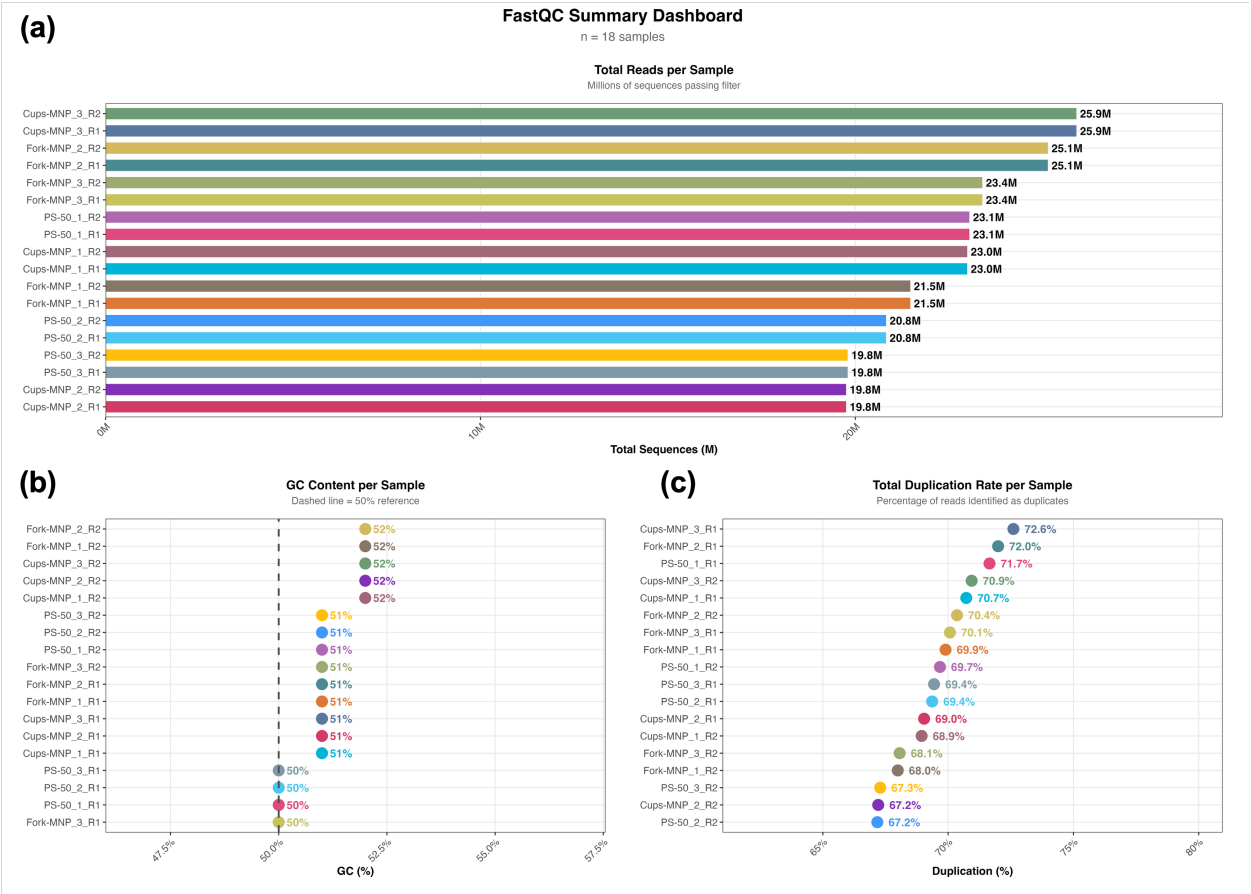

Figure B.2: FastQC Dashboard for Read Contents. (a) Total read counts per paired-end sample were found to range from 19.8M to 25.9M after trimming. (b) GC content per sample ranged from 50 - 52%, consistent with transcriptome composition. (c) Total duplication rates per sample ranging from 67.2 – 72.6%, typical of deep-coverage RNA-seq libraries where highly expressed transcripts produce abundant duplicate reads.

Table B.1: One-way ANOVA results for the top 500 differentially expressed genes across treatment groups (Cup-MNPs, Fork-MNPs, PS-50) as seen in Figure 3.3b. Genes are ranked by BH-adjusted p-value. Z-scores represent sample-average VST-normalized expression relative to the global mean.

Gene Name	**p value**	**padj**	**Cup-MNP Z-Score Average**	**Fork-MNP Z-Score Average**	**PS-50 Z-Score Average**
PPP1R15B	1.438e-05	1.283e-01	-0.7703	-0.5400	1.3103
ENSG00000227230	2.390e-05	1.283e-01	-0.6442	-0.6697	1.3139
MELK	1.904e-05	1.283e-01	-0.7184	-0.5951	1.3135
ANKRD20A2P	6.620e-06	1.283e-01	-1.1682	0.0504	1.1178
ENSG00000225213	3.231e-05	1.388e-01	-0.6987	-0.6123	1.3110
ZNF496-DT	1.105e-04	1.626e-01	1.2761	-0.4187	-0.8574
MTHFD2	2.076e-04	1.626e-01	-0.7307	-0.5588	1.2894
GALNT3	2.498e-04	1.626e-01	-0.9288	-0.3117	1.2405
ITPR1	1.545e-04	1.626e-01	-1.0834	-0.0759	1.1593
HHATL	2.199e-04	1.626e-01	0.9045	0.3473	-1.2518
PLA2G12A	2.485e-04	1.626e-01	-0.7899	-0.4891	1.2790
PLRG1	1.467e-04	1.626e-01	-0.8138	-0.4685	1.2823
GUCY1B1	1.970e-04	1.626e-01	-0.6672	-0.6266	1.2938
SLC30A5	1.232e-04	1.626e-01	-0.7106	-0.5871	1.2978
IFRD1	1.419e-04	1.626e-01	-0.5168	-0.7728	1.2897
SMU1	1.152e-04	1.626e-01	-0.9865	-0.2406	1.2271
PSAT1	1.548e-04	1.626e-01	-0.6251	-0.6717	1.2968
IARS1	9.569e-05	1.626e-01	-0.6236	-0.6785	1.3021
ZNF518A	2.303e-04	1.626e-01	-0.5804	-0.7093	1.2897
LTBP3	2.451e-04	1.626e-01	0.8731	0.3869	-1.2600
CHORDC1	8.172e-05	1.626e-01	-0.8873	-0.3839	1.2713
XPOT	2.256e-04	1.626e-01	-0.7597	-0.5253	1.2850
RN7SL1	2.395e-04	1.626e-01	0.6867	0.6037	-1.2904
RN7SL2	2.248e-04	1.626e-01	0.6986	0.5921	-1.2907
NUPR1	1.460e-04	1.626e-01	-0.2482	-0.9790	1.2273

Gene Name	p value	padj	Cup-MNP Z-Score Average	Fork-MNP Z-Score Average	PS-50 Z-Score Average
CAMKK1	9.490e-05	1.626e-01	0.6299	0.6725	-1.3023
MGAT5B	6.167e-05	1.626e-01	0.8158	0.4762	-1.2919
NARS1	9.333e-05	1.626e-01	-0.7120	-0.5888	1.3008
ENSG00000290058	2.328e-04	1.626e-01	-0.3223	1.2444	-0.9221
CEBPG	6.956e-05	1.626e-01	-0.7054	-0.5988	1.3042
TRIB3	2.297e-04	1.626e-01	-0.7621	-0.5224	1.2844
ENSG00000275496	1.290e-04	1.626e-01	-0.7600	-0.5326	1.2926
MIR155HG	1.599e-04	1.626e-01	0.5040	0.7827	-1.2866
AGRN	4.707e-04	1.914e-01	0.8515	0.4024	-1.2539
ENSG00000289694	6.996e-04	1.914e-01	1.1794	-1.0041	-0.1753
CMPK1	3.548e-04	1.914e-01	-0.8243	-0.4418	1.2662
SSX2IP	6.464e-04	1.914e-01	-0.6729	-0.6008	1.2737
ADAMTSL4	5.609e-04	1.914e-01	0.6847	0.5913	-1.2760
MAP3K21	3.177e-04	1.914e-01	-0.5696	-0.7147	1.2843
ASB3	5.541e-04	1.914e-01	-0.5926	-0.6837	1.2763
MRPL30	3.648e-04	1.914e-01	-0.7252	-0.5559	1.2811
SOWAHC	4.929e-04	1.914e-01	-0.7197	-0.5564	1.2761
TBC1D23	6.736e-04	1.914e-01	-0.5672	-0.7039	1.2711
C4orf3	5.687e-04	1.914e-01	0.8076	0.4527	-1.2604
TARS1	6.628e-04	1.914e-01	-0.8004	-0.4580	1.2584
SGTB	6.695e-04	1.914e-01	-0.5987	-0.6742	1.2729
TNPO1	5.693e-04	1.914e-01	-0.7871	-0.4772	1.2643
CKMT2-AS1	6.586e-04	1.914e-01	0.2414	-1.2040	0.9626
ARSK	3.751e-04	1.914e-01	-0.8237	-0.4416	1.2653
EGR1	5.429e-04	1.914e-01	-0.7921	-0.4722	1.2644
ARHGAP26	5.346e-04	1.914e-01	-0.6377	-0.6404	1.2781
CARMN	4.483e-04	1.914e-01	0.8360	0.4229	-1.2589
BOD1	3.471e-04	1.914e-01	-0.6411	-0.6446	1.2856
POU5F1	4.246e-04	1.914e-01	0.7281	0.5500	-1.2781

Gene Name	p value	padj	Cup-MNP Z-Score Average	Fork-MNP Z-Score Average	PS-50 Z-Score Average
ENSG00000272442	6.480e-04	1.914e-01	-0.6372	1.2743	-0.6372
PRIM2	4.212e-04	1.914e-01	-0.9381	-0.2881	1.2262
PSPH	7.265e-04	1.914e-01	-0.7880	-0.4707	1.2587
ASNS	5.861e-04	1.914e-01	-0.6011	-0.6745	1.2756
TCEA1	6.939e-04	1.914e-01	-0.5946	-0.6774	1.2720
PTEN	4.483e-04	1.914e-01	-0.8300	-0.4303	1.2603
GOT1	3.067e-04	1.914e-01	-0.5976	-0.6889	1.2865
TAF5	4.823e-04	1.914e-01	-0.8392	-0.4174	1.2566
MCMBP	4.687e-04	1.914e-01	-0.6206	-0.6597	1.2803
BTBD10	4.544e-04	1.914e-01	-0.4880	-0.7818	1.2698
NARS2	4.188e-04	1.914e-01	-1.1889	0.1780	1.0109
LNCOG	4.512e-04	1.914e-01	-0.3623	-0.8831	1.2454
PAWR	7.076e-04	1.914e-01	-0.6269	-0.6456	1.2725
APAF1	7.309e-04	1.914e-01	-0.5456	-0.7222	1.2678
TXNRD1	4.649e-04	1.914e-01	-0.5409	-0.7348	1.2757
IPO5	6.198e-04	1.914e-01	-0.6239	-0.6512	1.2751
MMP14	5.328e-04	1.914e-01	1.0714	0.0679	-1.1393
HEATR5A	6.835e-04	1.914e-01	-0.8317	-0.4191	1.2508
ITPKA	4.449e-04	1.914e-01	-0.4411	-0.8214	1.2625
PYGO1	7.015e-04	1.914e-01	-0.8803	-0.3559	1.2362
AARS1	5.674e-04	1.914e-01	-0.5612	-0.7128	1.2739
DUSP3	6.760e-04	1.914e-01	0.9789	0.2159	-1.1949
ARID3A	6.779e-04	1.914e-01	-0.0180	1.1117	-1.0937
IFNL1	7.171e-04	1.914e-01	0.9534	0.2529	-1.2063
BMP2	4.061e-04	1.914e-01	-1.2693	0.7966	0.4727
ETS2	6.273e-04	1.914e-01	-1.2713	0.5514	0.7198
COL18A1	3.924e-04	1.914e-01	0.9694	0.2439	-1.2133
RPL23AP7	5.639e-04	1.914e-01	-0.5745	-0.7005	1.2750
ENSG00000280327	7.427e-04	1.922e-01	0.3176	0.9075	-1.2251

Gene Name	p value	padj	Cup-MNP Z-Score Average	Fork-MNP Z-Score Average	PS-50 Z-Score Average
MYOSLID	7.614e-04	1.947e-01	1.2547	-0.4517	-0.8030
RAB10	8.367e-04	1.962e-01	-0.4308	-0.8183	1.2491
MMUT	8.472e-04	1.962e-01	-0.4288	-0.8197	1.2485
FAM135A	8.590e-04	1.962e-01	-0.5633	-0.7026	1.2658
CNOT4	8.526e-04	1.962e-01	-0.7847	-0.4709	1.2555
MTFR1	8.390e-04	1.962e-01	-0.3775	-0.8604	1.2379
DDX21	8.271e-04	1.962e-01	-0.8706	-0.3645	1.2351
INTS13	8.060e-04	1.962e-01	-0.7689	-0.4907	1.2596
MARS1	8.086e-04	1.962e-01	-0.6790	-0.5897	1.2687
ARFRP1	8.187e-04	1.962e-01	0.8481	0.3940	-1.2421
DGCR8	8.445e-04	1.962e-01	0.5034	0.7569	-1.2603
TBC1D20	8.689e-04	1.964e-01	-0.3691	-0.8661	1.2352
ENSG00000286504	8.943e-04	1.980e-01	-1.2671	0.6597	0.6074
ENSG00000288815	8.937e-04	1.980e-01	0.5411	0.7221	-1.2632
GIGYF1	9.448e-04	2.021e-01	0.7502	0.5084	-1.2585
VPS37A	9.384e-04	2.021e-01	-0.7199	-0.5423	1.2622
TMEM94	9.484e-04	2.021e-01	0.8827	0.3448	-1.2275
GRK3	9.505e-04	2.021e-01	-0.4971	-0.7599	1.2570
MAPK9	9.700e-04	2.023e-01	-0.5028	-0.7545	1.2572
ARIH1	9.794e-04	2.023e-01	-1.0111	-0.1534	1.1645
TMEM205	9.767e-04	2.023e-01	0.6572	0.6079	-1.2651
PDLIM2	9.896e-04	2.024e-01	0.5774	0.6862	-1.2636
PEX13	1.037e-03	2.086e-01	-0.5262	-0.7323	1.2584
ENSG00000271743	1.059e-03	2.086e-01	-1.1062	1.0820	0.0242
SLC26A11	1.044e-03	2.086e-01	0.2023	0.9793	-1.1816
SBF1	1.058e-03	2.086e-01	0.9972	0.1735	-1.1707
SUGT1P2	1.116e-03	2.101e-01	-1.1869	0.2213	0.9656
MAK	1.082e-03	2.101e-01	-1.1871	0.2199	0.9672
CNOT7	1.114e-03	2.101e-01	-0.7064	-0.5528	1.2592

Gene Name	p value	padj	Cup-MNP Z-Score Average	Fork-MNP Z-Score Average	PS-50 Z-Score Average
EML3	1.125e-03	2.101e-01	0.9316	0.2716	-1.2032
GAS6	1.120e-03	2.101e-01	0.9746	0.2073	-1.1819
ENSG00000272872	1.095e-03	2.101e-01	0.6438	0.6189	-1.2627
C11orf91	1.148e-03	2.107e-01	0.6680	0.5929	-1.2609
INHBE	1.145e-03	2.107e-01	-0.7261	-0.5305	1.2566
NAMPT	1.196e-03	2.165e-01	-1.0820	-0.0191	1.1011
NRBF2	1.204e-03	2.165e-01	-0.6497	-0.6105	1.2602
NUCB2	1.210e-03	2.165e-01	-0.6295	-0.6308	1.2603
MARCKSL1	1.634e-03	2.205e-01	0.7899	0.4467	-1.2366
SLC6A9	1.590e-03	2.205e-01	-0.7282	-0.5191	1.2473
CTH	1.420e-03	2.205e-01	-1.0420	-0.0865	1.1285
USP33	1.601e-03	2.205e-01	-0.7414	-0.5040	1.2454
ACBD3	1.521e-03	2.205e-01	-0.9836	-0.1823	1.1659
SH3BP5L	1.335e-03	2.205e-01	0.8416	0.3887	-1.2303
MTIF2	1.643e-03	2.205e-01	-0.6705	-0.5807	1.2511
OBSL1	1.610e-03	2.205e-01	0.7142	0.5342	-1.2484
NCK1	1.334e-03	2.205e-01	-0.4391	-0.8012	1.2403
PTX3	1.655e-03	2.205e-01	-0.9072	-0.2936	1.2008
MUC20-OT1	1.593e-03	2.205e-01	0.4425	0.7940	-1.2365
USP53	1.661e-03	2.205e-01	-0.9738	-0.1944	1.1682
SCLT1	1.562e-03	2.205e-01	-1.0654	-0.0394	1.1048
LARS1	1.549e-03	2.205e-01	-0.8122	-0.4211	1.2333
SKIC2	1.684e-03	2.205e-01	1.0033	0.1462	-1.1495
ENSG00000232702	1.384e-03	2.205e-01	1.0533	-1.1205	0.0672
GARS1	1.677e-03	2.205e-01	-0.7144	-0.5329	1.2472
ENSG00000288096	1.645e-03	2.205e-01	0.7568	0.4856	-1.2423
ABHD17B	1.599e-03	2.205e-01	-1.2263	0.3907	0.8357
RABGAP1	1.414e-03	2.205e-01	-0.7245	-0.5266	1.2511
ARHGAP22	1.274e-03	2.205e-01	0.5856	0.6724	-1.2580

Gene Name	p value	padj	Cup-MNP Z-Score Average	Fork-MNP Z-Score Average	PS-50 Z-Score Average
C10orf88	1.519e-03	2.205e-01	-0.9059	-0.2984	1.2043
COPB1	1.574e-03	2.205e-01	-0.8347	-0.3924	1.2271
FRMD8	1.617e-03	2.205e-01	0.7540	0.4893	-1.2433
PGM2L1	1.612e-03	2.205e-01	-0.7284	-0.5185	1.2469
G2E3	1.450e-03	2.205e-01	-0.8713	-0.3473	1.2186
WARS1	1.363e-03	2.205e-01	-0.6229	-0.6343	1.2572
LDAF1	1.278e-03	2.205e-01	-0.3301	-0.8870	1.2172
ENSG00000255439	1.607e-03	2.205e-01	-0.6004	1.2525	-0.6521
ARMC5	1.446e-03	2.205e-01	0.3408	0.8762	-1.2170
ATP6V0D1-DT	1.287e-03	2.205e-01	0.9646	0.2181	-1.1827
ENSG00000261996	1.441e-03	2.205e-01	0.6585	0.5968	-1.2553
DLG4	1.515e-03	2.205e-01	-0.5213	-0.7275	1.2488
NSF	1.246e-03	2.205e-01	-0.3600	-0.8653	1.2253
CALCOCO2	1.625e-03	2.205e-01	-0.6736	-0.5777	1.2513
RMC1	1.298e-03	2.205e-01	-1.2221	0.3507	0.8714
ENSG00000290812	1.666e-03	2.205e-01	-0.2544	-0.9342	1.1887
RTBDN	1.525e-03	2.205e-01	1.2185	-0.3517	-0.8668
ELL	1.293e-03	2.205e-01	-0.1350	1.1512	-1.0162
LINC02987	1.518e-03	2.205e-01	-0.1548	-1.0006	1.1554
ZNF30	1.425e-03	2.205e-01	-1.1657	0.1777	0.9880
PRNP	1.552e-03	2.205e-01	-0.7708	-0.4709	1.2418
KCNG1	1.465e-03	2.205e-01	-0.6172	-0.6381	1.2553
SOX18	1.465e-03	2.205e-01	-0.8964	-0.3129	1.2093
LEPR	1.893e-03	2.224e-01	-0.7022	-0.5425	1.2447
NIBAN1	1.773e-03	2.224e-01	-0.6049	-0.6449	1.2498
MCFD2	1.880e-03	2.224e-01	-0.3932	-0.8294	1.2227
GFPT1	1.723e-03	2.224e-01	-0.7294	-0.5154	1.2447
ANAPC1P2	1.797e-03	2.224e-01	-0.9058	-0.2926	1.1984
UBE2D3	1.813e-03	2.224e-01	-0.7015	-0.5446	1.2461

Gene Name	p value	padj	Cup-MNP Z-Score Average	Fork-MNP Z-Score Average	PS-50 Z-Score Average
NCOA7	1.873e-03	2.224e-01	-0.7152	-0.5286	1.2438
LURAP1L-AS1	1.895e-03	2.224e-01	0.4929	-1.2395	0.7465
SLC31A1	1.839e-03	2.224e-01	-0.8593	-0.3553	1.2146
POLD3	1.851e-03	2.224e-01	-0.4171	-0.8109	1.2279
USP12	1.867e-03	2.224e-01	-0.3800	-0.8400	1.2200
WDR76	1.763e-03	2.224e-01	-0.7987	-0.4337	1.2323
MIR22HG	1.801e-03	2.224e-01	0.6162	0.6334	-1.2496
FN3KRP	1.738e-03	2.224e-01	1.0971	-0.0287	-1.0684
EPG5	1.822e-03	2.224e-01	-1.0619	-0.0388	1.1008
ENSG00000281383	1.834e-03	2.224e-01	0.6763	0.5713	-1.2476
GART	1.830e-03	2.224e-01	-0.3036	-0.8975	1.2011
EWSR1	1.732e-03	2.224e-01	0.9476	0.2332	-1.1807
SUN2	1.748e-03	2.224e-01	0.8057	0.4253	-1.2310
SLC30A1	1.919e-03	2.228e-01	-1.2036	0.3168	0.8867
NDUFB5	1.919e-03	2.228e-01	-0.7010	-0.5434	1.2444
ATL2	1.983e-03	2.277e-01	-0.9529	-0.2199	1.1728
CD274	1.975e-03	2.277e-01	-0.9069	-0.2876	1.1945
DHTKD1	2.002e-03	2.287e-01	-0.4669	-0.7674	1.2344
EIF4A2	2.015e-03	2.289e-01	-0.6236	-0.6227	1.2463
ALDH1L2	2.044e-03	2.299e-01	-0.6738	-0.5707	1.2444
SNX6	2.039e-03	2.299e-01	-0.5922	-0.6532	1.2454
MOCOS	2.058e-03	2.300e-01	-0.4885	-0.7481	1.2366
ZNF512B	2.067e-03	2.300e-01	0.8894	0.3104	-1.1998
RCCD1	2.123e-03	2.339e-01	0.7297	0.5085	-1.2381
LINC02693	2.123e-03	2.339e-01	-0.8429	-0.3717	1.2146
TRMT1L	2.254e-03	2.362e-01	-0.5330	-0.7058	1.2388
ITPRID2	2.170e-03	2.362e-01	-0.7214	-0.5171	1.2384
RN7SL4P	2.206e-03	2.362e-01	0.5376	0.7023	-1.2399
RN7SL689P	2.242e-03	2.362e-01	0.4165	0.8060	-1.2225

Gene Name	**p value**	**padj**	**Cup-MNP Z-Score Average**	**Fork-MNP Z-Score Average**	**PS-50 Z-Score Average**
COG5	2.262e-03	2.362e-01	-0.9212	-0.2618	1.1830
ENSG00000285257	2.253e-03	2.362e-01	-1.0411	-0.0674	1.1085
IPO7	2.184e-03	2.362e-01	-0.6966	-0.5441	1.2407
ENSG00000203392	2.171e-03	2.362e-01	0.9864	0.1633	-1.1497
KLF2	2.277e-03	2.362e-01	-0.6990	-0.5402	1.2392
LIG1	2.268e-03	2.362e-01	1.1029	-0.0557	-1.0472
PSMD10P1	2.253e-03	2.362e-01	1.1319	-1.0106	-0.1213
ENSG00000272669	2.195e-03	2.362e-01	1.1132	-0.0764	-1.0369
RAB39A	2.299e-03	2.374e-01	-0.1792	-0.9749	1.1542
PKP3	2.372e-03	2.437e-01	0.2913	0.8993	-1.1906
RLF	2.413e-03	2.448e-01	-1.2280	0.7675	0.4604
TIPRL	2.439e-03	2.448e-01	-0.6311	-0.6092	1.2403
SPX	2.429e-03	2.448e-01	-0.6955	-0.5418	1.2373
LMAN1	2.438e-03	2.448e-01	-0.7186	-0.5163	1.2349
CSE1L	2.406e-03	2.448e-01	-0.7272	-0.5070	1.2343
USP19	2.483e-03	2.460e-01	0.6825	0.5551	-1.2376
MOCS2	2.532e-03	2.460e-01	-0.1613	-0.9834	1.1446
EGR2	2.497e-03	2.460e-01	-0.0736	1.1084	-1.0348
CDR2	2.531e-03	2.460e-01	-0.1842	-0.9691	1.1533
IGFBP4	2.475e-03	2.460e-01	0.9166	0.2648	-1.1814
ENSG00000279207	2.516e-03	2.460e-01	1.2221	-0.4324	-0.7896
LAMA5	2.518e-03	2.460e-01	0.8900	0.3019	-1.1919
PRORSD1P	2.582e-03	2.460e-01	0.8038	0.4141	-1.2179
PAPOLG	2.644e-03	2.460e-01	-0.6673	-0.5691	1.2364
LYSMD3	2.650e-03	2.460e-01	-0.3535	-0.8505	1.2039
ASCC3	2.642e-03	2.460e-01	-0.7669	-0.4579	1.2248
DNAJC30	2.565e-03	2.460e-01	0.7327	0.4986	-1.2313
DUSP6	2.658e-03	2.460e-01	-0.8701	-0.3271	1.1972
UBE2G1	2.578e-03	2.460e-01	-0.8806	-0.3140	1.1946

Gene Name	p value	padj	Cup-MNP Z-Score Average	Fork-MNP Z-Score Average	PS-50 Z-Score Average
CSNK1D	2.552e-03	2.460e-01	0.8063	0.4114	-1.2177
SKA1	2.615e-03	2.460e-01	-0.6507	-0.5868	1.2375
ENSG00000280800	2.617e-03	2.460e-01	0.6947	0.5402	-1.2348
HSPA13	2.590e-03	2.460e-01	-0.6238	-0.6146	1.2384
FBXL5	2.684e-03	2.463e-01	-0.6188	-0.6185	1.2372
ENSG00000226699	2.682e-03	2.463e-01	-0.9182	1.1773	-0.2590
BVES	2.727e-03	2.492e-01	-0.4657	-0.7593	1.2250
C1orf43	2.798e-03	2.494e-01	-0.7450	-0.4814	1.2264
C2orf74-DT	2.835e-03	2.494e-01	0.5613	-1.2337	0.6724
RND3	2.833e-03	2.494e-01	-0.9204	-0.2534	1.1738
CEP120	2.771e-03	2.494e-01	-0.6742	-0.5602	1.2344
TTK	2.773e-03	2.494e-01	-0.5579	-0.6763	1.2342
SLC6A15	2.840e-03	2.494e-01	-0.6356	-0.5995	1.2351
PPTC7	2.822e-03	2.494e-01	-0.9921	-0.1417	1.1338
EXOC5	2.864e-03	2.494e-01	-0.6857	-0.5467	1.2324
TMEM170A	2.869e-03	2.494e-01	-0.7122	-0.5177	1.2299
ZNF134	2.779e-03	2.494e-01	0.7192	-1.2302	0.5110
ENSG00000280614	2.867e-03	2.494e-01	0.7193	0.5097	-1.2291
CFAP410	2.808e-03	2.494e-01	0.5969	0.6386	-1.2355
ABLIM1	2.904e-03	2.512e-01	-1.2064	0.3763	0.8301
EXPH5	2.912e-03	2.512e-01	-0.5106	-0.7180	1.2286
NMNAT1	2.988e-03	2.516e-01	-0.5797	-0.6531	1.2329
MREG	2.981e-03	2.516e-01	-0.9917	-0.1396	1.1313
ZDHHC2	2.966e-03	2.516e-01	-0.4990	-0.7278	1.2267
WWP1	2.955e-03	2.516e-01	-0.6297	-0.6042	1.2339
VLDLR	2.982e-03	2.516e-01	-0.8674	-0.3260	1.1934
GABPB1-IT1	2.968e-03	2.516e-01	0.7584	0.4636	-1.2220
CNGA1	3.016e-03	2.522e-01	-0.6105	-0.6228	1.2332
ENSG00000260400	3.018e-03	2.522e-01	-0.9015	-0.2781	1.1796

Gene Name	p value	padj	Cup-MNP Z-Score Average	Fork-MNP Z-Score Average	PS-50 Z-Score Average
ZNF322	3.053e-03	2.523e-01	-0.6036	-0.6291	1.2327
PPP2R5C	3.066e-03	2.523e-01	-1.0142	-0.0997	1.1139
ENSG00000267342	3.039e-03	2.523e-01	1.1462	-0.1796	-0.9666
ENSG00000281181	3.056e-03	2.523e-01	0.6991	0.5298	-1.2289
RBBP5	3.221e-03	2.528e-01	-0.5348	-0.6928	1.2276
YIPF4	3.253e-03	2.528e-01	-0.7577	-0.4609	1.2186
ATF2	3.169e-03	2.528e-01	-0.5423	-0.6864	1.2287
ASNSD1	3.182e-03	2.528e-01	-0.8498	-0.3468	1.1966
IL1RAP	3.188e-03	2.528e-01	-1.0208	-0.0858	1.1067
UBA6	3.270e-03	2.528e-01	-0.7963	-0.4142	1.2105
FBXO5	3.207e-03	2.528e-01	-0.7284	-0.4954	1.2237
LURAP1L	3.107e-03	2.528e-01	-0.5483	-0.6816	1.2298
SPAG8	3.117e-03	2.528e-01	0.3881	0.8187	-1.2068
NIBAN2	3.096e-03	2.528e-01	0.7212	0.5048	-1.2260
OLR1	3.231e-03	2.528e-01	-1.1803	0.2880	0.8923
BLM	3.155e-03	2.528e-01	-1.0901	0.0486	1.0416
CES4A	3.168e-03	2.528e-01	0.8005	0.4102	-1.2108
MAP1LC3B	3.182e-03	2.528e-01	-0.6619	-0.5683	1.2302
CRLF3	3.262e-03	2.528e-01	-0.5510	-0.6773	1.2283
PMAIP1	3.272e-03	2.528e-01	-0.7675	-0.4490	1.2166
MAPK1	3.200e-03	2.528e-01	-0.9497	-0.2037	1.1534
ENSG00000289960	3.306e-03	2.544e-01	-0.6241	1.2300	-0.6059
TYW3	3.337e-03	2.550e-01	-0.8656	-0.3236	1.1892
ANKRD42	3.330e-03	2.550e-01	-0.7669	-0.4491	1.2160
SEL1L3	3.354e-03	2.552e-01	-0.7174	-0.5060	1.2234
SMC5-DT	3.363e-03	2.552e-01	1.0787	-0.0286	-1.0501
ETFB	3.378e-03	2.554e-01	1.1302	-0.1463	-0.9838
RAP1GDS1	3.557e-03	2.555e-01	-0.7028	-0.5200	1.2228
SLC7A11	3.514e-03	2.555e-01	-0.7178	-0.5038	1.2216

Gene Name	p value	padj	Cup-MNP Z-Score Average	Fork-MNP Z-Score Average	PS-50 Z-Score Average
MAT2B	3.442e-03	2.555e-01	-0.6774	-0.5490	1.2263
PDCD1LG2	3.534e-03	2.555e-01	-0.7747	-0.4373	1.2120
CHEK1	3.434e-03	2.555e-01	-0.7428	-0.4761	1.2190
ARHGEF25	3.523e-03	2.555e-01	1.0728	-0.0195	-1.0533
ZNF770	3.445e-03	2.555e-01	-0.8084	-0.3969	1.2053
MAPK6	3.501e-03	2.555e-01	-0.8303	-0.3683	1.1986
FHOD1	3.510e-03	2.555e-01	0.7574	0.4582	-1.2156
CMTR2	3.541e-03	2.555e-01	-0.8951	-0.2800	1.1750
ENSG00000260279	3.422e-03	2.555e-01	0.7800	0.4323	-1.2123
CADM4	3.549e-03	2.555e-01	0.9501	0.1980	-1.1481
ENSG00000268750	3.510e-03	2.555e-01	0.2486	-1.1656	0.9171
USP25	3.525e-03	2.555e-01	-0.5326	-0.6917	1.2242
URB1-AS1	3.464e-03	2.555e-01	0.5784	0.6493	-1.2276
ANKIB1	3.585e-03	2.566e-01	-0.4948	-0.7250	1.2198
CLTCL1	3.598e-03	2.567e-01	-0.6870	-0.5368	1.2239
MXRA8	3.723e-03	2.575e-01	0.5762	0.6488	-1.2249
EPRS1	3.740e-03	2.575e-01	-0.7260	-0.4920	1.2180
FOXN2	3.694e-03	2.575e-01	-0.7976	-0.4075	1.2051
GFM2	3.647e-03	2.575e-01	-0.9203	-0.2419	1.1622
PTTG1	3.665e-03	2.575e-01	0.5219	0.7001	-1.2219
CDC5L	3.740e-03	2.575e-01	-0.8415	-0.3508	1.1923
UHRF2	3.685e-03	2.575e-01	-0.7522	-0.4624	1.2146
UBQLN1	3.638e-03	2.575e-01	-0.8016	-0.4032	1.2048
KRT80	3.727e-03	2.575e-01	0.5817	0.6434	-1.2251
PCK2	3.737e-03	2.575e-01	-0.5139	-0.7066	1.2205
TNFAIP2	3.667e-03	2.575e-01	0.1553	0.9757	-1.1311
ZFYVE9	3.762e-03	2.579e-01	-0.6327	-0.5924	1.2251
WDR5	3.771e-03	2.579e-01	0.8135	0.3866	-1.2001
CHUK	3.818e-03	2.595e-01	-0.7476	-0.4662	1.2139

Gene Name	p value	padj	Cup-MNP Z-Score Average	Fork-MNP Z-Score Average	PS-50 Z-Score Average
MED24	3.811e-03	2.595e-01	0.6740	0.5486	-1.2226
MTO1	3.836e-03	2.599e-01	-0.7437	-0.4707	1.2143
PARP3	3.883e-03	2.611e-01	0.7829	0.4234	-1.2063
IPO8	3.897e-03	2.611e-01	-0.4336	-0.7744	1.2080
SCYL2	3.873e-03	2.611e-01	-0.9566	-0.1833	1.1399
MT1X	3.903e-03	2.611e-01	0.5689	0.6540	-1.2229
JMY	3.975e-03	2.651e-01	-0.7983	-0.4034	1.2017
ATAD2	4.026e-03	2.677e-01	-0.6118	-0.6109	1.2227
SIPA1L2	4.081e-03	2.683e-01	0.5536	-1.2204	0.6668
FAM171B	4.095e-03	2.683e-01	-0.6342	-0.5875	1.2217
SHMT2	4.093e-03	2.683e-01	-0.6002	-0.6218	1.2220
MVP	4.083e-03	2.683e-01	0.6250	0.5970	-1.2220
SNTB2	4.098e-03	2.683e-01	-0.8206	-0.3738	1.1945
MED8	4.135e-03	2.693e-01	-1.2034	0.4195	0.7839
ALPG	4.137e-03	2.693e-01	0.0174	1.0492	-1.0665
FBXO3	4.160e-03	2.699e-01	-0.4265	-0.7780	1.2044
MAP3K6	4.316e-03	2.700e-01	0.7798	0.4227	-1.2024
SDC3	4.435e-03	2.700e-01	0.8271	0.3618	-1.1889
SARS1	4.437e-03	2.700e-01	-0.5831	-0.6354	1.2185
CHRNB2	4.328e-03	2.700e-01	1.2161	-0.6908	-0.5253
THBS3-AS1	4.640e-03	2.700e-01	0.4809	0.7278	-1.2087
DESI2	4.418e-03	2.700e-01	-0.8068	-0.3881	1.1948
ENSG00000288988	4.740e-03	2.700e-01	0.0725	1.0151	-1.0876
CHMP2B	4.721e-03	2.700e-01	-0.3593	-0.8268	1.1860
HACD2	4.692e-03	2.700e-01	-0.9461	-0.1893	1.1354
IL20RB	4.454e-03	2.700e-01	-0.0771	-1.0148	1.0919
ZBTB12BP	4.644e-03	2.700e-01	-0.5759	1.2165	-0.6405
ATP10D	4.527e-03	2.700e-01	-0.1530	-0.9700	1.1230
GSTCD	4.491e-03	2.700e-01	-0.5241	-0.6905	1.2146

Gene Name	p value	padj	Cup-MNP Z-Score Average	Fork-MNP Z-Score Average	PS-50 Z-Score Average
SEC24B	4.472e-03	2.700e-01	-0.7774	-0.4240	1.2014
SMARCA5	4.211e-03	2.700e-01	-0.8312	-0.3589	1.1901
RAD1	4.585e-03	2.700e-01	-0.9129	-0.2413	1.1542
MIER3	4.608e-03	2.700e-01	-0.7294	-0.4794	1.2088
FHIP2B	4.649e-03	2.700e-01	0.7473	0.4582	-1.2055
KIF12	4.627e-03	2.700e-01	0.8093	0.3827	-1.1920
HERC4	4.468e-03	2.700e-01	-0.6308	-0.5876	1.2183
PCBD1	4.688e-03	2.700e-01	0.9689	0.1527	-1.1217
VSIR	4.395e-03	2.700e-01	0.9523	0.1833	-1.1355
TRUB1	4.487e-03	2.700e-01	-0.8637	-0.3124	1.1761
ENSG00000278518	4.294e-03	2.700e-01	0.4026	0.7962	-1.1988
EPS8L2	4.687e-03	2.700e-01	0.8540	0.3235	-1.1775
EIF4G2	4.176e-03	2.700e-01	-0.6721	-0.5470	1.2191
PIGCP1	4.270e-03	2.700e-01	-0.5935	1.2202	-0.6267
CTSF	4.493e-03	2.700e-01	0.8503	0.3306	-1.1808
RNF41	4.590e-03	2.700e-01	-0.7950	-0.4011	1.1961
STAT6	4.505e-03	2.700e-01	0.6561	0.5609	-1.2170
GPR180	4.731e-03	2.700e-01	-0.9368	-0.2035	1.1402
DHRS1	4.320e-03	2.700e-01	1.1275	-0.1603	-0.9672
PALS1	4.691e-03	2.700e-01	-1.1248	0.1609	0.9639
ENSG00000259033	4.189e-03	2.700e-01	0.7802	0.4234	-1.2036
UBL7	4.249e-03	2.700e-01	0.6395	0.5807	-1.2201
ENSG00000276571	4.617e-03	2.700e-01	-0.7969	1.1953	-0.3985
ENSG00000260757	4.474e-03	2.700e-01	0.7132	0.4990	-1.2123
CHMP1A	4.420e-03	2.700e-01	0.8707	0.3035	-1.1742
VAMP2	4.734e-03	2.700e-01	0.8470	0.3324	-1.1794
TVP23B	4.322e-03	2.700e-01	-0.8166	-0.3765	1.1932
AKAP10	4.722e-03	2.700e-01	0.1573	-1.1232	0.9659
U2AF2	4.531e-03	2.700e-01	0.8745	0.2970	-1.1715

Gene Name	p value	padj	Cup-MNP Z-Score Average	Fork-MNP Z-Score Average	PS-50 Z-Score Average
CTSA	4.550e-03	2.700e-01	0.6132	0.6046	-1.2179
ENSG00000223901	4.668e-03	2.700e-01	0.7337	0.4738	-1.2075
XBP1	4.567e-03	2.700e-01	-0.8799	-0.2891	1.1690
APOL1	4.698e-03	2.700e-01	0.7214	0.4876	-1.2091
DCAF10	4.760e-03	2.704e-01	-0.6935	-0.5184	1.2118
SRGAP2B	4.878e-03	2.714e-01	-0.8406	-0.3395	1.1801
LBH	4.854e-03	2.714e-01	0.0685	1.0165	-1.0850
SMIM13	4.872e-03	2.714e-01	-0.7420	-0.4623	1.2043
HOXC10	4.829e-03	2.714e-01	-1.1539	0.9076	0.2462
DDIT3	4.861e-03	2.714e-01	-0.9331	-0.2076	1.1407
LARP6	4.798e-03	2.714e-01	-0.4074	-0.7883	1.1956
CWC25	4.863e-03	2.714e-01	0.0989	0.9994	-1.0983
SLC9A8	4.857e-03	2.714e-01	-0.2287	1.1479	-0.9192
SP3	5.044e-03	2.738e-01	-0.5707	-0.6422	1.2129
ATG12	5.036e-03	2.738e-01	-0.7932	-0.3990	1.1922
PRR7-AS1	4.990e-03	2.738e-01	0.6370	0.5766	-1.2136
RN7SK	5.048e-03	2.738e-01	0.0356	1.0328	-1.0683
UBE3C	5.020e-03	2.738e-01	-0.6547	-0.5579	1.2125
ADAM32	4.993e-03	2.738e-01	0.5360	-1.2114	0.6754
DENND10	4.961e-03	2.738e-01	-0.5923	-0.6219	1.2142
ACOT1	4.962e-03	2.738e-01	0.5351	0.6764	-1.2116
RAB3D	5.024e-03	2.738e-01	-0.4125	-0.7823	1.1949
TRIOBP	4.989e-03	2.738e-01	1.0315	0.0389	-1.0703
SERPINE2	5.081e-03	2.742e-01	-0.5676	-0.6449	1.2125
ENSG00000260877	5.079e-03	2.742e-01	1.1517	-0.2452	-0.9065
C1orf159	5.175e-03	2.744e-01	0.7561	0.4429	-1.1990
COL16A1	5.163e-03	2.744e-01	0.4626	0.7395	-1.2021
SLC39A1	5.178e-03	2.744e-01	0.4987	0.7078	-1.2065
PLS1	5.181e-03	2.744e-01	-0.6151	-0.5974	1.2125

Gene Name	p value	padj	Cup-MNP Z-Score Average	Fork-MNP Z-Score Average	PS-50 Z-Score Average
FIP1L1	5.212e-03	2.744e-01	-0.8127	-0.3727	1.1853
STK38L	5.145e-03	2.744e-01	-0.5761	-0.6362	1.2123
SKA3	5.179e-03	2.744e-01	-0.6349	-0.5771	1.2121
SREBF1	5.203e-03	2.744e-01	0.6287	0.5833	-1.2120
S1PR4	5.163e-03	2.744e-01	0.7101	0.4962	-1.2063
CRNKL1	5.207e-03	2.744e-01	-0.8689	-0.2976	1.1666
SFXN3	5.230e-03	2.746e-01	0.9257	0.2148	-1.1405
WDR41	5.261e-03	2.749e-01	-0.7466	-0.4533	1.2000
LINC01271	5.248e-03	2.749e-01	0.7463	0.4538	-1.2001
HENMT1	5.360e-03	2.761e-01	1.2051	-0.7064	-0.4987
INTS7	5.400e-03	2.761e-01	-1.1480	0.2407	0.9072
RAB3GAP1	5.379e-03	2.761e-01	-0.7663	-0.4289	1.1951
CLOCK	5.349e-03	2.761e-01	-0.9468	-0.1807	1.1275
ENSG00000289112	5.369e-03	2.761e-01	0.8664	-1.1659	0.2995
ZNF707	5.452e-03	2.761e-01	1.0667	-0.0380	-1.0286
PUM3	5.334e-03	2.761e-01	-0.6660	-0.5432	1.2092
PPP1CC	5.340e-03	2.761e-01	-0.6222	-0.5888	1.2111
ZNF668	5.441e-03	2.761e-01	1.2082	-0.5413	-0.6669
SEPTIN4	5.427e-03	2.761e-01	0.9674	0.1464	-1.1138
IL11	5.403e-03	2.761e-01	0.1343	0.9749	-1.1092
HM13-IT1	5.421e-03	2.761e-01	-1.1616	0.8759	0.2857
ZNF295-AS1	5.337e-03	2.761e-01	-0.0345	1.0658	-1.0313
ANKRD13C	5.497e-03	2.771e-01	-0.4149	-0.7769	1.1918
NFU1	5.495e-03	2.771e-01	-0.2189	-0.9212	1.1400
ZNF330	5.559e-03	2.771e-01	-0.8906	-0.2634	1.1540
STAM	5.522e-03	2.771e-01	-1.0372	-0.0207	1.0579
ENSG00000249456	5.545e-03	2.771e-01	-1.0641	0.0339	1.0302
CDC42BPG	5.562e-03	2.771e-01	0.9458	0.1800	-1.1257
C18orf54	5.549e-03	2.771e-01	-0.3231	-0.8479	1.1710

Gene Name	p value	padj	Cup-MNP Z-Score Average	Fork-MNP Z-Score Average	PS-50 Z-Score Average
RSBN1L	5.585e-03	2.777e-01	-0.8061	-0.3776	1.1837
ZMYM4	5.676e-03	2.790e-01	-0.5861	-0.6223	1.2084
CISH	5.678e-03	2.790e-01	1.1731	-0.8383	-0.3348
PPIP5K2	5.656e-03	2.790e-01	-0.7186	-0.4825	1.2010
RRM1	5.674e-03	2.790e-01	-0.6467	-0.5608	1.2076
NAGPA	5.642e-03	2.790e-01	1.0279	0.0371	-1.0649
PDK1	5.826e-03	2.798e-01	-0.0808	1.0837	-1.0029
SGO1	5.850e-03	2.798e-01	-0.9641	-0.1472	1.1113
STAC	5.844e-03	2.798e-01	-0.6805	-0.5234	1.2039
PPP1R2	5.791e-03	2.798e-01	-0.7792	-0.4095	1.1887
SMAD5	5.830e-03	2.798e-01	-0.5748	-0.6321	1.2069
GOPC	5.714e-03	2.798e-01	-0.6837	-0.5209	1.2046
ARFGEF1	5.832e-03	2.798e-01	-0.5835	-0.6236	1.2072
UBE2W	5.794e-03	2.798e-01	-0.5105	-0.6926	1.2031
AZIN1	5.823e-03	2.798e-01	-1.0132	-0.0622	1.0754
PCGF5	5.757e-03	2.798e-01	-0.6416	-0.5655	1.2072
TMEM132D	5.845e-03	2.798e-01	-0.6760	-0.5283	1.2043
SNORD3A	5.828e-03	2.798e-01	-0.3644	1.1791	-0.8147
EPB41L4A	5.872e-03	2.802e-01	0.0175	-1.0540	1.0365
ENSG00000291208	5.891e-03	2.805e-01	0.8589	0.3049	-1.1638
MFGE8	5.905e-03	2.806e-01	0.7237	0.4745	-1.1982
FLAD1	5.938e-03	2.815e-01	0.4540	0.7411	-1.1951
CUEDC1	5.972e-03	2.820e-01	0.7460	0.4480	-1.1940
TTC39C	5.974e-03	2.820e-01	-1.1059	0.1356	0.9703
TAF1B	6.019e-03	2.831e-01	-1.0339	-0.0208	1.0546
SDCBP	6.037e-03	2.831e-01	-0.7145	-0.4840	1.1985
CTTN	6.038e-03	2.831e-01	0.7827	0.4031	-1.1858
OGFR	6.074e-03	2.842e-01	0.9441	0.1772	-1.1213
ENSG00000270696	6.121e-03	2.858e-01	-0.5534	1.2039	-0.6505

Gene Name	p value	padj	Cup-MNP Z-Score Average	Fork-MNP Z-Score Average	PS-50 Z-Score Average
ZC3H8	6.148e-03	2.858e-01	-1.1961	0.4711	0.7250
ENSG00000289182	6.148e-03	2.858e-01	0.8551	0.3078	-1.1629
RTCA-AS1	6.293e-03	2.867e-01	0.2390	0.9024	-1.1414
SLC25A24	6.412e-03	2.867e-01	-0.6689	-0.5316	1.2005
SYT14	6.539e-03	2.867e-01	-0.8844	-0.2631	1.1475
XPO1	6.281e-03	2.867e-01	-0.8483	-0.3159	1.1642
HS6ST1	6.572e-03	2.867e-01	0.5958	0.6062	-1.2020
TCEA1P2	6.499e-03	2.867e-01	-0.7277	-0.4652	1.1929
SEC62	6.346e-03	2.867e-01	-0.6646	-0.5367	1.2013
USO1	6.581e-03	2.867e-01	-0.7087	-0.4864	1.1951
HNRNPD	6.574e-03	2.867e-01	0.7487	0.4400	-1.1887
OCLN	6.463e-03	2.867e-01	-0.8273	-0.3424	1.1697
PNPLA8	6.550e-03	2.867e-01	-0.7432	-0.4467	1.1899
INTS8	6.532e-03	2.867e-01	-0.7265	-0.4663	1.1928
GPAA1	6.518e-03	2.867e-01	0.7209	0.4729	-1.1938
SNAPC3	6.327e-03	2.867e-01	-0.8410	-0.3253	1.1663
COL5A1	6.434e-03	2.867e-01	0.9490	0.1658	-1.1148
PRXL2A	6.312e-03	2.867e-01	-0.4401	-0.7503	1.1904
EXOC6	6.295e-03	2.867e-01	-0.4725	-0.7228	1.1953
RCN1	6.515e-03	2.867e-01	-0.4587	-0.7332	1.1919
ENSG00000280202	6.532e-03	2.867e-01	-0.6511	-0.5498	1.2008
BTG1	6.217e-03	2.867e-01	-0.8502	-0.3138	1.1640
SIX4	6.292e-03	2.867e-01	-0.5088	-0.6906	1.1994
ACOT2	6.255e-03	2.867e-01	0.6394	0.5641	-1.2035
ZSCAN2	6.491e-03	2.867e-01	0.4950	0.7016	-1.1966
ITGAE	6.454e-03	2.867e-01	0.8899	0.2558	-1.1458
METTL4	6.566e-03	2.867e-01	-0.8389	-0.3261	1.1650
CXXC1	6.467e-03	2.867e-01	1.0968	-0.1209	-0.9759
BCL2	6.554e-03	2.867e-01	-0.9179	-0.2134	1.1312

Gene Name	**p value**	**padj**	**Cup-MNP Z-Score Average**	**Fork-MNP Z-Score Average**	**PS-50 Z-Score Average**
CDC37	6.353e-03	2.867e-01	0.8313	0.3381	-1.1694
CPT1C	6.388e-03	2.867e-01	0.8534	0.3079	-1.1613
TOP1	6.388e-03	2.867e-01	-0.7096	-0.4868	1.1964
SMTN	6.323e-03	2.867e-01	0.4259	0.7621	-1.1880
LONRF1	6.605e-03	2.868e-01	-0.9541	-0.1558	1.1099
LIME1	6.611e-03	2.868e-01	0.8016	0.3746	-1.1762
FUS	6.630e-03	2.871e-01	0.6833	0.5143	-1.1976
CEP83-DT	6.692e-03	2.892e-01	0.3905	0.7885	-1.1790
GPT2	6.737e-03	2.905e-01	-0.5708	-0.6296	1.2004
IFITM10	6.798e-03	2.916e-01	1.1986	-0.5422	-0.6564
L2HGDH	6.801e-03	2.916e-01	-0.5384	-0.6600	1.1983